Development of Rheometric Tools to Investigate and Model Extrusion Flow Instabilities

Zur Erlangung des akademischen Grades eines
Doktors der Naturwissenschaften
(Dr. rer. nat.)
von der KIT-Fakultät für Chemie und Biowissenschaften
des Karlsruher Instituts für Technologie (KIT)
genehmigte
Dissertation
von
M. Eng. Christos Georgantopoulos
aus
Diakopto, Achaias, Greece

A ship in harbor is safe, but that is not what ships are built for…
Albert Einstein and John A. Shedd

This thesis is dedicated to each and everyone who have left their own countries to do what they love.

Die Arbeiten in dieser Arbeit wurden im Zeitraum von Oktober 2018 bis June 2022 am Institut für Technische Chemie und Polymerchemie (ITCP) des Karlsruher Instituts für Technologie (KIT) unter der Betreuung von Prof. Dr. Manfred Wilhelm durchgeführt.

Hiermit versichere ich, dass ich die vorgelegte Arbeit selbstständig verfasst habe, dass ich die verwendeten Quellen und Hilfsmittel sowie die Arbeitsstellen vollständig angegeben habe, die anderen Arbeiten sind im Wortlaut oder Sinn übernommen, entsprechend gekennzeichnet.

Christos Georgantopoulos
Karlsruhe,

Zusammenfassung

Im Rahmen dieser Arbeit wurden rheologische Charakterisierungsmethoden entwickelt und eingesetzt, um die zeitlichen und räumlichen Eigenschaften von Instabilitäten des Schmelzflusses während der Extrusion zu charakterisieren. Die experimentellen Daten zu den zeitlichen und räumlichen Eigenschaften von Schmelzfluss-instabilitäten, die mit den Charakterisierungsmethoden gewonnen wurden, wurden durch qualitative Modelle aus der Literatur modelliert. Zusätzlich zu den existierenden qualitativen Modellen wurden neue empirische und qualitative Modelle entwickelt. Die Kombination der experimentellen und theoretischen Arbeiten liefert Korrelationen zwischen den molekularen Eigenschaften der extrudierten Probe und ihrem Extrusionsverhalten. Anhand dieser Korrelationen wurden die in der Literatur vorgeschlagenen theoretischen Konzepte von experimentellen, rechnerischen und theoretischen Gruppen bewertet. Darüber hinaus sagen die qualitativen und empirischen Modelle das Extrusionsverhalten der Probe vom Labor- bis zum industriellen Maßstab voraus. Es wurden verschiedene handelsübliche reine Styrol-Butadien-Kautschuk (SBR) und Polybutadien (PBD)-Proben verwendet. Insbesondere der Einfluss der Molekulargewichtsverteilung (MWD) und der molekularen Architektur (linear, verzweigt) der untersuchten Proben wurde mit dem Extrusionsverhalten der Proben korreliert. Neben den reinen SBR- und PBD-Materialien wurden auch mit Kieselsäure gefüllte SBR-Mischungen entwickelt. Es wurde der Einfluss des Volumenfüllstoffanteils und der Füllstoffdispersion der Kautschukmischungen auf das Extrusionsverhalten untersucht. Korrelationen zwischen dem Volumenfüllstoffanteil und der Füllstoffdispersion mit dem Extrusionsverhalten wurden entwickelt.

Die Ergebnisse dieser Arbeit können als Richtlinien für die Quantifizierung und Modellierung von Extrusionsfließinstabilitäten sowohl im industrielle als auch im akademische Bereich dienen. Die Korrelationen zwischen dem Extrusionsverhalten der reinen Kautschuke und Kautschukmischungen und ihren molekularen und physikalischen Eigenschaften (MWD, molekulare Architektur, Füllstoffgehalt, charakteristische Relaxationszeit und Elastizität) könnten Informationen liefern, die von Mischungs- und Extrusionsingenieuren verwendet werden können, um die Extrusionsleistung einer neuen Formulierung zu bestimmen und vorherzusagen.

Abstract

Within this work rheological laboratory characterization methods were developed and used to characterize the time and spatial characteristics of extrusion flow instabilities. The experimental data of the time and spatial characteristics of extrusion flow instabilities obtained by the characterization methods were modeled by qualitative models available in literature. In addition to qualitative models, new empirical and qualitative models were developed. The combination of the experimental and theoretical work provide correlations between molecular properties of the extruded sample and its extrusion behavior. Through those correlations, theoretical concepts proposed in literature by experimental, computational and theoretical groups were evaluated. Furthermore the qualitative and empirical models predict the extrusion behavior of the sample from laboratory up to industrial scale extrusion lines.

Several commercial neat styrene-butadiene rubber (SBR) and polybutadiene (PBD) samples were used. In particular the influence of the molecular weight distribution (MWD) and the molecular architecture (linear, branched) of the investigated samples were correlated with the extrusion behavior of the samples. Except of the neat SBR and PBD materials, model silica filled SBR compounds were developed as well. Specifically the influence of the volume filler fraction and filler dispersion of the rubber compounds on extrusion behavior was investigated. Particularly correlations between the volume filler fraction and filler dispersion with the extrusion behavior were developed.

The outcome of this work could serve as guidelines to quantify and model extrusion flow instabilities for both industrials and academicals purposes. The correlations between the extrusion behavior of the neat rubbers and rubber compounds with their molecular and physical properties (MWD, molecular architecture, filler load, characteristic relaxation time and elasticity) could provide information which can be used from compound and extrusion engineers to determine and predict the extrusion performance of a new formulation.

Contents

Nomenclature

α_T Horizontal shift factor

E_a Activation energy, [kJ/mol]

T Temperature, [°C]

T_g Glass transition temperature, [°C]

$\sigma_{app.}$ Apparent shear stress, [Pa]

σ_{wall} Wall shear stress, [Pa]

σ_x Shear stress on the theoretical interface between the core and surface layer, [Pa]

Y_s Extensional stress at the die exit region, [Pa]

$\dot{\gamma}_{app.}$ Apparent shear rate, [s^{-1}]

$\dot{\gamma}_{wall}$ Wall shear rate, [s^{-1}]

$\dot{\varepsilon}$ Extensional rate, [s^{-1}]

ω Angular frequency, [rad/s]

Q Volumetric flow rate, [mm^3/s]

Q_s Volumetric flow rate of the surface layer, [mm^3/s]

$V_{ext.}$ Extrudate velocity, [mm/s]

V_{slip} Slip velocity, [mm/s]

$\langle V \rangle$ Average extrudate velocity, [mm/s]

$V_{ave.}$ Average velocity inside the die, [mm/s]

$V_{swelled}$ Velocity of the swelled extrudate after die exit, [mm/s]

$V_{extr.,surface}$ Velocity of the surface layer directly after die exit, [mm/s]

$|\eta^*(\omega)|$ Magnitude of complex viscosity, [Pa.s]

$\eta_{app.}$ Apparent steady state shear viscosity, [Pa.s]

η Correct steady state shear viscosity, [Pa.s]

η_0 Zero shear viscosity, [Pa.s]

$[\eta]$ Intrinsic viscosity, [mL/g]

τ Characteristic relaxation time form Cross and Carreau model, [s]

m Shear thinning exponent from Cross and Carreau mode, [-]

τ_d Reptation time, [s]

$\tau^*_{char.}$ Characteristic time periodicity, [s]

$f_{Char.}$ Characteristic frequency, [Hz]

λ Spatial characteristic wavelength, [mm]

λ_s Average width of the sharkskin stripe, [mm]

h Spatial characteristic height, [mm]

ΔP_{end} End pressure drop, [Pa]

$\Delta P_{end\,effects}$ Corrected end pressure drop, [Pa]

K, n Power law constants

$k, \dot{\gamma}_{crit.}$ Miller et al.,[27,28] constants

$|G^*|$ Magnitude of complex modulus, [Pa]

G' Storage modulus, [Pa]

G'' Loss modulus, [Pa]

δ Phase angle, [°]

H Slit die height, [mm]

W Slit die width, [mm]

H' Swelled height of extrudate, [mm]

W' Swelled width of extrudate, [mm]

H_f Theoretical swelled height of the extrudate if no fracture was developed, [mm]

W_f Theoretical swelled width of the extrudate if no fracture was developed, [mm]

L Die lenght, [mm]

D Capillary die diameter, [mm]

D' Swelled diameter of the extrudate, [mm]

R_0 Radius of capillary die, [mm]

$R_{swelled}$ Swelled radius of the extrudate, [mm]

R_f Theoretical swelled radius of the extrudate if no fracture was developed, [mm]

L/D Die length to diameter ratio, [-]

L/H Die length to height ratio, [-]

ρ Solid state density, [kg/cm^3]

ρ' Melt state density, [kg/cm^3]

N Number of entanglements, [-]

M_e Entanglement molecular weight, [kg/mol]

M_w Weight average molecular weight, [kg/mol]

M_z z-monomer of molecular weight, [kg/mol]

M_n Number average molecular weight, [kg/mol]

$Đ$ Polydispersity index, $M_w/M_n = Đ$ [-]

ξ Interfacial depth parameter, [-]

X_0 Theoretical radius of the core layer inside the die, [mm]

x_0, y_0 Theoretical dimensions of the core layer inside the slit die, [mm]

x_f, y_f Theoretical dimensions of the core layer outside the slit die, [mm]

X_f Theoretical radius of the core layer outside the die, [mm]

φ Volume fraction of filler, [-]

φ_m Maximum packing arrangement, [-]

b Slip length, [mm]

Thesis Outline

Measuring the flow instabilities during polymer extrusion is one of the most crucial challenges for the quality and the quantity of a production line. As the extrusion throughput is increased, extrudate can change appearance from smooth and transparent to matte and afterwards to various kinds of surface and/or volume distortions. Typical names for the flow instabilities as the shear rate increases are sharkskin, stick-slip, and gross melt fracture (GMF). Laboratory characterization methods and reliable models able to describe the flow behavior and predict the surface/volume distortions of the extrudate, are needed. Moreover, the necessity for characterization techniques, which can be adapted to extrusion lines and provide online information for the surface structure of the extrudate have major importance for the plastic and rubber industry. Understanding those needs inspired us to develop a highly pressure sensitive slit die coupled with a capillary rheometer which is able to fully characterize the process flow behavior of a polymer melt, that is steady state viscosity and flow instabilities. Additionally, an online optical method which monitoring the surface structure of the extrudate and obtains time characteristics of flow instabilities was developed as well.

With the data obtained previously, it is possible to adapt qualitative models that could predict the spatial characteristics from a capillary die to a slit die geometry from geometrical input parameters. Furthermore, the combination of experimental and theoretical work (qualitative models) help us to provide useful correlations between molecular properties such as molecular weight distribution (MWD) and molecular architecture (linear, branch) and extrusion behavior. Those correlations are evaluating theoretical concepts for the origin of the surface related extrusion instabilities, e.g. sharkskin, as well. Reviewing and using literature qualitative models for the spatial characteristics (wavelength λ, height h) of extrusion flow instabilities modifications and simplifications are suggested. Modifying and simplifying the literature models enable them to predict the spatial characteristic wavelength λ for slit die geometries and present simpler and easier to handle mathematical formulas. The correlation between the raw polymer properties with the extrusion behavior and the reviewing and modifying of qualitative models enable the investigation of more complex systems, like filled rubber compounds. In order to develop practical correlations between the filler volume fraction, filler dispersion and the extrusion behavior or rubber compounds characterization technics and qualitative models were used.

11

To elaborate the previous mentioned studies this thesis is organized in the following chapters:

Chapter 1: Introduction to capillary rheology, where the most common types of extrusion dies (slit and round), the mathematical formulation which describes their flow, and the two essential corrections for pressure exit and wall slippage effects are elaborated.

Chapter 2: Introduction to extrusion flow instabilities, where a literature review for the characterization and origin of extrusion flow instabilities is presented, focusing mainly on the surface fracture extrusion instability.

Chapter 3: Development of characterization technics, where the highly pressure sensitive slit die, online and offline optical analysis are presented.

Chapter 4: Qualitative models for the spatial characteristics of extrusion flow instabilities, where the available literature models for the spatial characteristics (wavelength λ, height h) of the extrusion flow instabilities are reviewed, modified and simplified.

Chapter 5: Influence of molecular properties on extrusion flow instabilities, where experimental data of the spatial characteristics of flow instabilities are fitted with the previously reported models and essential correlations between molecular properties (relaxation time and molecular architecture) and extrusion behavior are presented.

Chapter 6: Influence of processing parameters on extrusion flow instabilities, where the characteristic dimensions of slit (height, H) and capillary (diameter, D) dies are correlated with the magnitude of the spatial characteristic wavelength λ, and the impact of the extrusion temperature on the λ is investigated as well.

Chapter 7: Extrusion flow instabilities of model filled elastomers, where the influence of filler volume fraction on the spatial characteristics of extrusion flow instabilities is investigated.

Chapter 8: Extrusion flow instabilities of model filled elastomers, where the influence of filler dispersion on the spatial characteristics of extrusion flow instabilities is investigated.

Chapter 9: Conclusions and outlook, where the main outcome regarding the influence of molecular properties on the extrusion behavior, origin of extrusion instabilities, capabilities of the predictive models and practical correlations are summarized.

During the preparation of this PhD thesis the following manuscripts have been submitted and published to international scientific journals. This PhD thesis contains material which is adapted and reproduced with permission from the publishing houses of the below mentioned manuscripts.

C. K. Georgantopoulos, M. K. Esfahani, C. Botha, I. F. C. Naue, N. Dingenouts, A. Causa, R. Kádár, and M. Wilhelm, "*Mechano-optical characterization of extrusion flow instabilities in styrene-butadiene rubbers: investigating the influence of molecular properties and die geometry*", *Macromol. Mater. Eng.*, 306, *2*, **2021**. https://doi.org/10.1002/mame.202000801. Reproduced within this PhD thesis under the open access policy. This is an open access article distributed under the terms of the creative commons (CC) by license (https://creativecommons.org/licenses/), which permits unrestricted use, distribution, and reproduction in any medium, provided the original work is properly cited.

C. K. Georgantopoulos, M. K. Esfahani, C. Botha, M. A. Pollard, I. F. C. Naue, A. Causa, R. Kádár, and M. Wilhelm, "*Modeling the spatial characteristics of extrusion flow instabilities for styrene-butadiene rubbers: investigating the influence of molecular weight distribution, molecular architecture, and temperature*", *Phys. Fluids*, 33, *9*, **2021**. https://doi.org/10.1063/5.0061334. Reproduced within this PhD thesis under permission from AIP Publishing, **No. 5231930652686**.

Christos K. Georgantopoulos, Masood K. Esfahani, Michael A. Pollard, Ingo F. C. Naue, Andrea Causa, Roland Kádár, and Manfred Wilhelm, "*Derivation of a qualitative model for the spatial characteristic wavelength of extrusion flow instabilities: Investigation of a polybutadiene rubber through capillary, slit and complex geometry extrusion dies*", *Macromol. Mater. Eng.*, **accepted, 2022**. https://doi.org/10.1002/mame.202200313. Reproduced within this PhD thesis under the open access policy. This is an open access article distributed under the terms of the creative commons (CC) by license (https://creativecommons.org/licenses/), which permits unrestricted use, distribution, and reproduction in any medium, provided the original work is properly cited.

1. Introduction to Capillary Rheology

Within this chapter a literature review for the capillary rheology is presented. An introduction to capillary rheometer, mathematical formulations and corrections for this type of rheometry are elaborated. This chapter is discussing the most common types of extrusion dies (slit and round), the mathematical formulation which describes their flow, and the two essential corrections for pressure exit and wall slippage effects. After this section the reader will have the needed background for understanding the derivation of all experimental data obtained by capillary rheology.

1.1. Capillary viscometer

The viscometer is a scientific instrument which only measures the viscous properties of Newtonian and non- Newtonian fluids. Firstly, the fluid is placed inside the capillary barrel and then a pressure difference is applied. This force the fluid to flow from the inlet to the outlet of the capillary die.[1] The velocity and the shear stress profile of the fluid are presented in Figure 1.1. Typically, the velocity profile follows a well defined parabolic profile for Newtonian fluids where at the boundary condition, that is at the capillary wall, the magnitude of velocity is zero. For non-Newtonian fluids the velocity follows again a parabolic profile but this time the magnitude of velocity on the boundary condition is non-zero. The non-zero velocity on the boundary condition for the non-Newtonian fluids is known as slip velocity, see Figure 1.1 (a). In Figure 1.1 (b) the shear stress profile for either Newtonian or non-Newtonian fluids is presented.

Usually the driving force for a fluid to flow through the capillary can either be gravity or pressure difference. Two different modes are used in capillary rheometry, the control stress (CS) mode and the control rate (CR) mode.[1] During the CS-mode, the test measures with a given pressure the resulting flow rate. During the CR-mode, the test measures with a controlled flow rate the resulting pressure drop along the length of the die.
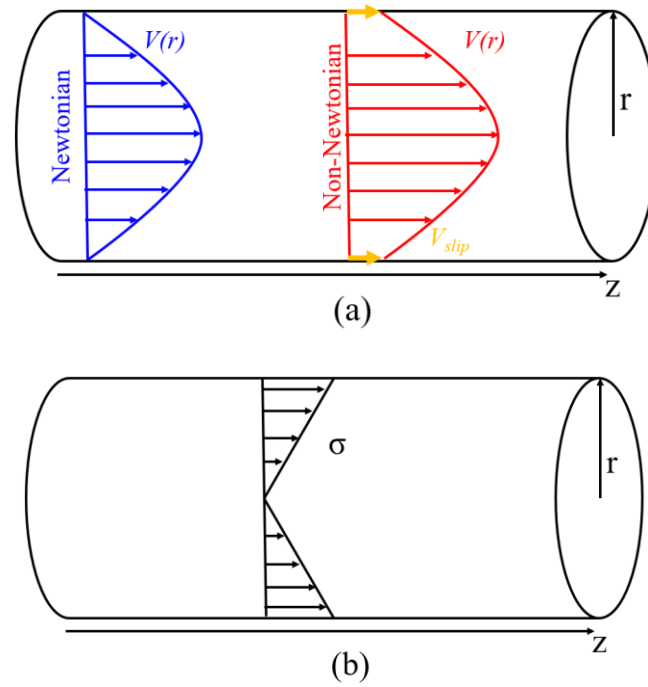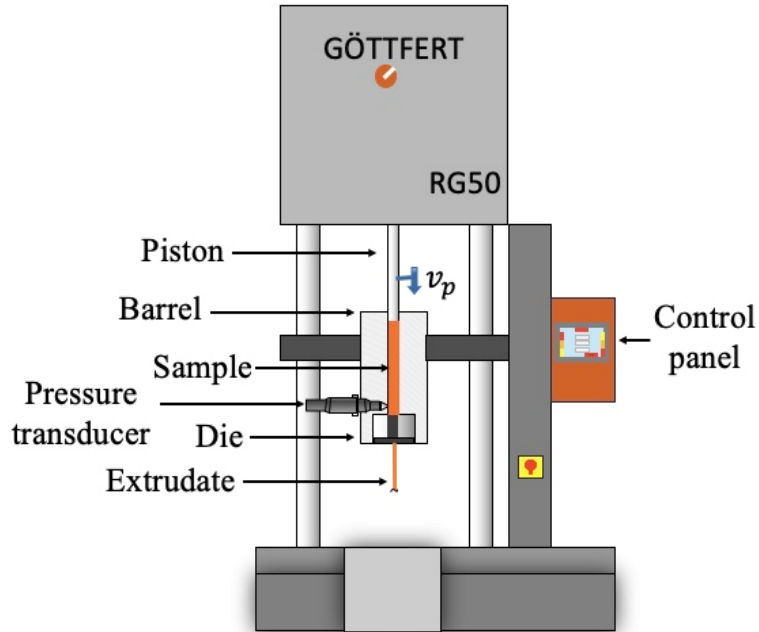
Figure 1.1. Schematic representation of the (a) parabolic velocity profile for Newtonian and non-Newtonian fluids, and (b) the shear stress at the round capillary die.

1.2. Typical extrusion dies and capillary rheometer

During a capillary rheology experiment a piston applies pressure on the fluid in a control fashion. Hence the test fluid is exposed to different constant or programmed flow rates. Depending on the extrusion die geometry, round or slit, the pressure transducer is placed in different position along the capillary rheometer. Usually there is always a pressure transducer at the entrance of the extrusion die, named as P_e. For extrusion dies with round capillary geometry (circular cross-section area), the die length L is the distance between the pressure at the entrance of the die, P_e and the ambient pressure. For extrusion dies with slit die geometry (rectangular cross-section area), pressure sensors are usually placed along the die length L. The pressure difference between the two or more pressure transducers along the die lentgh of the slit die is essential in order to calculate the shear stress.

Within this study, a capillary rheometer named as Rheograph (RG) 50 kN from Göttfert (Buchen, Germany) is used. The capillary rheometer has a single test barrel with a diameter of 30 mm and is equipped with a force transducer up to 50 kN. In Figure 1.2 a schematic representation of the capillary instrument is presented. The piston is attached to the head of the rheometer and drives the test sample through the barrel in a control way. The piston is capable of running with speeds between 0.0004 mm·s^{-1} to 40 mm·s^{-1}. The barrel is temperature

15

controlled with resolution of about 1 °C. A pressure transducer is located at the end of the barrel, that is at the entrance of the extrusion die.

Figure 1.2. Schematic representation of the capillary instrument, Rheograph (RG) 50 kN.

1.3. Mathematical formulation for capillary rheology

The following mathematical formulations enable the calculation of the apparent shear stress, apparent shear rate, volumetric flow rate and apparent steady state shear viscosity when round and slit extrusion dies are used.[1]

Capillaries round dies (circular cross-section area)

(1) Apparent shear stress $\sigma_{app.}$

$$\sigma_{app.} = \frac{r}{2 \cdot L} \cdot \Delta P \tag{1.1}$$

where $\sigma_{app.}$ is the apparent shear stress, r is the cylindrical coordinate in the radial direction, L is the capillary length and ΔP is the pressure drop along the capillary length.

(2) Apparent shear rate $\dot{\gamma}_{app.}$

$$\dot{\gamma}_{app.} = \left(\frac{4}{\pi \cdot r^3}\right) \cdot Q \tag{1.2}$$

where $\dot{\gamma}_{app.}$ is the apparent shear rate at the radial coordinate r and Q is the volumetric flow rate.

(3) Volumetric flow rate Q

Volumetric flow rate, Q, is defined as the product of the extrudate velocity with the circular cross-section area of the round extrusion die.

$$Q = \pi \cdot R^2 \cdot V_{extr.} \tag{1.3}$$

where R is the radius of the capillary cross-section area and $V_{extr.}$ is the extrudate velocity. Coupling Equation (1.2) and (1.3), the Equation (1.4) occurs.

$$\dot{\gamma}_{app.} = \frac{4}{R} \cdot V_{extr.} \tag{1.4}$$

Equation (2.4) correlates the apparent shear rate with the extrudate velocity for round capillary extrusion dies.

(4) Apparent steady state shear viscosity $\eta_{app.}$

The flow behaviour of a fluid is described by Equation (1.5).

$$\sigma_{app.} = \eta \cdot \frac{dV_z}{dr} = \eta \cdot \dot{\gamma} \tag{1.5}$$

Coupling Equation (1.1), (1.2) and (1.5) the apparent steady stare shear viscosity can be calculated:

$$\eta_{app.} = \frac{\sigma_{app.}}{\dot{\gamma}} = \frac{\pi \cdot r^4}{8 \cdot L} \cdot \frac{\Delta P}{Q} \tag{1.6}$$

Slit dies (rectangular cross-section area)

(1) Apparent shear stress $\sigma_{app.}$

$$\sigma_{app.} = \left(\frac{H}{2 \cdot L}\right) \cdot \Delta P \tag{1.7}$$

where $\sigma_{app.}$ is the apparent shear stress, H is the slit height, L is the length of the die and ΔP is the pressure drop along the length of the slit die.

(2) Apparent shear rate $\dot{\gamma}_{app.}$

$$\dot{\gamma}_{app.} = \left(\frac{6}{W \cdot H^2}\right) \cdot Q \tag{1.8}$$

where $\dot{\gamma}_{app.}$ is the apparent shear rate, W is the width, and H is the height of the slit die. Where Q is the volumetric flow rate.

(3) Volumetric flow rate Q

The volumetric flow rate, Q is defined as the product of the extrudate velocity with the cross-section area of the rectangular slit die.

$$Q = W \cdot H \cdot V_{extr.} \tag{1.9}$$

where $V_{extr.}$ is the extrudate velocity. Coupling Equation (1.8) with Equation (1.9), the following equation is derived,

$$\dot{\gamma}_{app.} = \frac{6}{H} \cdot V_{extr.} \tag{1.10}$$

(4) Apparent steady state shear viscosity $\eta_{app.}$

$$\eta_{app.} = \left(\frac{W \cdot H^3}{12 \cdot L}\right) \cdot \frac{\Delta P}{Q} \tag{1.11}$$

where L is the length of the slit die, ΔP is the pressure drop along the die length and Q is the volumetric flow rate.

Without the Bagley[1] and Rabinowitsch-Weissenberg[1] corrections, the use of the Equation (1.6) and (1.11) results in error for the absolute value of steady state shear viscosity on the order of 20 % or more.[1] Hence, it is often called "apparent". The following sub-chapter briefly elaborate the Bagley[1] and Rabinowitsch-Weissenberg[1] corrections.

1.4. Capillary flow corrections

In general, three corrections can be applied in capillary flow, either for slit or round extrusion dies, raw data with the following order: (1) Slip correction (Mooney Analysis), entrance and exit pressure correction (Bagley Plot) and non-parabolic velocity profile correction (Rabinowitsch-Weissenberg).[1]

Correction for the slip (Mooney analysis)

The slippage on the wall of the die reduces the apparent shear rate on the wall. In case of non-slip condition, the velocity on the wall causes an increase of the volumetric flow rate Q. The relationship of volumetric flow rate and the raw average velocity for round capillary die is defined as by Equation (1.12),

$$V_{raw} = \frac{Q}{\pi \cdot r^2}$$
(1.12)

The true or correct average velocity V_{true} is calculated by subtracting the slip velocity V_{slip} from the measured raw average velocity V_{raw},

$$V_{true} = V_{raw} - V_{slip}$$
(1.13)

The relationship between the wall or true shear rate and the apparent shear rate become visible by multiplying $4/r$ with Equation (1.13).

$$\frac{4 \cdot V_{true}}{r} = \frac{4 \cdot V_{raw}}{r} - \frac{4 \cdot V_{slip}}{r}$$
(1.14)

After rearranging Equation (1.14), the following Equation (1.15) is derived.

$$\frac{4 \cdot Q}{\pi \cdot r^3} = slope \cdot \frac{1}{R} + intercept = 4 \cdot V_{slip} \cdot \frac{1}{r} + \frac{4 \cdot V_{true}}{r}$$
(1.15)

Plotting $4 \cdot Q / \pi \cdot r^3$ versus $1/R$, a line with a slope equal to four times the slip velocity will be obtained. Calculating the slip velocity, the flow rate can be corrected through Equation (2.15). Hence, the Mooney correction is correcting the apparent shear rate. [1]

Correction for entrance and exit pressure effects (Bagley plot)

Losses of pressure are often observed at the entrance to the die during the reduction in radius from the barrel into the test die. Therefore, the true pressure-drop across the die is smaller than the raw pressure-drop and a correction is required. As mentioned previously in 1.2 the pressure is measured in the barrel just before the die entrance. This pressure divided by the die length L provides the raw pressure-drop. In order to obtain the correct pressure-drop along the extrusion die, the entrance pressure losses must be subtracted from the raw pressure.

The equation of apparent shear stress, Equation (1.1), is rewritten as,

$$\sigma_{app.} = \frac{r}{2 \cdot L} \cdot \Delta P \Rightarrow \Delta P = 2 \cdot \sigma_{app.} \cdot \frac{L}{r}$$
(1.16)

By performing experiments with several round capillary extrusion dies for various apparent shear rate, the plot of ΔP versus L/r is constructed, see Figure 1.3.
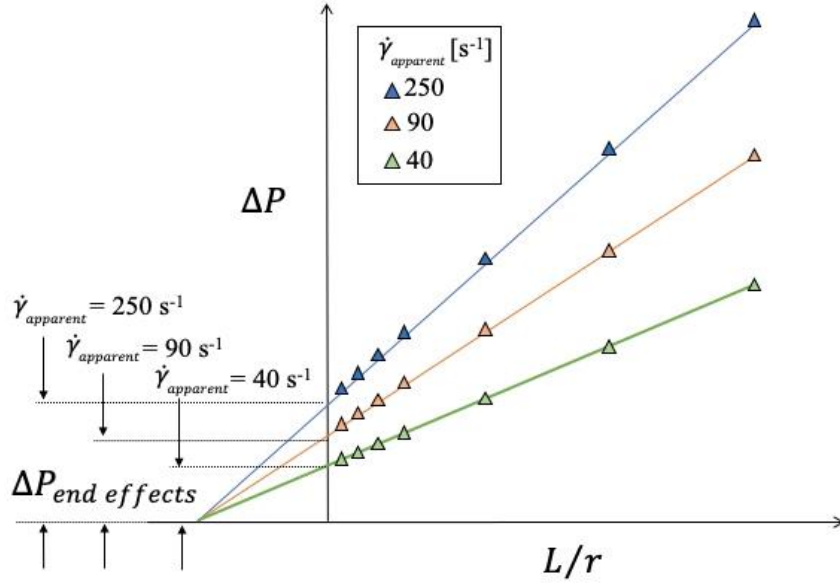
Figure 1.3. ΔP versus L/r with exit effects for different apparent shear rates $\dot{\gamma}_{app}$. This is a graphical explanation of the Bagley correction and does not refer to any experimental data.

Figure 1.3 presents a graphical description of Bagley correction with three sets of data taken at three different apparent shear rates. A liner fit is describing the three apparent shear rates at different L/r ratios. The interception of the linear fit provides the $\Delta P_{end\ effect}$. Hence, in order to calculate the corrected pressure-drop the following mathematical calculation are needed and the wall or true shear stress can be then calculated.

$$\Delta P_{corrected} = \left(\Delta P - \Delta P_{end\ effects}\right) = 2 \cdot \sigma_{app.} \cdot \frac{L}{r} \tag{1.17}$$

$$\sigma_{wall} = \frac{\Delta P_{corrected} \cdot r}{2 \cdot L} \tag{1.18}$$

Hence, by using the Bagley correction the wall shear stress, Equation (1.18), and then the corrected steady-state shear viscosity value can be calculated.

Correction for non-parabolic velocity profile, Rabinowitsch-Weissenberg (RW)

The velocity profile of a Newtonian fluid which flows through a capillary die presents a parabolic distribution, according to Equation (1.19).

$$V_z(r) = \frac{\Delta P \cdot R_0^2}{4 \cdot \eta \cdot L} \cdot \left(1 - \frac{r}{R_0}\right)^2 \tag{2119}$$

Where ΔP is the true pressure-drop along the capillary length, R_0 is the radius of the die, L is the length die, η is the corrected steady-state shear viscosity from the Bagley correction and r is the coordinate in the radial direction. Integration of this velocity profile gives the Hagen-Poiseuille equation, which represents the pressure-drop/flow rate relationship for Newtonian fluids which gives by Equation (1.20).[1]

$$Q = \frac{\pi \cdot R^4 \cdot \Delta P}{8 \cdot \eta \cdot L} \tag{1.20}$$

The measurement of pressure-drop and flow rate in a tube for Newtonian fluids may be plotted as $4 \cdot Q / \pi \cdot R_0^3$ versus $\Delta P \cdot R_0 / 2 \cdot L$ as a straight line of slope equal to the inverse of the corrected steady-state shear viscosity, see Equation (1.21).

$$\frac{4 \cdot Q}{\pi \cdot R_0^3} = \frac{1}{\eta} \cdot \frac{\Delta P \cdot R_0}{2 \cdot L} \tag{1.21}$$

The $\Delta P \cdot R / 2 \cdot L$ is the wall shear stress which has been corrected by the Bagley correction and the term $4 \cdot Q / \pi \cdot R_0^3$ is the apparent shear rate for a Newtonian fluid. For non-Newtonian fluids the shear rate will be different from the apparent shear rate, $\dot{\gamma}_{app.}$. In order to calculate to correct or wall shear rate the Equation (1.22) is needed.

$$\dot{\gamma}_{wall} = \dot{\gamma}_{app.} \cdot \left[\frac{1}{4} \cdot \left(3 + \frac{d \ln \dot{\gamma}_{app.}}{d \ln \sigma_{wall}}\right)\right] \tag{1.22}$$

The term in square brackets is known as Rabinowitsch-Weissenberg (RW) correction.[1] The RW is calculated through a plot of $\ln \dot{\gamma}_{apparent}$ versus $\ln \sigma_{wall}$. In case of a straight line, a regression yields to the needed term in the RW correction. If the line is not straight, it needs to be fitted with a polynomial.

$$y = \left(\ln \dot{\gamma}_{app.}\right) \tag{1.23}$$

$$x = \left(\ln \sigma_{wall}\right) \tag{1.24}$$

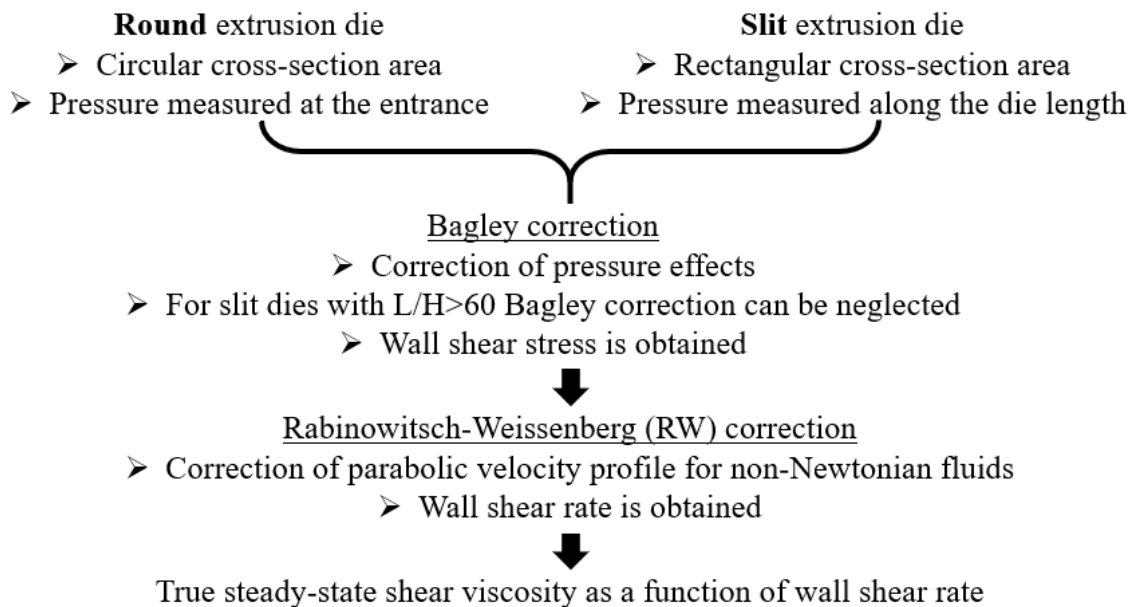$$y = a \cdot x^2 + b \cdot x + c \qquad (1.25)$$

The needed derivative can be calculated from the polynomial.

$$\frac{dy}{dx} = 2 \cdot a \cdot x + b \qquad (1.26)$$

Hence, the RW correction can be calculated and applied for every data point ($\sigma_{wall}, \dot{\gamma}_{apparent}$). After the apparent shear rate is corrected to the wall shear rate, the absolute value of true steady-state shear viscosity can be calculated as the ratio of the wall shear stress and the wall shear rate, see Equation (1.27).

$$\eta = \frac{\sigma_{wall}}{\dot{\gamma}_{wall}} \qquad (1.27)$$

Figure 1.4 summarize the series of the mentioned correction for the capillary flow of non-Newtonian fluids except for the Mooney analysis. This flow chart highlights the difference between the correction for capillary and slit die. For slit die with $L/H > 60$ the Bagley correction is not necessary since the pressure effect can be neglected.

Round extrusion die
➢ Circular cross-section area
➢ Pressure measured at the entrance

Slit extrusion die
➢ Rectangular cross-section area
➢ Pressure measured along the die length

Bagley correction
➢ Correction of pressure effects
➢ For slit dies with L/H>60 Bagley correction can be neglected
➢ Wall shear stress is obtained

Rabinowitsch-Weissenberg (RW) correction
➢ Correction of parabolic velocity profile for non-Newtonian fluids
➢ Wall shear rate is obtained

True steady-state shear viscosity as a function of wall shear rate

Figure 1.4 The sequel of Bagley and RW corrections for capillary flow.

2. Introduction to Extrusion Flow Instabilities

Within this chapter a literature review for the origin of the extrusion flow instabilities is presented. Experimental, theoretical and computational approaches are presented and giving their insights for the origin of the instabilities. The review is discussing all the sharkskin and stick-slip extrusion instabilities but is mainly focusing on the origin of the surface fracture, known as sharkskin. This specific focus on surface fracture is motivated, because it is a well discussed, explained and modeled phenomenon. Although none of the origin of the extrusion flow instabilities have been totally explained and understand in literature. Nonetheless, the surface fracture seems to be the most well studied phenomenon and gives the opportunity for deeper understanding.


2.1. Categorization of extrusion flow instabilities

Most of the polymer melts display extrusion instabilities[1-10] at the exit of the extrusion die when the wall shear stresses to which they are exposed become sufficiently high. As the wall shear stress is increased the first type of extrusion instabilities are appeared on the extrudate surface and then on the extrudate volume. Typical sequence of extrusion instabilities during extrusion of a commercial synthesized styrene-butadiene rubber (SBR, M_w = 400 kg mol^{-1}, Đ = 1.36) through a round capillary die with L = 30 mm and D = 2 mm is shown in Figure 2.1.[11-16]

Figure 2.1 displays that the surface of the extrudate is smooth up to a critical value of wall shear stress, below $\sigma_{wall} < 10^5$ Pa. After $\sigma_{wall} > 10^5$ Pa on the surface of the extrudate periodic distortions with small amplitude appeared; this instability is called sharkskin. After $\sigma_{wall} > 2$ 10^5 Pa a periodic distortion with significant larger amplitude than sharkskin is appeared, this instability is usually named as melt fracture. After $\sigma_{wall} > 4$ 10^5 Pa the flow becomes unsteady and the extrudate alternates between sharkskin and smooth or irregular-distorted segments, this instability is called stick-slip. Afterwards, at even higher wall shear stresses, $\sigma_{wall} > 6$ 10^5, the flow becomes steady again and extrudate present an irregular volume distortions, this instability

is called gross melt fracture (GMF). The behavior shown here is observed for many linear polymers, with most observations having been made on high-density polyethylenes (HDPEs) and LLDPEs, polybutadiene (PBD), styrene-butadiene rubbers (SBR), polyisoprene (PI), and linear polysiloxanes (silicone polymers).[2]
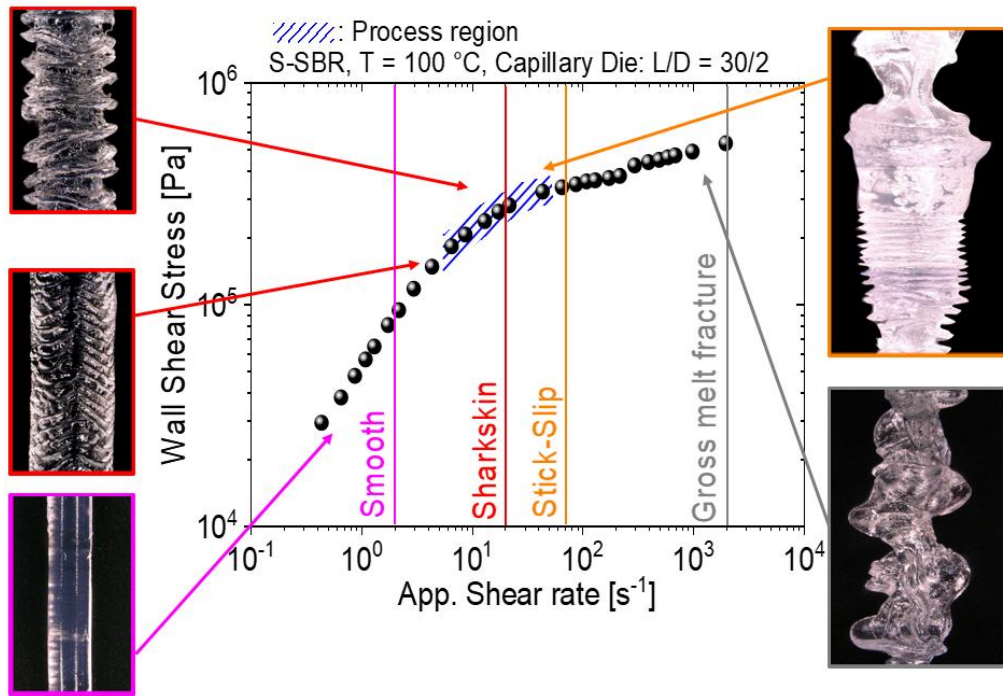
Figure 2.1. Typical flow curve of wall shear stress as a function of apparent shear rate for a linear synthesized styrene-butadiene rubber (S-SBR, $M_w = 390$ kg mol^{-1}, $Đ = 1.36$) sample. This curve is obtained by a capillary rheometer equipped with a capillary die (round cross-section area) with length $L = 30$ mm and diameter $D = 2$ mm at T = 100 °C. The flow curve is divided into four domains where the typical extrusion flow instabilities can be observed.

Definitions of the extrusion instabilities based on slit die geometry are discussed in literature.[8,11,15,17,18,19] These definitions are based on visual observations and on the characteristic frequency (or periodicity) of the instabilities. Sharkskin extrudates have a visual appearance characterized by superficial surface fractures perpendicular to the extrusion flow direction. Therefore, it is defined as having small amplitude surface distortions, compared to the extrudate thickness, with one dominant characteristic distortion frequency, e.g. $f_{char.} \approx 20$ Hz for a specific linear low density polyethylene (LLDPE)[17-20] at T = 140 °C, and $f_{char.} \approx 15$ Hz for a specific styrene-butadiene rubber (SBR)[11,14,15] at T = 120 °C. Conventional melt pressure transducers, commonly used in extrusion processing and in a capillary rheometers, are not capable of capturing pressure fluctuations associated to the sharkskin instability.

Stick-slip instability is visually characterized by smooth and/or sharkskin regimes in addition to irregular both surface and volume extrudate distortions.[8,15] Stick-slip appears with pressure fluctuations of about $\Delta p/p \approx 25$ % for $p \approx 200$ bar mean pressure as determined by conventional melt pressure transducers on capillary rheometers. The stick-slip instability is typically characterized by three characteristic periodicities (or frequencies): (i) one which occurred by the stick part, usually sharkskin instability, τ^*_{stick} (ii) one obtained by the slip part, usually volume distortion τ^*_{slip} and (iii) the last one obtained by the pressure fluctuations $\tau^*_{pressure}$ ($\Delta p/p \approx 25$ % for $p \approx 200$ bar). Based on literature and current findings, which investigated styrene-butadiene rubber (SBR),[8,15] and linear low density polyethylene (LLDE)[17-20] materials, these characteristic periodicities are typically different to each other by $\tau^*_{stick} \approx 3\tau^*_{slip}$, and $\tau^*_{stick} \approx 500\tau^*_{pressure}$.

Gross melt fracture (GMF) is characterized by significant irregular distortions of the whole extrudate and therefore can be designated as a volume instability. Usually GMF is observed after the stick-slip instability and the pressure profile become unstable with $\Delta p/p \approx 5$ % for $p \approx 300$ bar mean pressure.[15] No periodic pattern in space has been observed for the GMF. The GMF is not further investigated by this study.

Moreover Koopmans et al.[5] defined various types of surface and volume flow instabilities referring to extrudates obtained by round capillary dies (circular cross-section area). Firstly, they defined helix extrusion flow instability as a regular periodic volume distortion which has smooth surface and appearance of a screw thread. Secondly, spurt flow instability is defined as a volume distortion which manifests a periodic twists in all directions after the die exit. The spurt flow instability is not linked with any transition in the flow curve of shear stress versus the apparent shear rate. Finally, "sausage-like" flow instability is defined as periodic volume distortion with surface disturbances. Usually it appears for shear rates in the range between the helix and spurt type of flow instabilities. Within this thesis the "sausage-like" instability will be referred to as regular volume and surface (RVS) instability.[16]

2.2. Origin of surface fracture: sharkskin

The extrusion flow instability named as sharkskin or melt fracture is one of the most common surface instability in polymer process industrial sector.[1-10] Experimental, theoretical and computational studies have addressed the origin of this type of regular distortion on extrudate surface. First observations and theoretical concept for the origin on the sharkskin/surface melt fracture instability were made by N. El Kissi and J. M. Piau.[21] They rheologically investigated three polydimethylsiloxane (PDMS) samples named as BG (M_w = 428 kg mol^{-1}, Đ = 2.9), LG2 (M_w = 835 kg mol^{-1}, Đ = 4) and LG3 (M_w = 1840 kg mol^{-1}, Đ = 7.9). N. El Kissi and J. M. Piau[21] used a capillary rheometer equipped with a round capillary die, length L = 20 mm and diameter D = 2 mm, and extruded the investigated samples at T = 23 °C, see Figure 2.2.
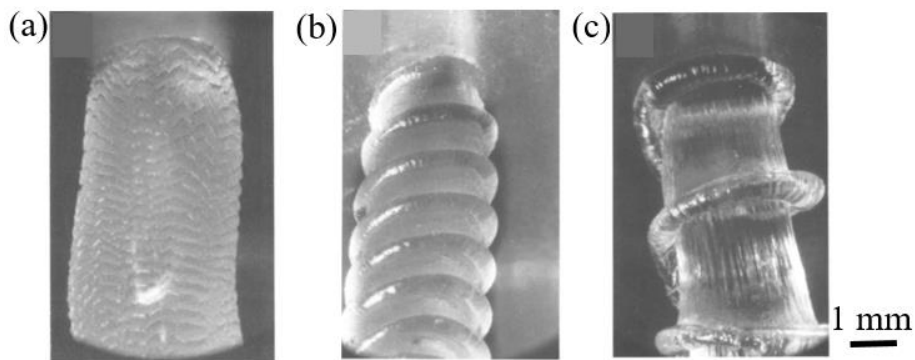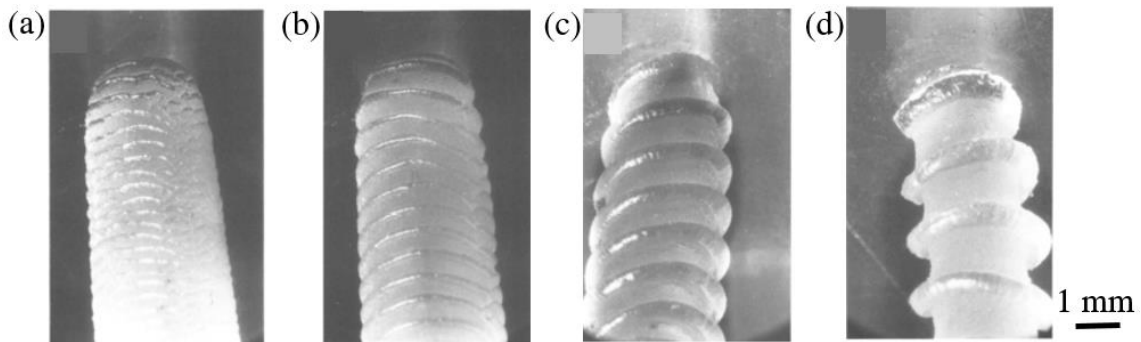

Figure 2.2. Extrusion of polydimethylsiloxane (PDMS) samples by a capillary die (round cross-section area) with length L = 20 mm and diameter D = 2 mm at T = 23 °C. (a) BG (M_w = 428 kg mol^{-1}, Đ = 2.9) at ΔP =20 bar, (b) LG2 (M_w = 835 kg mol^{-1}, Đ = 4) at ΔP =19 bar, and (c) LG3 (M_w = 1840 kg mol^{-1}, Đ = 7.9) at ΔP =20 bar. The melt fracture instability becomes more intensive as the weight average molecular weight of the sample is increased. Adapted from N. El Kissi et al., *Journal of Non-Newtonian Fluid Mechanics* 37, *55*, **1990**, Figure 4 (d), 5 (f) and 6 (g).[20]

N. El Kissi and J. M. Piau[21] stated three main observations:

(i)   The onset of the surface melt fracture was observed under steady flow.

(ii)   No disturbance of the flow inside the round capillary die was observed during the appearance of the surface melt fracture.

(iii)   The surface melt fracture instability was less pronounced for the relatively low molecular weight sample (BG, M_w = 428 kg mol^{-1}, Đ = 2.9), and more pronounced for the high molecular weight sample (LG3, M_w = 1840 kg mol^{-1}, Đ = 7.9), see Figure 2.2.

Observing the formation of the surface melt fracture at the die exit, it is noticed that the development of cracks is associated with the existence of wrap-around phenomena at the die exit region, see Figure 2.3. As the extrusion rate increases, high level stresses are reached, then the wrap-around phenomenon gives rise to the formation of a thick ridge, which can be easily noticed on Figure 2.3 (c) and (d).


Figure 2.3. Extrusion of polydimethylsiloxane (PDMS, M_w = 835 kg mol^{-1}, Đ = 4) sample by a capillary die (round cross-section area) with length L = 20 mm and diameter D = 2 mm at T = 23 °C. (a) ΔP =14 bar, (b) ΔP =15 bar, (c) ΔP =19 bar, and (d) ΔP =26 bar. (a) Sharkskin instability which is followed by the (b) formation of cracks at the outlet from the die. (c) – (d) The polymer runs round the capillary exit and sticks to the wall, forming a ridge around the die outlet. When the ridge reaches a certain thickness becomes detached from the wall and then regular ring formations are on the surface of the extrudate. Adapted from N. El Kissi et al., *Journal of Non-Newtonian Fluid Mechanics* 37, *55*, **1990**, Figure 5.[20]

Based on the previous experimental observations and on early state numerical simulations,[22] N. El Kissi and J. M. Piau[21] conclude that at the die exit region intensive extensional flow causes intensive extensional stresses. Thus, when the extensional stresses reach a critical value the extrudate present regular cracks.

Despite the macroscopic observations of N. El Kissi and J. M. Piau,[21] which are focusing on the extensional stresses at the die outlet in order to explain the cause of the surface melt fracture, Wang et al.[23] proposed a molecular mechanism in order to explain the origin of sharkskin/surface melt fracture instability. Wang et al.[23] focused on the internal part of die exit region where an unsteady hydrodynamic boundary condition exists on the die wall. This unsteady hydrodynamic boundary condition occurs by the alternating entanglement and disentanglement process between the physically captured polymer chains on the die wall and the bulk polymer chains. This molecular process of entanglement – disentanglement generates a fluctuation which is associated with the stretched (disentanglement state) and re-coil

(entanglement state) configuration of the macromolecular chains.[23] This stretch – coil oscillation is assumed by Wang et al.[23] to be the molecular origin of sharkskin. Figure 2.4 displays the previously mentioned molecular concept of the entanglement – disentanglement process which generate the unsteady boundary condition on the internal side wall of the die lip.
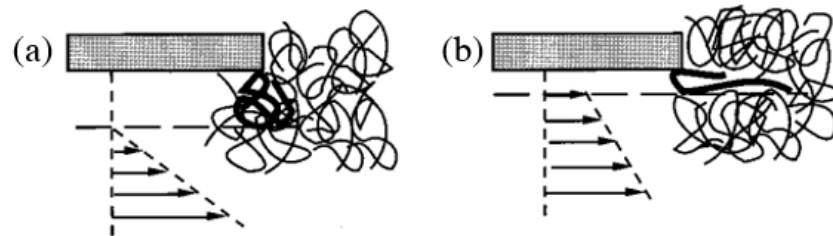
Figure 2.4. Schematic representation of the (a) entanglement and (b) disentanglement state by the physical adsorbed polymer chains on the lip of the die exit. This periodic entanglement – disentanglement process is blamed for the origin of sharkskin. Adapted from S.Q. Wang et al., *Journal of Rheology* 40, *875*, **1996**, Figure 9.[23]

Plethora of studies[16,23-28] defined the spatial characteristics of the sharkskin/surface melt fracture instability. Specifically the spatial characteristic wavelength λ and height h. Spatial characteristic wavelength (SCW) λ is defined as the average distance between two similar consecutive surface distortions. Spatial characteristic height (SCH) h is defined as the average distance between the swelled core of the extrudate and the tip of the distortion, see Figure 2.5.
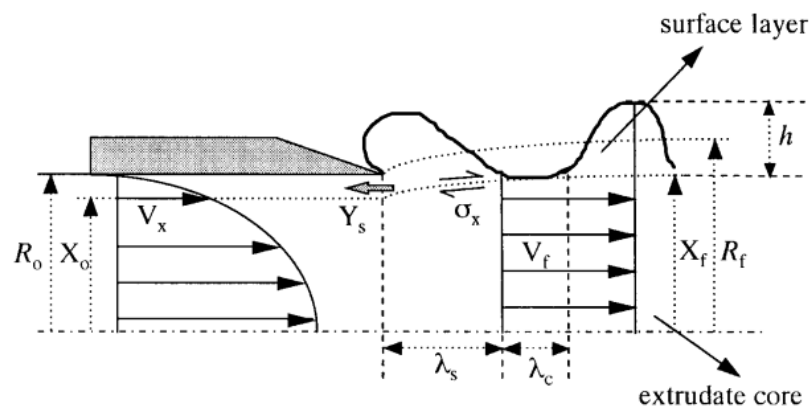

Figure 2.5. Schematic drawing of "two layer" model showing development of sharkskin at the die exit for the sharkskin ridge formation. The sharkskin ridge is formed by fracture at the skin-core interface X_o. After the surface fracture the ridge and core moves with velocity V_f. The thickness of surface layer of the extrudate (R_f - X_f) is assumed to be a half of the height of the sharkskin ridge h. Adapted from Y. W. Inn et al., *Rheologica Acta* 37, *357*, **1998**, Figure 10.[26]

S. Q. Wang and coworkers[23-25] modeled the formation of SCW λ based on the average extrudate velocity $\langle V \rangle$ and the time characteristic periodicity (TCP) τ^* of the instability, $\lambda = \langle V \rangle / \tau^*$. Inn et al.[26] based on the theoretical concept of the "two layer" extrudate, proposed by Cogswell[22] and experimentally confirmed by N. El Kissi and J. M. Piau,[21,29-32] to model the SCW λ. Specifically Inn et al.[26] assumed that the extrudate is separated into two theoretical layers, the surface and the core layer, see Figure 2.5.

The surface layer experiences the intensive extensional stress during the outcome from the die, so a pealing behavior which propagate perpendicular to the flow generates the distortion on the surface extrudate. Both groups, S. Q. Wang and coworkers[23-25] and Inn et al.,[26] modeled the SCW λ in order to evaluate the proposed molecular and macroscopic concepts for the origin of sharkskin-melt fracture.

Inn et al.,[26] in order to derive the qualitative model for the SCW λ based on the "two layer"[22] concept. They[26] did numerous of extrusion experiments using two round capillary dies with length of $L = 76.2$ mm, and $L = 50.8$ mm where both dies have the same diameter $D = 12.7$ mm. Polybutadiene (PBD, $M_w = 182$ kg mol^{-1}, $Đ = 1.87$) sample at T = 50 °C was extruded.[26] Testing the concept of the unsteady hydrodynamic boundary condition on the die exit region they[26] applied by a cotton swab a soap solution on the die exit area. According to their[26] experimental observations, Figure 2.6, the sharkskin instability is eliminated during the influence of the soap on the die lip.
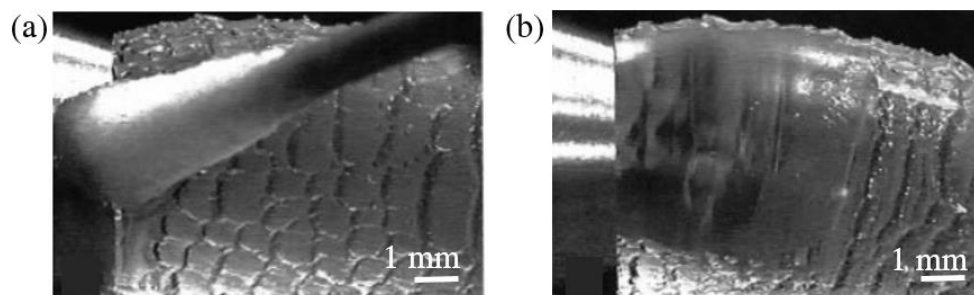
Figure 2.6. Extrusion of polybutadiene (PBD, $M_w = 182$ kg mol^{-1}, $Đ = 1.87$) sample by a capillary die (round cross-section area) with length $L = 50.8$ mm and diameter $D = 12.7$ mm at T = 50 °C. (a) Application of the soap solution to the outside rim of the die exit by using swab and (b) appearance of the extrudate after soap solution coating. This application investigates the influence of the die exit on the extrusion appearance of the extrudate. Adapted from Y. W. Inn et al., *Rheologica Acta* 37, *357*, **1998**, Figure 9.[26]

Similar observations are reported in literature for polyethylene samples on which flouro-elastomer (slip agents) have been added.[23-25] The slip agent, either added in the polymer matrix or deposit on the die exit, eliminate the sharkskin formation. This strengthens the concept that the sharkskin/surface melt fracture instability is originated on the die exit region, although can not clarify which is the original mechanism of the origin of sharkskin. Because the slip agent while is deposited on the die exit increases the slippage on the area and on the same time decrease the extensional stresses.

Relying on the experimental studies, theoretical concepts and qualitative models C. Venet and B. Verges[33] combine experiments and numerical simulations in a comparative study. Numerical simulations based on finite element method investigates the onset of sharkskin for a linear low density polyethylene (LLDPE, $M_w = 125$ kg mol^{-1}, $Đ = 1.70$) sample. The simulation uses experimental data obtained by a capillary die (round cross-section area) with $L = 22.4$ mm and $D = 1.39$ mm at T = 190 °C. Performing the numerical simulations they[33] observed that elongation rates are near to zero in the die land, although intensive elongation rates manifest themselves at the periphery of the extrudate, just around the die exit lip, see Figure 2.7.
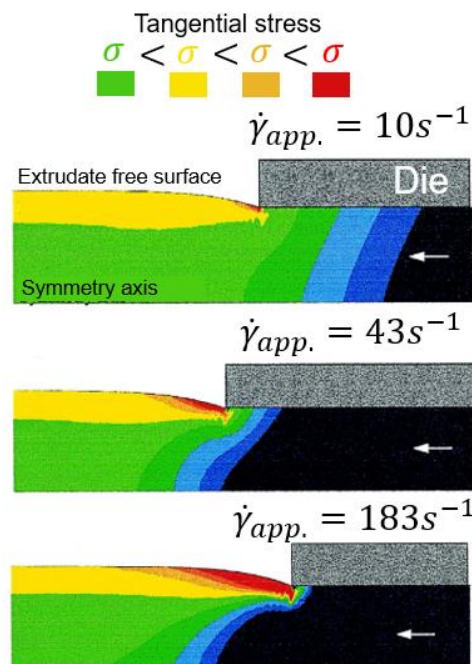

Figure 2.7. Numerical simulations based on finite element method investigates the onset of sharkskin for a linear low density polyethylene (LLDPE, $M_w = 125$ kg mol^{-1}, $Đ = 1.70$) sample. The simulation uses data obtained by a capillary die (round cross-section area) with $L = 22.4$ mm and $D = 1.39$ mm at T = 190 °C. The white arrow indicates the flow direction. The color gradation represents the magnitude value of the tangential stress, with red to be the maximum and green the minimum. As the apparent shear rate increases the tangential stress directly at the

die exit region overcomes a critical value. Afterwards a propagation of the tangential stress perpendicular to the flow field is observed; slightly at $\dot{\gamma}_{app.}= 43$ s^{-1} and intensively at $\dot{\gamma}_{app.}=$ 183 s^{-1}. This propagation is blamed for the sharkskin formation. Adapted from C. Venet et al., *Journal of Non-Newtonian Fluid Mechanics* 93, *117*, **2000**, Figure 10.[33]

Increasing the mass rate through the constant die ($L= 22.4$ mm and $D = 1.39$ mm) the shear rate and shear stress are increased. Specifically, it is observed in Figure 2.7 that the magnitude of the tangential stress at the die exit region increases and a perpendicular stress propagation towards to the shear flow is generated. Comparing the magnitude stress obtained by the onset of sharkskin from the experimental and computational observations a qualitative agreement between them is mentioned.[33] Hence, the computational simulation have a qualitative agreement with the experiment and they[33] provide a possible explanation for the origin of the sharkskin instability, that is the increasing tangential stress at the die exit region.

Based on the previous theoretical approaches and possible scenarios for the origin of sharkskin Milger et al.,[34] used an optical velocimetry technique and proposed a flow kinetic scheme which describes the formation of sharkskin. They[34] extrudate a commercial linear low density polyethylene (LLDPE) through a capillary die (round cross-section area) with length $L = 33$ mm and diameter $D = 1.6$ mm at T = 177 °C. At the end of the extrusion die a velocimetry device is positioned and able to obtain the velocity profile and capture the optical formation of the sharkskin. In Figure 2.8 (a) the surface of the extrudate LLDPE is presented and the sharkskin instability can be designated. In Figure 2.8 (b) snapshots from the high speed video recorded at the die exit are presented and associated with the extrudate appearance is Figure 2.8 (a). Specifically, in Figure 2.8 (b) at (i)-(ii) a valley formation is generated directly after the die exit, then (iii)-(iv) present the development of an instability ridge as the material experiences the extensional stress and finally (v)-(vi) the sharkskin instability ridge is moving far from the die and again a valley type of formation is ready to begin. Based on the snapshots from the high-speed video Milger et al.[34] proposed a scheme which explains the formation mechanism of sharkskin, see Figure 2.8 (c). The Latin numerals of Figure 2.8 (c) associated with the snapshots in Figure 2.8 (b).
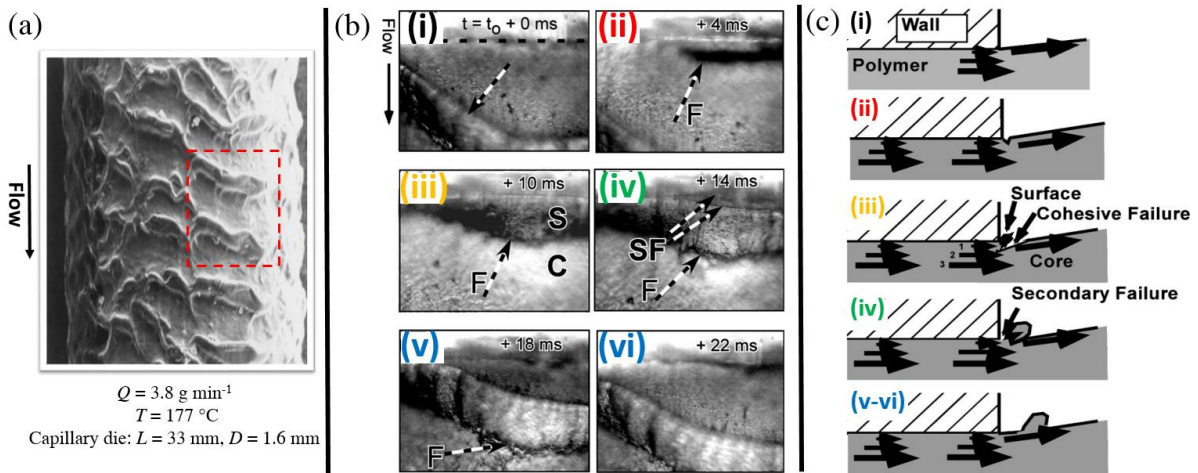
Figure 2.8. Conceptual explanation of sharkskin formation at the exit of a capillary die (round cross-section area) with length $L = 33$ mm and diameter $D = 1.6$ mm at $T = 177$ °C using a linear low density polyethylene (LLDPE). (a) Extrudate appearance of the LLDPE at throughputs of 3.8 g min^{-1}. This appearance is call sharkskin instability. It is designated by the regular well-developed pattern. (b) High-speed video microscopy images of the evolution of the sharkskin structure. This sequence is associated with one oscillation of the sharkskin structure, red rectangular area on (a). The flow is downward the exit of the die, which is shown by the dotted line at the top of the (i). Specifically the high-speed video represents the formation of (a). Initially, at the die exit a formation of a valley type is generated (i)-(ii), then becomes more intensive and it starts move out of the die exit (iii)-(iv). Finally the sharkskin ridge is out of the die and on the surface of the extrudate as the (v)-(vi) depict. (c) Sketch of the steps for the formation of sharkskin instability, side view. This sketch is attempting to describe the process that has been captured by the high-speed video of (b). Adapted from K. B. Milger et al., *Journal of Rheology* 46, *383*, **2002**, Figures 1 (c), 5 and 6.[34]

Burghelea et al.[35,36] studied the theoretical concept suggested by Cogswell[22] for the intensive extensional stress at the die exit region and confirming the existence of this stress on the surface of the extrudate by the computational studies of C. Venet and B. Verges.[33] Burghelea et al.[35,36] used an experimental set up combined by a laser-Doppler velocimeter which allows the extraction of velocity and stress distribution at the slit die. The slit die (rectangular cross-section area) has length $L = 50$ mm, width $W = 14$ mm and height $H = 1$ mm and it is adapted in a capillary rheometers.
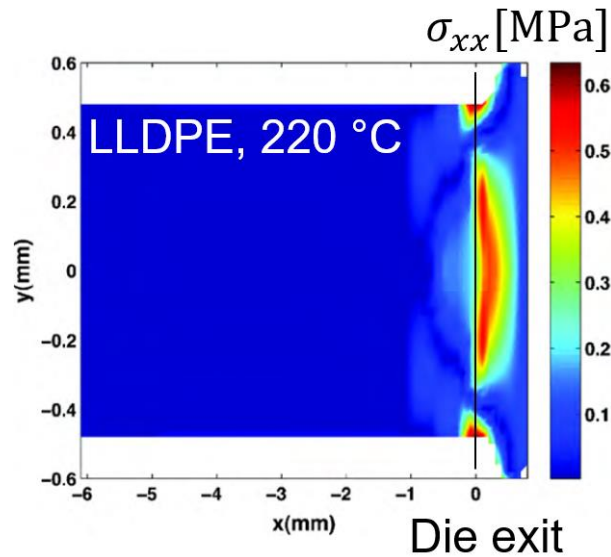
Figure 2.9. Extrusion of linear low density polyethylene (LLDPE, M_w = 144 kg mol^{-1}, Đ = 4.4) sample by a slit die (rectangular cross-section area) with length L = 50 mm, width W = 14 mm and height H = 1 mm at T = 220 °C. Part of the slit die is transparent glass and a laser-Doppler velocimeter allows the extraction of the velocity and stress distribution at the slit die. The color gradation represents the magnitude value and the spatial distribution of the extensional stresses σ_{xx} for LLDPE during the onset of sharkskin instability at the slit die. This experimental set up provide the evidence for the existence of the extensional stress at the die exit region. When the extensional stress on the die exit region overcome a critical value the sharkskin instabilities starts to form. Adapted from T. I. Burghelea et al., *Journal of Non-Newtonian Fluid Mechanics* 165, *1093*, **2010**, Figure 12 (a).[35]

Through this experimental set up they[35,36] extruded a specific linear low density polyethylene (LLDPE, M_w = 144 kg mol^{-1}, Đ = 4.4) at T = 220 °C. Burghelea et al.[35,36] experimentally observed that the onset of sharkskin instability on the surface of the LLDPE extrudate is accompany with an increase of the extensional stress on the die exit. Moreover, the increase of the extensional stress generates a perpendicular stress propagation towards the flow direction as Figure 2.9 presents. This experimental evidence confirms the simulation studies from C. Venet and B. Verges,[33] and state that the onset of sharkskin instability is connected with the intensive extensional stress at the die exit region.[35,36]

The scientific computational group of J. Tsamopoulos and coworkers[37-39] performed several advanced computational studies to understand, quantify and evidence the instability of sharkskin at the end of extrusion dies. The simulations performed by Karapetsas et al.[37] and Pettas et al.[38] proposed that the onset of sharkskin instability is related to the singularity of the die exit region. There an intensive extensional deformation is observed, however none of these

studies[37,38] were able to overcome the numerical limitations and simulate the distorted surface of the extrudate after the die exit. Recently, the same group developed numerical algorithms[39] which allow them to simulate the whole phenomenon of sharkskin including the stress distribution in the die exit region and the wavy distorted surface after the die exit. Varchanis et al.[39] performed computational simulations and proposed that the origin of sharkskin is a combination of two contributions, (i) the intensive extensional stress at the die exit region and (ii) the recoil configuration, that is the relaxation process, after the experience of the extensional stress. In Figure 2.10 an animation which explains the possible molecular mechanism for the origin of sharkskin is presented.[39] The intensive extensional stress at the corner of the die is applied only on the surface of the extrudate and forces the macromolecular chains to a fully stretched configuration. When the fully stretched macromolecular chain escape from the intensive extensional stress area, after the die exit, returns back to a coil configuration.[39] This process is blamed for the generation of the regular pattern of sharkskin on the extrudate surface.
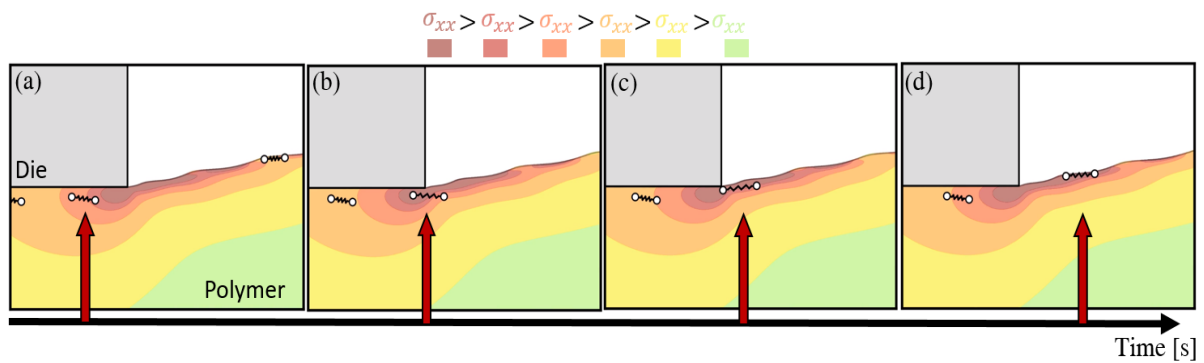

Figure 2.10. Numerical simulations based on finite element method investigate the origin of sharkskin. The color gradation represents the magnitude value of the extensional stress σ_{xx}, with red to be the maximum and green the minimum. In addition to the color gradation of the extensional stress a spring is represents the behavior of a polymer chain which is feeling the extensional flow directly at the die exit region. It is suggested that the origin of the sharkskin formation is a combination of extension thinning of the polymer melt in its bulk and recoil of the polymer chains in transient extensional flow. Adapted from S. Varchanis et al., *Physics Review Letters* 127, *088001*, **2021**.[39]

Reviewing the previously mentioned theoretical, experimental and computational studies over the last thirty (30) years the following theoretical concept for the origin and formation of the sharkskin instability can be described. Increasing the extrusion volumetric flow rate the wall shear stress is increasing. When a critical value of wall shear stress is overcome then an

intensive extensional stress on the die exit periphery is developed. The extensional stress is applied only on the outer surface of the extrudate, however as the extrusion volumetric flow rate increases the magnitude of the extensional stress increases as well. Hence, a perpendicular propagation of this extensional stress towards the flow is generated and a tear behavior is initiated. Based on this the extrusion flow can be categorized into two theoretical layers, the surface layer where the propagation of the extensional stress cause the tearing behavior and the core layer where the shear stress is dominant. Within the surface layer where the intensive extensional stress is dominant the macromolecular chains are forced to a fully stretched configuration. At the time that the macromolecular chain flows away from this extensional deformation area, it starts to form a recoil configuration again. This relaxation process from a fully stretched to a recoil conformation of the macromolecular chain possibly generates the well-developed pattern formation on the extrudate surface, so called sharkskin.

2.3. Origin of stick-slip

The extrusion flow instability named as stick-slip, see Figure 2.11, is one of the most severe extrusion instability in polymer process.[2,6] Is usually occurs for highly entangled polymer melts which they have a strong physical interaction with the surface of the die wall.[2] Strong physical interaction between the polymer and the surface of the die may occur due to the surface energy of the material and the roughness of its.[6] This physical interaction either capture polymer material inside the surface roughness or generates a polymer material deposition on top of the surface. These captured or deposited polymeric material on the surface of the die is entangled with the macromolecular chains from the bulk flow. This physical network of constrains is existing up to a critical shear stress value. When this critical wall shear stress value is overcome then a disentanglement process is happened and an intensive slippage between the surface of the die and the bulk flow is developed.[6] Based on this theoretical concept the iteration of entanglement and disentanglement process between the physical grafted macromolecular chains on the surface of the die and the polymer chains within the bulk flow is the origin of the stick-slip instability.[1,2,6]
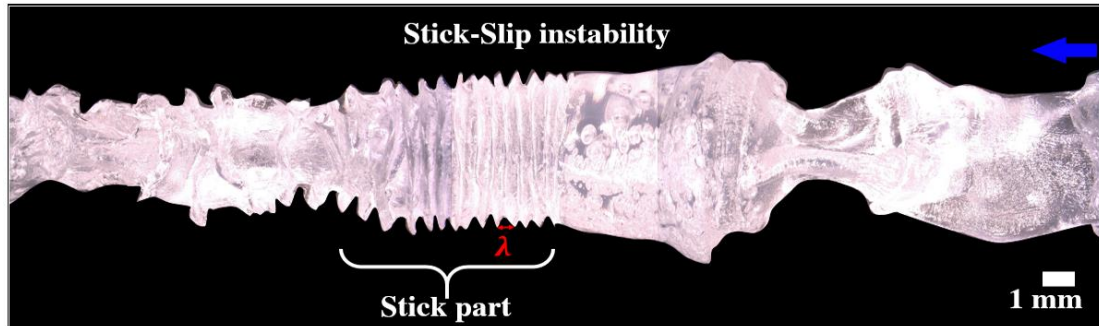
Figure 2.11. Extrusion of polybutadiene (PBD, M_w = 610 kg mol^{-1}, Đ = 2.95) sample by a capillary die (round cross-section area) with length L = 30 mm and diameter D = 2 mm at T = 100 °C. Stick-slip instability is depicted at $\dot{\gamma}_{app.}$ = 20 s^{-1}. Two regions are appeared: (i) stick part (mentioned in the image) where a regular pattern is observed and (ii) slip part (the rest of the extrudate) where a non-regular pattern with volume distortions are observed. The spatial characteristic wavelength λ is indicated on stick part of the extrudate. The blue arrow indicates the extrusion direction.

In contrast with the sharkskin phenomenon the stick-slip is originated on the die land and not on the die exit region. However, the extrudate of the stick-slip instability is composed by two different region the stick part and the slip part, see Figure 2.11. Each part is associated with a characteristic part of the pressure profile.[15] The slip part is associated with the rapid decrease of the pressure and the stick part is connected with the pressure build up. Based on the origin of the stick-slip instability, which is the entanglement-disentanglement process in the die land, the rapid pressure decrease can be explained and the volume distorted appearance of the extrudate is expected. Although, the stick part which is associated with the pressure build up represent a regular pattern on the surface of the extrudate which is similar to the sharkskin instability, see Figure 2.11.[15] The reason for the generation of the sharkskin pattern during the stick-slip instability is something which is has not been clarified in literature yet.

3. Development of Characterization Methods for the Extrusion Flow Instabilities

Within this chapter an online characterization technique for the extrusion flow instabilities is presented. This technique is a combination of capillary rheology and optical analysis. The capillary rheometer is equipped with a custom made highly pressure sensitive slit die (HPSSD) with length of L = 30 mm and a rectangular cross-section area of 0.5 x 5 mm² (H x W). The HPSSD comprises a series of three highly pressure sensitive piezoelectric (Kistler 6182CA) pressure transducers (Tr) distributed along the slit die. At the die exit of the capillary rheometers an online optical device (camera) is positioned perpendicular to the extrudate width. This optical device records a full high-definition video during the extrusion process. The raw pressure signal obtained by the HPSSD is further processed and then Fourier transformed, hence the characteristic frequency of the pressure signal which is associated with the extrusion flow instabilities is obtained. The high-definition video is also further processed and the construction of a space-time diagram is enabled. This space-time diagram provides the characteristic time periodicity (or frequency) of the extrusion flow instabilities. Hence, the same information, such as the characteristic frequency of extrusion flow instabilities, is obtained by capillary rheology and optical analysis. This combination enables the adaption of an optical system like that in the production line and a direct comparison and evaluation with laboratory equipment, such as capillary rheometers.

3.1. Materials used in the development of the method

The purpose of developing this technique is the online characterization of extrusion flow and surface appearance of the extrudate. To prove the concept and the capabilities of this technique two commercial styrene-butadiene rubber (SBR) samples which they have similar molecular properties but different extrusion flow and extrusion instabilities are used.

The two commercial styrene-butadiene rubbers (SBR), are anionically synthesized and named as SBR A and SBR B. To obtain the molecular weight distribution (MWD) of the SBRs, the size-exclusion chromatography (SEC) is calibrated with linear polystyrene standards. The elution volume distributions of the investigated samples are displayed in Figure 3.1. The elution volume distributions of the two samples are similar, thus similar molecular weight distribution is expected. The molecular weight component, presented at elution volume between 10 mL and 15 mL, is assumed to be bimodal distribution with a distinct separation point of the two distinguish modes at ~12.5 mL. In addition, significantly low molecular weight fractions, are observed within the investigated samples between 20 mL and 22.5 mL.
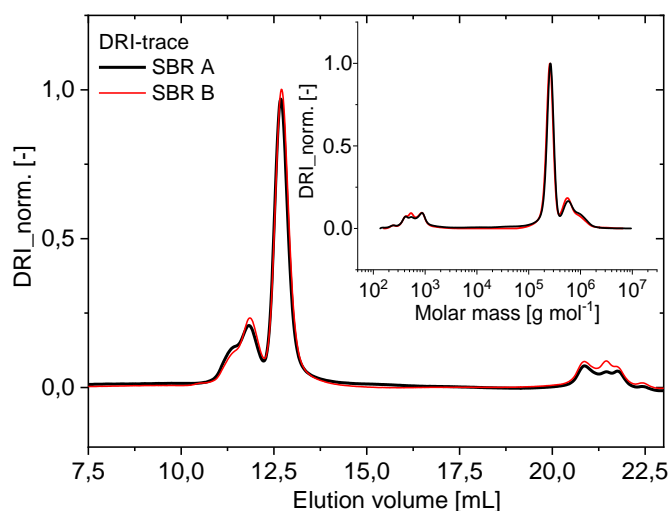
Figure 3.1. Normalized differential refractive index (DRI) detector response as a function of the elution volume for both SBR samples as obtained by SEC. The inset is the molecular weight distribution (MWD) of both samples. This SEC is equipped with an analytical column with length of 300 mm and inner diameter of 8 mm. Adapted from C. K. Georgantopoulos et al., *Macromolecular Material and Engineering* 306, *2000801*, **2021**, Figure 1.[15]

For the relative weight composition of the bimodal fraction (elution volume of 10 mL to 15 mL) the two modes are similar as well, see Table 3.1. The weight average molecular weight M_w, of each component vary by a factor of 3 and ~2.5 for SBR A and B, respectively, see Table

5.1. Moreover, the complete M_w values of the investigated samples are similar for both of them, $M_w = 390$ kg mol^{-1}. The total M_n values and the M_n values of the medium molecular weight component of the SBR A and B have similar values, ~290 kg mol^{-1} and ~255 kg mol^{-1}, respectively, see Table 5.1. The significantly lower molecular weight component, between 20 mL to 22.5 mL, has a roughly estimated average molecular weight value of $M_w \approx 0.62$ kg mol^{-1} for both investigated samples. Those substantially lower molecular weight component are recognized as hydrocarbons and not SBR. This information is obtained by the new combined method 2D NMR – SEC.[40] This method is using a low field benchtop NMR (62 MHz, 1.45 Tesla, ^{1}H) spectrometer coupled to SEC. Within this chapter this method is used to characterize the chemical composition of each different molecular weight component within the investigated samples, SBR A and B.[40]

Table 3.1. Molecular weight characteristics of the two investigated SBR samples.

Name	Elution volume [mL]	Weight percent [wt.%]	M_n [kg·mol^{-1}]	M_w [kg·mol^{-1}]	Đ [-]
SBR A	10.0 – 15.0		286	391	1.36
b)High - MW	10.0 – 12.5	45.3	688	757	1.10
b)Medium - MW	12.5 – 15.0	49.7	258	260	1.02
a)Low - MW	20.0 – 22.5	5.0	0.46	0.65	1.40
SBR B	10.0 – 15.0		287	390	1.35
b)High - MW	10.0 – 12.5	44.8	610	650	1.05
b)Medium - MW	12.5 – 15.0	49.2	252	256	1.01
a)Low - MW	20.0 – 22.5	6.0	0.42	0.60	1.42

a)The weight percent is calculated from the 2D SEC-NMR data presented in Figure 6 at Georgantopoulos et al., Macromolecular Material and Engineering 306, 2000801, 2021.[15] b)The weight percent is calculated by the DRI detector, insert of Figure 3.1. Adapted from C. K. Georgantopoulos et al., *Macromolecular Material and Engineering* 306, *2000801*, **2021**, Table 1.[15]

To determine the chemical composition of the investigated SBR samples, high field NMR spectroscopy (400 MHz, 9.4 Tesla, ^{1}H) is used, see Table 3.2. Furthermore, the glass transition temperature T_g of the samples is obtained by differential scanning calorimetry (DSC) characterization, see Table 3.2. Each of the samples has only one glass transition temperature, thus phase separation is not detectable at a large length scale (i.e. $l > 3 - 5$ nm) in these two systems.[15]

Table 3.2. Molecular weight characteristics of the two investigated SBR samples.

Name	Styrene [wt.%]	Butadiene 1.2 [wt.%]	Butadiene 1,4 (*cis* and *trans*) [wt.%]	[a)]T_g [°C]
SBR A	23.5	47.3	29.2	-36.3
SBR B	16.3	25.2	58.5	-60.7

[a)] The heating/cooling rate was 5 K min^{-1} with a temperature range of -90 °C and 160 °C. The second heating run was analyzed. Adapted from C. K. Georgantopoulos et al., *Macromolecular Material and Engineering* 306, *2000801*, **2021**, Table 2.[15]

3.2. Capillary rheology - Highly pressure sensitive slit die (HPSSD)

An online highly pressure sensitive in-situ mechanical detection extrusion slit die was developed to characterize the flow instabilities during extrusion.[8,11,14,15,17-20] Specifically the extrusion die is named as a highly pressure sensitive slit die (HPSSD). This HPSSD can be coupled to capillary rheometers and lab size extruders.[8] The HPSSD is equipped with three highly sensitive piezoelectric pressure transducers (Tr) along the die. These piezoelectric pressure transducers can detect pressure fluctuations of about $\Delta p \approx 10^{-5}$ bar which are associated with the onset of extrusion instabilities and specifically with the regular distortions on the surface of the extrudate. Within this study[15] the HPSSD is coupled to a capillary rheometer named Göttfert RG 50 (Buchen, Germany) and has dimensions of width $W = 5$ mm and height $H = 0.5$ mm over a length of $L = 30$ mm. This HPSSD comprises a series of three highly pressure sensitive piezoelectric (Kistler 6182CA) transducers (Tr) distributed along the slit die. The transducers are placed, at (Tr1) 5 mm, (Tr2) 15 mm and (Tr3) 25 mm from the die entrance and the tip of them is flashed to the flow channel, see Figure 3.2.[15]

The measuring element of the pressure piezoelectric transducers has diameter of 2.5 mm and provides detection of the pressure fluctuations during the extrusion experiment. These piezoelectric transducers have $\Delta t \approx 10^{-3}$ s time and $\Delta p \approx 10^{-5}$ bar pressure resolution, up to $p = 2000$ bar extrusion pressure inside the capillary rheometer.[15] The time depended pressure signal obtained by those piezoelectric pressure transducers is subjected to oversampling (online; sampling rate of 400 data points per second) to improve the signal to noise ratio and acting as a low pass filter as well. Next, the signal is baseline corrected with a first order polynomial fit function to remove the signal drift and random noise. Afterwards, the processed signal is fitted by an auto-correlation function. The processed data are then apodized by using an exponential function and double zero filled with the amount of data points prior to Fourier transformation (FT) to enhance the signal-to-noise ratio. The data processing of the raw time depended pressure signal is adopted by nuclear magnetic resonance (NMR) spectroscopy data processing

technique. Further details regarding the experimental system and time data processing can be found elsewhere. [8,15,17-19]
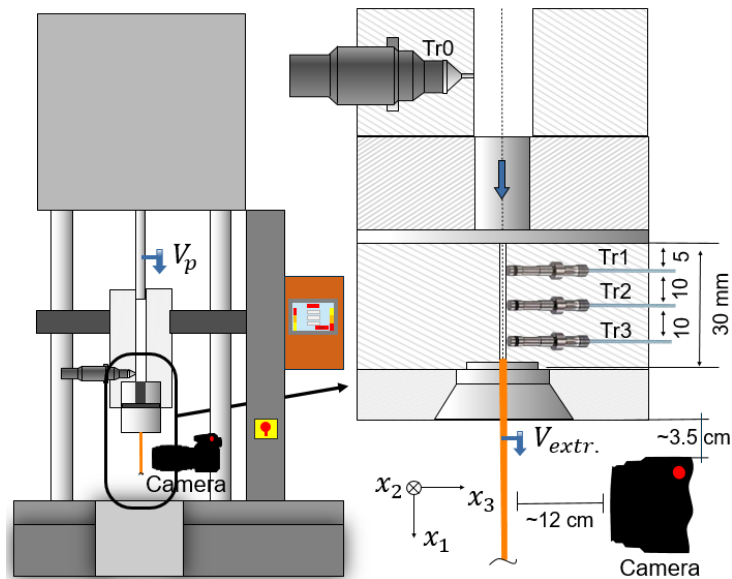
Figure 3.2. Schematic representation of the capillary rheometer and the highly pressure sensitive slit die. Marked transducers: Tr0 – conventional pressure transducer, Tr1 – Tr3 – Kistler (6182CA) highly sensitive piezoelectric pressure transducers. The ex-situ online optical visualization system (camera) is placed at a distance of ~3.5 cm below the die exit and ~12 cm from the extrudate surface. The x_2 is the direction of the width (W) and the x_3 is the direction of the height (H). Adapted from C. K. Georgantopoulos et al., *Macromolecular Material and Engineering* 306, *2000801*, **2021**, Figure 2.[15]

Two geometries of extrusion dies are used to characterize the processing behavior of the investigated SBRs within this study: (i) the HPSSD and (ii) three round capillary (circular cross-section area) dies. The extrusion HPSSD has a rectangular cross-section of width, $W = 5$ mm and height, $H = 0.5$ mm, over a length of $L = 30$ mm. The three round capillary dies have diameter of $D = 2$ mm, and aspect ratios of $L/D = 5$, 10, 15. Hence the raw data obtained by the round capillary dies should be Bagley[3] and Rabinowitsch-Weissenberg[3] corrected by using this series of the three round capillary dies with length to diameter ratios of $L/D = 5$, 10, 15 and $D = 2$ mm. The raw data obtained by the HPPSD data are only in need of Rabinowitsch-Weissenberg[3] correction. Because the aspect ratio of the die is $L/H = 60$ and it is known that the pressure exit effects can be neglected if L/H ≥ 60.[41] Hence the correct steady state viscosity η and the wall shear stress σ_{wall} can directly be obtained.

The corrected steady state viscosity as a function of wall shear rate obtained by HPSSD and round capillary dies are presented and compared in Figure 3.3. The steady state viscosity obtained by HPSSD and capillary dies has similar values for the SBR A, see Figure 3.3 (a). However, for the SBR B deviation between the steady state viscosities obtained by the two geometries is observed after $\dot{\gamma}_W \approx 30$ s^{-1} due to the onset of stick-slip instability in the slit die, see Figure 3.3 (b). It is found that SBR B presents stick-slip instability in shear rate range between $\dot{\gamma}_W \approx 30$ s^{-1} and 60 s^{-1} while is extruded by round capillary die, and in shear rate range between $\dot{\gamma}_W \approx 40$ s^{-1} and 300 s^{-1} while is extruded by slit die, see Figure 3.3 (b). Based on this experimental observation, it is assumed that stick-slip instability appears over a wider range of shear rates in the slit die than the round capillary die. The latter, explains the slight deviation of the steady state viscosity obtained by the slit and round capillary die in Figure 3.3 (b). The steady state viscosity data is fitted by the Carreau model,[42] $\eta(\dot{\gamma}) = \eta_0/(1 + (\tau\dot{\gamma})^2)^{\frac{1-m}{2}}$, to quantify the difference between the SBR A and B. The fitting parameters are presented in Table 3.3 at T = 120 °C.
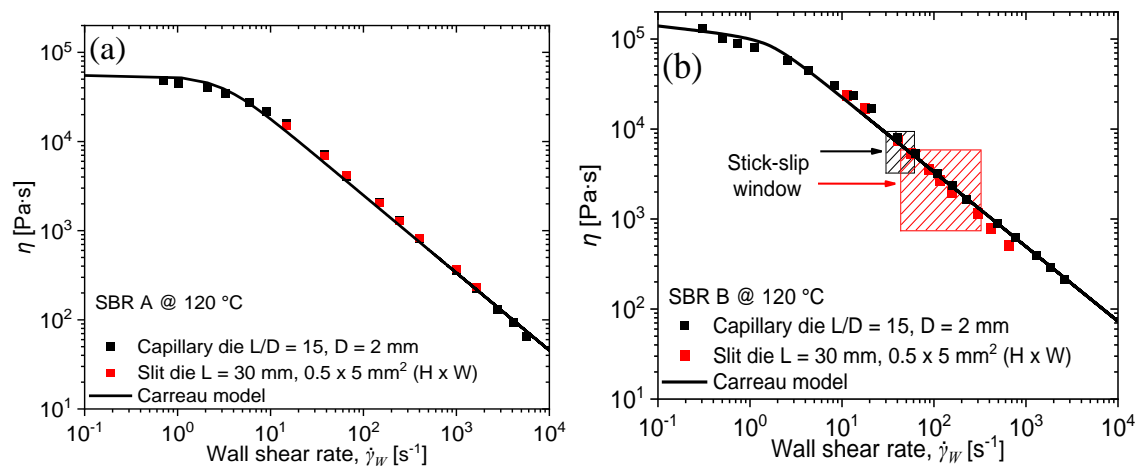

Figure 3.3. Absolute values of the steady state viscosity as a function of wall shear rate $\dot{\gamma}_W$ for slit and round capillary dies. Agreement between both geometries is observed for (a) SBR A where only sharkskin instability appears. Deviation between the two geometries occurs for (b) SBR B after $\dot{\gamma}_W > 30$ s^{-1} where the stick-slip instability appears at the slit die between $\dot{\gamma}_W \approx 40$ s^{-1} to 300 s^{-1}, afterwards gross melt fracture instability occurs. (b) The shear rate range of the stick-slip instability for the SBR B material at the round capillary and slit dies is displayed by the shaded areas in the plot. Adapted from C. K. Georgantopoulos et al., *Macromolecular Material and Engineering* 306, *2000801*, **2021**, Figure 9.[15]

Table 3.3. Carreau model fitting parameters obtained at T = 120 °C.

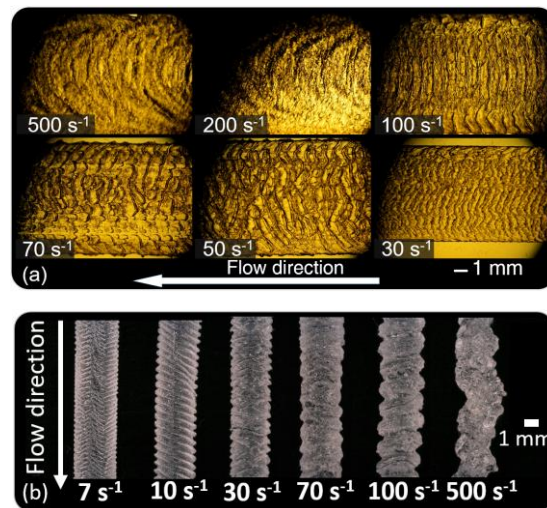| Name	Carreau		
	m	τ [s]	η_0 [kPa·s]
SBR A	0.13	0.35	55
SBR B	0.17	0.90	140

Adapted from C. K. Georgantopoulos et al., *Macromolecular Material and Engineering* 306, *2000801*, **2021**, Table 3.[15]

In Figure 3.4 the raw pressure signals obtained by the piezoelectric pressure transducers of the HPSSD for both investigated samples are presented. Figure 3.4 (a) shows the trend and behavior of the raw pressure signal during the sharkskin instability, in the range of apparent shear rate between $\dot{\gamma}_{app.} = 10$ s^{-1} and 200 s^{-1}. Figure 3.4 (b) presents the raw pressure signal during sharkskin and stick-slip flow instabilities in the range of apparent shear rate $\dot{\gamma}_{app.} = 7$ s^{-1} and 20 s^{-1}, and $\dot{\gamma}_{app.} = 30$ s^{-1} and 200 s^{-1}, respectively. Particular offline optical images of the extrudates for the SBR A and B are given by Figure 3.5 (a) and 3.6 (a), respectively.
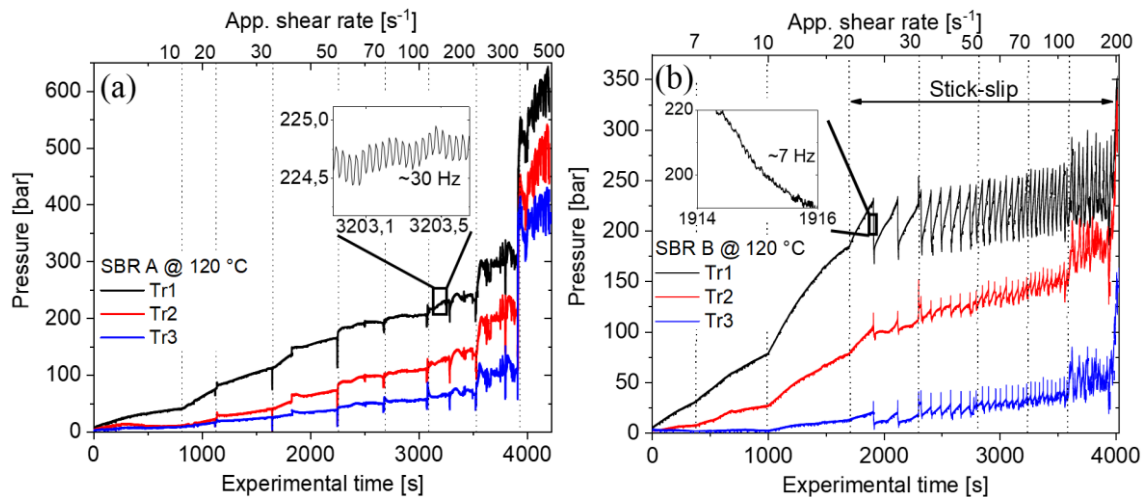
Figure 3.4. Profile of pressure signal during capillary extrusion at 120 °C, as detected by the three piezoelectric transducers within the slit die. The dimensions of the slit die are $L = 30$ mm and 0.5 x 5 mm^2 (*H* x *W*) cross-section area. (a) SBR A presenting sharkskin and an enlarged part of the pressure profile from Tr1 to depict the pressure oscillations. (b) SBR B presenting sharkskin up to $\dot{\gamma}_{app} = 20$ s^{-1} and afterwards stick-slip up to $\dot{\gamma}_{app} = 200$ s^{-1}. Adapted from C. K. Georgantopoulos et al., *Macromolecular Material and Engineering* 306, *2000801*, **2021**, Figure 10.[15]

In order to capture a representative time dependent pressure signal for sharkskin and stick-slip extrusion instabilities ~500 s of pressure recorded is chosen. In Figure 3.4 (a) the time dependent pressure signal presents sharp peaks any time that the shear rate is changed in order the collect the extrudate. Those peaks caused by the intensive motion of the extrudate during its collection. Due to the inherent detection mechanism of the sensitive piezoelectric pressure transducers,[8] the absolute numerical values of the pressure signal are not reliable. However, the pressure signal fluctuations deliver the characteristic frequency (or periodicity) of the extrusion flow instability through the previously mentioned data analysis. Typical characteristic frequency value of sharkskin instability for SBR material, at $\dot{\gamma}_{app.} = 200$ s^{-1} and T = 120 °C, is presented by Figure 3.4 (a). For the stick-slip instability three characteristic frequencies can be mentioned: (i) one which occurred by the stick part, usually sharkskin instability, τ^*_{stick} (ii) one obtained by the slip part, usually volume distortion τ^*_{slip} and (iii) the last one obtained by the pressure fluctuations $\tau^*_{pressure}$ ($\Delta p/p \approx 25$ % for $p \approx 200$ bar).[15,20]

Figure 3.5. Offline optical analysis of SBR A extruded at T = 120 °C by (a) transmission polarization microscopy and (b) incident light microscopy. Extrudates from (a) slit die of H = 0.5 mm, W = 5 mm and L = 30 mm and (b) round capillary die of L/D = 15 with D = 2 mm. The apparent shear rate $\dot{\gamma}_{app}$ is mentioned at each extrudate. Adapted from C. K. Georgantopoulos et al., *Macromolecular Material and Engineering* 306, *2000801*, **2021**, Figure 11.[15]
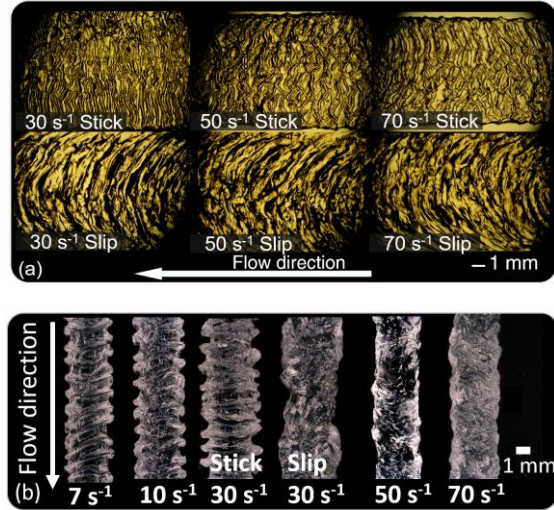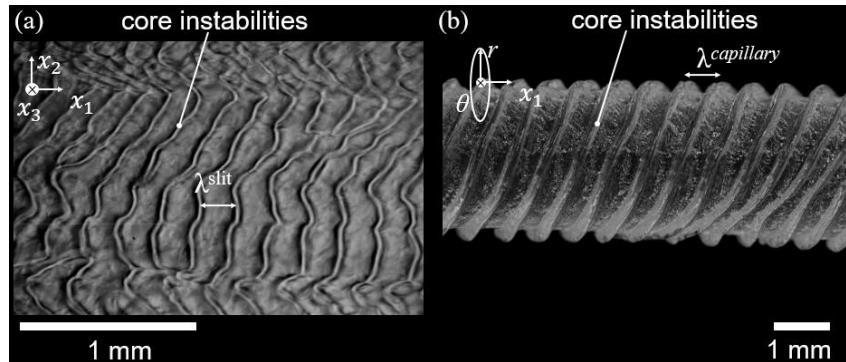
Figure 3.6. Offline optical analysis of SBR B extruded at T = 120 °C by (a) transmission polarization microscopy and (b) incident light microscopy. Extrudates with the stick-slip instability from (a) slit die of H = 0.5 mm, W = 5 mm and L = 30 mm in the shear rate range between $\dot{\gamma}_{app} = 30\ \mathrm{s}^{-1}$ to $70\ \mathrm{s}^{-1}$ and (b) round capillary die of L/D = 15 with D = 2 mm at $\dot{\gamma}_{app} = 30\ \mathrm{s}^{-1}$. The apparent shear rate $\dot{\gamma}_{app}$ is mentioned at each extrudate. Adapted from C. K. Georgantopoulos et al., *Macromolecular Material and Engineering* 306, *2000801*, **2021**, Figure 12.[15]

3.3. Offline optical analysis

Offline optical analysis of the collected extrudates was carried out by transmission polarized microscopy and incident light microscopy at room temperature. Transmission polarized microscopy is a contrast-enhancing technique allowing to evaluate the surface structure of the extrudate, which uses polarizing filters. Incident light microscopy is the method of choice for the imaging of specimens, specifically surfaces that remain opaque even at thickness of 30 μm. The extrusion flow instabilities are characterized based on their spatial characteristic wavelength (SCW) λ and their characteristic time periodicity (CTP) $\tau^{*}_{Char.}$ (or frequency $f_{Char.}$) of the surface and volume distortions. Wavelength λ is defined as the average spatial distance between two consecutive similar distortions, see Figure 3.7. The characteristic time periodicity $\tau^{*}_{Char.}$ is identified via offline optical analysis on the already collected extrudates at room temperature. Offline optical characteristic time periodicity $\tau^{*,offline}_{Char.}$ is defined as the ratio of the wavelength λ and the extrudate velocity $V_{ext.}$, see Equation (3.1).

$$\tau^{*,offline}_{Char.} = \lambda/V_{ext.}\ \left(f^{offline}_{Char.} = V_{ext.}/\lambda\right) \tag{3.1}$$

In case of multiple wavelengths, for example in case of stick-slip, more than one CTPs are obtained. In terms of stick-slip instability, one extrudate velocity is assumed and the characterization takes place in both regions, stick and slip.
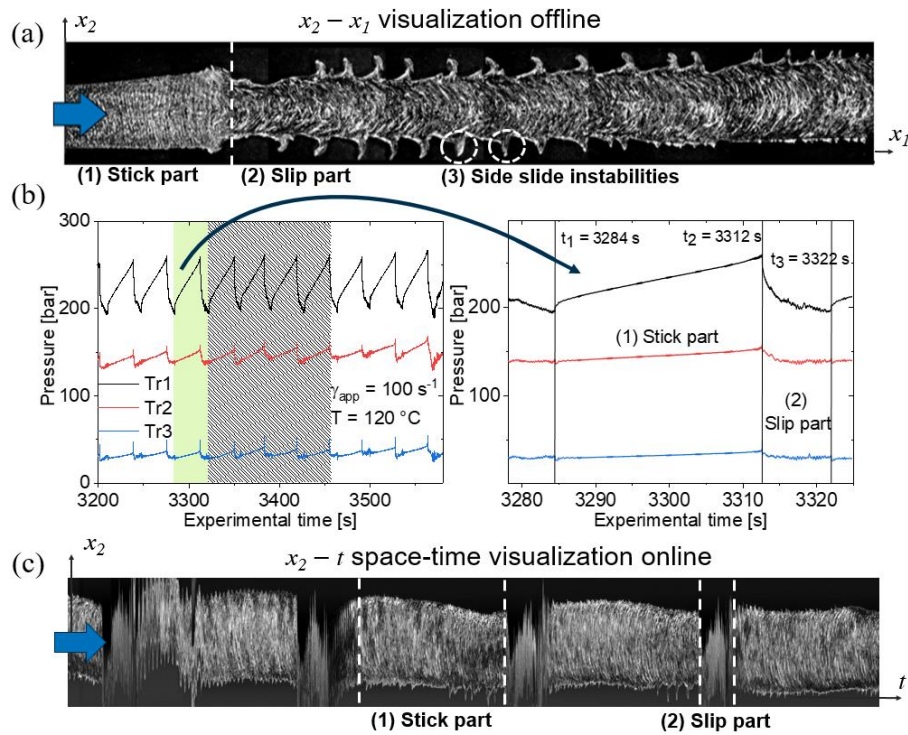

Figure 3.7. Offline optical analysis with (a) transmission polarization microscopy for a rectangular shape extrudate at $\dot{\gamma}_{app.}^{Slit} = 20$ s^{-1} and (b) incident light microscopy for a cylindrical shape extrudate at $\dot{\gamma}_{app.}^{Capillary} = 10$ s^{-1} for SBR A at T = 120 ºC. The x_1 indicates the extrusion direction. At both images there is indication for the typical spatial characteristic wavelength. The core instability indication refers to the main flow instability which is observed in the extrudate. Adapted from C. K. Georgantopoulos et al., *Macromolecular Material and Engineering* 306, *2000801*, **2021**, Figure 5.[15]

3.4. Online optical analysis

The online or on-fly optical monitoring of the extrudate during extrusion process has crucial importance for the polymer processing industry. Specifically, the online optical monitoring of the swelling and surface of the extrudate may ensure the quality of the material in proper time before the final process stage of the product. For the development of an online optical setup, a Pentax XP (Tokyo, Japan) camera is used. This camera is placed of about ∼3.5 cm from the slit die exit, perpendicular to the extrudate width (front view, x_1 - x_2, see Figure 3.2). The camera lens is a Sigma 105 mm DC Macro EX (Kawasaki, Japan) to allow proper magnification while is placed at a distance of ∼12 cm from the extrudate.[15] Then a fully high definition (1960 x 1080 pixels) video with 60 frames-per-second (fps) records the extrusion process at the die exit region for 5–7 minutes via this online remote acquisition system. Finally, offline and online optical methods are used to obtain the spatial and time characteristics of the extrusion flow instabilities.

The full high definition (HD) video is post-processed in order to construct a space-time visualization diagram.[43-46] The main idea for the space-time visualization construction from a video is explained and presented in Figure 3.8.
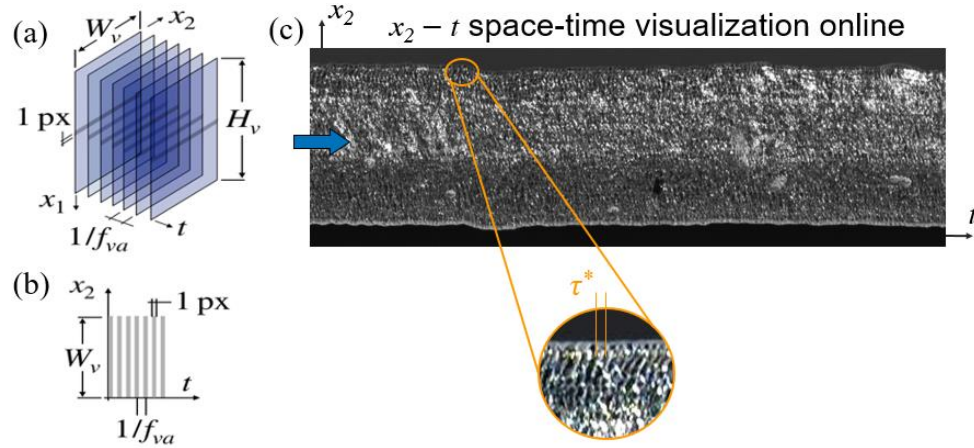
Figure 3.8. (a) – (b) Illustration of the basic principle for constructing a space-time visualization from a video with frame dimensions W_v x H_v and frame (acquisition) rate of f_{va}. (c) Example of an online $x_2 - t$ space-time visualization. An enlarged part of the visualization diagram presents the sharkskin stripes and the characteristic time periodicity of them. The investigated sample is SBR A at T = 120 °C and $\dot{\gamma}_{app}$ = 7 s^{-1} obtained by the slit die with H = 0.5 mm, W = 5 mm and L = 30 mm. The blue arrow indicates the extrusion direction. Adapted from C. K. Georgantopoulos et al., *Macromolecular Material and Engineering* 306, *2000801*, **2021**, Figure 3.[15]

The full HD video is recorded with frame dimensions W_v x H_v and a frame (acquisition) rate of f_{va}. A given line of pixels (px) at a fixed position along x_1 direction is extracted successively from each frame of the video and then added to a new created diagram, see Figure 3.8 (a) and (b). Consequently, the y-axis (x_2) corresponds to the width of the video frame W_v, and the x-axis (t) to the experimental time t.[15] The time between each line of pixels is determined by 1/f_{va}. In Figure 3.8 (c) the SBR A sample at T = 120 °C and $\dot{\gamma}_{app}$ = 7 s^{-1} is presented as an example.[15] The space-time diagram permits an easier extraction of the CTP τ* of the extrusion flow instability, without using estimated values such as the extrudate velocity, $V_{ext.}$. The online characteristic time periodicity $\tau_{Char.}^{*,online}$ obtained by the online optical analysis is defined as the time between two consecutive similar distortions, see Figure 3.8 (c).

Figure 3.9. (a) Offline optical analysis of an extrudate with stick-slip instability, which represents one pressure oscillation. The first part of the extrudate represents the stick and the second part the slip and the side slide instabilities. In (b) – (c) the gray shaded area represents the pressure signal from the three piezoelectric transducers corresponding to four stick-slip events which have been video recorded and their space-time diagram is presented. The investigated sample is the SBR B at T = 120 °C and $\dot{\gamma}_{app} = 100$ s^{-1} obtained by the slit die with $H = 0.5$ mm, $W = 5$ mm and $L = 30$ mm. The blue arrows indicate the extrusion direction. Adapted from C. K. Georgantopoulos et al., *Macromolecular Material and Engineering* 306, *2000801*, **2021**, Figure 4.[15]

An example of space-time diagram for stick-slip instability is presented in Figure 3.9. The offline image of the extrudate obtained by the slit die ($H = 0.5$ mm, $W = 5$ mm and $L = 30$ mm) for the SBR B is presented in Figure 3.9 (a). This extrudate is obtained at $\dot{\gamma}_{app} = 100$ s^{-1} and T = 120 °C , and it is the result off one pressure oscillation during stick-slip instability as depicted in Figure 3.9 (b). The first part of the extrudate has sharkskin instability and represents the stick part, that is the pressure increases for ~30 s from $p = 200$ bar to 250 bar, see Figure 3.9 (b). The second part has volume and surface distortions and represents the slip part, that is the rapid pressure decrease of ~10 s from 250 bar to 200 bar, see Figure 3.9 (b). Within the slip part, regular distortions on the side of the extrudate are observed. These distortions are defined as side slide instabilities, see Figure 3.9 (a).[15]

The characteristic pressure fluctuations of the stick-slip instability are presented in Figure 3.9 (b). The shaded are of the pressure fluctuations within Figure 3.9 (b) have been video recorded by the online optical monitoring system. The associated to those pressure fluctuation space-time diagram is shown in Figure 3.9 (c), where the four stick-slip events are presented.
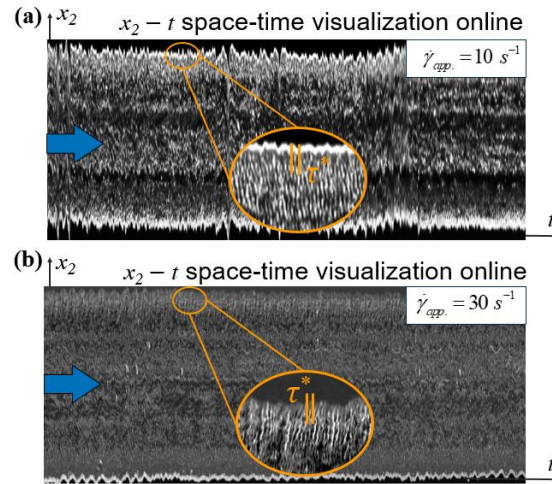
Figure 3.10. Space-time diagram of the SBR A at T = 120 °C for two different apparent shear rates $\dot{\gamma}_{app}$ obtained by the slit die. The extrudate (a) at $\dot{\gamma}_{app} = 10$ s^{-1} and (b) at $\dot{\gamma}_{app} = 30$ s^{-1} exhibit sharkskin instability. At each diagram a snapshot for a specific region of the extrudate is displayed enlarged and the characteristic periodicity can be identified. The blue arrows indicate the extrusion direction. Adapted from C. K. Georgantopoulos et al., *Macromolecular Material and Engineering* 306, *2000801*, **2021**, Figure 13.[15]

During the extrusion of the investigated samples by the HPSSD, the online optical analysis setup developed space-time diagrams and the online CTP $\tau_{Char.}^{*,online}$ of the flow instabilities is obtained. The space-time diagrams of SBR A at $\dot{\gamma}_{app} = 10$ s^{-1} and 30 s^{-1} at T = 120 °C present sharkskin instability, see Figure 3.10. Selected space-time diagrams of the SBR B for $\dot{\gamma}_{app} = 10$ s^{-1} and 70 s^{-1} at T = 120 °C are presented in Figure 3.11. Sharkskin instability is presented at $\dot{\gamma}_{app} = 10$ s^{-1} (Figure 3.11 (a)) and stick-slip instability is presented at $\dot{\gamma}_{app} = 70$ s^{-1} (Figure 3.11 (b)). In both Figure 3.10 and 3.11 an enlarged snapshot better visualizes the CTP $\tau_{Char.}^{*,online}$.
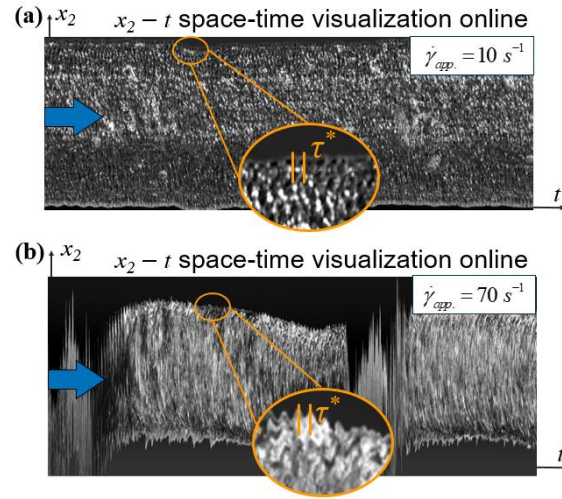
Figure 3.11. Space-time diagram of the SBR B at T = 120 °C for two different shear rates obtained by the slit die. The extrudate (a) at $\dot{\gamma}_{app} = 10$ s^{-1} exhibits sharkskin instability and (b) at $\dot{\gamma}_{app} = 70$ s^{-1} two stick-slip oscillations are presented. At each diagram a snapshot for a specific region of the extrudate is displayed enlarged and the characteristic periodicity is identified. The blue arrows indicate the extrusion direction. Adapted from C. K. Georgantopoulos et al., *Macromolecular Material and Engineering* 306, *2000801*, **2021**, Figure 14.[15]

3.5. Comparison of HPSSD, On- and Off-line optical analysis technics

The obtained characteristic frequencies (or periodicities) of the extrusion flow instabilities by the HPSSD, offline and online optical analysis are compared and presented in Figure 3.12. The characteristic frequencies of the extrusion instabilities for the SBR A are presented in Figure 3.12 (a). The offline and online optical analysis techniques for both dies, HPSSD and round capillary, present a linear increase trend as a function of shear rate within $\dot{\gamma}_{app} = 3$ s^{-1} to 700 s^{-1}. The data of the characteristic frequency obtained by the HPSSD, present a 'plateau'-like behavior within $\dot{\gamma}_{app} = 10$ s^{-1} to 300 s^{-1}. Observing the overall trend of the characteristic frequency, a monotonic linear increased as a function of shear rate in log-log scale can be asserted. Thus, the data are fitted by Equation (3.2).

$$f_{Char.} = \frac{1}{\tau^*} = a\dot{\gamma}_{app.}^{0.5} \tag{3.2}$$

Specifically for the SBR A, $f_{Char.} = 2\dot{\gamma}_{app.}^{0.5}$ is used. The total deviation of each technique from the fitting function is estimated to vary at most by 30%.
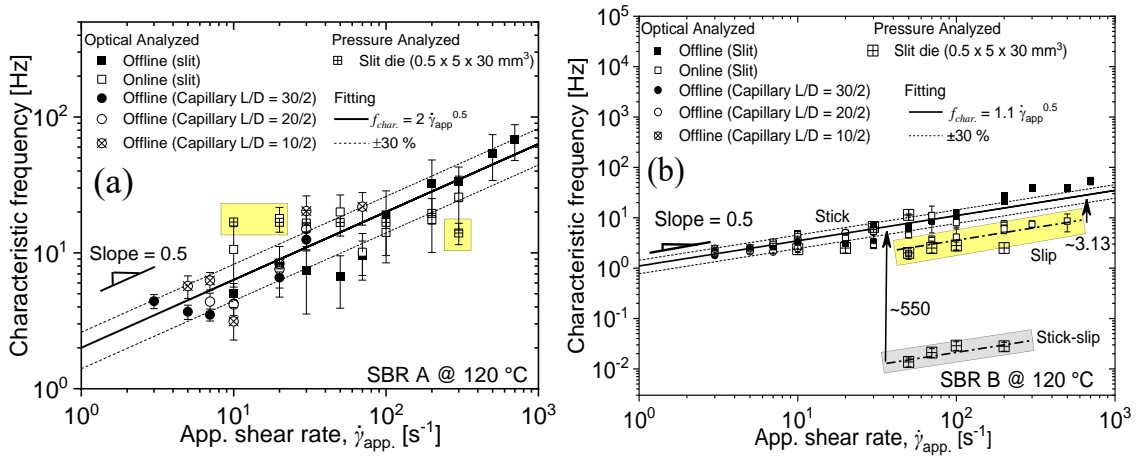
Figure 3.12. Characteristic frequency of the flow instability as measured by the three different techniques, online, offline optical analysis and highly pressure sensitive slit die for (a) SBR A and (b) SBR B. In (a) the highlighted regions represent the deviation of more than 30% from the fitting and in (b) the yellowish highlighted region depicts the low frequency components which are caused by the slip part of the extrudate and the grayish highlighted region depicts the characteristic frequency of the stick-slip pressure oscillation. Adapted from C. K. Georgantopoulos et al., *Macromolecular Material and Engineering* 306, *2000801*, **2021**, Figure 17.[15]

The characteristic frequency as a function of apparent shear rate for the SBR B is presented in Figure 3.12 (b). The offline and online optical analysis techniques for both dies, HPSSD and round capillary, present a linear increase trend as a function of shear rate within $\dot{\gamma}_{app} = 3$ s^{-1} to 700 s^{-1} which can be described by a power law behavior, Equation (3.2). The characteristic frequency obtained by the HPSSD presents an increased trend as well. Low frequency components, below $f_{Char.} \approx 5$ Hz, are observed during the stick-slip instability above the $\dot{\gamma}_{app} > 30$ s^{-1} due to side slide instabilities at the slip part of the extrudate, see Figure 3.9 (a). Significantly low frequency components, $f_{Char.} \approx 10^{-2}$ Hz, are mentioned during the stick-slip instability above the $\dot{\gamma}_{app} > 30$ s^{-1} as well. These Significantly low frequency components characteristic frequencies occur from the stick-slip pressure oscillation, see Figure 3.9 (b). Observing the characteristic frequency as a function of apparent shear rate for the SRB B in Figure 3.12 (b), a monotonic linear increase is observed and can be modeled by $f_{Char.} = 1.1\dot{\gamma}_{app}^{0.5}$. Similarly to SBR A, the deviation of each technique from the fitting function is estimated to vary at most by 30% up to $\dot{\gamma}_{app} = 100$ s^{-1}. The low frequency components within $\dot{\gamma}_{app} = 50$ s^{-1} to 500 s^{-1}, scale also with the power of 0.5 and differ by a factor of about ~3.13 from the main fitting function, see Figure 3.12 (b). This difference can be explained by the

51

inherent variation in extrudate velocity during the stick-slip instability. Above the $\dot{\gamma}_{app} > 200$ s^{-1} for the SBR B a deviation of the offline optical analyzed data from the fitting function is observed. This deviation occurs from the difficulties to estimate the SCW λ on the slip part of the extrudate, see Figure 3.9 (a).

3.6. Conclusions

Within this chapter an online characterization technique for the extrusion flow instabilities is presented combining optical analysis and capillary rheology. Specifically the design of the highly pressure sensitive slit die (HPSSD) and the post process of the raw pressure data is elaborated. In addition the setup and the working principal of the online optical analysis system is presented. By using the developed methods to characterize the extrusion flow instabilities the following outcomes have been drawn:

1. The three discussed methods, HPSSD, offline and online optical analysis, to obtain the characteristic frequency of the extrusion flow instabilities agree to each other with less than 30% deviation.

2. The characteristic frequency of the extrusion flow instabilities obtained by the HPSSD, offline and online optical analysis techniques as a function of apparent shear rate can be described by a power law model independent of the die geometry, $f_{Char.} = \frac{1}{\tau^*} = a\dot{\gamma}_{app.}{}^{0.5}$.

3. For the slit die geometry, the stick-slip instability manifests itself in a broader range of shear rates compared to the round capillary die.

4. Qualitative Models for the Spatial Characteristics of Extrusion Flow Instabilities

Within this chapter qualitative models for the spatial characteristics of extrusion flow instabilities, that is wavelength (λ) and height (h), are presented. Those qualitative models are based on theoretical concepts for the origin of surface related extrusion instabilities, i.e. melt fracture, which have been detailed presented in chapter 2. The presented models are also modified to be able to predict the spatial characteristic wavelength for capillary (round cross-section area) and slit (rectangular cross-section area) as well. In addition to the qualitative models, simple, practical and die geometry dependent models able to predict the spatial characteristic wavelength (λ) from a capillary to slit die and vice versa are also presented.

4.1. Model for spatial characteristic wavelength λ by S. Q. Wang and coworkers

Wang et al.,[23,24] and Barone et al.,[25] studied linear low density polyethylene (LLDPE, M_w = 112 kg mol^{-1}, $Đ$ = 4.15) in a wide range of temperatures, from T = 160 °C to 220 °C, with various round capillary dies (circular cross-section area). Then, they proposed an analytical model for the spatial characteristic wavelength (SCW) λ which is associated to the diameter D of the die, the swelled diameter of the extrudate D', the characteristic time periodicity τ^* of the phenomenon and the apparent shear rate, $\dot{\gamma}_{app.}$.

The extrusion flow instabilities are characterized based on their spatial and time characteristics. Wang et al.,[23,24] deal with the characteristic spatial wavelength λ and their characteristic time periodicity τ^* (or frequency) of the surface distortions, so called surface melt fracture. The characteristic spatial wavelength λ is defined as the spatial average distance between two consecutive similar distortions, see Figure 3.7. The characteristic time periodicity τ^* is defined as the time needed between two consecutive similar distortions, see Figure 3.8 (c).

Firstly, Wang et al.,[23,24] defined the wavelength as,

$$\lambda = \langle V \rangle \tau^*$$

(4.1)

where $\langle V \rangle$ is the average extrudate velocity and τ^* is the characteristic time periodicity of the flow instabilities. The average extrudate velocity is obtained by,

$$\langle V \rangle = V_{extr.}(D/D')^2 \tag{4.2}$$

where $(D/D')^2$ is the swelling factor referring to capillary dies (circular cross-section area), D is the diameter of the die, D' is the swelled diameter of the extrudate. The extrudate velocity $V_{extr.}$ is given by,

$$V_{extr.}^{Capillary} = (D/8)\dot{\gamma}_{app.} \tag{4.3}$$

For round capillary dies.

Thus, the model for the SCW λ proposed by Wang et al.,[23,24] for extrudates obtained by round capillary dies is occurred by combining Equation (4.1), (4.2) and (4.3) which gives Equation (4.4).

$$\lambda^{Capillary} = \frac{D}{8}\left(\frac{D}{D'}\right)^2 \dot{\gamma}_{app.}\tau^* \tag{4.4}$$

Barone et al.,[25] implemented on the proposed model,[23,24] Equation (4.4), the density ratio between the melt state ρ' inside the extrusion process and the solidified state ρ directly outside of the extrusion process. Hence, Equation (4.4) becomes,

$$\lambda^{Capillary} = \frac{D}{8}\left(\frac{\rho}{\rho'}\right)\left(\frac{D}{D'}\right)^2 \dot{\gamma}_{app.}\tau^*. \tag{4.5}$$

4.2. Modification of the model for spatial characteristic wavelength λ by S. Q. Wang and coworkers

Based on the Wang and coworkers methodology,[23,24,25] Equation (4.5) is here derived for slit die (rectagular cross-section area) geometry. Firstly, the volumetric flow rate Q inside the die is given by Equation (4.6) and directly after the die exit by Equation (4.7).

$$Q = W \cdot H \cdot V_{extr.}^{Slit} \tag{4.6}$$

$$Q = W' \cdot H' \cdot \langle V \rangle \tag{4.7}$$

Where H is the height, W is the width of the slit die, H' and W' are the swelled dimensions of the extrudate after extrusion. Assuming volume conservation, Equation (4.6) and (4.7) can be connected,

$$\langle V \rangle = \left(\frac{W}{W'}\frac{H}{H'}\right) V_{extr.}^{Slit}, \tag{4.8}$$

knowing that the extrudate velocity for slit die is obtained by,

$$V_{extr.}^{Slit} = (H/6)\dot{\gamma}_{app.} \tag{4.9}$$

and coupling Equation (4.8) and (4.9), Equation (4.10) is derived.

$$\langle V \rangle = \left(\frac{W}{W'}\frac{H}{H'}\right)(H/6)\dot{\gamma}_{app.} \tag{4.10}$$

Coupling Equation (4.1) with Equation (4.10) the analytical formula for the spatial characteristic wavelength λ for the slit die geometry is given by Equation (4.11).

$$\lambda^{Slit} = \left(\frac{W}{W'}\frac{H}{H'}\right)(H/6)\dot{\gamma}_{app.}\tau^* \tag{4.11}$$

Consistent with experimental observations from the extrudates,[15,25] it is assumed that $(H/H') \approx 1$. Thus, Equation (4.11) becomes Equation (4.12).

$$\lambda^{Slit} = \frac{H}{6}\left(\frac{W}{W'}\right)\dot{\gamma}_{app.}\tau^* \tag{4.12}$$

4.3. Prediction of the spatial characteristic wavelength λ from capillary to slit dies and vice versa

A crucial challenge for the modeling of the extrusion flow instabilities is the prediction of the spatial characteristics from the laboratory scale experiments up to industrial scale extrusion dies. Georgantopoulos et al.[15] inspired by the need for the prediction from laboratory to industrial scale equipment proposed an analytical correlation. Equation (4.5) is used assuming $\rho/\rho' = 1$, similar extrusion process between a capillary and a slit die under the same apparent shear rate and same temperature, that is:

$$\dot{\gamma}_{app.}^{Capillary} = \dot{\gamma}_{app.}^{Slit} \Rightarrow \langle V \rangle^{Capillary}\left(\frac{D}{8}\right)^{-1}\left(\frac{D'}{D}\right)^2 = \langle V \rangle^{Slit}\left(\frac{H}{6}\right)^{-1}\left(\frac{H'}{H}\frac{W'}{W}\right) \tag{4.13}$$

Consistent with optical experimental observations,[15] it is suggested that the swelling ratio is remained similar between the capillary and slit dies, $(D'/D)^2 \approx [(W'H')/(HW)]$ for the same material under similar processing temperature and deformation rates.

Based on Equation (4.4), the assumption $(D'/D)^2 \approx [(W'H')/(HW)]$ and that the characteristic time periodicity τ^* is material dependent (see Figure 3.12), the following geometrical correlation is proposed by Georgantopoulos et al.,[15]

$$\lambda^{Slit} = \lambda_{Barone\ et\ al.}^{Capillary}\left(\frac{8H}{6D}\right). \tag{4.14}$$

4.4. Model for spatial characteristic wavelength λ by Y. W. Inn and coworkers

Inn et al.,[26] developed a constitutive model for the spatial characteristic wavelength λ of the extrusion flow instabilities, based on optical observations of a polybutadiene (PBD, M_w= 182 kg mol^{-1}, $Đ$ = 1.90) sample extruded by capillary dies (round cross-section area) at T = 50 °C. This model is derived by the force balance[47] at the die exit region and describes the development of the extrusion surface instability. It is assumed that the surface fracture distortions originate at the die exit region due to the extensional stresses which are developed at the periphery of the die exit. This model is based on the "two layers", concept proposed by Cogswell,[22] see Figure 4.1. For those two theoretical layers Inn et al.,[26] assumed that they are existing inside and outside of the die.
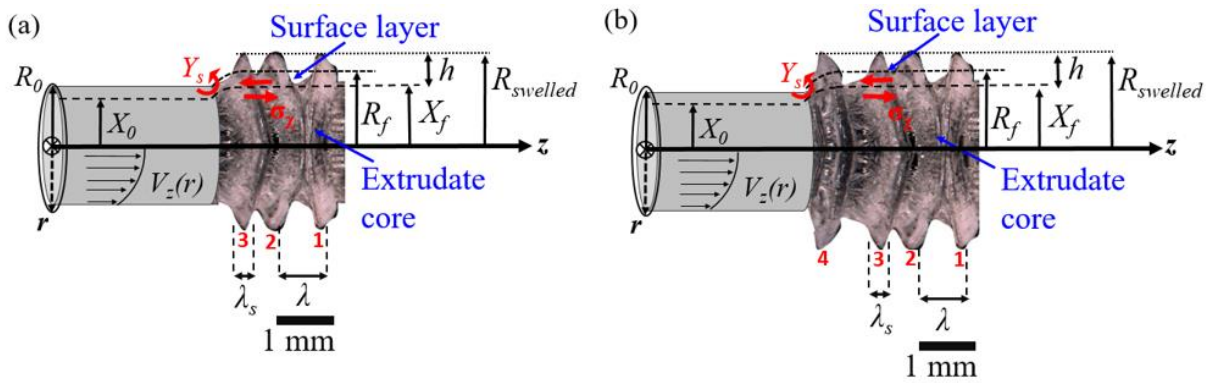
Figure 4.1. Schematic representation of the "two layer" model which shows the development of flow instabilities. From (a) to (b) the 4th instability ridge is developed. The instability ridge, λ_s is defined as the average width of the sharkskin stripe and it is formed by fracture at the skin/core interface, $r = X_f$. Where X_0 and X_f are the theoretical radius of the core layer inside and outside of the die, respectively. Where R_0 and R_f are the radius of the die and the theoretical swelled radius of the extrudate if no fracture was developed, respectively. Where h is the spatial characteristic height of the instabilities defined as the average distance between the swelled core and the tip of the instability. Inn et al.[26] assumed that $R_f = X_f + h/2$. The $R_{swelled}$ is the swelled radius of the extrudate taking into account the surface instability. Where σ_x is the shear stress on the theoretical interface between the core and surface layer and Y_s is the extensional stress at the die exit region. Adapted from C. K. Georgantopoulos et al., *Macromolecular Material and Engineering* submitted, **2022**, Figure 4.[48]

Those two layers have a theoretical interface which is placed inside the die at $r = X_0$ and outside the die at $r = X_f$. It is considered that directly after the die exit where the swelling has already happened the central core layer of the extrudate swells from a radius X_0 to X_f and moves with the average extrudate velocity $V_{swelled}$. The surface layer is assumed to move with a velocity, so called surface extrudate velocity $V_{extr.,surface}$. The $V_{extr.,surface}$ is the velocity of the outer layer of the extrudate which experience an intensive extensional deformation at the periphery of the die exit. Because of the two diverse deformations, extensional and shear, at the die exit region the declaration of two different velocities is a reasonable assumption.

This model considers a power-law fluid, with the velocity profile, Equation (4.15), to be given by Poiseuille flow field for capillary die and neglecting the slip velocity.

$$V_r(r,n) = \frac{3n+1}{n+1}\left[1 - \left(\frac{r}{R_0}\right)^{\frac{1}{n}+1}\right]\frac{Q}{\pi R_0^2} \tag{4.15}$$

Where R_0 is the radius of the round capillary die, Q is the volumetric rate and n is the power law constant defined by $n \equiv d(log\sigma_{wall})/d(log\dot{\gamma}_{app.})$. The mean average velocity inside the capillary die (round cross-section area) is given by Equation (6.16).

$$V_{ave.} = \frac{Q}{\pi R_0^2} \tag{4.16}$$

The extrudate velocity after the die swell is given by:

$$V_{swelled} = \frac{Q}{\pi R_{swelled}^2}, \tag{4.17}$$

where $R_{swelled}$ is radius of the swelled extrudate and is equal to $D' = 2R_{swelled}$, see Figure 4.2. Coupling Equation (4.16) and (4.17), Equation (4.18) occurs.

$$V_{ave.} = \frac{Q}{\pi R_0^2} = \frac{Q}{\pi R_{swelled}^2}\left(\frac{R_{swelled}}{R_0}\right)^2 = V_{swelled}\left(\frac{R_{swelled}}{R_0}\right)^2 \tag{4.18}$$

On the interface between the inner and outer layer, $V_r(r,n) = V_r(X_0,n)$, Equation (4.15) becomes Equation (4.19).

$$V_r(X_0,n) = \frac{3n+1}{n+1}\left[1 - \left(\frac{X_0}{R_0}\right)^{\frac{1}{n}+1}\right]V_{ave.} \tag{4.19}$$

The theoretical interfacial depth parameter ξ is defined by Inn et al., as the ratio of the central core layer radius and the hypothetical radius for the surface layer if no melt fracture happen, $\xi = X_0/R_0 = X_f/R_f$. The theoretical interfacial depth parameter has the following limits $0 < \xi < 1$. This is explained by Equation (4.20), where at low shear rates $\dot{\gamma} \to 0$, the swelling is not noticeable so $X_f \approx R_f$, and at high shear rates $\dot{\gamma} \to \infty$, the swelling effect is pronounced, thus $X_f \ll R_f$.

$$\xi = X_0/R_0 = X_f/R_f$$
$$\dot{\gamma} \to 0, X_f \approx R_f, \xi \to 1$$
$$\dot{\gamma} \to \infty, X_f \ll R_f, \xi \to 0 \tag{4.20}$$

Thus, Equation (4.15) coupled with (4.19) and (4.20) becomes,

$$\frac{V_{swelled}}{V_r(X_0,n)} = \frac{n+1}{3n+1}\left[1 - (\xi)^{\frac{1}{n}+1}\right]^{-1}\left(\frac{R_{swelled}}{R_0}\right)^{-2}. \tag{4.21}$$

The $V_{extr.,surface}$ can be calculated by,

$$V_{extr.,surface} = \frac{Q_s}{\pi R_0^2 - \pi X_0^2} = \frac{Q_s}{\pi R_0^2(1-\xi^2)} \tag{4.22}$$

where Q_s is the volumetric flow rate of the assuming surface layer and can be calculated by Equation (4.23).

$$Q_s = \int_{X_0}^{R_0}(V_r 2\pi r)\,dr = \left[1 - \left(\frac{3n+1}{n+1}\right)\xi^2 + \left(\frac{2n}{n+1}\right)\xi^{1+\frac{1}{n}}\right]Q \tag{4.23}$$

Considering the development of the fracture instability on the surface layer of the extrudate, the ratio of the $V_{swelled}/V_{extr.,surface}$, Equation (4.24), is obtained by combing Equation (4.23), (4.22) and (4.18).

$$\frac{V_{swelled}}{V_{extr.,surface}} = \frac{1-\xi^2}{\left(\frac{R_{swelled}}{R_0}\right)^2}\left[1 - \left(\frac{3n+1}{n+1}\right)\xi^2 + \left(\frac{2n}{n+1}\right)\xi^{1+\frac{1}{n}}\right]^{-1} \tag{4.24}$$

Direct on the periphery of the round capillary die exit region the force balance is given by Equation (4.25).

$$2\pi X_0 \lambda_s \sigma_x = Y_s(\pi R_0^2 - \pi X_0^2) \tag{4.25}$$

Equation (4.25) describes the force balance between the shear stress σ_x on the theoretical interface between the core and surface layer, and the extensional stress Y_s at the die exit region for a capillary die (circular cross-section area), see Figure 4.1. The thickness of the instability stripe λ_s is defined as the average width of the sharkskin stripe and the average distance between two consecutive similar surface distortions, that is the spatial characteristic wavelength is λ. Inn et al.[26] considered that the characteristic time periodicity τ^* of the instabilities is a constant ratio of $\tau^* = \lambda_s/V_{extr.,surface} = \lambda/V_{swelled}$, so $\lambda = \lambda_s(V_{swelled}/V_{extr.,surface})$. Thus, an analytical equation for the spatial characteristic wavelength λ, Equation (4.26), is resulting by coupling Equation (4.24), (4.25) and $\lambda = \lambda_s(V_{swelled}/V_{extr.,surface})$.

$$\lambda = \frac{R_0}{2}\left(\frac{Y_s}{\sigma_x}\right)\left(\frac{1}{\xi} - \xi\right)\frac{1-\xi^2}{\left(\frac{R_{swelled}}{R_0}\right)^2}\left[1 - \left(\frac{3n+1}{n+1}\right)\xi^2 + \left(\frac{2n}{n+1}\right)\xi^{3+\frac{1}{n}}\right]^{-1} \tag{4.26}$$

## 4.5. Modification for the model of spatial characteristic wavelength λ by Y. W. Inn and coworkers

Adopting the same assumptions and methodology of Inn et al.[26] model, a qualitative model for the slit die geometry (rectangular cross-section) is derived.[48] This model uses the force balance[47] at the die exit as well and assumes that the fracture instability formats at the die exit region as well. In addition, it uses the Cogswell[22] "two layers", concept, see Figure 4.2. The two layers are assumed to exist inside and outside of the die as well. Those two layers have a theoretical interface which is locatced at $x = x_0$ and $y = y_0$ inside the die and at $x = x_f$ and $y = y_f$ outside of the die. It is considered that directly after the die exit where the swelling has already happened the central core layer of the extrudate swells from x_0 to x_f and from y_0 to y_f. The core layer is assumed that moves with $V_{swelled}$. The $V_{extr.,surface}$ is the velocity of the outer layer of the extrudate which experience an intensive extensional deformation at the perimeter of the die exit.
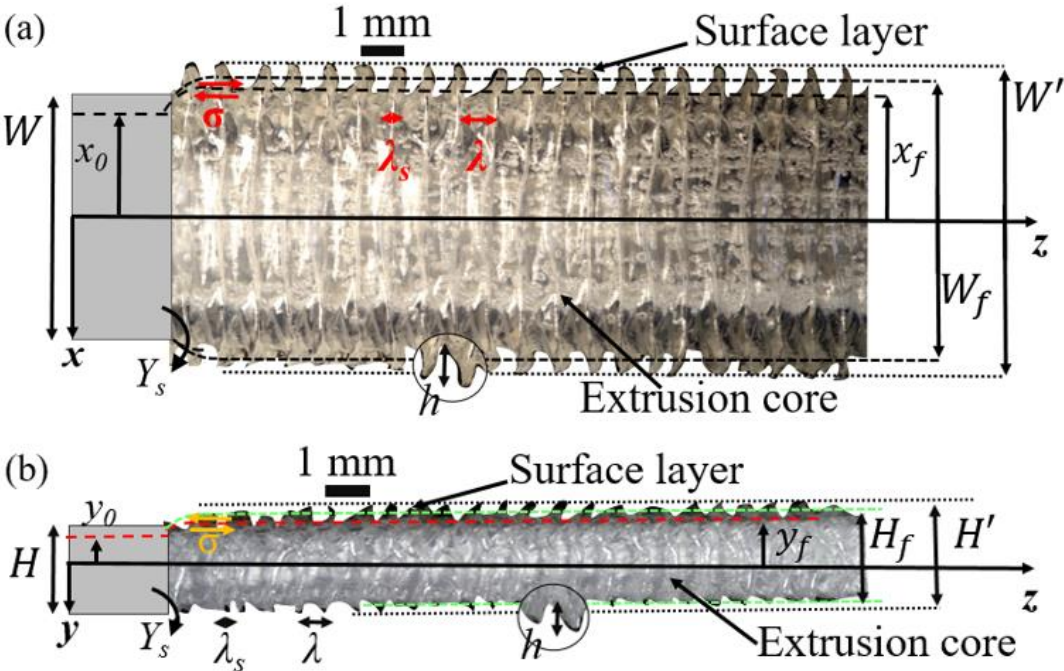
Figure 4.2. Schematic representation of the "two layer" model for slit die (rectangular cross-section area) geometry. The (a) depicts the x − z top-view and (b) displays the y − z top-view of the slit die and extrudate. The instability ridge, λ_s is defined as the average width of the sharkskin stripe and it is formed by fracture at the skin/core interface. Where x_0, y_0 and x_f, y_f are the theoretical dimensions of the core layer inside and outside of the die, respectively. Where H_f and W_f are the theoretical swelled height and width of the extrudate if no fracture was

developed, respectively. Where h is the spatial characteristic height of the instabilities defined as the average distance between the swelled core and the tip of the instability. Using Inn et al.[26] assumption $W_f = x_f + h/2$ and $H_f = y_f + h/2$. Where H' and W' are the swelled height and width of the extrudate taking into account the surface instability. Where σ_x is the shear stress on the theoretical interface between the core and surface layer and Y_s is the extensional stress at the die exit region. Adapted from C. K. Georgantopoulos et al., *Macromolecular Material and Engineering* submitted, **2022**, Figure 5.[48]

Figure 4.3 represents the development of melt fracture at the die exit region of a slit die at three different time snapshots. The conditions of the extrusion process are apparent shear rate of $\dot{\gamma}_{app.}$= 20 s^{-1} and temperature of T = 100 °C.
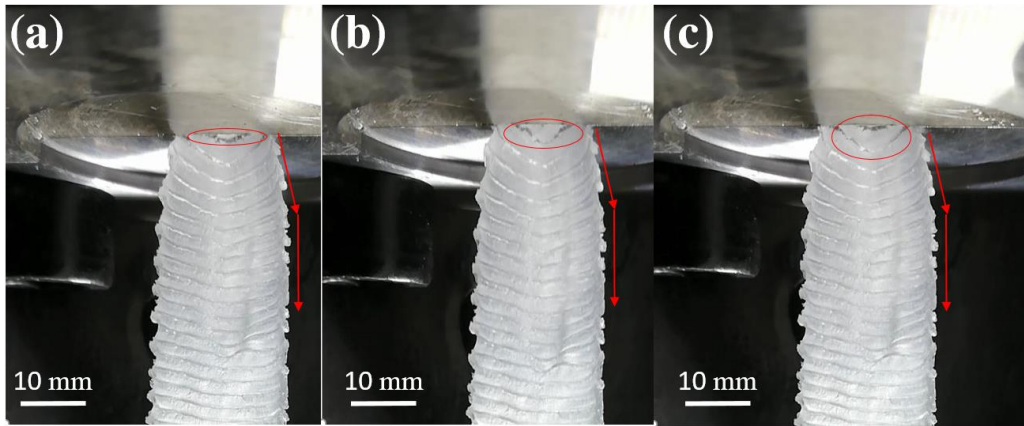
Figure 4.3. Online optical monitoring of the extrusion of the investigated PBD sample with the L/H = 10, H = 3 mm slit die. The sequel of the images (a) to (c) present the same sample at three different time snapshots. The development of the instability ridge is captured in the red circle and presents its evolution with the extrusion time. The extrusion conditions are T = 100 °C and $\dot{\gamma}_{app.}$= 20 s^{-1}.

This model considers a power-law fluid, with the velocity profile, Equation (4.27), to be given by Poiseuille flow field for slit die and neglecting the slip velocity.

$$V_z(y,n) = \frac{2n+1}{n+1}\left[1 - \left(\frac{2y}{H}\right)^{\frac{1}{n}+1}\right]\frac{Q}{HW} \tag{4.27}$$

Where H is the height, W is the width of the slit die, Q is the volumetric rate and n is the power law constant. The mean average velocity inside the slit die is given by Equation (4.28).

$$V_{ave.} = \frac{Q}{HW} \tag{4.28}$$

The extrudate velocity after the die swell is given by Equation (4.29).

$$V_{swelled} = \frac{Q}{H'W'} \tag{4.29}$$

Combining Equations (4.28) and (4.29), Equation (4.30) results.

$$V_{ave.} = \frac{Q}{HW} = \frac{Q}{H'W'}\left(\frac{H'W'}{HW}\right) = V_{swelled}\left(\frac{H'W'}{HW}\right). \tag{4.30}$$

On the theoretical interface between the inner and the outer layer, $V_z(y,n) = V_z(y_0,n)$, Equation (4.27) converts to Equation (4.31).

$$V_z(y_0,n) = \frac{2n+1}{n+1}\left[1 - \left(\frac{2y_0}{H}\right)^{\frac{1}{n}+1}\right]\frac{Q}{HW} \tag{4.31}$$

Two theoretical interfacial depth parameters ξ can be defined for slit extrusion die geometry. For the y-direction $\xi^H = 2y_0/H = 2y_f/H_f$ and for the x-direction $\xi^W = 2x_0/W = 2x_f/W_f$. The theoretical interfacial depth parameter has the following limits $0 < \xi < 1$. The two theoretical interfacial depth parameters for the slit die geometry are assumed to have similar absolute values, $\xi^H \approx \xi^W$, this hypothesis is later proved by experimental results, see sub-chapter 4.6. Combining Equation (4.30) and (4.31), Equation (4.32) results.

$$\frac{V_z(y_0,n)}{V_{swelled}} = \frac{2n+1}{n+1}\left[1 - (\xi^H)^{\frac{1}{n}+1}\right]\left(\frac{H'W'}{HW}\right) \tag{4.32}$$

The $V_{extr.,surface}$ can be estimated by,

$$V_{extr.,surface} = \frac{Q_s}{HW-2x_0 2y_0} = \frac{Q_s}{HW(1-\xi^W\xi^H)} = \frac{Q_s}{HW(1-\xi^2)} \tag{4.33}$$

where Q_s is the flow rate of the surface layer and can be calculated by Equation (4.34).

$$Q_s = Q - 4\int_0^{y_0}\int_0^{x_0} V_z\,dxdy = Q - 4\int_{y_0}^{y_0}\int_{x_0}^{x_0}\left(\frac{2n+1}{n+1}\frac{Q}{HW}\left[1 - \left(\frac{2y}{H}\right)^{\frac{1}{n}+1}\right]\right)dxdy \rightarrow$$

$$Q_s = Q - 4\frac{2n+1}{n+1}\frac{Q}{HW}\int_0^{y_0}\left[1 - \left(\frac{2y}{H}\right)^{\frac{1}{n}+1}\right]dy \rightarrow$$

$$Q_s = Q - 4\frac{2n+1}{n+1}\frac{Q}{HW}x_0\left[y_0 - \left(\frac{2}{H}\right)^{1+\frac{1}{n}}\frac{n}{1+2n}y_0^{2+\frac{1}{n}}\right] \rightarrow \frac{Q_s}{Q} = 1 - \frac{2n+1}{n+1}\xi^2 + \frac{n}{n+1}\xi^{3+\frac{1}{n}}$$

$$\tag{4.34}$$

Considering the development of the melt fracture instability on the surface of the extrudate the ratio of the $V_{swelled}/V_{extr.,surface}$, Equation (4.35), is obtained by combining Equation (4.34), (4.33) and (4.31).

$$\frac{V_{swelled}}{V_{extr.,surface}} = \frac{HW}{H'W'}(1-\xi^2)\left[1 - \left(\frac{2n+1}{n+1}\right)\xi^2 + \left(\frac{n}{n+1}\right)\xi^{3+\frac{1}{n}}\right]^{-1} \tag{4.35}$$

Direct on the perimeter of the slit die exit region the force balance is given by Equation (4.36).

$$Y_s(HW - 4x_0y_0) = \sigma_x\lambda_s 2x_0 + \sigma_y\lambda_s 2y_0 \tag{4.36}$$

Equation (4.36) describes the force balance between the shear stress σ_i on the theoretical interface between the core and surface layer, and the extensional stress Y_s at the die exit region for a slit die (rectangular cross-section area), see Figure 4.2. The thickness of the instability ridge on the surface layer λ_s based on experimental observations is assumed to be similar for the x and y direction. Moreover, the shear stress for both directions σ_x, σ_y is assumed to have similar magnitude, $\sigma_x \approx \sigma_y$.

Thus, the instability ridge λ_s is described by Equation (4.37).

$$\lambda_s = \frac{Y_s}{\sigma_x}\frac{(HW - 4x_0y_0)}{2(x_0+y_0)} \rightarrow \lambda_s = \frac{Y_s}{\sigma_x}\frac{\left(\frac{HW}{HW}-\frac{4x_0y_0}{HW}\right)}{\frac{2(x_0+x_0)}{HW}} \rightarrow \lambda_s = \frac{Y_s}{\sigma_x}\frac{HW}{W+H}\left[\frac{1}{\xi}-\xi\right] \tag{4.37}$$

Using the assumption of Inn et al.[26] that the characteristic time periodicity τ^* of the instabilities is a constant ratio $\tau^* = \lambda_s/V_{extr.,surface} = \lambda/V_{swelled}$, hence $\lambda = \lambda_s(V_{swelled}/V_{extr.,surface})$ occurs. Then the analytical model for the spatial characteristic wavelength λ, Equation (4.38), can be derived by combining Equation (4.35), (4.37) and $\lambda = \lambda_s(V_{swelled}/V_{extr.,surface})$.

$$\lambda = \frac{Y_s}{\sigma_x}\frac{(HW)^2}{(H+W)H'W'}\left(\frac{1}{\xi}-\xi\right)(1-\xi^2)\left[1 + \left(\frac{2n+1}{n+1}\right)\xi^2 + \left(\frac{n}{n+1}\right)\xi^{3+\frac{1}{n}}\right]^{-1} \tag{4.38}$$

4.6. Simplification of models by 4.4 and 4.5

Within this section experimental evidence for the simplification of the models, Equation (4.26) and (4.38) are provided. The models are not taking into consideration the slip velocity since the derivation of the models is based on the lip of the die exit. Regarding the theoretical interfacial depth parameter ξ for extrudates obtained by capillary die it is suggested in literature that it can be described by a power law model as a function apparent shear rate, $\xi = b\dot{\gamma}_{app.}^{-c}$. Inn et al.[26] suggested that the R_f, that is the theoretical swelled radius of the extrudate if no fracture was developed, can be calculated by $R_f = X_f + h/2$. Similarly for slit die geometry it is assumed that $W_f = x_f + h/2$ and $H_f = y_f + h/2$. The experimental results for the theoretical interfacial depth parameter from extrudates obtained by slit and capillary extrusion dies are presented in Figure 4.4 (a). In Figure 4.4 (a) the interfacial depth parameter for the same material obtained by different die geometries is presented. The experimental data confirm that the magnitude of the interfacial depth parameter remains similar for the same material which is extrudate under the same temperature from different extrusion die geometries. Hence, the experimental data in Figure 4.4 (a) can be fitted by $\xi^H = \xi^W = \xi = b\dot{\gamma}_{app.}^{-c}$. Specifically for the

investigated polybutadiene (PBD) sample which is extruded at T = 100 °C the fitting parameters are $b = 0.99$ and $c = 0.02$.
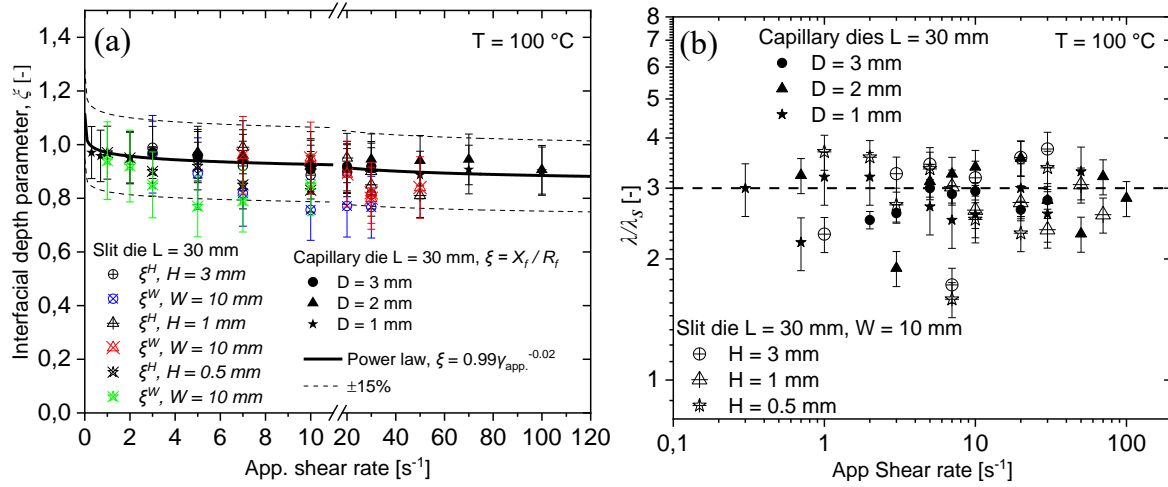
Figure 4.4. (a) Experimental data of the calculated interfacial depth parameter ξ from extrudates obtained by round capillary and slit dies at T = 100 °C. (b) Ratio of the spatial characteristic wavelength and the instability ridge λ/λ_s for the investigated sample obtained by capillary and slit dies at T = 100 °C. The extruder dies which have been used are: capillary dies with L = 30 mm and D = 1, 2, and 3 mm and slit dies with L = 30 mm and H = 0.5, 1 and 3 mm. Adapted from C. K. Georgantopoulos et al., *Macromolecular Material and Engineering* submitted, **2022**, Figure 7.[48]

According to Inn et al.[26] the ratio of the spatial characteristic wavelength λ and the instability ridge λ_s is given by $\lambda = \lambda_s(V_{swelled}/V_{extr.,surface})$. In Figure 4.4 (b) the experimental results gained by slit and round capillary dies for the ratio of the SCW λ and the instability ridge λ_s of the investigated PBD sample at T = 100 °C are presented. It is found that within the range of shear rate $0.5\ s^{-1} < \dot{\gamma}_{app.} < 100\ s^{-1}$ at T = 100 °C, the $\lambda/\lambda_s \approx 3$. The same ratio of $\lambda/\lambda_s \approx 3$ has been reported in literature[16] for SBR samples obtained by capillary dies at T = 120 °C. The formerly reported experimental evidences confirm the assumptions which have been taken in order to simplify the Equation (4.26) and (4.38). Hence the Equation (4.39) and (4.40) are the simplified qualitative models for the SCW λ of extrusion flow instabilities developed at the die exit of capillary and slit dies, respectively. The model for the theoretical interfacial depth parameter is given by $\xi = b\dot{\gamma}_{app.}^{-c}$.

$$\lambda_{Inn\ et\ al.}^{Capillary} = 3\frac{R_0}{2}\left(\frac{Y_S}{\sigma_x}\right)\left(\frac{1}{\xi} - \xi\right) \tag{4.39}$$

$$\lambda_{current\ work}^{Slit} = 3\frac{HW}{W+H}\left(\frac{Y_S}{\sigma_x}\right)\left(\frac{1}{\xi} - \xi\right) \tag{4.40}$$

4.7. Review of models for spatial characteristic height h

Inn et al.[26] except of the model for the SCW λ, had also suggested an empirical model which defines the formation of the spatial characteristic height (SCH) h of the extrusion flow instabilities. This empirical model is given by Equation (4.41).

$$h = 2R_0(1 - \xi) \tag{4.41}$$

Where ξ is the theoretical interfacial depth parameter and R_0 is the radius of the round capillary die. Miller et al.,[27,28] investigated the influence of temperature on extrusion flow instabilities by using round capillary and slit extrusion dies for specific LLDPE (M_w = 85 kg mol^{-1}, Đ = 2.30) samples. They quantify the SCH h of the instabilities and created a master curve of the SCH h as a function of shear rate.[27,28] Hence, they fitted the master curve with a new proposed empirical model given by Equation (4.42).

$$h = k\left(\dot{\gamma}_{app.} - \dot{\gamma}_{crit.}\right)^{0.5} \tag{4.42}$$

Where, k and the $\dot{\gamma}_{crit.}$ are a fitting parameter. Furthermore, a simple linear relationship,[16] Equation (4.43), describes the trend of the SCH h of the extrusion flow instabilities as a function of apparent shear rate. It is experimentally observed[16] in literature that the SCH h is developed linearly with the shear rate at small deformations, $\dot{\gamma}_{app.} < 20\ s^{-1}$, see chapter 5. Where h_0 is a fitting parameter.

$$h = h_0\dot{\gamma}_{app.} \tag{4.43}$$

4.8. Conclusions

Within this chapter a literature review of the qualitative models for the spatial characteristics of extrusion flow instabilities, that is wavelength (λ) and height (h), was presented. The models for the spatial characteristic wavelength (SCW) λ proposed by Wang et al.[23,24] and Inn et al.,[26] are here derived and presented. The theoretical concept[22] for the "two layer" extrudate and the origin of the extrusion instabilities was presented in details. Based on the idea, methodology, and assumptions from the model of Wang et al.[23,24] and Inn et al.[26] two qualitative models for the SCW λ of the extrusion instabilities obtained by slit dies geometries were also proposed. Furthermore, the available empirical models for the spatial characteristic height (SCH) h of the extrusion flow instabilities proposed by Inn et al.[26] and Miller et al.,[27,28] were summarized and explained. In the following Chapter 5 and 6, the above mentioned models for the spatial

characteristics of extrusion flow instabilities are used to describe experimental data. Hence, correlations of the molecular properties (MWD, branching), and processing parameters (temperature, die geometry) with the spatial characteristics of the extrusion flow instabilities are presented.

5. Influence of Molecular Properties on Extrusion Flow Instabilities

This chapter uses the previous reported qualitative models in chapter 4 and enables correlations of molecular properties, such as the longest relaxation time and the molecular architecture (linear, branched), with the extrusion behavior. Three commercial styrene-butadiene rubbers (SBR) are investigated as a function of molecular weight distribution (MWD), and molecular architecture. Hence, the fitting of the qualitative models to the experimental data of the spatial characteristic wavelength λ provides the ratio of the extensional and shear stress at the die exit region which is correlated with the molecular properties. This chapter presents correlations between the molecular properties and the extrusion behavior which allows to understand the impact of the relaxation time and the molecular architecture on the extrusion process.

5.1. Material used in this chapter

Three styrene-butadiene rubbers, named as SBR A, SBR B and SBR C are investigated as a function of molecular weight distribution (MWD) and molecular architecture (linear, branched). The molecular characterization of the samples was achieved by using: (1) a recent method-development[40] which couples a size exclusion chromatography (SEC) to a benchtop nuclear magnetic resonance spectrometer (NMR, 80 MHz, 1.86 T, ^{1}H), so called 2D SEC-NMR, (2) a quadruple-detection SEC to investigate the MWD and the molecular architecture, and (3) a high field NMR spectroscopy (400 MHz, 9.4 Tesla, ^{1}H) to identify the chemical composition of the SBR samples. Differential scanning calorimetry (DSC) is used to obtain the glass-transition temperature T_g, of the studied samples.[16]

By using the 2D SEC-NMR method[40] the chemical composition of the different molecular weight fractions within the studied samples is qualified and quantified. The NMR (80 MHz, 1.86 T, ^{1}H) spectra and the elution volume distribution of the investigated samples are presented in Figure 5.1 (a) and (b), respectively. In Figure 5.1 (b) roughly two main elution volume ranges are observed, one at $30 - 45$ mL and one at $57 - 65$ mL. Figure 5.1 (c) displays the combination

of Figure 5.1 (a) and (b), that is the 2D SEC-NMR contour plot.[16,40] This 2D SEC-NMR contour plot includes the respective normalized 1D NMR spectral cuts and SEC elugram plots for the investigated SBR A as an example.
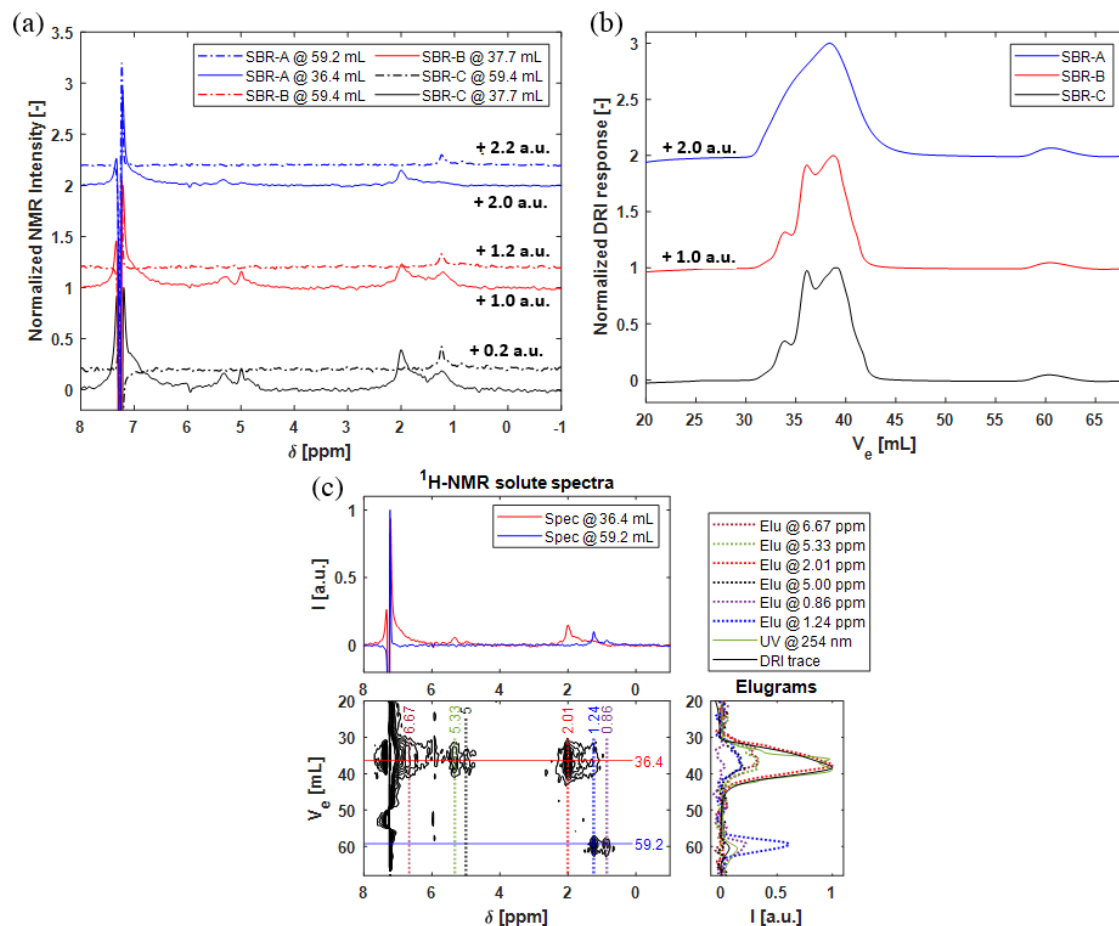
Figure 5.1. (a) Benchtop NMR spectra as cuts from the 2D SEC-NMR combination and (b) elution volume distributions for all the investigated samples. (c) 2D SEC-NMR contour plots for the example of SBR A. The 2D SEC-NMR for the other investigated samples can be found in Appendix A. This SEC is equipped with a semi-preparative column with length of 300 nm and inner diameter of 20 mm. The SBR B within this chapter is the SBR A of chapter 3. Adapted from C. K. Georgantopoulos et al., *Physics of Fluids* 33, *093108*, **2021**, Figure 1.[16] Reproduced with permission from AIP Publishing, No. 5231930652686.

In Figure 5.1 (c) two separate components can be designated, one at 30 – 45 mL and one at 57 – 65 mL. Based on the ¹H-NMR spectra, the first component at 30 – 45 mL is assigned to the SBR component. The second component at 57 – 65 mL is assigned to low molecular weight hydrocarbon. This low molecular weight hydrocarbon component at 57 – 65 mL exists in all of the investigated SBR A, B and C.[16] For the 2D SEC-NMR of all the investigated samples see

Appendix A. The SBR B and C samples have multimodal elution volume distributions, see Figure 5.1 (b). Both samples present roughly a bimodal distribution within 30 – 45 mL. Specifically the first mode is at 30.0 – 35.0 mL and the second is at 35.0 – 42.0 mL. The SEC is calibrated with narrowly distributed linear polystyrene standards. Table 5.1 presents the molecular weight characteristics of all investigated SBR samples.[16] Owing to the difference in chemical composition in the same SBR sample the weight fraction of the low molecular weight hydrocarbon is approximately estimated by performing a 2D integration on the 2D contour plots.

The weight average molecular weight is $M_w = 340$ kg mol^{-1} for SBR A, $M_w = 274$ kg mol^{-1} for SBR B and $M_w = 263$ kg mol^{-1} for SBR C. The SBR C has a bigger fraction of the medium molecular weight fraction than SBR B. In addition all of the investigated samples have a similar amount ~8.5 wt.% of the low molecular weight hydrocarbon, see Table 5.1.[16]

Table 5.1. Molecular weight characteristics of the investigated SBR samples obtained by the SEC-NMR method.

Name	Elution volume [mL]	Weight fraction [wt.%]	[c)]M_n [kg·mol^{-1}]	[c)]M_w [kg·mol^{-1}]	Đ [-]
SBR A	30.0 – 45.0	93.10	150	340	2.30
[a)]Low - MW	57.0 – 65.0	6.90	0.51	0.61	1.21
[b)]SBR B	30.0 – 42.0	90.30	170	274	1.62
High - MW	30.0 – 35.0	10.80	748	763	1.02
Medium - MW	35.0 – 42.0	79.50	154	192	1.25
[a)]Low - MW	57.0 – 63.0	9.70	0.49	0.61	1.23
SBR C	30.0 – 42.0	91.50	157	263	1.67
High - MW	30.0 – 37.0	9.50	733	746	1.02
Medium - MW	37.0 – 42.0	82.00	140	180	1.30
[a)]Low - MW	57.0 – 63.0	8.50	0.51	0.62	1.20

The quadruple-detection SEC is used to provide information about the estimated bimodal distributions (see Figure 5.1 (b)) for SBR B and C. In Figure 5.2 the elution volume distribution obtained by the quadruple-detection SEC for the SBR C is presented as an examples. All the quadruple-detection SEC profiles for the investigated samples, SBR A, B and C can be found in Appendix A.
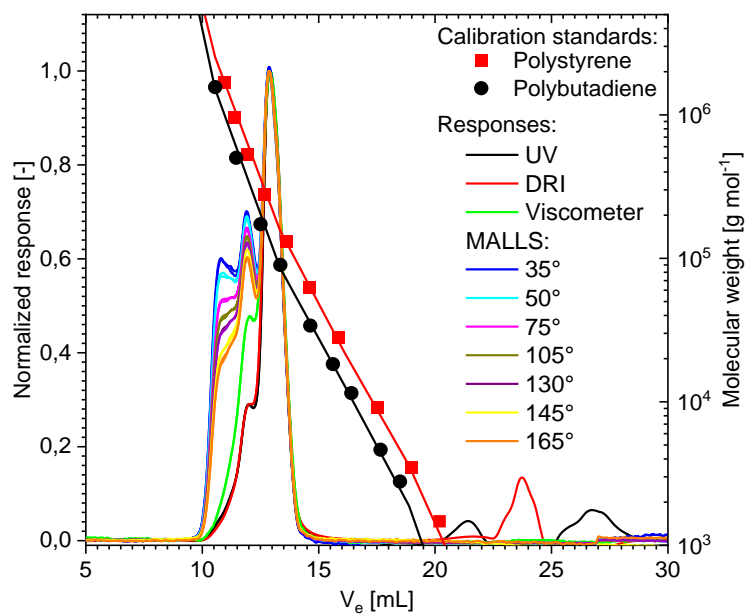
Figure 5.2. Quadruple detection SEC for the example of SBR C. Four different responses are shown: Ultra-violet at 254 nm (UV), differential refractive index (DRI), viscometer, and multi-angle laser light-scattering (MALLS). The accompanying overlay illustrates elution of linear homopolymer standards of polystyrene (red squares) and polybutadiene (black circles). This SEC is equipped with an analytical column with length of 300 mm and inner diameter of 8 mm. Therefore, the elution volume has lower values if compared to Figure 7.1 (b). Adapted from C. K. Georgantopoulos et al., *Physics of Fluids* 33, *093108*, **2021**, Figure 2.[16] Reproduced with permission from AIP Publishing, No. 5231930652686.

In Figure 5.2 two characteristic peaks between 10 and 15 mL are obtained by the differential refractive index (DRI), Viscometer and ultra-violet (UV) detectors. The fourth detector which is a multi-angle laser-scattering (MALLS) displays three peaks at ~10.5 mL, ~12 mL and at ~13 mL. The specific refractive index increment in MALLS is assumed to be a weighted average of the pure linear homopolymers of polystyrene and polybutadiene, namely $dn/dc = 0.145$ mL g^{-1} at tetrahydrofuran (THF) solvent. Hence the MALLS detector obtains the following absolute molecular weight at the respective three peaks. At ~10.5 mL is $M_w \approx 1800$ kg mol^{-1}, at ~12 mL is $M_w \approx 260$ kg mol^{-1} and at ~13 mL is $M_w \approx 110$ kg mol^{-1}. Difference

between the molecular weight values obtained by the MALLS and the SEC-NMR are observed due to the different measurement principal. The SEC-NMR based on calibration standards and the MALLS values are obtained as an absolute measurement and therefore closer to the true copolymer molecular weight.[16]

The molecular architecture (linear, branched) of the studied SBR samples is investigated by Mark-Houwink[49,50] plot in Figure 5.3. The Mark-Houwink[49,50] analysis is plotting the intrinsic viscosity [η] as a function of molecular weight of the studied SBR. The intrinsic viscosity [η] is measured by the viscometer of the quadruple-detection and the absolute molecular weight is obtained by the MALLS detector.
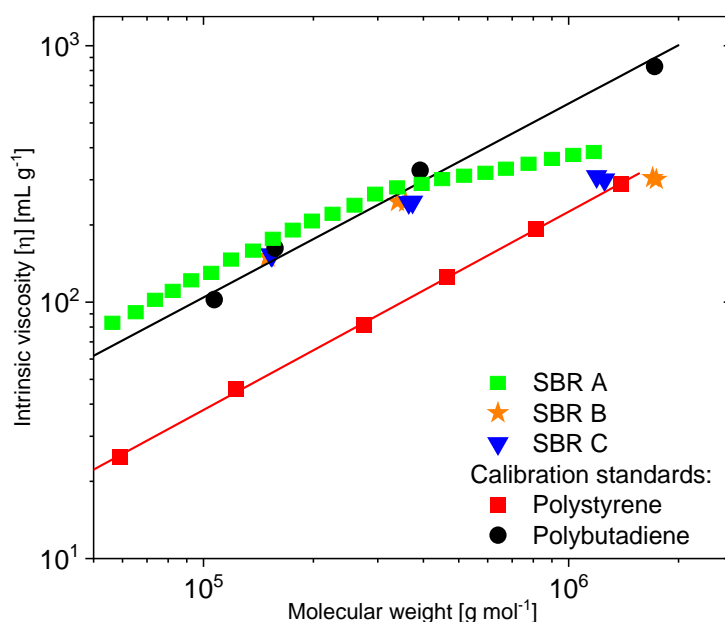
Figure 5.3. Intrinsic viscosity as a function of molecular weight as obtained via MALLS. Calibration standards of homopolymer polystyrene (red squares) and polybutadiene (black circles) with linear molecular architecture are included in the graph. The deviation of the SBR A, B, and C from the polybutadiene standard after ~ 400 kg mol^{-1} indicate branched molecular architecture. Adapted from C. K. Georgantopoulos et al., *Physics of Fluids* 33, *093108*, **2021**, Figure 3.[16] Reproduced with permission from AIP Publishing, No. 5231930652686.

In Figure 5.3 calibration standards of polystyrene and polybutadiene with linear molecular architecture are included as well. Above the 400 kg mol^{-1} the intrinsic viscosity presents a decreasing trend and deviates from the linear polybutadiene standard. As the molecular weight increases this deviation becomes bigger. This deviation suggests that the studied SBR samples are branched at high molecular weight above ~400 kg mol^{-1}.

To determine the chemical composition of the investigated SBR samples, high field NMR spectroscopy (400 MHz, 9.4 Tesla, ^{1}H) is used, see Table 5.2. Furthermore, the glass transition temperature T_g of the samples is obtained by differential scanning calorimetry (DSC) characterization, see Table 5.2. Each of the samples has only one glass transition temperature, thus phase separation is not detectable at a large length scale (i.e. $l > 3 - 5$ nm) in these two systems.[15,16]

Table 5.2. Chemical composition in weight percentage (wt.%) and the determined glass-transition temperature of the investigated SBR samples.

Name	Styrene [wt.%]	Butadiene 1,2 [wt.%]	Butadiene 1,4 (*cis* and *trans*) [wt.%]	a)T_g [°C]
SBR A	28.9	19.5	51.6	-48.8
SBR B	21.8	41.4	36.8	-25.5
SBR C	23.5	47.3	29.2	-36.3

a) The heating/cooling rate was set on 5 K min^{-1} between -90 °C to 160 °C. The second heating cycle was analyzed. Adapted from C. K. Georgantopoulos et al., *Physics of Fluids* 33, *093108*, **2021**, Table 2.[16] Reproduced with permission from AIP Publishing, No. 5231930652686.

5.2. Models for the small amplitude oscillatory shear rheology

The storage ($G'(\omega)$) and loss ($G''(\omega)$) modulus obtained by the small amplitude oscillatory shear (SAOS) can be fitted by the Maxwell Model,[42] Equation (5.1).

$$G'(\omega) = \sum_{i=1}^{N} \frac{g_i \tau_i^2 \omega^2}{1 + \tau_i^2 \omega^2}, G''(\omega) = \sum_{i=1}^{N} \frac{g_i \tau_i \omega}{1 + \tau_i^2 \omega^2} \tag{5.1}$$

For bimodal homopolymer melts a proper model to describe the storage ($G'(\omega)$) and loss ($G''(\omega)$) modulus is the Doi-Edwards,[51,52] Equation (5.2). This model is used to estimate the repation time of each molecular component, that is $\tau_{d,medium}$ and $\tau_{d,high}$. The subscript *medium* and *high* represent the medium and high molecular weight components. The physical interpretation of Doi-Edwards model is based on the reptation of each macromolecular chain inside its theoretical tube independent of the motion of the other macromolecular chains. Specifically, the storage ($G'(\omega)$) and loss ($G''(\omega)$) modulus of the Doi-Edwards model for bimodal homopolymer sample are given by,

$$G'(\omega) = \frac{8G_N^0}{\pi^2} \sum_{\substack{n \\ odd}} \frac{1}{n^2} \left[\frac{\varphi_{low}\left(\omega\tau_{d,medium}\right)^2}{\left(\omega\tau_{d,medium}\right)^2 + n^4} + \frac{\varphi_{high}\left(\omega\tau_{d,high}\right)^2}{\left(\omega\tau_{d,high}\right)^2 + n^4} \right]$$

(5.2)

$$G''(\omega) = \frac{8G_N^0}{\pi^2} \sum_{\substack{n \\ odd}} \left[\frac{\varphi_{low}\left(\omega\tau_{d,medium}\right)^2}{\left(\omega\tau_{d,medium}\right)^2 + n^4} + \frac{\varphi_{high}\left(\omega\tau_{d,high}\right)^2}{\left(\omega\tau_{d,high}\right)^2 + n^4} \right]$$

where, G_N^0 is the plateau modulus and φ is the volume fraction for each component.[51,52] The volume fraction and the weight fraction have similar numerical values because the density is considered not to change.[16] It is known that the reptation time is proportional to the number of entanglements (N) to the third power, $\tau_d \sim N^3$. Based on this, Doi-Edwards suggested that the ratio of the number of entanglements (N) of each component to the third power is equal to the ratio of the reptation times, that is $\tau_{d,medium} / \tau_{d,high} = \left(N_{medium}/N_{high}\right)^3$.[51] The number of entanglements is calculated by the ratio of the weight average molecular weight of each component, $M_{w,i}$ and the entanglement molecular weight, M_e, that is $N = M_{w,i}/M_e$.[53,54] For styrene-butadiene rubbers (SBR) with 25 % wt. of styrene the entanglement molecular weight is $M_e = 2900$ g mol^{-1}.[53,54]

5.3. Rheological characterization: linear and non-linear regime

The master curve of the magnitude of complex viscosity, storage ($G'(\omega)$) modulus, loss ($G''(\omega)$) modulus and phase angle δ from the investigated SBR samples at reference temperature T = 120 °C are presented in Figure 5.4. In Figure 5.4 (a) the magnitude of complex viscosity of the SBR A is higher that the two bimodal samples (SBR B and C) at $\omega < 10^0$ rad s^{-1}. At $\omega > 10^0$ rad s^{-1} all the investigated samples present similar viscosity. In Figure 5.4 (b) the storage ($G'(\omega)$) and loss ($G''(\omega)$) modulus of the investigated samples are presented. None of the studied SBR samples have reached the terminal region where $G'' \sim \omega^1$ and $G' \sim \omega^2$. The reptation time τ_d, that is the longest characteristic relaxation time of a polymer melt and can be obtained by the inverse of the existing crossover point of G' and G'' (Figure 5.4 (b)). The reptation times of the studied SBR samples obtained by the crossover point of G' and G'' are listed in Table 5.3.
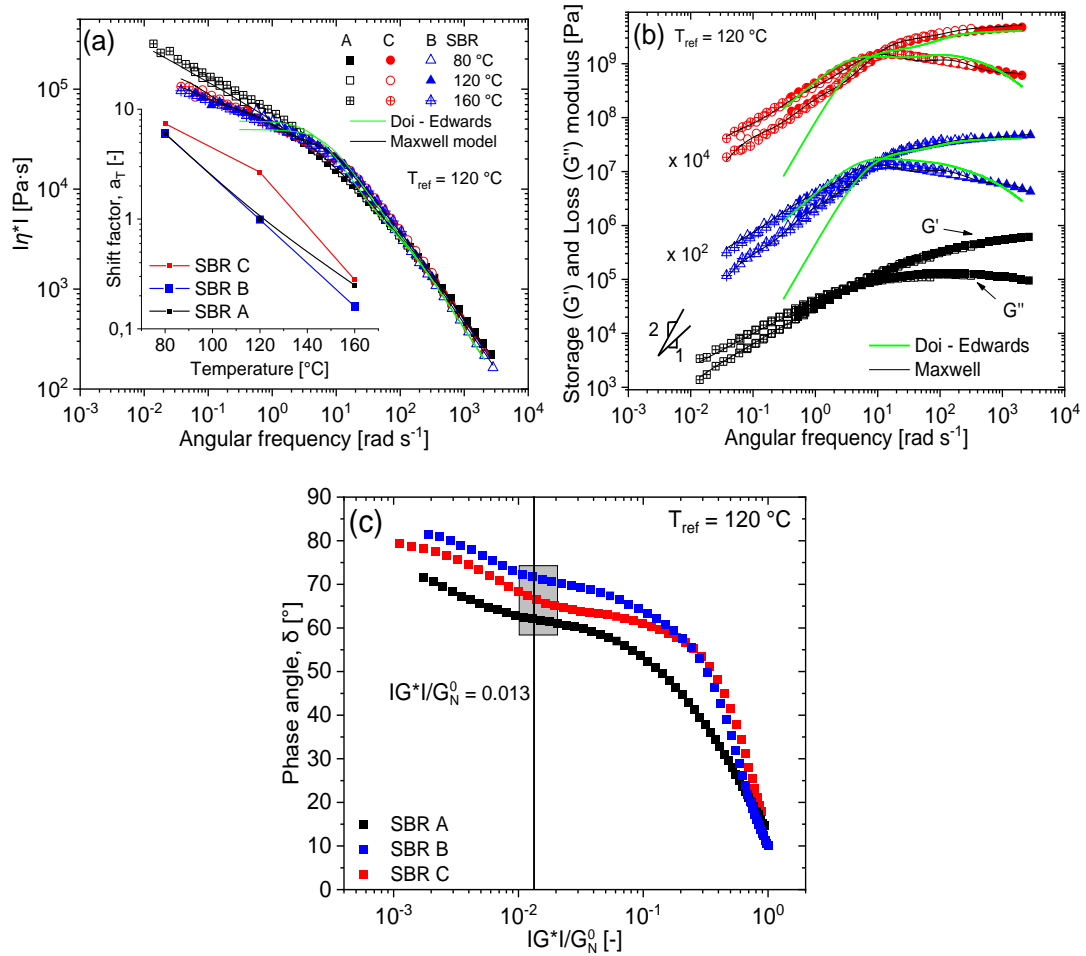
Figure 5.4. Master curves of (a) magnitude of complex shear viscosity and (b) storage and loss modulus for the three investigated SBR samples at T_{ref} = 120 °C. (a) - (b) The Maxwell model (black solid line) is fitted to the experimental results. (a) - (b) Doi-Edwards model (green solid line) for bimodal samples is fitted to the experimental data to obtain the relaxation time for each component. (c) van Gurp – Palmen plot of the investigated samples. The magnitude of the complex modulus is normalized by the plateau modulus. Adapted from C. K. Georgantopoulos et al., *Physics of Fluids* 33, *093108*, **2021**, Figure 5.[16] Reproduced with permission from AIP Publishing, No. 5231930652686.

The Doi-Edwards model[51,52] estimates two relaxation times for the bimodal samples, one for the medium-MW component, $\tau_{d,medium}$ and one for the high-MW component, $\tau_{d,high}$. To estimate the ratio of relaxation times for the two modes, $\tau_{d,\ medium}/\tau_{d,\ high}$, the number of entanglements for each molecular component should be calculated. For the SBR B, N_{medium} = 63, N_{high} = 254, and $\tau_{d,\ medium}/\tau_{d,\ high}$ = 0.01. For the SBR C, N_{medium} = 60, N_{high} = 248, and $\tau_{d,\ medium}/\tau_{d,\ high}$ = 0.014. By using Doi-Edwards model,[51,52] Equation (5.2), to fit the experimental results of G' and G" in Figure 5.4 (b) the reptation times for the bimodal samples are obtained

73

and listed in Table 5.3. The $\tau_{d,\ medium}$ remains constant for both of the bimodal samples due to similar $M_{w,\ medium} \approx 185$ kg mol^{-1}. Deviation of the ratio for the relaxation times $\tau_{d,\ medium}/\tau_{d,\ high}$ between the theoretical and the fitting parameters is observed for the following reasons: (i) none of the studied SBR samples have reached the flow regime, (ii) the low molecular weight hydrocarbons have not included into the theoretical calculation, and (iii) the average molecular weight of each component was estimated by polystyrene standards.[16] Figure 5.4 (c) displays the van Gurp – Palmen plot of the studied SBR samples at T = 120 °C. A relaxation process can be observed between $|G^*|/G_N^0 = 0.01$ and 0.02 for all of the investigated samples. This relaxation process is possibly associated with the presence of branched molecules.[16,55,56]

Table 5.3. The overall relaxation time for the SBR A, and each relaxation time for the SBR B and C at T =120 °C.

Sample	[a]Overall relaxation time, τ_d [s]	[b]Medium relaxation time, $\tau_{d,\ medium}$ [s]	[b]High relaxation time, $\tau_{d,\ high}$ [s]
SBR A	1.66	-	-
SBR B	0.77	0.009	0.14
SBR C	0.61	0.009	0.22

[a]Obtained by the inverse of the cross-over. [b]Obtained by the Doi-Edwards model, Equation (5.2). Adapted from C. K. Georgantopoulos et al., *Physics of Fluids* 33, *093108*, **2021**, Table 4 in Appendix.[16] Reproduced with permission from AIP Publishing, No. 5231930652686

The non-linear transient extensional viscosity of the studied SBRs is presented in Figure 5.5. The extensional rates are $\dot{\varepsilon} = 0.01, 0.05, 0.1, 0.2, 0.5$, and 1 s^{-1} at T = 120 °C. Strain hardening factor (SHF) is defined[42] as the ratio between the steady state extensional viscosity and the viscosity which is predicted from the linear viscoelasticity (LVE), $SHF = \eta_{max}(\dot{\varepsilon})/3\eta_{LVE}(\dot{\varepsilon})$. For the SBR A at strain hardening factor of SHF = 2.7 is observed at $\dot{\varepsilon} = 0.01$ s^{-1}. For the SBR B and C a strain hardening behavior only at low extensional rate is observed. Specifically, SBR B presents $SHF = 1.4$ at $\dot{\varepsilon} = 0.2$ s^{-1} and SBR C shows $SHF = 1.3$ at $\dot{\varepsilon} = 0.01$ s^{-1} and 0.05 s^{-1}. The strain hardening behavior at low extensional rates is usually observed for polymers with a fairly low degree of branching which belong in a high molecular weight tail.[57,58]

In combination the van Gurp – Palmen plot (Figure 5.4 (c)), the transient extensional viscosity (Figure 5.5), and the Mark-Houwink (Figure 5.3) plot endorse the existence of branched molecular architecture in the high molecular weight tail (> 400 kg mol^{-1}) of the studied SBR

samples. Based on transient extensional viscosity and on van Gurp – Palmen plot it is clear that the SBR A is more branched than SBR C which is more branched than the SBR B.[16]
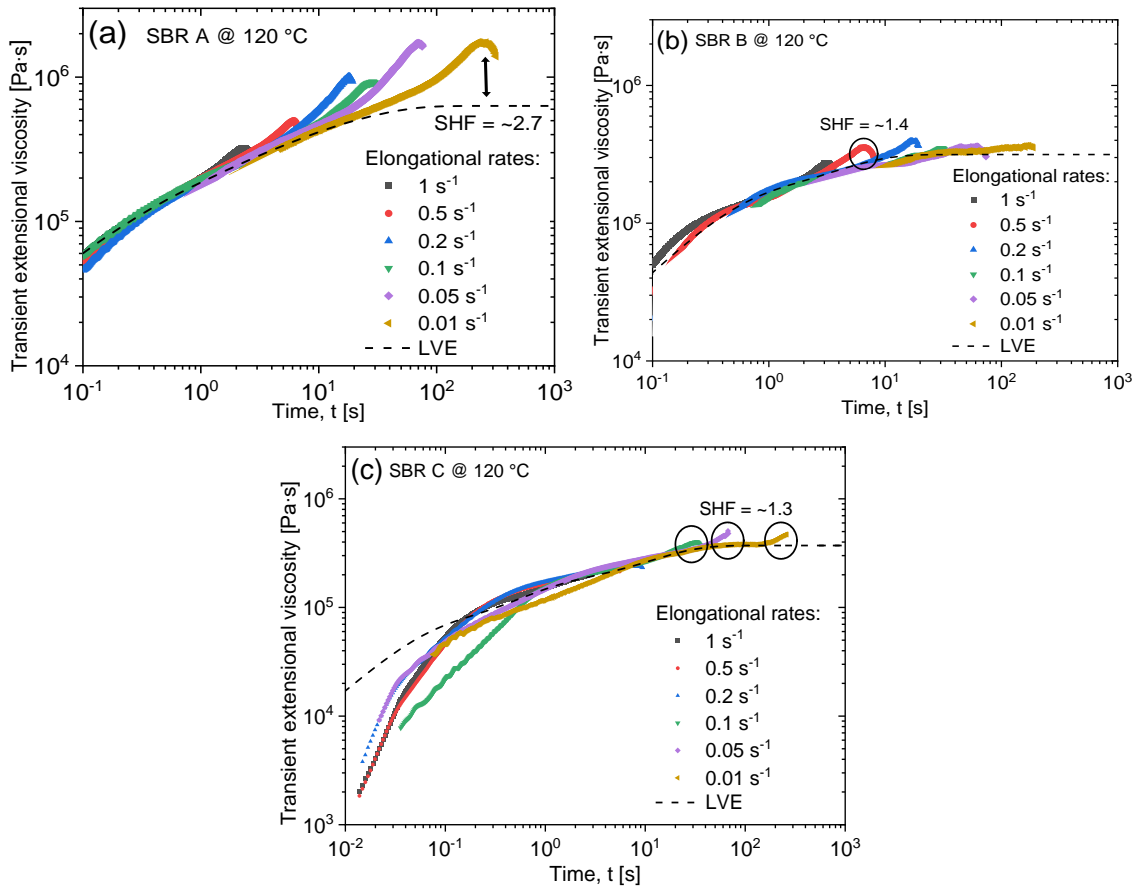
Figure 5.5. Transient extensional viscosity at 120 °C. The dashed line represents the linear viscoelasticity (LVE). Samples (a) SBR A and (b) SBR B present strain hardening effect which depends on the extensional rate. (c) SBR C displays indications of strain hardening effect at $\dot{\varepsilon} = 0.01$, 0.05, and 0.1 s^{-1}. This behavior of the weak strain hardening at the low extensional rates is associated with low degree of branching which belong in a high molecular weight tail. Part of the experimental data of the (b) SBR B have been adopted by Georgantopoulos et al. Adapted from C. K. Georgantopoulos et al., *Physics of Fluids* 33, *093108*, **2021**, Figure 6.[16] Reproduced with permission from AIP Publishing, No. 5231930652686.

## 5.4. Extrusion flow instabilities

The extrusion flow instabilities of the investigated SBR samples are displayed in Figure 5.6. The extrudates were obtained by capillary die (round cross-section area) with diameter $D = 2$ mm and length $L = 30$ mm at T = 120 °C. The extrusion instabilities of SBR A are presented in Figure 5.6 (a). Sharkskin instability is presented at $\dot{\gamma}_{app.} = 7$ s^{-1}, helicoidal distortion starts at $\dot{\gamma}_{app.} = 10$ s^{-1}, regularly volume and surface (RVS) instability at $\dot{\gamma}_{app.} = 20$ s^{-1}, helicoidal

instabilities at $\dot{\gamma}_{app.}=30$ s^{-1} and spurt instability at $\dot{\gamma}_{app.}=50$ s^{-1}. Non-regular volume distortions manifest themselves at higher shear rates $\dot{\gamma}_{app.}>50$ s^{-1}, thus the extrusion flow instability of the extrudates is classified as gross melt fracture (GMF). The SBR B presents helix at $\dot{\gamma}_{app.}=7$ s^{-1}, RVS distorted extrudate at $\dot{\gamma}_{app.}=10$ s^{-1} and then spurt instabilities at $\dot{\gamma}_{app.}=50$ s^{-1}, see Figure 5.6 (b). The extrusion flow instabilities of SBR C are displayed in Figure 5.6 (c). Sharkskin instabilities begins at $\dot{\gamma}_{app.}=7$ s^{-1}, helicoidal defects at $\dot{\gamma}_{app.}=10$ s^{-1}, RVS distorted extrudate at $\dot{\gamma}_{app.}=20$ s^{-1} and finally spurt instability at $\dot{\gamma}_{app.}=100$ s^{-1}.
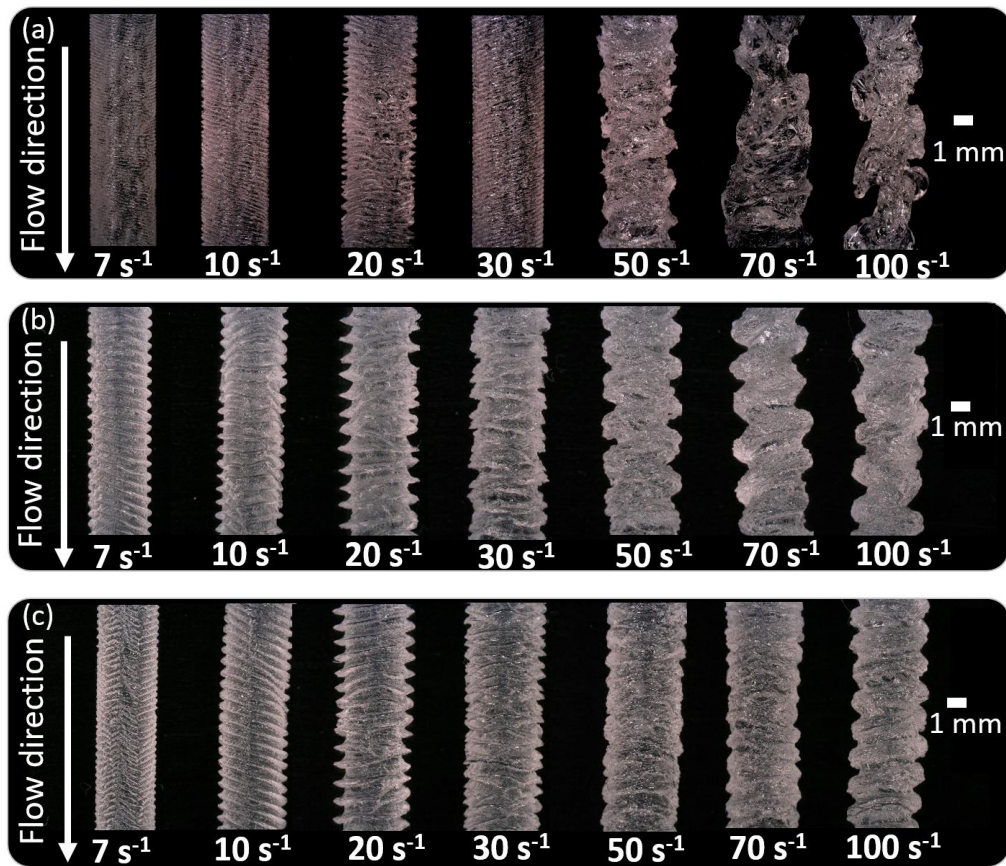
Figure 5.6. Extrusion flow instabilities of the investigated SBR samples obtained by $L/D = 15$ with $D = 2$ mm capillary die at T = 120 °C. (a) SBR A with intensive volume distortions after $\dot{\gamma}_{app.}=50$ s^{-1}. (b) – (c) SBR B and C are presenting a transition zone with the regular volume and surface (RVS) distortions. The (c) SBR C has a broader transition zone ($\dot{\gamma}_{app.}=30$, 50 and 70 s^{-1}) than the SBR B ($\dot{\gamma}_{app.}=30$ s^{-1}). Adapted from C. K. Georgantopoulos et al., *Physics of Fluids* 33, *093108*, **2021**, Figure 8.[16] Reproduced with permission from AIP Publishing, No. 5231930652686..

Based on the experimental results, Figure 5.6, and specifically on the SBR B and C the RVS distortion is a transition zone between the helix and spurt instabilities. The onset and the type of the extrusion flow instabilities are listed on Table 5.4.

Table 5.4. Onset of the extrusion flow instabilities for the investigated samples at T = 120 °C.

Sample	Sharkskin		Helix		RVS		Helix		Spurt		GMF	
	$\dot{\gamma}_{app.}$ $[s^{-1}]$	σ_{wall} $[kPa]$	$\dot{\gamma}_{app.}$ $[s^{-1}]$	σ_{wall} $[kPa]$	$\dot{\gamma}_{app.}$ $[s^{-1}]$	σ_{wall} $[kPa]$	$\dot{\gamma}_{app.}$ $[s^{-1}]$	σ_{wall} $[kPa]$	$\dot{\gamma}_{app.}$ $[s^{-1}]$	σ_{wall} $[kPa]$	$\dot{\gamma}_{app.}$ $[s^{-1}]$	σ_{wall} $[kPa]$
SBR A	7	160	10	182	20	220	30	243	50	265	70	294
SBR B	-	-	7	156	10	182	-	-	50	267	200	303
SBR C	7	186	10	197	20	246	-	-	100	284	200	311

To better qualify and quantify the spatial characteristics, wavelength λ and height h, of the extrusion flow instabilities 3D images of the extrudates are obtained. In Figure 5.7 the 3D images of the SBR C are presented at different shear rate, from $\dot{\gamma}_{app.}$= 5 s^{-1} up to 30 s^{-1}, at T = 120 °C. Qualitatively speaking the magnitude values of the λ and h increased as the shear rate increases.
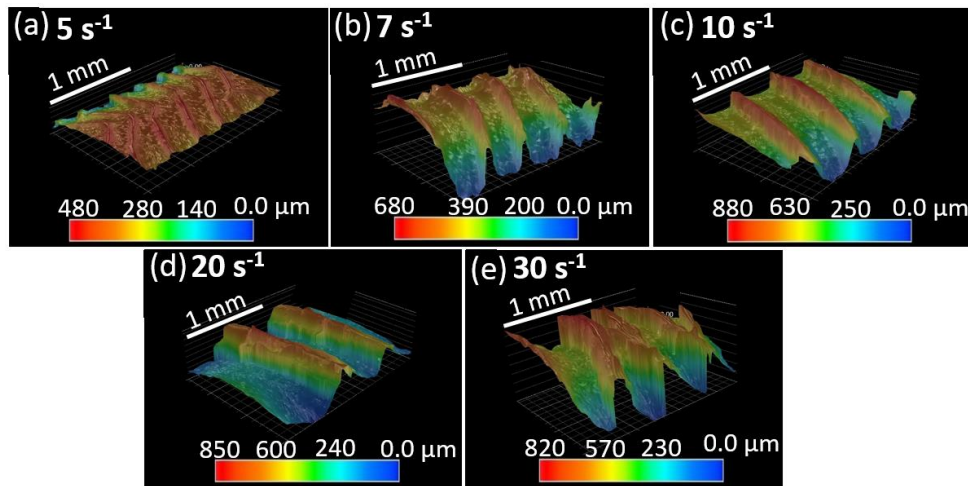
Figure 5.7. The 3D images developed by the depth composition technique for SBR C. The 3D image allows the accurate determination of the spatial characteristic height of the flow instabilities. The extrudates were obtained by *L/D* = 15 with *D* = 2 mm capillary die at T = 120 °C. Adapted from C. K. Georgantopoulos et al., *Physics of Fluids* 33, *093108*, **2021**, Figure 9.[16] Reproduced with permission from AIP Publishing, No. 5231930652686.

5.5. Spatial characteristics of extrusion flow instabilities

The spatial characteristic wavelength (SCW) λ is quantified via offline optical analysis (chapter 3.3) and the experimental results from the investigated samples, SBR A, B and C are presented in Figure 5.8. The experimental results of the SCW λ are fitted by the previously mentioned qualitative models of Wang and coworkers[23-25] (Equation (4.5)) and Inn et al.[26] (Equation (4.39)). To investigate the extrusion flow instabilities capillary rheology experiments were carried out using a series of three round capillary dies with L = 10, 20, 30 mm and D = 2 mm at T = 120 °C. In Figure 5.8 it is observed that the magnitude of the SCW λ remains similar for all the extrudates obtained by all three round capillary dies no matter the length of them.
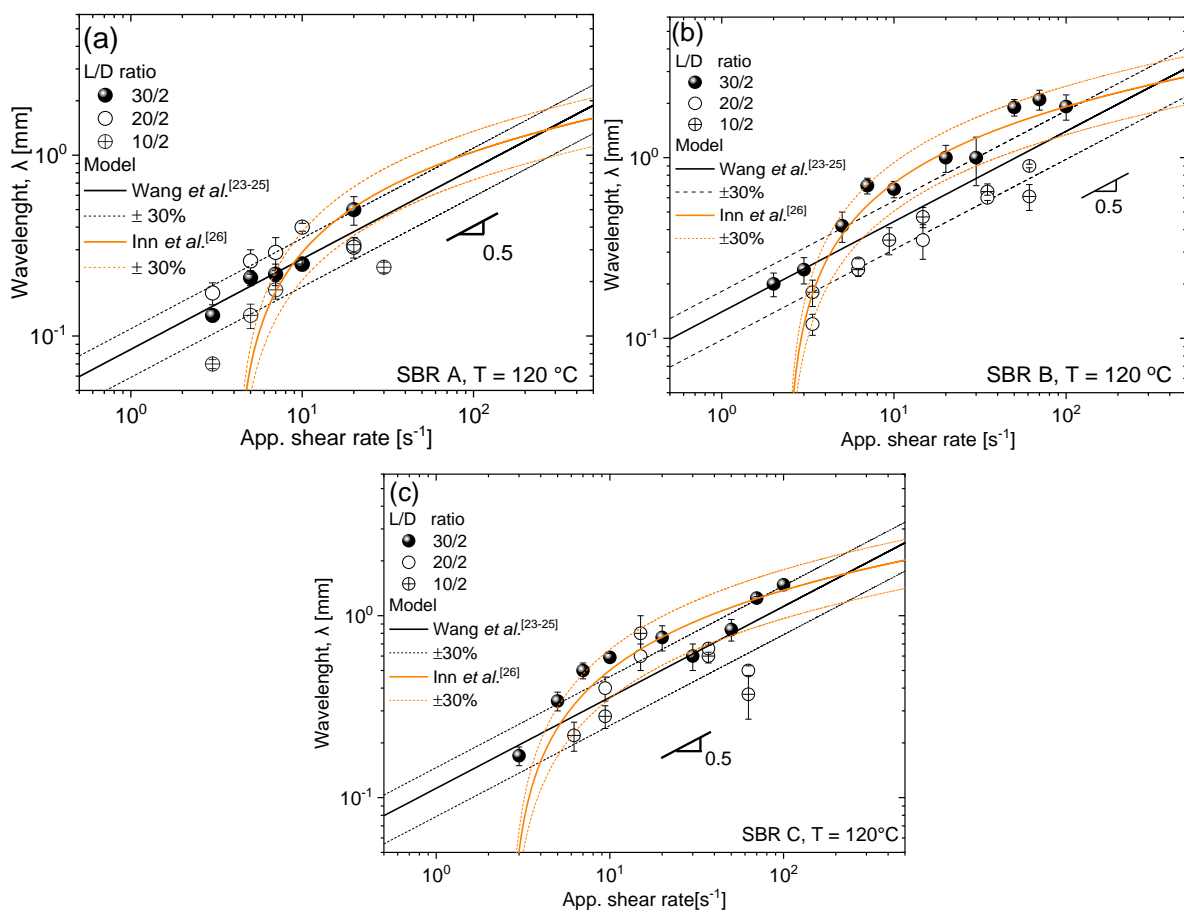
Figure 5.8. Spatial characteristic wavelength of the melt flow instabilities as a function of apparent shear rate for (a) SBR A, (b) SBR B and (c) SBR C at T = 120 °C. The absolute values of the spatial characteristic wavelength estimation vary up to 30% from each L/D ratio. Adapted from C. K. Georgantopoulos et al., *Physics of Fluids* 33, *093108*, **2021**, Figure 11.[16] Reproduced with permission from AIP Publishing, No. 5231930652686.

Both qualitative models Wang and coworkers[23-25] (Equation (4.5)) and Inn et al.[26] (Equation (4.39)) requesting as an input the average value of the swelling diameter D', that is the diameter of the swelling extrudate including the surface distortions, see Figure 4.1 where $D' = 2R_f$. The swelling diameter is calculated as an average value from the extrudates with surface distortions at room temperature. Furthermore, Wang and coworkers[23-25] (Equation (4.5)) model needs as an input the characteristic time periodicity (CTP) τ^* of the instabilities as well. The CTP of the extrusion instabilities is described (Equation (3.2)) as a power law function of apparent shear rate, $\tau^* = a\dot{\gamma}_{app.}^{-0.5}$ where a is a material dependent fitting parameter.[15,17-19] The a fitting parameter for the investigated samples is listed in Table 5.5.

Table 5.5. The material dependent parameter a for the characteristic time periodicity, $\tau^* = a\dot{\gamma}_{app.}^{-0.5}$ at T = 120 °C.

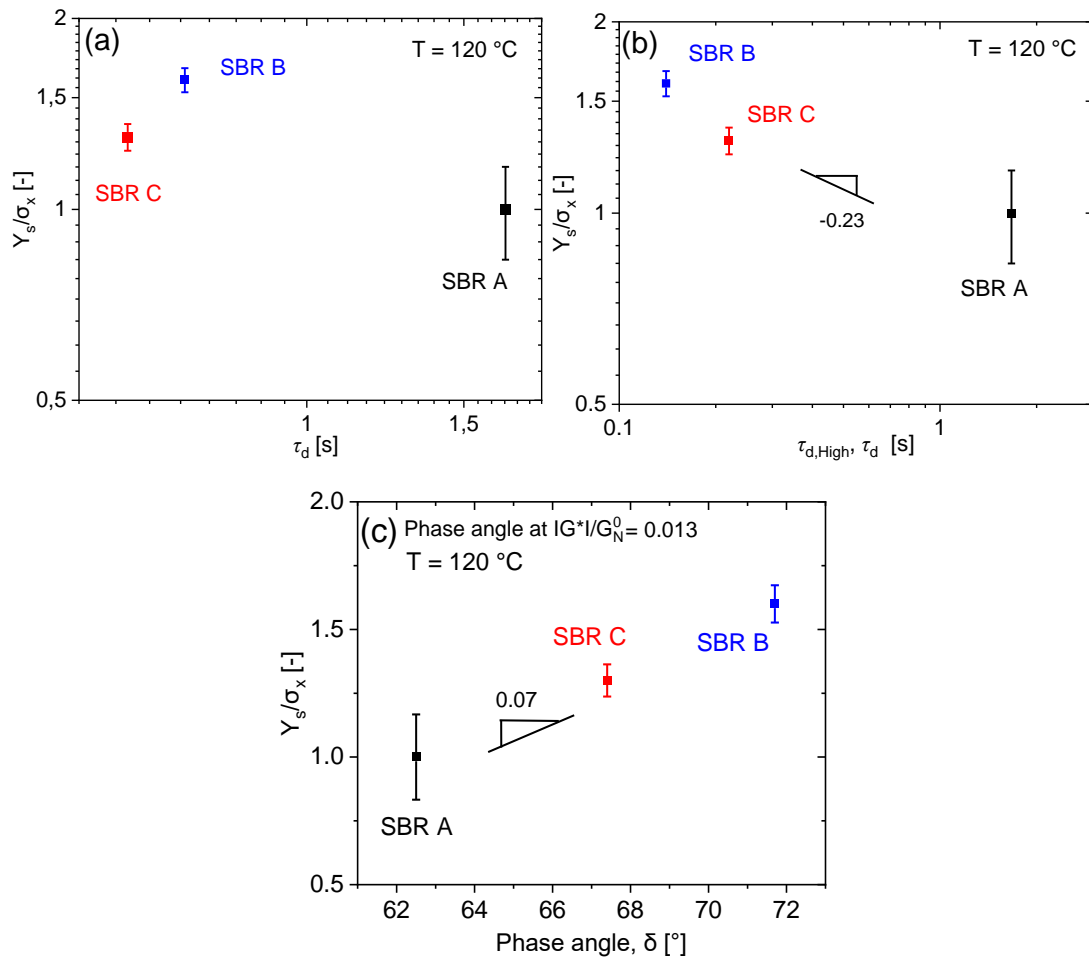| Sample	a
SBR A	0.5
SBR B	0.7
SBR C	0.9

Adapted from C. K. Georgantopoulos et al., *Physics of Fluids* 33, *093108*, **2021**, Table 6 from Appendix.[16] Reproduced with permission from AIP Publishing, No. 5231930652686.

Inn et al.[26] (Equation (4.39)) model needs as an input the theoretical interfacial depth parameter ξ. The interfacial depth parameter is described (chapter 4.6) as a power law function of apparent shear rate, $\xi = b\dot{\gamma}_{app.}^{-c}$, where b and c are fitting parameters.[16,48] The power law function, $\xi = b\dot{\gamma}_{app.}^{-c}$, of the interfacial depth parameter is fitting the experimental data obtained by the investigated SBR samples in Figure 5.9. The b and c fitting parameters are listed in Table 5.9. Moreover, the ratio of the extensional and shear stresses Y_s/σ_x, on the the extrudate remains as a free fitting parameter as Inn et al.[26] suggested. The extensional and shear stress ratio is obtained by the fitting of Inn et al.[26] (Equation (4.39)) to the experimental data of the SCW λ.
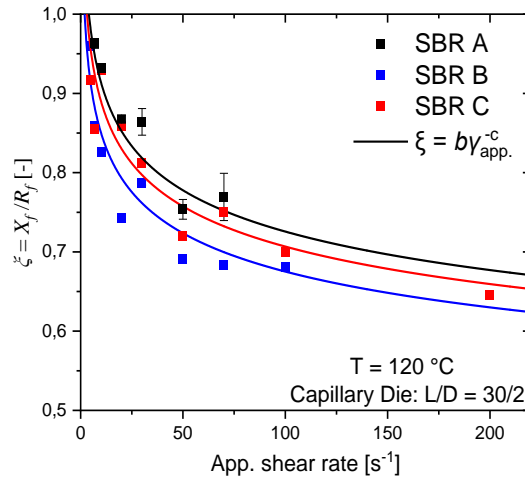
Figure 5.9. Experimental data of the calculated interfacial depth parameter $\xi = X_f/R_f$ from all the investigated samples at T = 120 °C and obtained by a capillary die *L/D* = 15 with *D* = 2 mm. Adapted from C. K. Georgantopoulos et al., *Physics of Fluids* 33, *093108*, **2021**, Figure S3 (b).[16] Reproduced with permission from AIP Publishing, No. 5231930652686.

Table 5.6. The fitting parameters *b* and *c* for the interfacial depth parameter, $\xi = b\dot{\gamma}_{app.}^{-c}$ at T = 120 °C.

Sample	*b*	*c*
SBR A	1.15	0.10
SBR B	1.09	0.10
SBR C	1.08	0.08

Adapted from C. K. Georgantopoulos et al., *Physics of Fluids* 33, *093108*, **2021**, Table 7 from Appendix.[16] Reproduced with permission from AIP Publishing, No. 5231930652686.

Comparing the Wang and coworkers[23-25] (Equation (4.5)) and Inn et al.[26] (Equation (4.39)) models for the SCW λ with the experimental results and to each other the following conclusions have been drawn:

(i) Both models have qualitative agreement with the experimental data of the SCW λ at T = 120 °C.

(ii) The experimental results of SBR C, see Figure 5.8 (c), within the shear rate range of $\dot{\gamma}_{app.} = 10\ \text{s}^{-1}$ to $50\ \text{s}^{-1}$ indicate a plateau like trend. Within this region Inn et al.[26] (Equation (4.39)) describes better than the Wang and coworkers[23-25] (Equation (4.5)) the experimental data.

(iii)   The SCW λ of the same material under the same temperature condition present similar magnitude values while is extruded by the round capillary dies (L = 10, 20, 30 mm, D = 2 mm) no matter the length of them, see Figure 5.68 This observation is also discussed in literature.[23-25]

The spatial characteristic height (SCH) h is quantified via offline optical analysis, see Figure 4.1, and the experimental results from the investigated samples, SBR A, B and C are presented in Figure 5.10. The experimental results of the SCH h are fitted by the previously mentioned qualitative models of Inn et al.[26] (Equation (4.41)), Miller et al.[27,28] (Equation (4.42)) and the linear relationship[16] (Equation (4.43)).
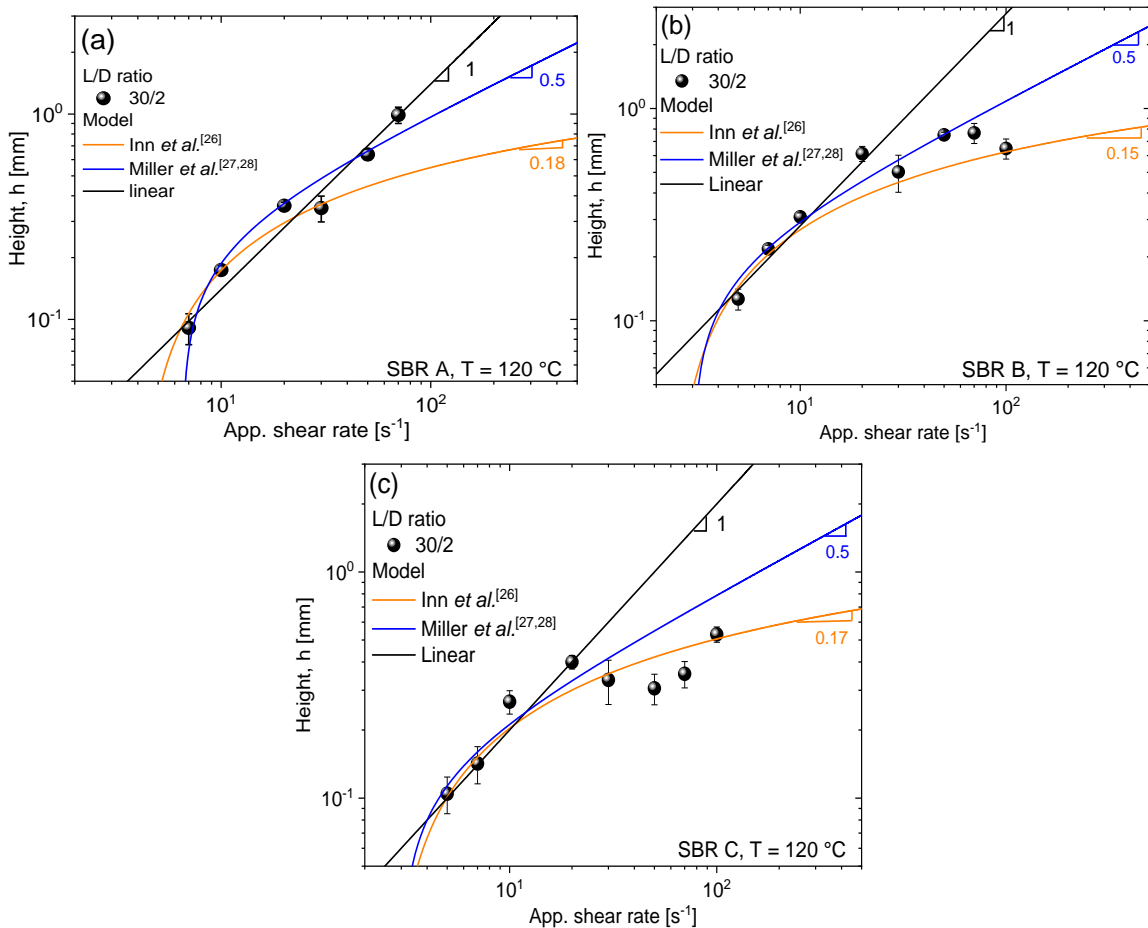
Figure 5.10. Spatial characteristic height h of flow instabilities as a function of apparent shear rate for (a) SBR A, (b) SBR C and (c) SBR B obtained by a capillary die L/D = 15 with D = 2 mm at T = 120 °C. Adapted from C. K. Georgantopoulos et al., *Physics of Fluids* 33, *093108*, **2021**, Figure 12.[16] Reproduced with permission from AIP Publishing, No. 5231930652686.

The experimental results are obtained by the capillary die (round cross-section area) with $L = 30$ mm and $D = 2$ mm at T = 120 °C. The linear relationship (Equation (4.43)) is describing the SCH h at $\dot{\gamma}_{app.} < 20 \ s^{-1}$. The behavior of the experimental results presents a linear increase, subsequently a slope of one, and then an asymptotic trend for SBR B and C is observed. The Inn et al.[26] model uses the same power law function for the interfacial depth parameter, $\xi = b\dot{\gamma}_{app.}^{-c}$, and the same fitting parameter b and c as predicted by the SCW λ, see Table 5.5. For the Miller et al.[27,28] model, the initial height h_0 of the instabilities and the critical shear rate $\dot{\gamma}_{crit.}$ are listed in Table 5.7.

Table 5.7. The fitting parameters k and $\dot{\gamma}_{crit.}$ for the Miller et al.,[27,28] at T = 120 °C.

Sample	k	$\dot{\gamma}_{crit.}$
SBR A	0.10	6.5
SBR B	0.11	3.0
SBR C	0.08	3.0

Comparing the Inn et al.[26] (Equation (4.41)), Miller et al.[27,28] (Equation (4.42)), and the linear relationship[16] (Equation (4.43)) models the following conclusions have been drawn:

(i)   The linear[16] (Equation (4.43)) increase of the SBR A experimental SCH h has a scaling exponent of one. For SBR B and SBR C the deviation from the slope of one begins after $\dot{\gamma}_{app.} = 20 \ s^{-1}$.

(ii)   The Miller et al.[27,28] (Equation (4.42)) model agrees with the experimental data at low and medium shear rates, $\dot{\gamma}_{app.} < 40 \ s^{-1}$ for all the investigated samples.

(iii)   In general the Inn et al.[26] (Equation (4.41)) model describes better than Miller et al.[27,28] (Equation (6.42)) the experimental data for the SBR B and C samples, specifically in the region of the asymptotic behavior, $\dot{\gamma}_{app.} > 20 \ s^{-1}$.

5.6. Correlation between the molecular properties and extrusion behavior

The derivation of the qualitative model of Inn et al.[26] (Equation (4.39)) for the SCW λ of the extrusion flow instabilities includes the ratio of the extensional and shear stresses Y_s/σ_x of the extrudate at the die exit region. Due to the difficulties of experimentally estimate the magnitude value of the extensional and shear stresses ratio, Inn et al.[26] suggested that the ratio is a free fitting parameter. The fitting values of the Y_s/σ_x ratio are obtained by the fitting of Equation (4.39) to the experimental data of SCW λ in Figure 5.8. Fiugre 5.11 presents the fitting values of the Y_s/σ_x ratio as a function of molecular properties.

Figure 5.11. The ratio of tensile and shear stresses at the die exit region as a function of (a) reptation time, (b) the reptation time for the high molecular weight component of the bimodal samples, and (c) the phase angle δ at $|G^*|/G_N^0 = 0.013$ at T = 120 °C. Adapted from C. K. Georgantopoulos et al., *Physics of Fluids* 33, *093108*, **2021**, Figure 13.[16] Reproduced with permission from AIP Publishing, No. 5231930652686.

Specifically, in Figure 5.11 (a) the stress ratio as a function of the overall reptation time of the investigated SBR samples agrees with the assumption of Inn et al.,[26] that the stresses ratio Y_s/σ_x is correlated with the material relaxation time. The reptation time τ_d, is experimentally determined by the inverse frequency of the existence crossover point of the, G' and G'', see Table 5.3. Based on the studied SBR samples and the overall reptation time, it is not clear if any correlation exists, Figure 5.11 (a). By using the Doi-Edwards model[51,52] for the bimodal systems, Equation (5.2), the reptation times of each molecular component are estimated, see Table 5.3. Thus stress ratio Y_s/σ_x as a function of the $\tau_{d,\ high}$ of the SBR B, C and the τ_d of the SBR A is presented in Figure 5.11 (b). A power law with a slope of -0.23 in a log-log scale is presented and confirms that the stress ratio Y_s/σ_x is larger for the samples with higher amount of high molecular weight. Except of the molecular weight influence on the stresses ratio, the molecular architecture (linear, branch) affects the stresses ratio and the extrusion behavior as well. In Figure 5.11 (c) the stresses ratio Y_s/σ_x as a function of the absolute value of the phase angle δ at $|G^*|/G_N^0 = 0.013$ is presented. This specific numerical value $|G^*|/G_N^0 = 0.013$ is chosen because an indication of a relaxation process which is possibly associated with the molecular architecture take place, see Figure 5.4 (c). A scaling law in a lin-lin plot is presented with a slope of 0.07. Based on Figure 5.11 (c) the branched samples present lower values of the stresses ratio Y_s/σ_x at the die exit region than the linear. Within this study the obtained fitting values of the stress ratio Y_s/σ_x point toward that the extensional stress has higher absolute values than the shear stress on the interface of core/surface layer, $Y_s > \sigma_x$. This observation agrees with the literature assumptions and theoretical concept for the origin of the surface melt fracture, sharkskin.[16,26,30-39]

5.7. Conclusions

The outcome of this chapter could serve as guidelines to quantify and model extrusion flow instabilities during extrusion process. The correlations between the extrusion behavior of the neat styrene-butadiene rubber (SBR) and their molecular properties (longest relaxation time and the molecular architecture) could provide information which can be used from extrusion engineers to determine the extrusion performance. The following conclusions have been drawn based on the previously reported outcome:

(i)   Both models have qualitative agreement with the experimental data of the SCW λ at T = 120 °C. Nonetheless, the model of Inn et al.[26] underestimates the SCW λ at low shear rates, $\dot{\gamma}_{app.} < 8$ s^{-1}, of all samples.

(ii)   It is observed that the Inn et al.,[26] describes better the experimental results of SCH *h* than the Miller et al.[27,28] in the whole range of apparent shear rates.

(iii)   The Y_s/σ_x on the core/surface interface of the extrudate is correlated with the molecular properties such as, relaxation time and the molecular architecture (linear and branch). It is observed, see Figure 5.11 (b), that the higher amount of high-molecular weight component indicates higher value for the stress ratio. In addition, the most elastic material of the investigated samples indicates lower value for the stress ratio are obtained, see Figure 5.11 (c).

6. Influence of Processing Parameters on Extrusion Flow Instabilities

This chapter uses the previous reported qualitative models in chapter 4 and enables the correlations of processing parameter, such as the extrusion die cross-section and the die temperature, with the spatial characteristic wavelength (λ) of the extrusion flow instabilities. A commercial polybutadiene (PBD) sample is used due to its pronounced sharkskin instability. The well-developed pattern of sharkskin makes the PBD an ideal model system for the study of surface fracture. The fitting of the constitutive model to the experimental data of the spatial characteristic wavelength (λ) provides the ratio of the extensional and shear stress at the die exit region which is correlated with the height (H) and the diameter (D) of the extrusion slit and capillary dies, respectively. Thus, useful correlations for the impact of the die geometry on the extrusion behavior are presented. In addition to the constitute models, a simple, practical and die geometry dependent models able to predict the spatial characteristic wavelength (λ) from a capillary to slit die and vice versa are also presented. Furthermore the influence of extrusion temperature on the spatial characteristic wavelength (λ) of extrusion instabilities is discussed as well.

6.1. Material used in this chapter

The investigated material is a commercial polybutadiene (PBD). The molecular weight distribution of PBD is obtained by a quadruple-detection size exclusive chromatography (SEC) using homopolymer linear polybutadiene standards. The four detectors of the quadruple-detection SEC are, a differential refractive index (DRI) detector, an ultra-violet (UV) detector, a viscometer and a multi-angle laser light-scattering (MALLS) detector.[48] The relative MWD of the PBD obtained by the DRI detector is displayed by Figure 6.1 (a). The detection signal from the rest of the responses are displayed in Appendix B. The relative MWD of the investigated PBD is unimodal with a weight average molecular weight of $M_w = 375$ kg·mol^{-1} and dispersity index $Đ = M_w/M_n = 3.5$, see Table 6.1.

In order to investigate the molecular architecture of the PBD the Mark-Houwink[49,50] method is used. Particularly, the Mark-Houwink[49,50] plot is presented in Figure 6.1 (b) where the

intrinsic viscosity [η] of the sample obtained by the viscometer detector is plotted as function of the absolute molecular weight obtained by the multi-angle laser light-scattering (MALLS) detector. The results obtained by the viscometer and the MALLS are compared with the homopolymer linear polybutadiene standards in Figure 6.1 (b). Within the molecular weight range of 400 kg·mol^{-1} and 3000 kg·mol^{-1} the [η] of the investigated PBD deviates from the calibration standards.[48] This behavior implies the existence of branches in the range of 400 kg·mol^{-1} to 3000 kg·mol^{-1} molecular weight.
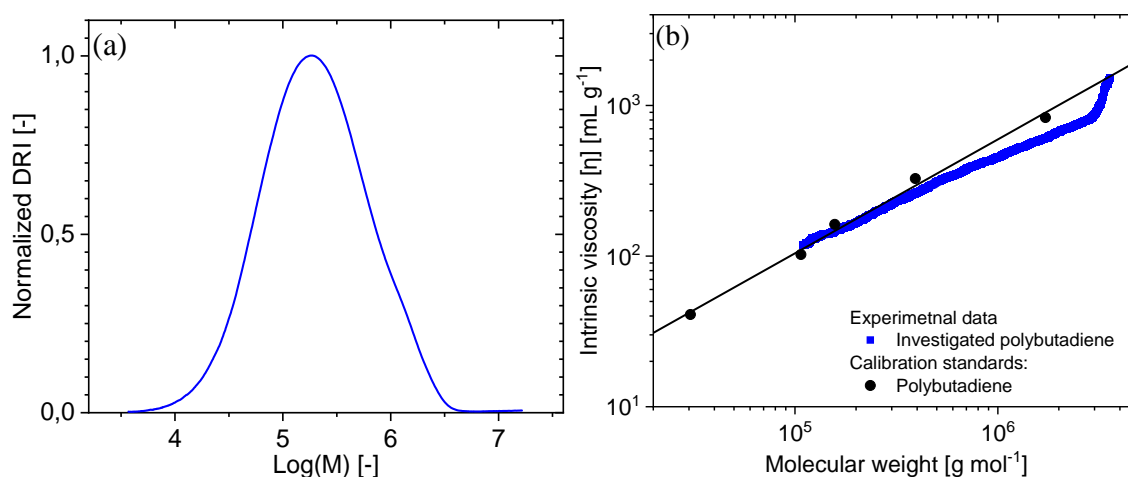
Figure 6.1. (a) Normalized differential refractive index (DRI) detector response as a function of the molar mass for the PBD sample as obtained by SEC. (b) The intrinsic viscosity [η] as a function of molecular weight as obtained via MALLS. The black circles are calibration standards of homopolymer polybutadiene with linear molecular architecture are included in the graph. The deviation of PBD from the standard between 400 kg·mol^{-1} and 3000 kg·mol^{-1} indicates branched molecular architecture. For the ultra-violet (UV), viscometer and MALLS responses see Appendix B. Adapted from C. K. Georgantopoulos et al., *Macromolecular Material and Engineering* submitted, **2022**, Figure 1.[48]

Table 6.1. Molecular weight characteristics and glass transition temperature T_g of the investigated PBD sample.

Name	M_n [kg·mol^{-1}]	M_w [kg·mol^{-1}]	$Đ$ [-]	T_g [°C] [a)]
PBD	107	375	3.5	-108

[a)]98 wt.% cis 1,4 butadiene obtained by the material data sheet. Adapted from C. K. Georgantopoulos et al., *Macromolecular Material and Engineering* submitted, **2022**, Table 1.[48]

6.2. Experimental procedure

Small amplitude oscillatory shear (SAOS) experiments were performed with a rubber process analyzer (RPA), TA Instruments, close cavity rheometer. This rheometer has a 40 mm dimeter grooved geometry in order to minimize the slippage between the material and the geometry. The SAOS experiments were done at T = 100 °C within angular frequency of $\omega = 0.06$ rad·s^{-1} and 300 rad·s^{-1}. The Maxwell model[42] is used to fit the magnitude complex viscosity, storage and loss moduli are with 5-element Maxwell modes.

In order to obtain the steady state viscosity of the investigated PBD within $\dot{\gamma}_{app.} = 0.004$ s^{-1} and 0.05 s^{-1} at T = 100 °C the ARES-G2, TA Instruments, rheometer equipped with a 8 mm grooved plate-plate geometry is used. In addition the non-linear transient extensional viscosity of the PBD sample is obtained by the extensional viscosity fixture (EVF) equipped to the ARES-G2 rheometer. The extensional rates of $\dot{\varepsilon} = 0.01$ s^{-1} and 10 s^{-1} at T = 100 °C are used.

Furthermore, capillary rheology is used and the processing behavior as well as the apparent steady state viscosity under processing conditions are obtained. The capillary rheometer is a Göttfert RG 50 equipped with a reservoir of 30 mm diameter and several extrusion die geometries. Specifically, six commercially available dies were used: (i) three round capillary (circular cross-section area) dies with diameter of $D = 1$, 2 and 3 mm, and length of $L = 30$ mm and (ii) three slit (rectangular cross-section are) dies with height of $H = 0.5$, 1 and 3 mm, keeping constant the length of $L = 30$ mm and width of $W = 10$ mm. These specific dies were chosen based on the systematic difference of the of diameter D and height H size, because it is known in literature[23-25] that the SCW λ is influenced by that.

Moreover, two custom made slit die geometries with complex cross-section area are used as well. These custom made dies are inspired by the automotive related manufacturers which they are extrudate products with complex geometries.[59] In this work the first one is named as *slit-die-simple-profile* with length of $L = 30$ mm, width of $W = 10$ mm and heights of $H = 2$ and 3 mm, and the second one is named as *slit-die-scalar-profile* with length of $L = 30$ mm, width of $W = 10$ mm, heights of $H = 1.5$, 2 and 3 mm. In Figure 6.2 the *slit-die-simple-profile* and *slit-die-scalar-profile* are presented. These specific designs were inspired by the study of J. F. T. Pittman.[59]

6.3. Rheological characterization: linear and non-linear regime

The SAOS experimental results, that is the loss $(G''(\omega))$ modulus, storage $(G'(\omega))$ modulus and the magnitude of complex viscosity $(|\eta^*(\omega)|)$ as a function of angular frequency (ω) at $T = 100$ °C are presented in Figure 6.3 (a) and (b), respectively. These experimental results are

fitted by a 5-element Maxwell model[42] (Equation (5.1)) where the Maxwell modes can be found in Appendix B.
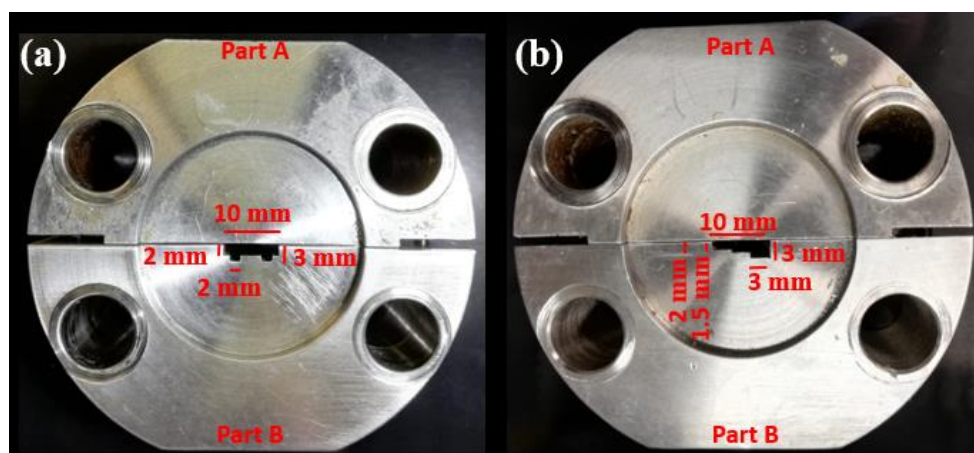
Figure 6.2. Images of the two slit die geometries with different cross-section profile (a) *slit-die-simple-profile* and (b) *slit-die-scalar-profile*. The computer-aided design (CAD) drawings can be found in Appendix B. Adapted from C. K. Georgantopoulos et al., *Macromolecular Material and Engineering* submitted, **2022**, Figure 2.[48]

In Figure 6.3 (a) the loss ($G''(\omega)$) modulus and storage ($G'(\omega)$) modulus is observed at $\omega_{crossover}$=1.66 rad·s^{-1}. Below the crossover angular frequency $\omega < \omega_{crossover}$, the terminal flow regime where $G'' \sim \omega^1$ and $G' \sim \omega^2$ is not reached for the investigated PBD yet, at T = 100 °C. The loss ($G''(\omega)$) modulus and storage ($G'(\omega)$) modulus scale with the angular frequency to the 0.5 power, that is $G'' \sim G' \sim \omega^{0.5}$. This scaling behaviour is known as Rouse dynamic and is usually mentioned in unentangled polymer melts, and in the rubbery region of highly branched polymer melts.[60¬63] In literature[60¬63] similar behaviour of the $G''(\omega)$ and $G'(\omega)$ as in Figure 6.3 (a) is observed for comb like molecular architectures. According to Larson et al.,[61] this parallel trend and scaling behavior of the $G''(\omega)$ and $G'(\omega)$ before the crossover angular frequency ($\omega < \omega_{crossover}$) is associated with a very slow relaxation process which takes longer than the reputation time, that is $\tau_d = 1/\omega_{crossover}$. This slow relaxation process is assumed to caused by the entanglements between the backbone and the branches of the polymer chain. Those entanglements are characterized by the literature[60¬63] as permanent entanglements because they have so slow relaxation process. Based on this theoretical explanation the terminal regime is not reached due to the polymeric chains which are not fully relaxed from the existence of "permanent" entanglements between the backbone and the branches.[60¬63] In order to verify this theoretical explanation the molecular architecture of the

studied PBD needs to be further investigated. A typical power law viscosity behavior for rubbery materials[15,16] is observed in Figure 6.3 (b) for this investigated PBD sample. The magnitude of complex viscosity as a function of angular frequency is fitted by a power law model, $|\eta^*(\omega)| = K\omega^{n-1}$, as well. The fitting parameters of the power law model at T = 100 °C are $K = 57000$ Pa·s^n and $n = 0.4$.[48]
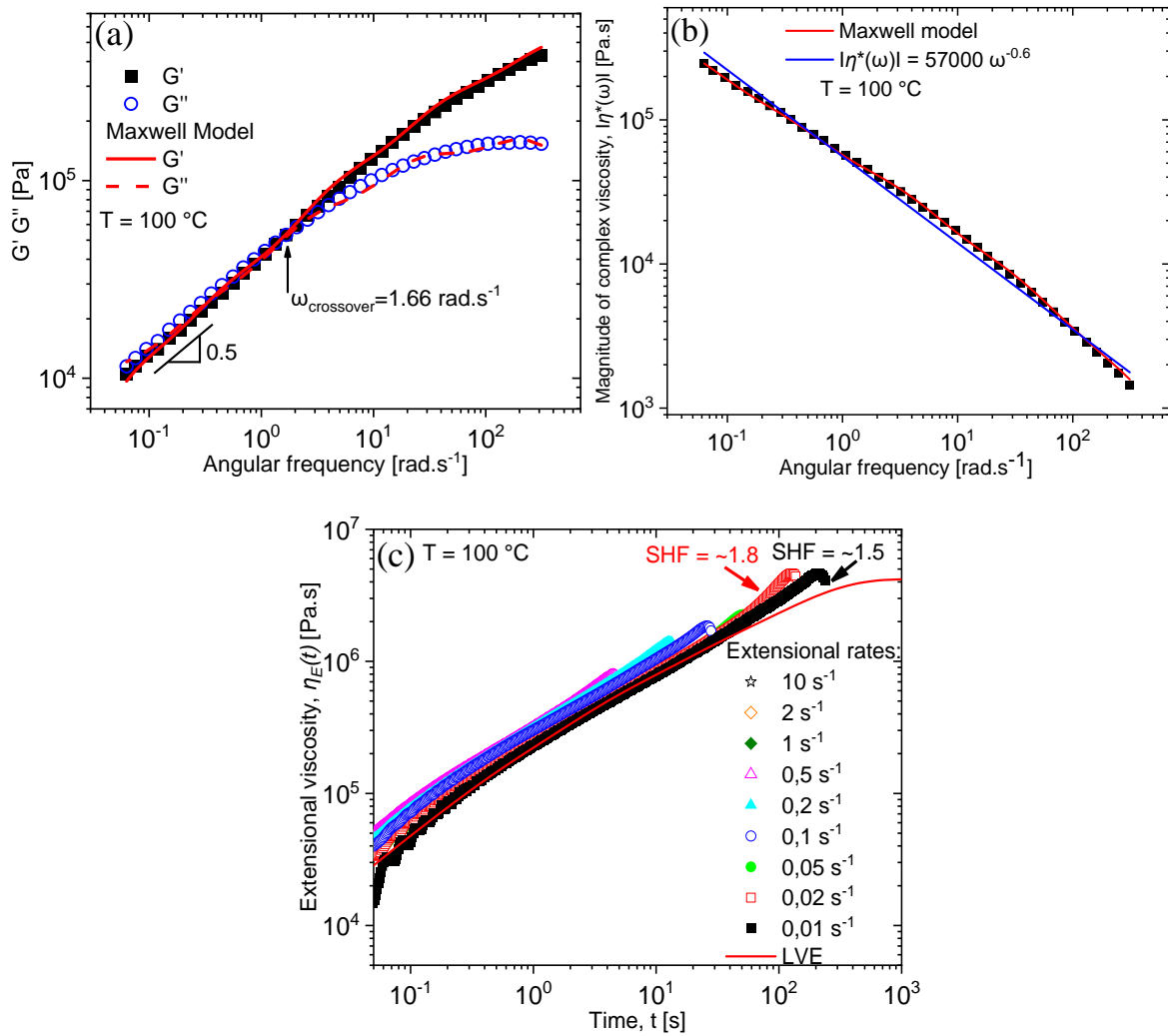
Figure 6.3. (a) Loss and storage moduli, (b) magnitude of complex viscosity as a function of angular frequency fitted by a 5-element Maxwell model, see Appendix B. (c) Transient extensional viscosity and the linear viscoelasticity (LVE). Adapted from C. K. Georgantopoulos et al., *Macromolecular Material and Engineering* submitted, **2022**, Figure 8.[48]

The non-linear transient extensional viscosity of the studied PBD is presented in Figure 6.3. The extensional rates are $\dot{\varepsilon} = 0.01, 0.02, 0.05, 0.1, 0.2, 0.5, 1, 2$ and 10 s^{-1} at $T = 100$ °C. Strain hardening factor (SHF) is defined[42] as the ratio between the steady state extensional viscosity

and the viscosity which is predicted from the linear viscoelasticity (LVE), $SHF = \eta_{max}(\dot{\varepsilon})/3\eta_{LVE}(\dot{\varepsilon})$. For the investigated PBD a strain hardening factor of $SHF = 1.8$ and 1.5 is observed at $\dot{\varepsilon} = 0.02$ s^{-1} and 0.02 s^{-1} respectively, see Figure 6.3 (c). This strain hardening behavior at low extensional rates is usually observed for polymers with a fairly low degree of branching which belong in a high molecular weight tail.[57,58] Similar observation has been mentioned for several SBR samples as well, see Figure 5.5.[15,16]

Based on the analytical method of Mark-Houwink[49,50] plot (Figure 6.1 (b)) and the given strain hardening behavior of the transient extensional viscosity can be conclude that the investigated PBD sample has a given degree of branched in the high molecular weight tail between 400 kg·mol^{-1} and 3000 kg·mol^{-1}. The evidence for the existence of branches agrees with the theoretical explanation of the unusual behavior of the loss ($G''(\omega)$) and storage ($G'(\omega)$) modulus in Figure 6.3 (a).

The apparent steady state viscosity ($\eta_{app.}$) and magnitude of complex viscosity ($|\eta^*(\omega)|$) as a function of apparent shear rate ($\dot{\gamma}_{app.}$) and angular frequency (ω) at $T = 100$ C are presented in Figure 6.4. The apparent steady state viscosity ($\eta_{app.}$) as a function of apparent shear rate ($\dot{\gamma}_{app.}$) for the studied slit and round capillary dies are presented in Figure 6.4 (a) and (b). Within the Figure 6.4 (a) and (b) apparent steady state viscosity ($\eta_{app.}$) as a function of apparent shear rate ($\dot{\gamma}_{app.}$) obtained by the ARES-G2 strain controlled rheometer between $\dot{\gamma}_{app.} = 0.004$ s^{-1} and 0.05 s^{-1} at $T = 100$ °C is presented as well.

The apparent steady state viscosity ($\eta_{app.}$) as a function of apparent shear rate ($\dot{\gamma}_{app.}$) at Figure 6.4 (a) and (b) is fitted by the Cross model,[42] $\eta(\dot{\gamma}) = \eta_0/(1 + (\tau\dot{\gamma})^m)$ where $\eta_0 = 750$ kPa·s, $\tau = 6$ s, and $m = 0.92$. Differences between the apparent steady state viscosity ($\eta_{app.}$) obtained by the different slit dies and round capillary dies are observed in Figure 6.4 (a) and (b). Those deviations occurred by the influence of wall slippage on the die wall and the pressure exit effect. To minimize the deviation between the dies, Figure 6.4 (a) and (b), the Bagley[4] and Rabinowitsch-Weissenberg[4] corrections are required. However, it is know in literature[41] that the Bagley correction can be neglected if the aspect ratio (L/D or L/H) of the extrusion die is equal or larger than 60. Within this study the slit die with $H = 0.5$ mm has aspect ratio of $L/H = 60$, thus the obtained apparent shear stress $\sigma_{app.}$ is the correct wall shear stress σ_{wall} without requiring a Bagley correction.[4,41] Hence only Rabinowitsch-Weissenberg[4] correction, $\dot{\gamma}_{wall} = [(2n + 1)/3n]\dot{\gamma}_{app.}$ and n is defined by the $n \equiv d(log\sigma_{wall})/d(log\dot{\gamma}_{app.})$, can be applied.
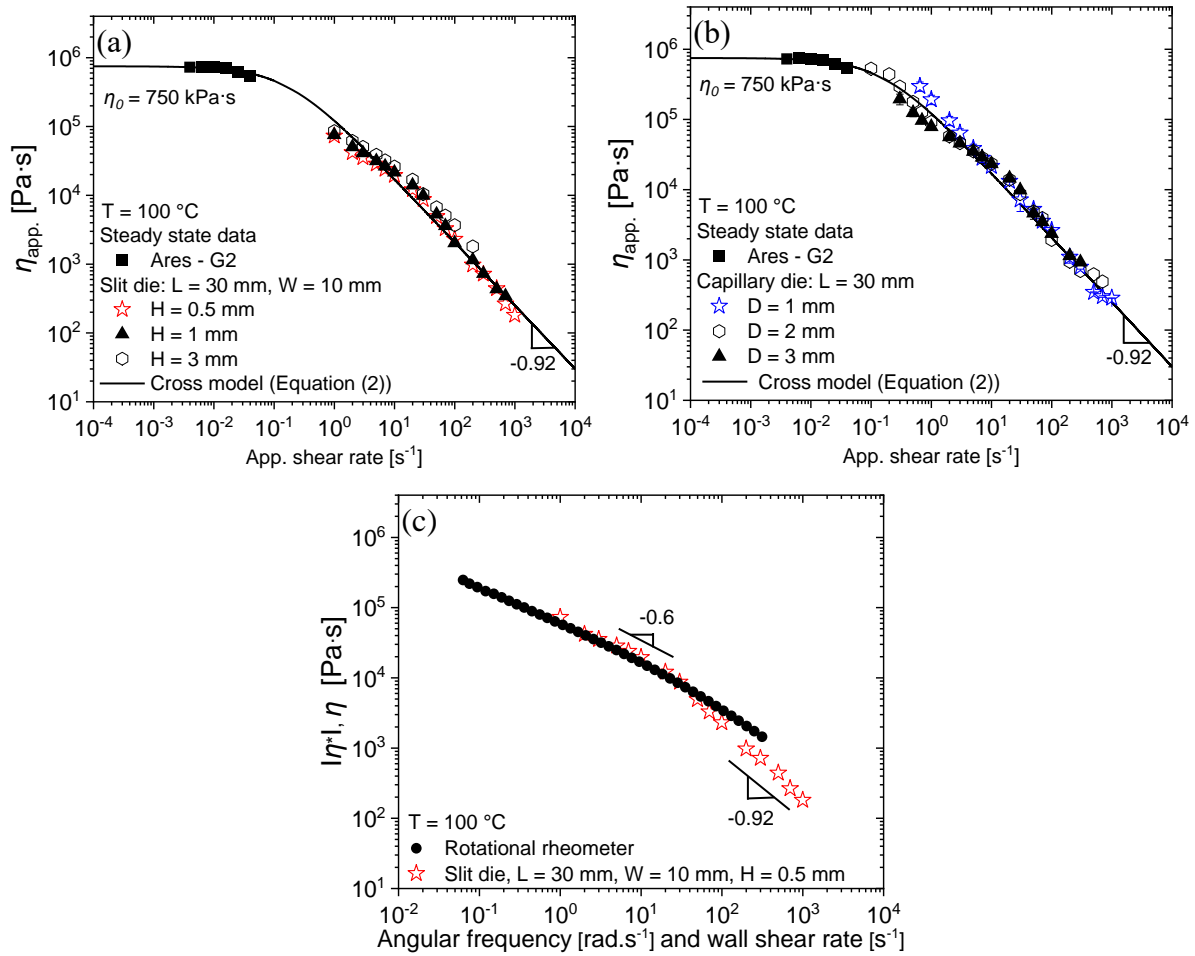
Figure 6.4. (a) – (b) Apparent steady state viscosity as a function of apparent shear rate for the slit and capillary die geometries, respectively. (c) Comparison between the magnitude of complex viscosity obtained by oscillatory shear experiment (black solid circles) and the steady state viscosity (red open stars) obtained by capillary rheology with slit die $L/H = 60$ mm, and $H = 0.5$ mm. All the experiments carried out at $T = 100$ °C. Adapted from C. K. Georgantopoulos et al., *Macromolecular Material and Engineering* submitted, **2022**, Figure 9.[48]

In order to check the validity of the Cox-Merz[64] rule the obtained and corrected data of the steady state viscosity (η) and wall shear rate ($\dot{\gamma}_{wall}$) from the slit die with $H = 0.5$ mm and $L/H = 60$ are compared with the magnitude of complex viscosity ($|\eta^*(\omega)|$) and angular frequency (ω) at T = 100 °C in Figure 6.4 (c). It is know that the Cox-Merz[64] rule is valid for linear, homopolymer, monodispersed polymer melts. However several deviations from these assumptions have been observed in literature.[15,16,65¬67] Figure 6.4 (c) shows that the Cox-Merz[64] rule is valid until $\dot{\gamma}_{wall} \approx 50$ s^{-1} where both viscosities are overlapping, after $\dot{\gamma}_{wall} >$ 50 s^{-1} the steady state viscosity scales with the slope of -0.92 and deviates from the magnitude

of complex viscosity. This deviation of the Cox-Merz[64] rule is further elaborated in literature and explained by the intensive slippage on the die wall.[15,15,20,65¬67]

6.4. Correlation of spatial characteristic wavelength λ with extrusion die dimensions

Within this chapter the quantitative experimental results of the SCW λ and the fitting of them by the qualitative models, Equation (4.14), (4.39) and (4.40), are presented. Should by mentioned that the apparent shear rate is defined as $\dot{\gamma}_{app.} = (6Q)/(WH^2)$ for slit dies and $\dot{\gamma}_{app.} = (4Q)/(\pi R^3)$ for round capillary dies.[4]

Figure 6.5 displays the images of extrudates obtained from the three different round capillary dies, with diameters of D = 1 mm, 2 mm, 3 mm, and L = 30 mm. Observing the extrudates in Figure 6.5 it can be easily mentioned that the SCW λ increases as the diameter of the die increased. Same observation has been published by Wang and coworkers[23¬25] for polyethylene samples.
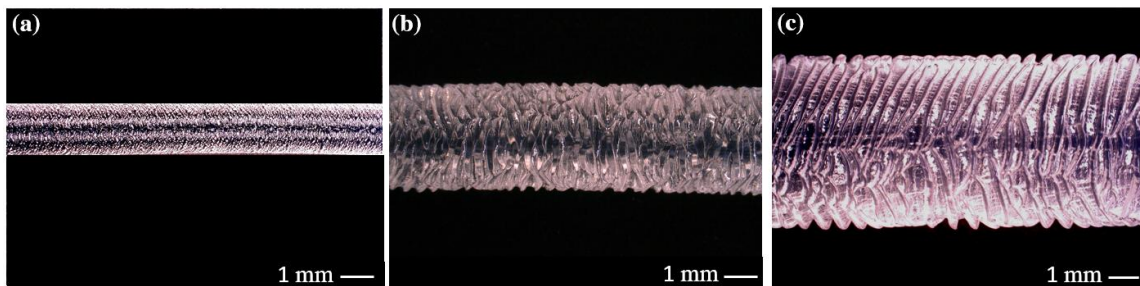
Figure 6.5. Images of the extruded PBD sample with capillary dies (a) D = 1 mm, (b) D = 2 mm, (c) D = 3 mm, and L = 30 mm at T = 100 °C and $\dot{\gamma}_{app.}$= 5 s^{-1}. Adapted from C. K. Georgantopoulos et al., *Macromolecular Material and Engineering* submitted, **2022**, Figure 10.[48]

The numerical values of the SCW λ for the experiments conducted by the round capillary dies with D = 1, 2 and 3 mm at T = 100 °C are presented in Figure 6.6 (a). The marked data in Figure 6.6 (a) are occurred by the stick part of the stick-slip instability, see Figure 2.11 and 3.6 (b). The simplified model of Inn et al.,[26] Equation (4.39), is used to describe the experimental data in Figure 6.6 (a). This model presents qualitative and quantitative agreement with the experimental data. After the fitting the stresses ratio Y_s/σ_x of the extensional and shear stress on the interface between the surface and core layer, see Figure 4.1, of the extrudate is obtained. The obtained Y_s/σ_x ration is plotted as a function of the diameter D of the round capillary dies

in Figure 6.6 (b). The stresses ratio Y_s/σ_x presents a minor decrease trend as the diameter D of the round capillary die increases.
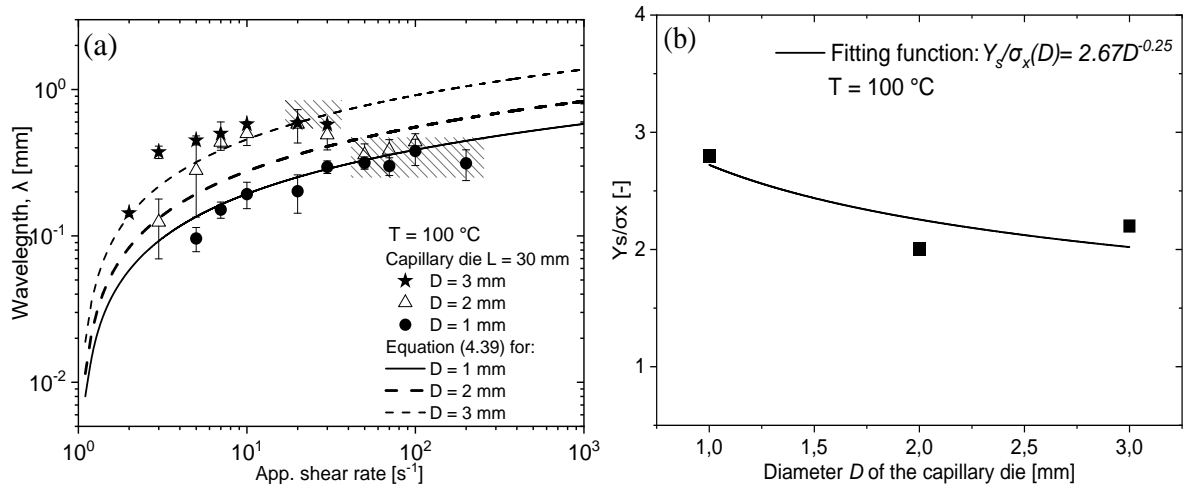
Figure 6.6. (a) Spatial characteristic wavelength λ obtained by capillary dies with $D = 1, 2$ and 3 mm, and $L = 30$ mm. The experimental data are fitted by the Inn et al.[26] model, Equation (4.39). The marked data were obtained by the stick part of the stick-slip instability. (b) The ratio of the stresses ratio Y_s/σ_x at the die exit region as a function of the diameter D of the round capillary die. Adapted from C. K. Georgantopoulos et al., *Macromolecular Material and Engineering* submitted, **2022**, Figure 11.[48]

Figure 6.7 displays the images of extrudates obtained from the three different slit dies, with diameters of $H = 0.5, 1$ and 3 mm, and $L = 30$ mm. Observing the extrudates in Figure 6.7 it can be easily mentioned that the SCW λ increases as the height of the die increased.
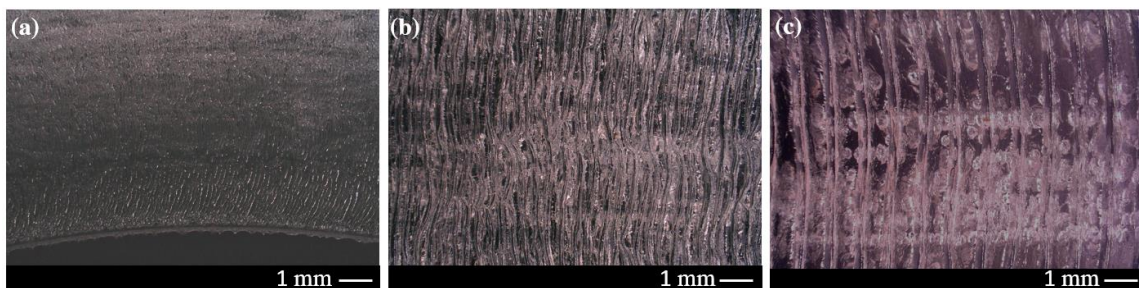
Figure 6.7. Images from the extruded PBD from slit dies with (a) $H = 0.5$ mm, (b) $H = 1$ mm, (c) $H = 3$ mm, and $L = 30$ mm at T = 100 °C and $\dot{\gamma}_{app.} = 10$ s^{-1}. Adapted from C. K. Georgantopoulos et al., *Macromolecular Material and Engineering* submitted, **2022**, Figure 12.[48]

The numerical values of the SCW λ for the experiments conducted by the slit dies with $H = 0.5$, 1 and 3 mm at T = 100 °C are presented in Figure 6.8 (a). The marked data in Figure 6.8 (a) are occurred by the stick part of the stick-slip instability, see Figure 3.6 (a) and 3.9 (a). The new proposed simplified model based on Inn et al.,[26] for slit dies, Equation (4.40), is used to describe the experimental data in Figure 6.8 (a). This model presents qualitative and quantitative agreement with the experimental data. After the fitting the stresses ratio Y_s/σ_x of the extensional and shear stress on the interface between the surface and core layer, see Figure 4.2, of the extrudate is obtained. The obtained Y_s/σ_x ration is plotted as a function of the height H of the slit dies in Figure 6.8 (b). The stresses ratio Y_s/σ_x presents a decrease trend as the height H of the slit die increases.
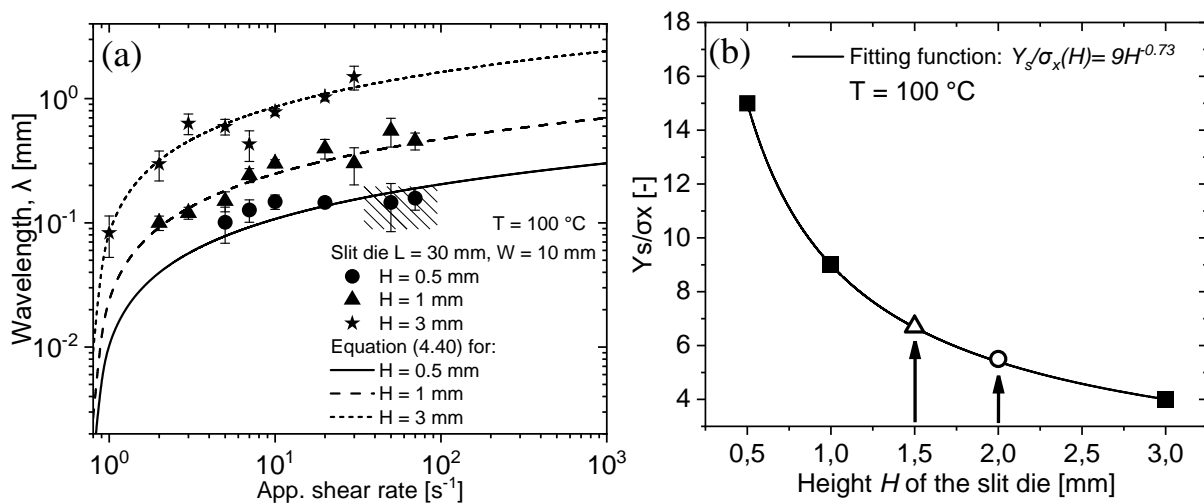
Figure 6.8. (a) Spatial characteristic wavelength λ obtained by slit dies with $H = 0.5$, 1and 3 mm, $W = 10$ mm and $L = 30$ mm. The experimental data are fitted by the proposed model, Equation (4.40). (b) The ratio of the stresses Y_s/σ_x at the die exit region as a function of the height H of the die. The solid symbols are obtained by the fitting of Equation (4.40) to the experimental data. The open triangle and rectangular symbols are estimating the Y_s/σ_x ratio for the $H = 1.5$ mm and $H = 2$ mm, respectively. The estimated values are used below. Adapted from C. K. Georgantopoulos et al., *Macromolecular Material and Engineering* submitted, **2022**, Figure 13.[48]

The fitting numerical values of stresses ratio Y_s/σ_x obtained by the models, Equation (4.39) and (4.40), verify the assumption[16,26,34-39] that the extensional stress Y_s on the surface layer of the extrudate has greater absolute values than the theoretical shear stress σ_x on the interface between the two layers (surface and core), $Y_s > \sigma_x$. See Figure 6.6 (b) and 6.8 (b).

In order to increase the complexity of the slit die geometry and simulate similar extrusion dies as the industrial automotive industry,[59] two slit dies with complex cross-section profile are investigated within this study, see Figure 6.2. Figure 6.9 presents the *slit-die-simple-profile*. In particular Figure 6.9 (a) presents the cross-section area of the die exit, Figure 6.9 (b) displays the flow channel where the last $L_{\text{profile}} = 3$ mm is the area where the profile is made and last in Figure 6.9 (c) an online image of the extrudate during the extrusion process of the studied PBD at T = 100 °C and $\dot{\gamma}_{app.}^{H=2\,mm} = 10\ s^{-1}$, $\dot{\gamma}_{app.}^{H=3\,mm} = 11.11\ s^{-1}$ is displayed. The arrows show the flow direction of the polymer in different heights of the profile, specifically the blue arrows represent the flow at $H = 3$ mm and the red arrow at $H = 2$ mm. In Figure 6.9 (c) the main two different SCW λ can be identified.
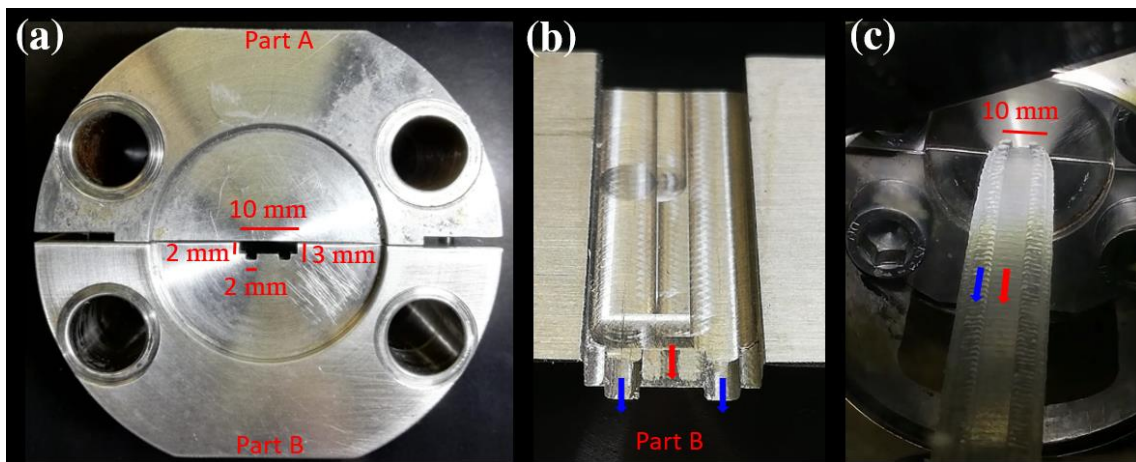
Figure 6.9. *Slit-die-simple-profile*. (a) The cross-section area, (b) the flow channel part, where the profile is existing at the last $L_{\text{profile}} = 3$ mm of the die exit, and (c) visualization of the flow during extrusion of the investigated PBD at T = 100 °C and $\dot{\gamma}_{app.}^{H=2\,mm} = 10\ s^{-1}$, $\dot{\gamma}_{app.}^{H=3\,mm} = 11.11\ s^{-1}$. Adapted from C. K. Georgantopoulos et al., *Macromolecular Material and Engineering* submitted, **2022**, Figure 14.[48]

Figure 6.10 displays extrudates of the investigated PBD sample obtained by the *slit-die-simple-profile* at T = 100 °C. The arrows identify the area of the extrudate which was extruded by $H = 2$ mm (red arrows) and $H = 3$ mm (blue arrows). In Figure 6.10 it is easily mentioned that the SCW λ obtained by the $H = 3$ mm has larger numerical values than the SCW λ obtained by $H = 2$ mm.
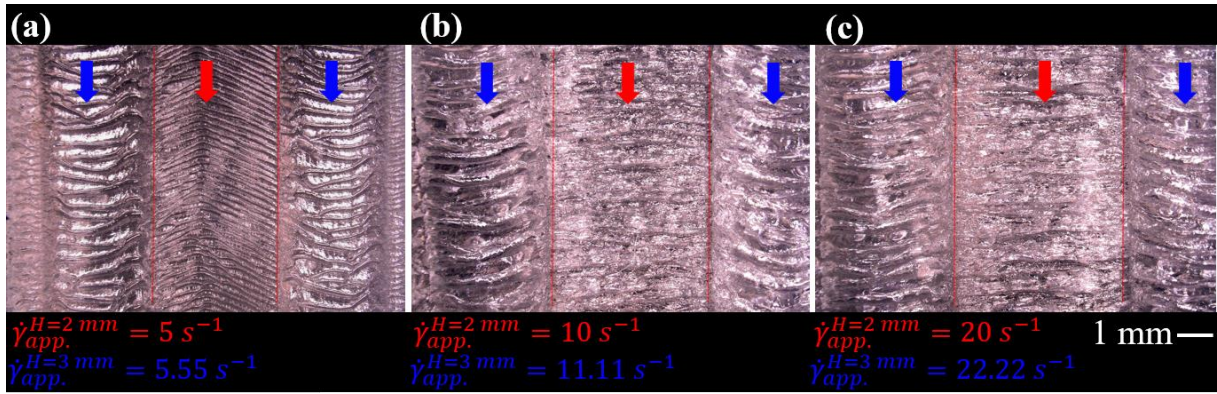
Figure 6.10. Images of the extruded PBD from *slit-die-simple-profile* (Figure 6.9 (a)) at (a) $\dot{\gamma}_{app.}^{H=2\ mm} = 5\ s^{-1}$, $\dot{\gamma}_{app.}^{H=3\ mm} = 5.55\ s^{-1}$, (b) $\dot{\gamma}_{app.}^{H=2\ mm} = 10\ s^{-1}$, $\dot{\gamma}_{app.}^{H=3\ mm} = 11.11\ s^{-1}$, and (c) $\dot{\gamma}_{app.}^{H=2\ mm} = 20\ s^{-1}$, $\dot{\gamma}_{app.}^{H=3\ mm} = 22.22\ s^{-1}$, at T = 100 °C. The arrows indicate the flow direction, the red arrow represents the flow at the die section with H = 2 mm and the blue arrows at the die section with H = 3 mm. Adapted from C. K. Georgantopoulos et al., *Macromolecular Material and Engineering* submitted, **2022**, Figure 15.[48]

Due to the cross-section profile of the *slit-die-simple-profile*, see Figure 6.9 (a), different shear rates are calculated based on $\dot{\gamma}_{app.} = (6Q)/(WH^2)$ at on each section of the profile. In Table 6.2 the shear rates are listed.

Table 6.2. Calculation of shear rate for the *slit-die-simple-profile* with length L = 30 mm, width W = 10 mm, and height H = 3 mm and 2 mm. The calculation of shear rate based on $\dot{\gamma}_{app.} = (6Q)/(WH^2)$, where Q is the volumetric flow rate in mm³·s⁻¹.

Q [mm³·s⁻¹]	$\dot{\gamma}_{app.}$ [s⁻¹] at H = 2 mm W = 10 mm	$\dot{\gamma}_{app.}$ [s⁻¹] at H = 3 mm W = 4 mm
13.33	2	2.22
20	3	3.33
33.33	5	5.55
46.66	7	7.77
66.66	10	11.11
133.33	20	22.22
200	30	33.33
333.33	50	55.55

Adapted from C. K. Georgantopoulos et al., *Macromolecular Material and Engineering* submitted, **2022**, Table S4 in supplementary information.[48]

The numerical values of the SCW λ for the experiments conducted by the *slit-die-simple-profile* with $H = 2$ and 3 mm, and by the slit die with $H = 3$ mm at T = 100 °C are presented in Figure 6.11. It is observed that the values of the SCW λ obtained by the slit die with $H = 3$ mm and the section with $H = 3$ mm from the *slit-die-simple-profile* are overlapping. Further more the SCW λ obtained by the section with $H = 2$ mm from the *slit-die-simple-profile* has lower numerical values. This behavior is expected as the SCW λ is dependent on the characteristic dimension of the die, height H for the slit dies and diameter D for the capillary dies. The new proposed[48] simplified model based on Inn et al.,[26] for slit dies, Equation (4.40), is used to describe the experimental data in Figure 6.11. This model presents qualitative and quantitative agreement with the experimental data. Specifically the Equation (4.40) is fitting the experimental results obtained by the slit die with $H = 3$ mm and then predicting the experimental results which are obtained by the $H = 2$ mm from the *slit-die-simple-profile*. This prediction is using the stress ratio $Y_s/\sigma_x = 5.5$ obtained by Figure 6.8 (b) for the $H = 2$ mm and $\xi = 0.99\dot{\gamma}_{app.}^{-0.02}$ obtained by Figure 4.4 (a).
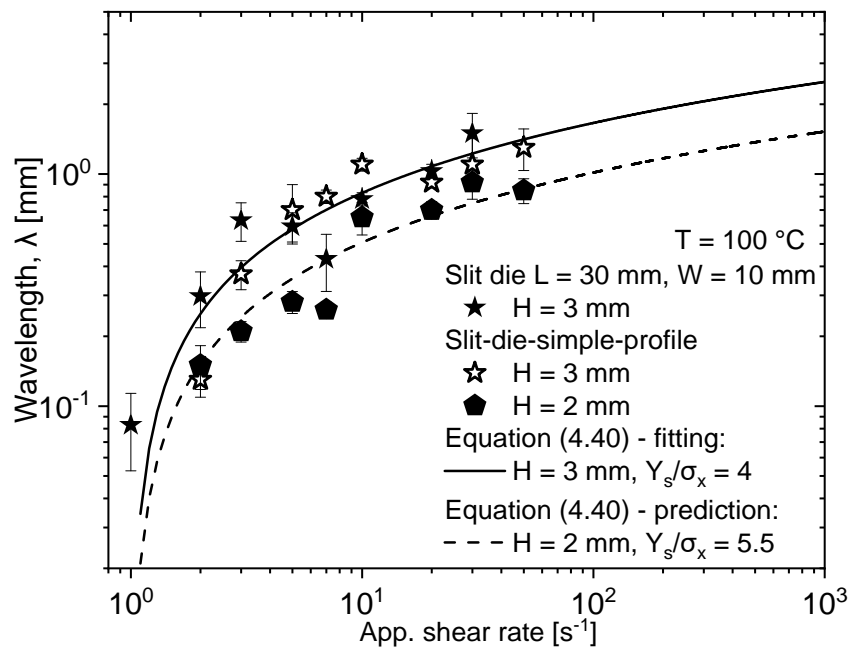
Figure 6.11. Spatial characteristic wavelength λ obtained by slit die with $H = 3$ mm (solid star symbol) and by *slit-die-simple-profile* (Figure 6.9 (a)) with $H = 3$ mm (open star symbol) and $H = 2$ mm (solid pentagon symbol). Adapted from C. K. Georgantopoulos et al., *Macromolecular Material and Engineering* submitted, **2022**, Figure 16.[48]

Figure 6.12 presents the *slit-die-scalar-profile*. In particular Figure 6.12 (a) presents the cross-section area of the die exit, Figure 6.12 (b) displays the flow channel where the last $L_{\text{profile}} = 3$ mm is the area where the profile is made and last in Figure 6.12 (c) an online image of the extrudate during the extrusion process of the studied PBD at T = 100 °C and $\dot{\gamma}_{app.}^{H=1.5\,mm} = 106.67\,s^{-1}$, $\dot{\gamma}_{app.}^{H=2\,mm} = 20\,s^{-1}$, and $\dot{\gamma}_{app.}^{H=3\,mm} = 26.7\,s^{-1}$ is displayed. The arrows show the flow direction of the polymer in different heights of the profile, specifically the blue arrows represent the flow at $H = 3$ mm, the red arrow at $H = 2$ mm and the green arrow at $H = 1.5$ mm. In Figure 6.12 (c) the main three different SCW λ can be visual identified.
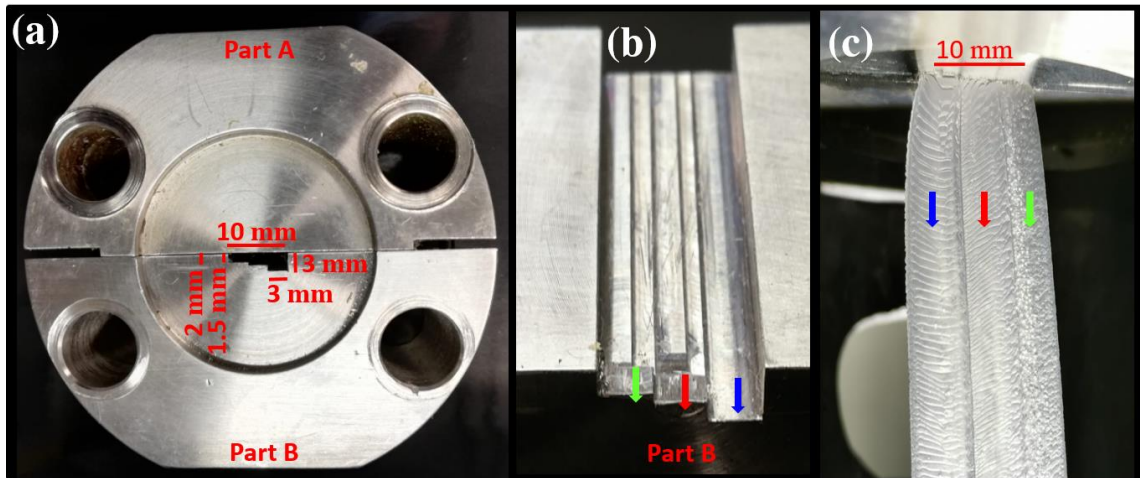
Figure 6.12. *Slit-die-scalar-profile*. (a) The cross-section area, (b) the flow channel part, where the profile is existing at the last $L_{\text{profile}} = 3$ mm of the die exit, and (c) visualization of the flow during extrusion of the investigated PBD at T = 100 °C and $\dot{\gamma}_{app.}^{H=1.5\,mm} = 106.67\,s^{-1}$, $\dot{\gamma}_{app.}^{H=2\,mm} = 20\,s^{-1}$, and $\dot{\gamma}_{app.}^{H=3\,mm} = 26.7\,s^{-1}$.

Figure 6.13 displays extrudates of the investigated PBD sample obtained by the *slit-die-scalar-profile* at T = 100 °C. The arrows identify the area of the extrudate which was extruded by $H = 1.5$ mm (green arrows), $H = 2$ mm (red arrows) and $H = 3$ mm (blue arrows). In Figure 6.13 it is easily mentioned that the SCW λ obtained by the $H = 3$ mm has larger numerical values than the SCW λ obtained by $H = 1.5$ mm.

Due to the cross-section profile of the *slit-die-scalar-profile*, see Figure 6.12 (a), different shear rates are calculated based on $\dot{\gamma}_{app.} = (6Q)/(WH^2)$ at on each section of the profile. In Table 6.3 the shear rates are listed.
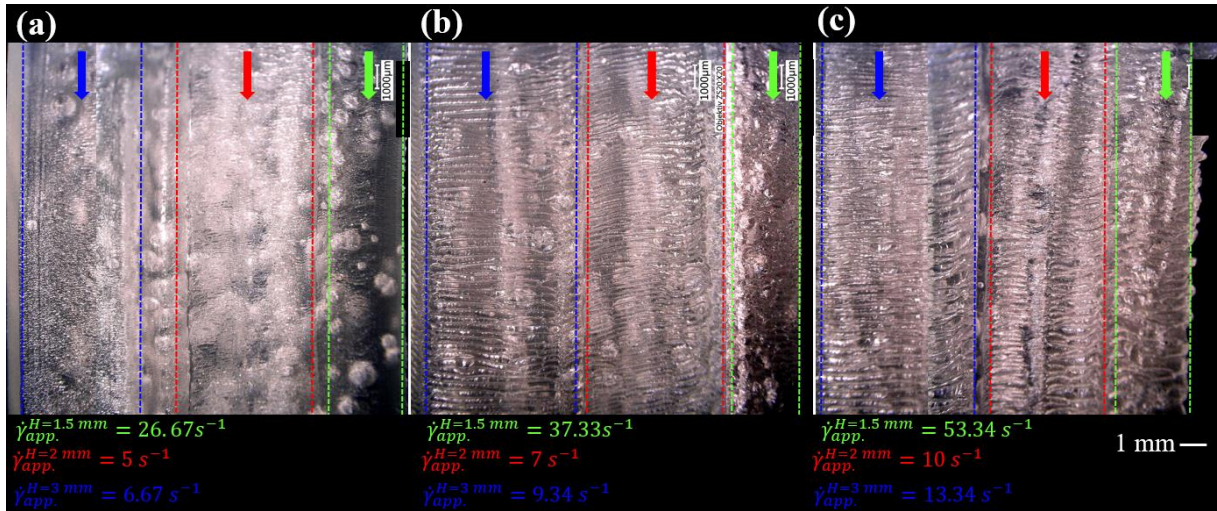
Figure 6.13. Images of the extruded PBD from *slit-die-scalar-profile* (Figure 6.12 (a)) at (a) $\dot{\gamma}_{app.}^{H=1.5\,mm} = 26.67\,s^{-1}$, $\dot{\gamma}_{app.}^{H=2\,mm} = 5\,s^{-1}$, and $\dot{\gamma}_{app.}^{H=3\,mm} = 6.67\,s^{-1}$, (b) $\dot{\gamma}_{app.}^{H=1.5\,mm} = 37.33\,s^{-1}$, $\dot{\gamma}_{app.}^{H=2\,mm} = 7\,s^{-1}$, and $\dot{\gamma}_{app.}^{H=3\,mm} = 9.34\,s^{-1}$, and (c) $\dot{\gamma}_{app.}^{H=1.5\,mm} = 53.34\,s^{-1}$, $\dot{\gamma}_{app.}^{H=2\,mm} = 10\,s^{-1}$, and $\dot{\gamma}_{app.}^{H=3\,mm} = 13.34\,s^{-1}$, at T = 100 °C. The arrows indicate the flow direction, the green arrow represent the flow at die section with $H = 1.5$ mm, the red arrow at $H = 2$ mm and the blue arrows at $H = 3$ mm. Adapted from C. K. Georgantopoulos et al., *Macromolecular Material and Engineering* submitted, **2022**, Figure 18.[48]

Table 6.3. Calculation of shear rate for the *slit-die-scalar-profile* with length $L = 30$ mm, width $W = 10$ mm, and height $H = 3$ mm and 2 mm and 1,5 mm. The Calculation of shear rate based on $\dot{\gamma}_{app.} = (6Q)/(WH^2)$, where Q is the volumetric flow rate in mm³·s⁻¹.

Q [mm³·s⁻¹]	$\dot{\gamma}_{app.}$ [s⁻¹] at $H = 2$ mm $W = 10$ mm	$\dot{\gamma}_{app.}$ [s⁻¹] at $H = 3$ mm $W = 3.33$ mm	$\dot{\gamma}_{app.}$ [s⁻¹] at $H = 1.5$ mm $W = 3.33$ mm
6.66	1	1.33	5.33
13.33	2	2.67	10.66
20	3	4.00	16.00
33.33	5	6.67	26.67
46.66	7	9.34	37.33
66.66	10	13.34	53.34
133.33	20	26.70	106.67

Adapted from C. K. Georgantopoulos et al., *Macromolecular Material and Engineering* submitted, **2022**, Table S4 in supplementary information.[48]

The numerical values of the SCW λ for the experiments conducted by the *slit-die-simple-profile* with $H = 2$ and 3 mm, the *slit-die-scalar-profile* with $H = 1.5$, 2 and 3 mm, and the slit die with $H = 3$ mm at T = 100 °C are presented in Figure 6.14. It is observed that the SCW λ obtained by the same height H of the extrudate die are overlapping.
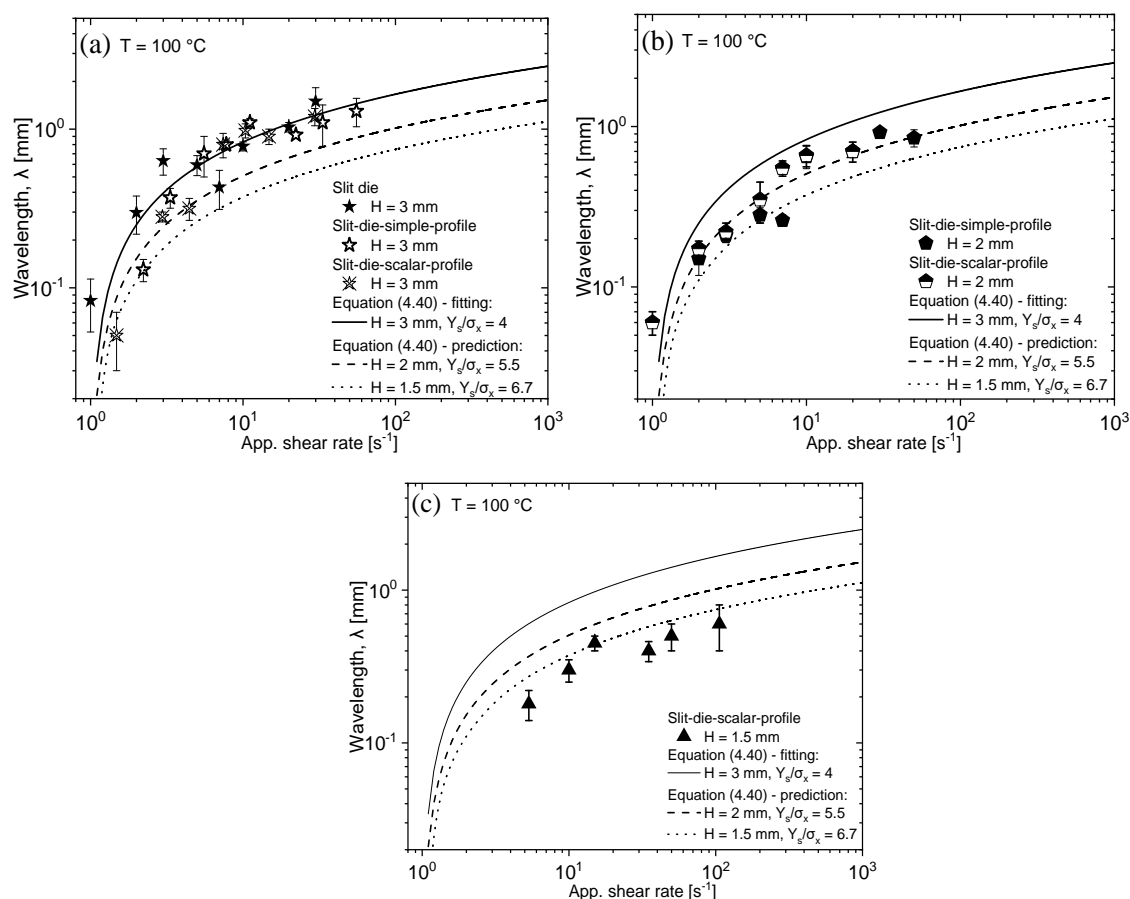
Figure 6.14. Spatial characteristic wavelength λ obtained (a) by slit die with $H = 3$ mm (solid star symbol), *slit-die-simple-profile* (Figure 6.9 (a)) with $H = 3$ mm (open star symbol) and *slit-die-scalar-profile* (Figure 6.12 (a)) with $H = 3$ mm (semi-open star symbol). (b) Wavelength obtained by *slit-die-simple-profile* with $H = 2$ mm (solid pentagon symbol) and *slit-die-scalar-profile* with $H = 2$ mm (semi-open pentagon symbol). (c) Wavelength obtained by *slit-die-scalar-profile* with $H = 1.5$ mm (solid triangle symbol). The solid lines are the fitting of Equation (4.40) to the experimental data obtained by the slit die with $H = 3$ mm. The dash and dot lines are predictions of Equation (4.40) for the $H = 2$ mm and $H = 1.5$ mm. The choice of the ratio of the stresses Y_s/σ_x for the $H = 2$ mm and $H = 1.5$ mm has been based on Figure 6.7 (b). The fitting and the predictions of Equation (4.40) includes to all the figures to emphasize the difference between the heights. Adapted from C. K. Georgantopoulos et al., *Macromolecular Material and Engineering* submitted, **2022**, Figure 20.[48]

Specifically, In Figure 6.14 (a) the SCW λ from the slit die with $H = 3$ mm, the *slit-die-simple-profile* section with $H = 3$ mm, and *slit-die-scalar-profile* section with H = 3 mm are merging to each other. Similar behavior is obtained for the SCW λ from $H = 2$ mm in Figure 6.14 (b). Finally, in Figure 6.14 (c) the numerical values of the SCW λ obtained by the *slit-die-scalar-profile* section with $H = 1.5$ mm are displayed.

The new proposed[48] simplified model based on Inn et al.,[26] for slit dies, Equation (4.40), is used to describe the experimental data in Figure 6.14. Specifically, Equation (4.40) is fitting the experimental results obtained by the slit die with $H = 3$ mm in Figure 6.14 (a). Then predicts the experimental results which are obtained by the $H = 1.2 = 5$ and 2 mm from the *slit-die-simple-profile* and *slit-die-simple-profile*. This prediction is using the stress ratio $Y_s/\sigma_x = 5.5$ for the $H = 2$ mm, and $Y_s/\sigma_x = 6.7$ for $H = 1.5$ mm obtained by Figure 6.8 (b) as well as $\xi = 0.99\dot{\gamma}_{app.}^{-0.02}$ obtained by Figure 4.4 (a). An agreement between the predictions and the experimental data is observed.

6.5. Prediction of the spatial characteristic wavelength λ from capillary to slit extrusion dies and vice versa

Predicting the spatial characteristics of extrusion flow instabilities from laboratory to industrial scale dies is a very important subject for the polymer processing industry. Typically, in research laboratories round capillary dies (circular cross-section area) are more common than slit dies (rectangular cross-section area). Hence the prediction of the spatial characteristics of extrusion instabilities from round capillary to rectangular slit dies is an imperative need. Within this study a proposed[15] geometrical correlation, Equation (4.14), is used and predicts the SCW λ of extrusion instabilities from round capillary to slit dies and vice versa.

Within this subchapter three different materials and several round capillary and slit dies are used in order to investigate the validity of the geometrical correlation, Equation (4.14). In Figure 6.15 the spatial characteristic wavelengths λ as a function of apparent shear rate at T = 120 °C of the SBR A ($M_w = 391$ kg mol^{-1}, $Đ = 1.36$) and SBR B ($M_w = 390$ kg mol^{-1}, $Đ = 1.35$) from chapter 3 are presented. The SCW λ is obtained from three round capillary dies with $D = 2$ mm and $L = 10, 20$ and 30 mm as well as a slit die with $H = 0.5$ mm, $W = 10$ mm and $L = 30$ mm. Assumption that the swelling factor remains the same for the same material while is extruded by different die geometries under the same conditions,[15,48] that is $(D'/D)^2 \approx [(W'H')/(HW)]$ and that the characteristic time periodicity τ^* is material dependent (see Figure 3.12),[15,48] the Equation (4.14) is used to predict the SCW λ of the samples SBR A and B obtained by the slit die. In Figure 6.15 (a) and (b) the SCW λ obtained by the capillary dies is

fitted by Equation (4.4) and then the Equation (4.14) is used to predict the SCW λ obtained by the slit die. The geometrical correlation, Equation (4.14), presents agreement between its predictions and the experimental data.
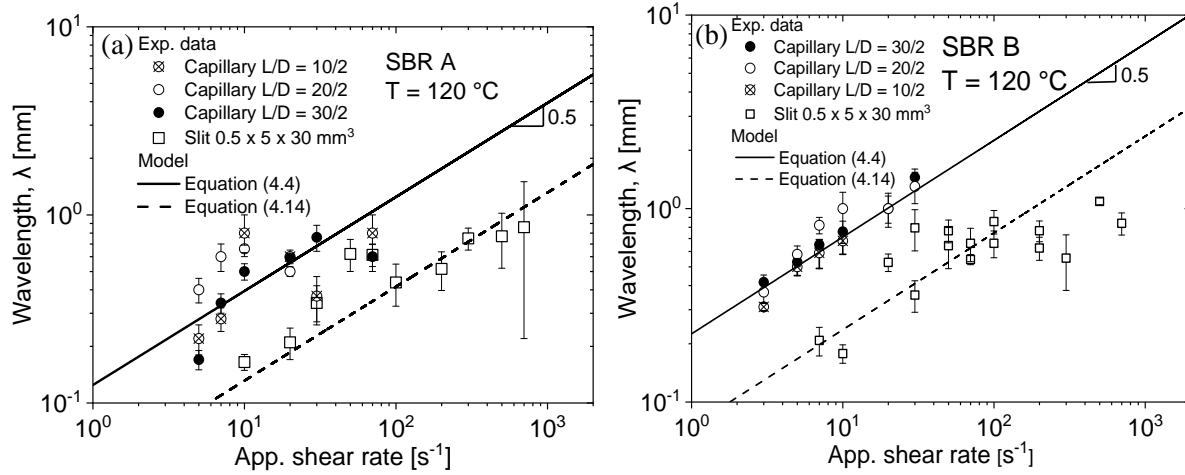
Figure 6.15. Spatial characteristic wavelength λ of the flow instability for (a) SBR A and (b) SBR B from chapter 3, see Figure 3.5 and 3.6. In (b) systematic deviation from the fitting function is observed at shear rates above $\dot{\gamma}_{app} > 100$ s^{-1}, this happens due to difficulties to measure the wavelength of the distortions in the slip part of the slit shaped extrudate, see Figure 3.9 (a). Adapted from C. K. Georgantopoulos et al., *Macromolecular Material and Engineering* 306, *2000801*, **2021**, Figure 18.[15]

Additional to the SBRs the investigated PBD (see Figure 6.1, $M_w = 375$ kg mol^{-1}, Đ = 3.5) is extruded by a round capillary die with $D = 2$ mm and $L = 30$ mm, and three slit dies with $H = 0.5$, 1 and 3 mm and $L = 30$ mm at T = 100 °C. The experimental data of the SCW λ of the instabilities from the PBD are presented in Figure 6.16. In Figure 6.16 (a) the SCW λ obtained by the round capillary die with $D = 2$ mm is fitted by Equation (4.4). The marked experimental results in Figure 6.16 (a), between 50 s^{-1} ≤ $\dot{\gamma}_{app.}$ ≤100 s^{-1}, are excluded from the fitting of the Equation (4.4). Those experimental data were obtained by the stick part of the stick-slip instability, see Figure 2.11. The Barone et al.[25] model, Equation (4.4), is developed based on visual observations of linear low density polyethylene (LLDPE, $M_w = 112$ kg mol^{-1}, Đ = 4.15) with pronounced sharkskin instability. Hence, only data associated to the sharkskin instability are fitted by Equation (4.4) in Figure 6.16 (a). In Figure 6.16 (b) the experimental data of the SCW λ obtained by the slit die with $H = 0.5$, 1 and 3 mm are in agreement with the predictions by Equation (4.14).
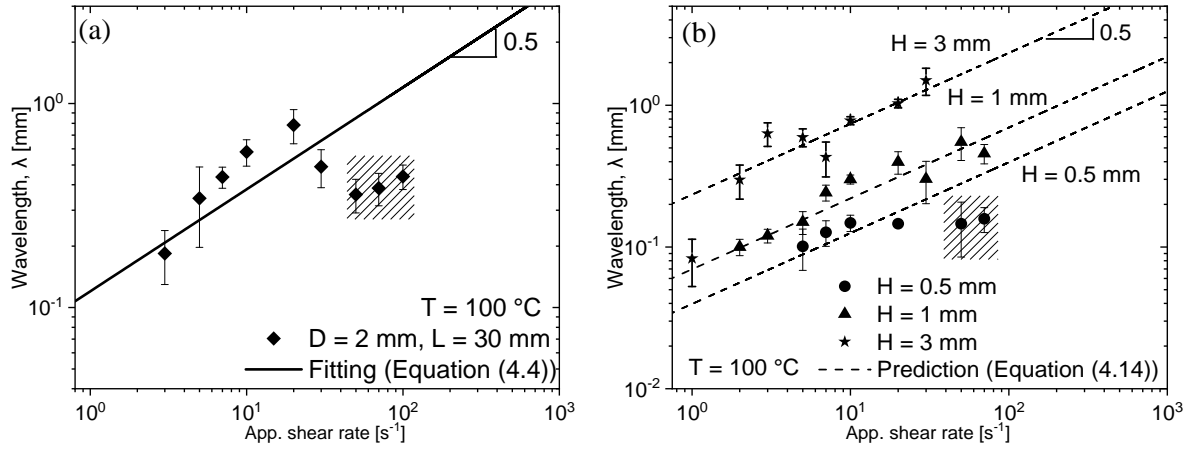
Figure 6.16. (a) Spatial characteristic wavelength λ obtained by capillary dies with $D = 2$ mm, $L = 30$ mm and fitted by the Barone et al.[25] model, Equation (4.4). (b) Spatial characteristic wavelength λ obtained by slit dies $H = 0.5$ mm, $H = 1$ mm, $H = 3$ mm, with $L = 30$ mm, and predicted by the proposed correlation, Equation (4.14). The marked experimental data are obtained by the stick part of the stick-slip instability. Adapted from C. K. Georgantopoulos et al., *Macromolecular Material and Engineering* submitted, **2022**, Figure 21.[48]

6.6. Correlation of spatial characteristic wavelength λ with extrusion temperature

One of the most important processing parameters for the polymer processing industry is the extrusion temperature. In order to investigate the influence of the extrusion temperature on the extrusion flow instabilities the SBR C ($M_w = 263$ kg mol^{-1}, Đ $= 1.67$) from chapter 5, is extruded by a round capillary die with $D = 2$ mm and $L = 30$ mm at T $= 80$ °C, 120 °C and 160 °C. Figure 6.17 presents the extrudates of the SBR C at T $= 80$ °C, 120 °C and 160 °C under the same apparent shear rate of $\dot{\gamma}_{app.} = 30$ s^{-1}. It is observed that as the temperature decreases the SCW λ increases. This observation initiated the investigation of the temperature-dependent behavior of the SCW λ. In Figure 6.18 (a) the SCW λ as a function of apparent shear rate over three different temperatures is presented. It is mentioned that the SCW λ presents smaller numerical values at higher shear rates as the extrusion temperature is increased. Similar shift factors a_T obtained by the linear master curve, see chapter 5 Figure 5.4 (a) and (b), using an Arrhenius form[68] $a_T = exp\left[(E_a/R)\left(1/T - 1/T_{ref.}\right)\right]$ are used to develop the master curve of the SCW λ at reference temperature of T $= 120$ °C, see Figure 6.18 (b). The a_T shift factors obtained by linear rheology (see chapter 5 Figure 5.4 (a) and (b)) can be successfully applied to the non-linear SCW λ. The SCW λ master curve is fitted by Equation (4.4) at T $= 120$ °C. Similar observation for the applicability of the TTS principal on the spatial characteristic of extrusion instabilities have been reported in literature.[23-28]
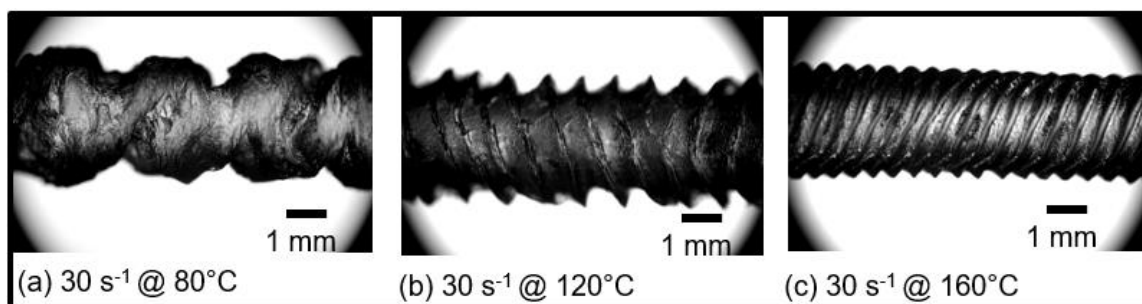
Figure 6.17. Images of extrudates of SBR C (M_w = 263 kg mol^{-1}, Đ = 1.67) at $\dot{\gamma}_{app.}$ = 30 s^{-1} at three different temperatures (a) T = 80 $^{\circ}$C, (b) T = 120 $^{\circ}$C and (c) T = 160 $^{\circ}$C from the *L/D* = 15 with *D* = 2 mm round capillary die. Adapted from C. K. Georgantopoulos et al., *Physics of Fluids* 33, *093108*, **2021**, Figure 15.[16] Reproduced with permission from AIP Publishing, No. 5231930652686.
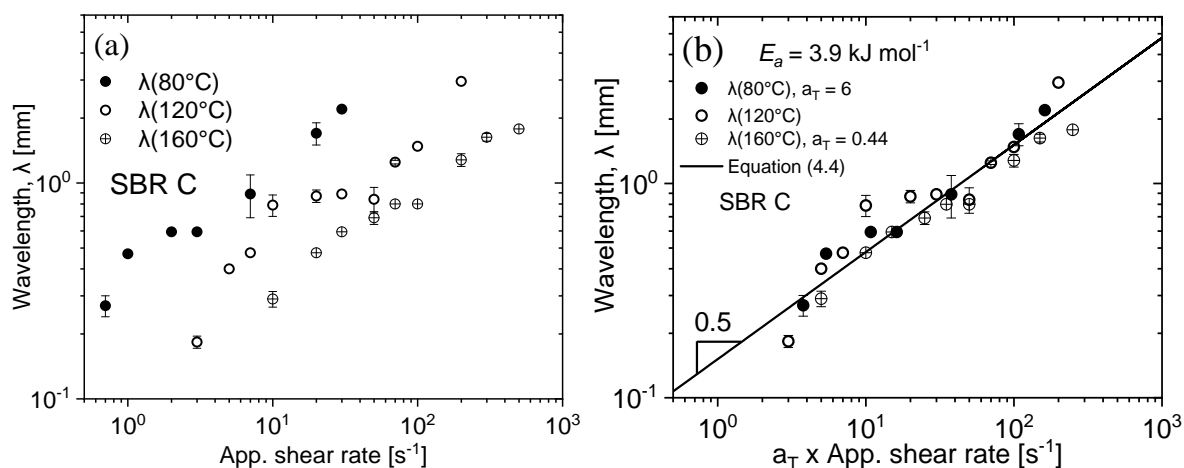
Figure 6.18. (a) The spatial characteristic wavelength λ profile at three different temperatures T = 80 $^{\circ}$C, 120 $^{\circ}$C and 160 $^{\circ}$C, obtained by the *L* = 30 mm with *D* = 2 mm. (b) Master curve of spatial characteristic wavelength developed by the a_T shift factors at reference temperature of T = 120 $^{\circ}$C. The a_T shift factors have been obtained by the linear master curve of the dynamic moduli (see Figure 7.4). The activation energy of the SBR C is estimated by the Arrhenius equation at E_a = 3.9 kJ mol^{-1}. Adapted from C. K. Georgantopoulos et al., *Physics of Fluids* 33, *093108*, **2021**, Figure 14.[16] Reproduced with permission from AIP Publishing, No. 5231930652686.

6.7. Conclusions

Within this chapter the previous reported qualitative models in chapter 4 used in order to develop correlations between processing parameters and extrusion behavior of rubbery materials. The correlations between the extrusion behavior of the neat polybutadiene (PBD) and neat styrene-butadiene rubbers (SBR) with their processing parameters such as the extrusion die geometry and temperature enable the following outcomes:

(i) The Inn et al.[26] model (Equation (4.39)) and the new proposed model[48] (Equation (4.40)) have agreement in a qualitative and quantitative level with the experimental data of SCW λ from the investigated PBD extruded by several round capillary, slit and complex slit die geometries.

(ii) The obtained by the models (Equation (4.39) and (4.40)) magnitude of the stress ratio Y_s/σ_x decreases as the characteristic dimension, height H for the slit dies and diameter D for the round capillary dies, of the extrusion die increases. Hence, low magnitude values of Y_s/σ_x implies large numerical values of SCW λ.

(iii) The geometrical correlation[15] (Equation (4.14)) is able to predict the SCW λ of extrusion flow instabilities occurred by different rubbery materials from round capillary to slit die geometries.

(iv) The increase of extrusion temperature postpone the appearance of extrusion flow instabilities at higher shear rates and decrease the numerical values of the SCW λ.

7. Extrusion Flow Instabilities of Filled Elastomers: Influence of Filler Volume Fraction, Die Geometry and Temperature

Within this chapter the extrusion behavior of a series of model silica filled rubber compounds is investigated as a function of filler fraction, extrusion die geometry and temperature. Discussion for the filler dispersion under small amplitude oscillatory shear (SAOS) deformation is presented. Quantification of the spatial characteristic wavelength (λ) of the extrusion flow instabilities and the modelling of them by the previous reported models in chapter 4 develops useful correlations with molecular properties. Quantification of the slippage in the slit die geometry presents beneficial correlations with the filler fraction as well. Hence, a mapping for the extrusion behavior of the model filled systems as a function of filler fraction is presented.

7.1. Material used in this chapter

The raw materials for the formulation of the investigated model compounds within this chapter are: (1) commercial styrene-butadiene rubber (SBR), (2) commercial silica (Ultrasil 7000 GR, Evonik Industries AG), (3) commercial silane (Si-69, Evonik Industries AG) and (4) commercial stearic acid (Evonik Industries AG). The SBR is already investigated by the chapter 3 which is named as SBR B. A brief reminder for the molecular properties of the SBR sample are listed on Table 7.1. This SBR has a bimodal molecular weight distribution (see Figure 3.1) with a weight average molecular weight of $M_w = 390$ kg·mol^{-1} and contains approximately 6 wt.% of low molecular hydrocarbons which are possibly processing agents.[15]

Table 7.1. Molecular weight characteristics of the investigated SBR polymer matrix.

Name	Elution volume [ml]	Weight percent [wt.%]	M_n [kg·mol^{-1}]	M_w [kg·mol^{-1}]	Đ [-]
SBR	35.0 – 50.0		287	390	1.35
[b]High - MW	35.0 – 37.5	26.0	610	650	1.05
[b]Medium - MW	37.5 – 50.0	68.0	252	256	1.01
[a]Low - MW	60.0 – 63.0	6.0	0.42	0.60	1.42

[a]The weight percent is calculated from the 2D SEC-NMR data presented in Figure 6 at Georgantopoulos et al., Macromolecular Material and Engineering 306, 2000801, 2021.[15] [b]The weight percent is calculated by the DRI detector, insert of Figure 3.1. Adapted from C. K. Georgantopoulos et al., *Macromolecular Material and Engineering* 306, *2000801*, **2021**, Table 1.[15] This material is referred in Table 3.1 as SBR B.

The properties of the investigated silica (Ultrasil 7000 GR, Evonik Industries AG) are presented in Table 7.2. The particle size distribution (PSD) of the silica is obtained by strong ultrasonic treatment and it is presented in Figure 7.1 (a).[69] The average silica diameter of a cluster is ~ 0.1 μm, although bigger agglomerated particles are also observed with a rough diameter bigger than ~ 0.3 μm. Figure 7.1 (b) displays a scanning electron microscopy (SEM) image of the investigated silica where the spherical shape of it can be designated.

Table 7.2. Properties of the silica Ultrasil 7000 GR.

Name	SSA: CTAB [m^2·g^{-1}]	SSA: BET (MP) [m^2·g^{-1}]	Loss on drying [%]	pH [-]
Ultrasil 7000 GR	160	175	5.5	6.5

Adapted from the scientific presentation of J. Kiesewetter and A. Wehmeier.[69]

The formulations of the model compounds are listed in Table 7.3. To develop the formulation of the model systems, a typical compounding process is performed in a 1.8 liter internal mixer at chamber temperature of 50 °C and the rotor speed of 70 rpm. The dumping temperature is 150 °C and the duration of mixing is 5 to 6 min, depending on the filler amount. Silica and 90 % of the silane amount are added after an initial rubber mastication of 20 s. Then, after 90 s of mixing, the remaining 10 % of silica and stearic acid are added. The final compounds are then homogenized in a two-roll open mill at 50 °C.

The variable in the formulation is the silica amount which increases from 10 phr up to 70 phr. The ratio of the silica to coupling agent (silane) and lubricant (stearic acid) remains constant. Hence, the impact of the silica volume fraction can be investigated. Silane serves two main

purposes in the compound: (i) disperses the silica nanoparticles avoiding their agglomeration and (ii) increases the efficiency of curing in the last step of the tire process.[70-72]
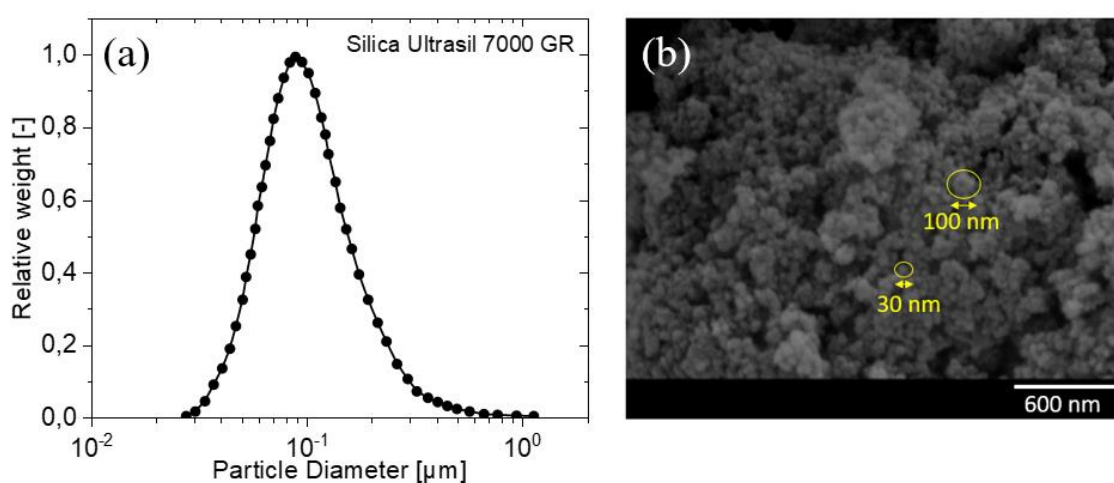
Figure 7.1. (a) Particle size distribution of the silica Ultrasil 7000 GR after strong ultrasonic treatment. Adapted from the scientific presentation of J. Kiesewetter and A. Wehmeier from Evonik Industries 2018 which is available online.[69] (b) Scanning electron microscopy (SEM) image for the silica Ultrasil 7000 GR.

Table 7.3. Formulations of the model compounds based on filler volume.

Name	a)Silica (Si) [phr]	b)Silane (S) [phr]	c)Stearic acid (SA) [phr]	Volume fraction of silica, φ [-]	d)T_g [°C]
Si10 S0.77 SA0.2	10	0.77	0.2	0.044	-60.9
Si20 S1.44 SA0.4	20	1.44	0.4	0.084	-60.3
Si30 S2.16 SA0.6	30	2.16	0.6	0.120	-60.5
Si40 S2.88 SA0.8	40	2.88	0.8	0.155	-60.7
Si50 S3.60 SA1.0	50	3.60	1.0	0.182	-60.5
Si60 S4.30 SA1.2	60	4.30	1.2	0.210	-60.5
Si70 S5.10 SA1.4	70	5.10	1.4	0.235	-60.6
SBR					-60.7

aUltrasil 7000 GR, Evonik Industries AG. bSi-69, Evonik Industries AG, cEvonik Industries AG. dThe heating/cooling rate was 5 K min-1 with a temperature range of -90 °C and 160 °C. The second heating run was analyzed.

Differential scanning calorimetry (DSC) investigates the T_g of the model compounds as well. The T_g is not influenced by the filler volume fraction of this specific silica, see Table 7.3.[73]

7.2. Experimental procedure

Small amplitude oscillatory shear (SAOS) experiments were performed with a rubber process analyzer (RPA), TA Instruments, close cavity rheometer. This rheometer has a 40 mm diameter grooved geometry in order to minimize the slippage between the material and the geometry. The SAOS experiments were done at T = 100 °C within angular frequency of $\omega = 0.6$ rad·s^{-1} and 300 rad·s^{-1}. The Maxwell model[42] is used to fit the magnitude complex viscosity, storage and loss moduli are with 5-element Maxwell modes.

The slippage and the extrusion flow instabilities are studied via capillary rheology. A capillary rheometer Göttfert RG 50 equipped with a capillary die, diameter $D = 2$ mm and length $L = 30$ mm, and a slit die with width $W = 5$ mm, height $H = 0.5$ mm and length $L = 30$ mm is used. Each investigated sample remained in the barrel of the capillary rheometers at T = 100 °C for 10 min to ensure uniform isothermal condition in the whole sample.

The extrudates are collected, and then optically investigated at room temperature. The optical investigation is conducted by a Keyence VHX 900F (Osaka, Japan) incident light microscope which is equipped with two zoom lenses and magnification range between 20 and 2000.

7.3. Qualitative models for the influence of the filler volume fraction

The dynamic rheological behavior of concentrated suspension systems was investigated by Krieger and Dougherty.[74] They proposed the generic Equation (7.1) to estimate the viscoelastic properties of the concentrated suspensions, which are influenced by the filler volume, assuming that the filler particles are monodispersed hard spheres.

$$G^*(\omega, \varphi) = G_m^*(\omega)f(\varphi) \tag{7.1}$$

Where $f(\varphi)$ is the function which describes the influence of the volume fraction and G_m^* is the magnitude of complex modulus of the polymer matrix. Several theoretical and empirical function $f(\varphi)$ are reported in literature.[75] The base of most of these functions is the Einstein formula, $f(\varphi) = 1 + 2.5\varphi$,[75] where extra terms that further describe the interaction of the particles in a continuous material are added. One of those extended Einstein formulas is the Guth-Gold equation,[76] given by Equation (7.2):

$$f(\varphi) = 1 + 2.5k\varphi + 14.1(k\varphi)^2, \tag{7.2}$$

where k is fitting parameter and the extra term of φ^2 is describing the interaction between two particles. Although, Guth-Gold equation is reported in literature that it fails to describe high

volume fractions of filler. A further formula which is widely used to describe high volume fractions of filler is Maron-Pierce,[77] given by Equation (7.3):

$$f(\varphi) = \left(1 - \frac{\varphi}{\varphi_m}\right)^{-2},$$ (7.3)

where φ is the volume fraction of filler, and φ_m is the maximum packing arrangement,[75] that is the arrangement of the particles while they are placed in a continuous material, like a polymer matrix. In this study both Guth-Gold[76] and Maron-Pierce[77] are used and compared.

7.4. Qualitative models for the wall slippage

According to S. G. Hatzikiriakos,[3,4] Equation (7.4) and (7.5) can be used to estimate the slip velocity of a polymer melt while it flows through a slit and round capillary die geometry, respectively.

$$V_s^{Slit} = \frac{H}{6}\left(\dot{\gamma}_{app} - \frac{3n}{2n+1}\left[\frac{\sigma_{wall}}{K}\right]^{\frac{1}{n}}\right)$$ (7.4)

$$V_s^{Capillary} = \frac{D}{8}\left(\dot{\gamma}_{app} - \frac{4n}{3n+1}\left[\frac{\sigma_{wall}}{K}\right]^{\frac{1}{n}}\right)$$ (7.5)

Where K and n values are obtained by the fitting of the flow curve, wall shear stress σ_{wall} as a function of apparent shear rate $\dot{\gamma}_{app}$, with a power law function $\sigma_{wall} = K\dot{\gamma}_{app}^n$.[3,4] The wall shear stress σ_{wall} can be obtained: (i) by using three or more round capillary dies, keeping constant the diameter D and change the length L of them, so that the Bagley[3,4] correction can be applied, or (ii) by the use of a slit or capillary die where the L/D, L/H ratio is equal or larger than sixty (60).[41] Experimental data obtained differently is the apparent shear rate $\sigma_{app.}$ and is affected by the die exit pressure influence.

The Rabinowitsch-Weissenberg[3,4] correction can be used to obtain the wall shear rate $\dot{\gamma}_{wall}$, by the Equation (7.6), knowing the n value from the fitting of the $\sigma_{wall} = K\dot{\gamma}_{app}^n$ to the flow curve, σ_{wall} versus $\dot{\gamma}_{app.}$.

$$\dot{\gamma}_{wall} = \left(\frac{2n+1}{3n}\right)\dot{\gamma}_{app.}$$ (7.6)

Typically for a non-Newtonian fluid like a polymeric melt the n, is between $0 < n < 1$.[3,4] Hence, the numerical values of the wall shear rate $\dot{\gamma}_{wall}$ are larger than the apparent shear rate $\dot{\gamma}_{app.}$, $\dot{\gamma}_{wall} > \dot{\gamma}_{app.}$.

7.5. Model for spatial characteristic wavelength λ of the extrusion flow instabilities for the slit and capillary die geometry

The spatial characteristic wavelength (SCW) λ of the extrusion flow instabilities is defined as the average distance between two consecutive similar distortions, see Figure 7.2.[15,16] This definition can be applied to extrudates obtained by slit and round capillary die geometries. Moreover, the SCW λ is obtained on the surface of the extrudate where a well-developed pattern is formatted. Hence, the SCW λ can be obtained by the sharkskin-melt fracture instability and by the stick part of the stick-slip instability as Figure 3 (b) is presented, see also Figure 2.11, 3.6 and 3.9 (a).[15,16]
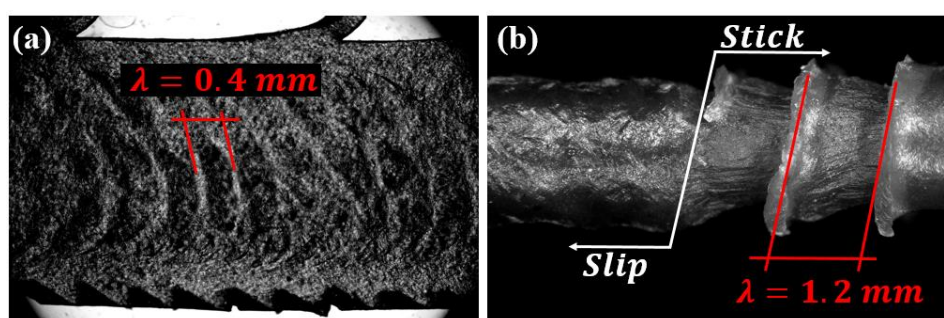
Figure 7.2. Visual observation of the extrudates from Si40S2.88SA0.8 (Table 7.3) compound obtained by the (a) slit die with $L = 30$ mm and $H = 0.5$ mm and (b) round capillary die with $L = 30$ mm and $D = 2$ mm. The sample was investigated at T = 100 °C and $\dot{\gamma}_{app.} = 10$ s^{-1} for both dies. The spatial characteristic wavelength λ is visualized at (a) for sharkskin type instability, $\lambda = 0.4$ mm and (b) at the stick part of the stick-slip instability, $\lambda = 1.2$ mm.

Within this chapter, the qualitative models from Inn et al.,[26] (Equation (4.39)) and Georgantopoulos et al.,[48] (Equation (4.40)) are used to fit the experimental data of the SCW λ obtained by round capillary and slit extrusion die geometries. Furthermore, the proposed[15,48] geometrical correlation (Equation (4.14)) is used to predict the SCW λ of the filled model compounds (Table 7.3) from round capillary to slit dies and vice versa.

7.6. Rheological characterization: linear and non-linear regime

Figure 7.3 shows the shear storage moduli, loss moduli and the magnitude of complex viscosity as a function of angular frequency for the investigated samples at T = 100 °C. In Figure 7.3 it is observed that as the filler volume fraction is increased the magnitude values of the storage moduli, loss moduli and the magnitude of the complex viscosity increases. The investigated materials become more elastic and more viscous as the silica volume fraction is increased.
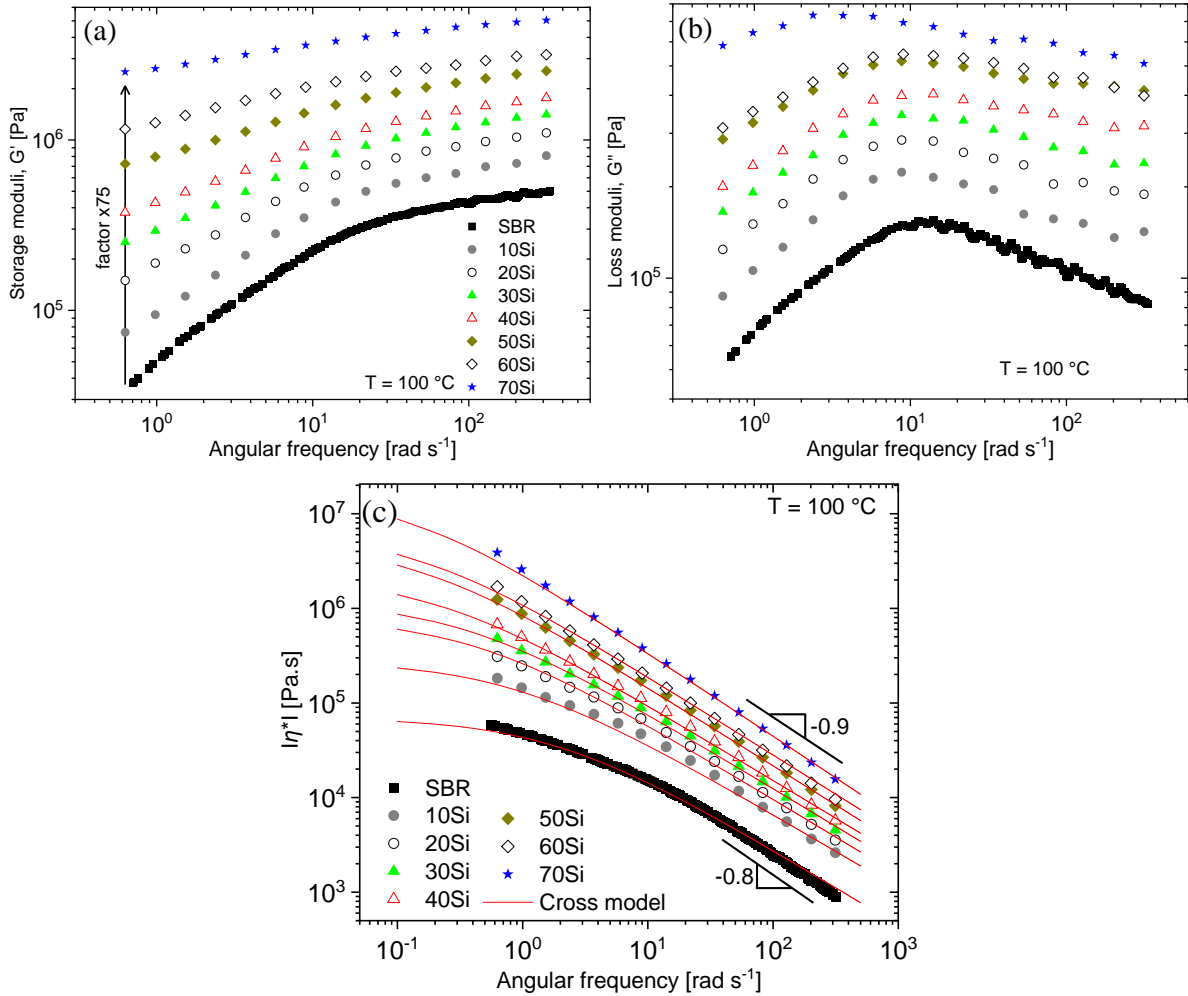
Figure 7.3. (a) Storage G' moduli, (b) loss G'' moduli and (c) magnitude of complex viscosity $|\eta^*|$ of the investigated samples as a function of angular frequency at T = 100 °C and $\gamma_0 = 0.3\%$. The (c) magnitude of complex viscosity $|\eta^*(\omega)|$ is fitted by the Cross model where the fitting parameters are listed in Table 7.4.

In Figure 7.3 (a) a typical behavior for the storage moduli at low angular frequencies ($\omega < 20$ rad·s^{-1}) is observed for filled systems.[78-87] As the amount of silica volume fraction increases the storage modulus deviates from the typical behavior of the polymer melts at the terminal flow regime, where $G' \sim \omega^2$.[42] As the silica volume fraction is increased, a plateau like behavior is observed at the low frequency regime ($\omega < 20$ rad·s^{-1}). This plateau like behavior is associated with the formation of a filler network, which is not influenced by this flow field ($\omega < 20$ rad·s^{-1}).[78-87] Similar behavior is observed for the loss modulus as well, Figure 7.3 (b). In Figure 7.3 (c) the magnitude of complex viscosity as a function of the angular frequency is observed at T = 100 °C. For the neat SBR, Si10 S0.77 SA0.2, and Si20 S1.44 SA0.4 a typical behavior for the magnitude of complex viscosity is shown the tendency to reach the zero shear

113

viscosity at low angular frequencies and a power law behavior at high angular frequency range.[42] For the rest of the samples, only a power law behavior is observed. The magnitude of complex viscosity is fitted by the Cross model,[42] $\eta(\dot{\gamma}) = \eta_0/(1 + (\tau\dot{\gamma})^m)$, and the fitting parameters are listed on Table 7.4. The Cross model[42] is used because it has the characteristic relaxation time as fitting parameter and after the fitting to the experimental data it can be obtained. The investigated compounds, except the neat SBR, do not present any crossover point of the G' and G'', hence the relaxation time can not be obtained directly by the inverse of the crossover.[83]

Table 7.4. Fitting parameters of the Cross model,[42] obtained by the fitting to the magnitude of complex viscosity in Figure 7.3 (c) at T = 100 °C.

Name	Cross model parameters		
	m	τ [s]	η_0 [kPa·s]
SBR	0.80	0.55	70
Si10 S0.77 SA0.2	0.78	1.20	280
Si20 S1.44 SA0.4	0.80	1.50	700
Si30 S2.16 SA0.6	0.80	2.00	1200
Si40 S2.88 SA0.8	0.80	3.00	2200
Si50 S3.60 SA1.0	0.83	3.50	5000
Si60 S4.30 SA1.2	0.83	6.00	6500
Si70 S5.10 SA1.4	0.88	8.50	16000

The influence of the filler load on the polymer matrix is presented in Figure 7.4. Figure 7.4 (a) presents the numerical value of storage moduli for the filled rubber compounds $G'(\varphi)$ obtained at $\omega = 0.63$ rad·s^{-1} normalized by the numerical value of the storage moduli for the neat SBR sample $G'(0)$ at $\omega = 0.63$ rad·s^{-1}. In Figure 7.4 (b) the characteristic relaxation time $\tau(\varphi)$ obtained by the Cross model,[42] see Table 7.4, normalized by the relaxation time $\tau(0)$ of the neat SBR is presented. The proposed models by Guth-Gold,[76] Equation (7.2), and Maron-Pierce,[77] Equation (7.3), are used to fit the experimental data. Observing the behavior of the experimental data in Figure 7.4 an exponential increase is observed after $\varphi > 0.17$. Hassanabadi et al.,[88] investigated the rheological behavior of ethylene-vinyl-acetate (EVA) filled with carbon nanotubes and clay with volume fraction up to $\varphi = 0.14$. The authors[88] similarly plotted the numerical values of the storage modulus in the lowest angular frequency that they measured it as a function of filler volume fraction. Hassanabadi et al.,[88] mention that the numerical value

of the volume fraction, where the plot exhibit the exponential increase, is representing the percolation threshold of the specific filler. Percolation threshold $\varphi_{perc.}$ is defined as the critical filler volume fraction, above which the filler particles generate a continuous network.[89] By using the approximation of Hassanabadi et al.,[88] and the models of and Guth-Gold,[76] Equation (7.2), and Maron-Pierce,[77] Equation (7.3), the percolation threshold of the investigated silica is estimated to about $\varphi_{perc.} \approx 0.17$. At this specific volume fraction and above the Guth-Gold,[76] Equation (7.2), is not able to fit the experimental data any more.
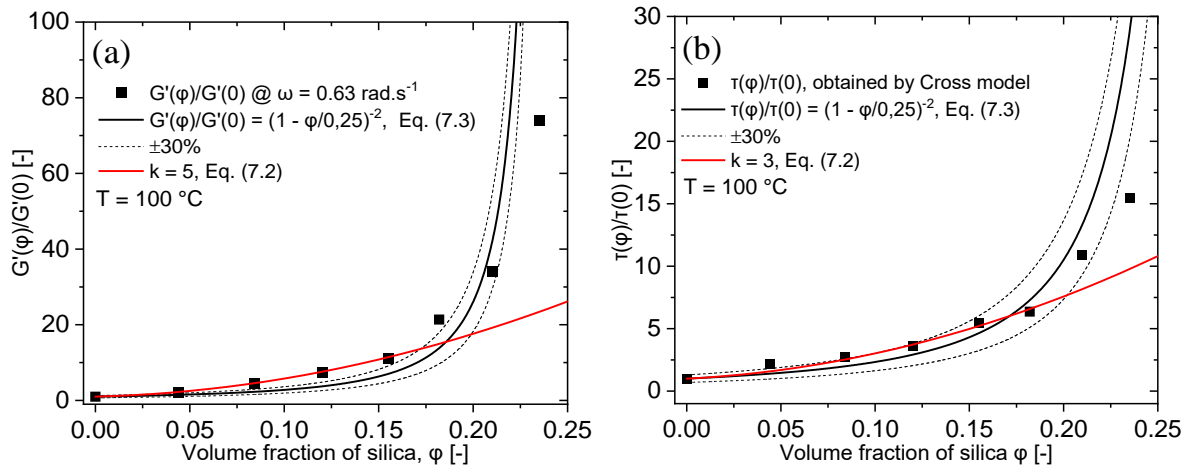
Figure 7.4. (a) Normalized storage $G'(\varphi)$ moduli of the rubber compounds by the storage $G'(0)$ moduli of the neat SBR polymer matrix, obtained by the angular frequency $\omega = 0.63$ rad·s^{-1} at T = 100 °C. (b) Normalized relaxation time $\tau(\varphi)$ of the rubber compounds by the relaxation time of the neat SBR polymer matrix $\tau(0)$ at T = 100 °C. Both experimental data are fitted with the Guth-Gold,[76] Equation (7.2), and Maron-Pierce,[77] Equation (7.3).

Mongruel and Cartault[87] rheologically investigated SBR sample filled with carbon black and the same silica grade as within this study, silica Ultrasil 7000 GR. Mongruel and Cartault[87] similarly plotted the normalized numerical values of the storage modulus of the filled systems by the neat SBR sample, see Figure 7.4 (a). They used the same models (Guth-Gold and Maron-Pierce),[76,77] as in this chapter, for fitting the experimental data. Similarly to this study the Guth-Gold[76] fails to fit the experimental result after the $\varphi > 0.17$, where the Maron-Pierce[77] present a qualitative agreement with the experimental results in the whole volume fraction range. In addition, Mongruel and Cartault[87] estimated the percolation threshold of the silica about $\varphi_{perc.} \approx 0.16$ that is similar to percolation threshold obtained by Figure 7.4 (a). In Figure 7.4 (b) the behavior of the experimental data corresponds qualitatively with the Figure 7.4 (a), that is the exponential increases of the normalized relaxation time begins at $\varphi > 0.17$. The Maron-

Pierce[77] model, Equation (7.3), uses the same fitting parameter, that is the maximum packing arrangement φ_m, to fit both sets of experimental data. The maximum packing arrangement for the investigated silica is found about $\varphi_m = 0.25$.

The effect of filler load on the polymer matrix is the increases of elastic modulus, and viscous behavior. In addition, deviation of the storage modulus from the typical behavior of the polymer melts at the terminal flow regime, where $G' \sim \omega^2$, is observed.[42,78-87] This deviation is associated with the formation of filler network. The question which occurs is how this filler network behaves under the whole range of shear flow field, from $\omega = 0.6$ rad·s^{-1} up to 300 rad·s^{-1}. Two approximations in order to understand the behavior of the filler network under shear flow field are discussed. Firstly, the storage modulus $G'(\varphi)$ of all the investigated compounds is presented in Figure 7.5 (a) at T = 100 °C. The neat SBR sample is fitted by a 6-element Maxwell model, see Appendix C. Then, Equation (7.1) uses Maron-Pierce,[77] Equation (7.3), with the maximum packing arrangement to be $\varphi_m = 0.25$, and predict the storage modulus for the filled systems. Equation (7.1), becomes $G'(\varphi) = G'(0)(1 - \varphi/0.25)^{-2}$.
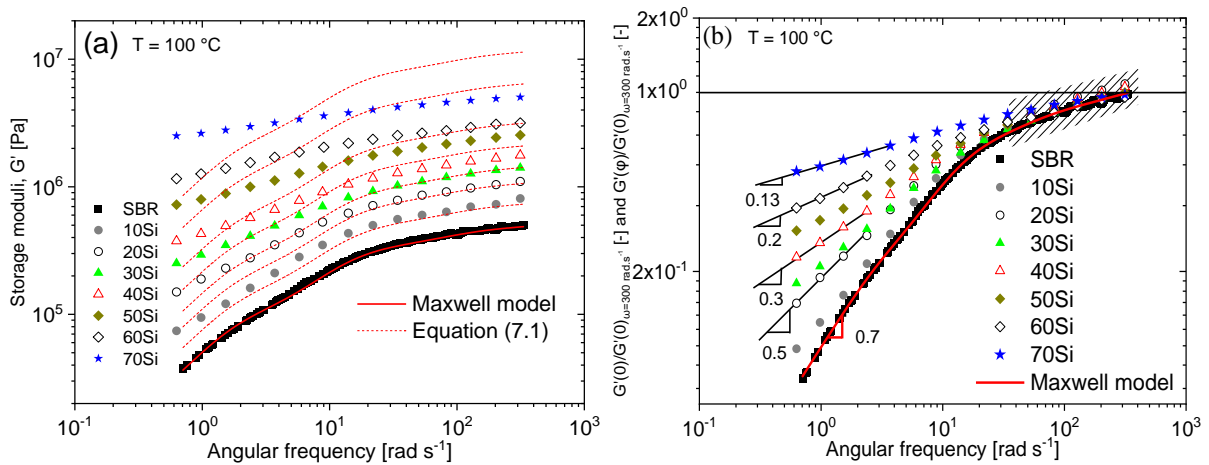
Figure 7.5. (a) Storage G' moduli of the investigated samples. The SBR polymer is fitted by the Maxwell model (5.1) and the rubber compounds are fitted by the Equation (7.1). (b) Storage $G'(0)$ moduli of the SBR polymer matrix and normalized storage $G'(\varphi)$ moduli of the rubber compounds by the $G'(0)$ of the polymer matrix at $\omega = 300$ rad·s^{-1}.

In Figure 7.5 (a) the predictions of Equation (7.2) with red dash lines are presented. For the rubber compound with 10 phr of silica agreement between the experimental data and the prediction is observed. For the rubber compounds between 20 phr and 50 phr of silica the predictions of the Maxwell predictions agree with the experimental data only at angular frequency region $\omega > 20$ rad·s^{-1}. For the compounds with 60 phr and 70 phr of silica the

Maxwell predictions fail to describe the experimental data. The Maxwell model[42] (Equation (5.1)) was developed to describe the flow behavior of polymer melts, although within this chapter, the influence of filler volume fraction is taken into account. The influence of the filler volume fraction increases the modulus according to Maron-Pierce,[77] Equation (7.3). Hence, the agreement of Maxwell predictions with the rubber compounds, 20 to 50 phr of silica, at the angular frequency region $\omega > 20$ rad·s^{-1} describe only the influence of polymer matrix and fails to capture the influence of filler network formation which is observed at low angular frequencies, $\omega < 20$ rad·s^{-1}. Based on this observation, it is concluded that in fast shear flows, $\omega > 20$ rad·s^{-1}, for rubber compounds filled with silica up to 50 phr the polymer matrix is the dominant factor. The failure of the Maxwell predictions for the compounds with 60 phr and 70 phr of silica possibly occurred because the Maron-Pierce,[77] Equation (7.3), does not fit well the experimental data in Figure 7.4 (a) after $\varphi > 0.22$.

The second approximation to investigate how the filler network behaves under the whole range of shear flow was suggested by Mongruel and Cartault.[87] The suggested approximation is presented in Figure 7.5 (b), where the storage modulus $G'(0)$ of the neat SBR is normalized by the storage modulus of the neat SBR at $\omega = 300$ rad·s^{-1}, $G'(0)_{\omega\,=\,300\,\text{rad s}^{-1}}$, then the storage modulus $G'(\varphi)$ of the rubber compounds is also normalized by the $G'(0)_{\omega\,=\,300\,\text{rad s}^{-1}}$. Hence, the storage modulus of the investigated samples overlap at high frequency of $\omega = 300$ rad·s^{-1} and have a normalized value of one. This representation of the data depicts better the influence of the filler network formation at low frequencies, $\omega < 20$ rad·s^{-1}, and the influence of polymer matrix at high frequencies, $\omega > 20$ rad·s^{-1}, where all the curves overlapped.

Based on the two previous reported approximations[87,88] it is concluded that the filler network formation has dominant influence at low shear flow field and the polymer matrix dictates on the flow at high shear flow fields. This is based on the investigated model compounds with maximum silica volume fraction of $\varphi = 0.235$.

In order to investigate the non-linear rheology, capillary rheology experiments using a capillary round die with diameter $D = 2$ mm, length $L = 30$ mm and a slit die with height $H = 0.5$ mm, width $W = 5$ mm and length $L = 30$ mm are performed. Hence, the steady shear viscosity and slip velocities of the investigated compounds are obtained. It is known[3,4] that the raw data obtained by capillary rheology need the Bagley[3,4] and then Rabinowitsch-Weissenberg[3,4] correction to obtain the wall shear stress σ_{wall} and the wall shear rate $\dot{\gamma}_{wall}$. In Figure 7.6 the apparent and the corrected steady state viscosities of the investigated compounds are presented.
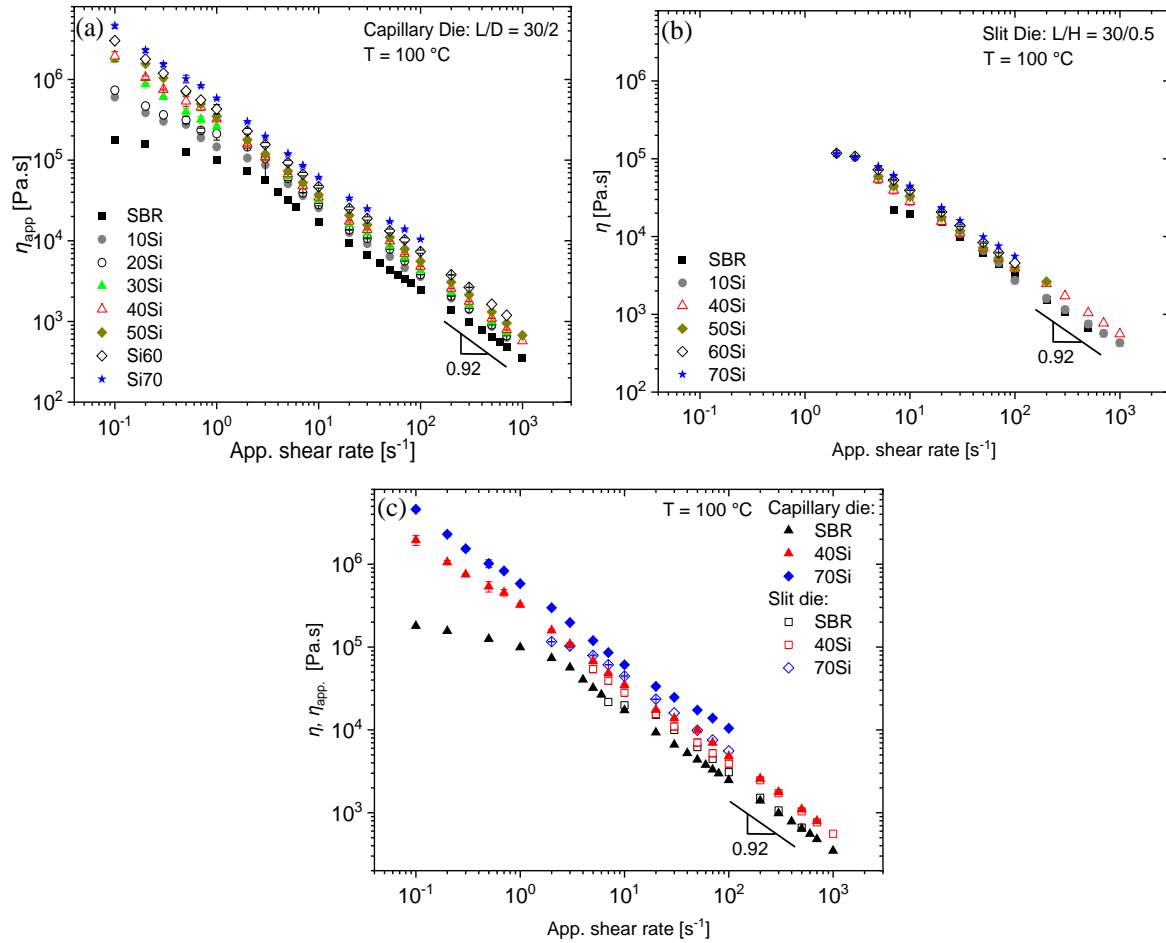
Figure 7.6. (a) Apparent steady state viscosity $\eta_{app.}$ as a function of apparent shear rate obtained from capillary die with $D = 2$ mm and $L = 30$ mm. (b) Steady state viscosity η as a function of apparent shear rate obtained from slit die with $H = 0.5$ mm, $W = 5$ mm and $L = 30$ mm. (c) Comparison of apparent steady state viscosity $\eta_{app.}$ and steady state viscosity η as a function of apparent shear rate between capillary and slit dies. An overlap between the $\eta_{app.}$ and η is observed up to $\varphi = 0.155$ (40 phr) of silica. The experiments carried out at T = 100 °C.

In Figure 7.6 (a) the apparent steady state viscosity $\eta_{app.}$ as a function of apparent shear rate $\dot{\gamma}_{app.}$ obtained from the capillary die with $D = 2$ mm and $L = 30$ mm at T = 100 °C is presented. In Figure 7.6 (b) the steady state viscosity η as a function of apparent shear rate $\dot{\gamma}_{app.}$ obtained from the slit die with $H = 0.5$ mm, $W = 5$ mm and $L = 30$ mm at T = 100 °C is presented. The direct derivation of the steady state viscosity η is based on the aspect ratio $L/H = 60$[41] of the slit die which allows to neglect the die exit pressure influence, therefore no Bagley[3,4] correction is required. A comparison between the η and $\eta_{app.}$ as a function of apparent shear rate $\dot{\gamma}_{app.}$ is presented on Figure 7.6 (c). It is observed that the η and $\eta_{app.}$ are different and the

deviation between them increases as the sample becomes more elastic, that is the filler volume fraction is increased.

7.7. Influence of filler volume fraction on wall slippage

To investigate the slip velocity V_s of the investigated compounds, the experimental data obtained from the slit die ($L/H = 60$) is used, since the steady state viscosity η (or wall shear stress σ_{wall}) is directly acquired. In Figure 7.7 (a) the wall shear stress σ_{wall} as a function of apparent shear rate $\dot{\gamma}_{app.}$ obtained from the slit die ($L/H = 60$) is presented. The σ_{wall} increases as the silica volume fraction increases. Fitting the experimental results of the wall shear stress σ_{wall} with the suggested[3,4] power law function $\sigma_{wall} = K\dot{\gamma}_{app.}^n$ the K and n parameters are obtained. The K and n parameters found at T = 100 °C are listed in Table 7.5. Using Equation (7.4) and the listed K and n values from the Table 7.5, the slip velocity V_s is obtained and presented in Figure 7.7 (b). It is observed that for the same magnitude of slip velocity higher wall shear stress values are required for the highly filled compounds rather than the neat SBR. To simplify, at the same magnitude value of wall shear stress the numerical value of the slip velocity is higher for the neat SBR polymer and lower for the highly filled rubber compound with 70 phr of silica. Similar behavior is observed in the literature for numerous concentrated suspensions with different fillers such as kaolinite,[90] sodium alginate and hydroxypropyl methylcellulose (HPMC),[91] and glass spheres.[92] As the filler volume fraction is increased the numerical value of slip velocity is decreased for the same magnitude value of wall shear stress.[90-92]

A possible explanation is based on the definition for the apparent slip mechanism. According to D. M. Kalyon[93] during the flow of a suspension of solid particles, the particles cannot physically occupy the space adjacent to a die wall as efficiently as they can away from the wall.[93] This phenomenon causes the formation of the slip layer which is a layer in between the die wall and the bulk flow region. It is assumed that the slip layer it is not affected by the die geometry and the volumetric flow rate.[93] Within this study high molecular weight SBR sample is the matrix for silica particles with a unimodal particle size distribution (PSD). Investigating this complex formulation, multiple aspects need to be taking into account in order to explain the slippage mechanism and why the magnitude of slip velocity decreases as the amount of filler increases.
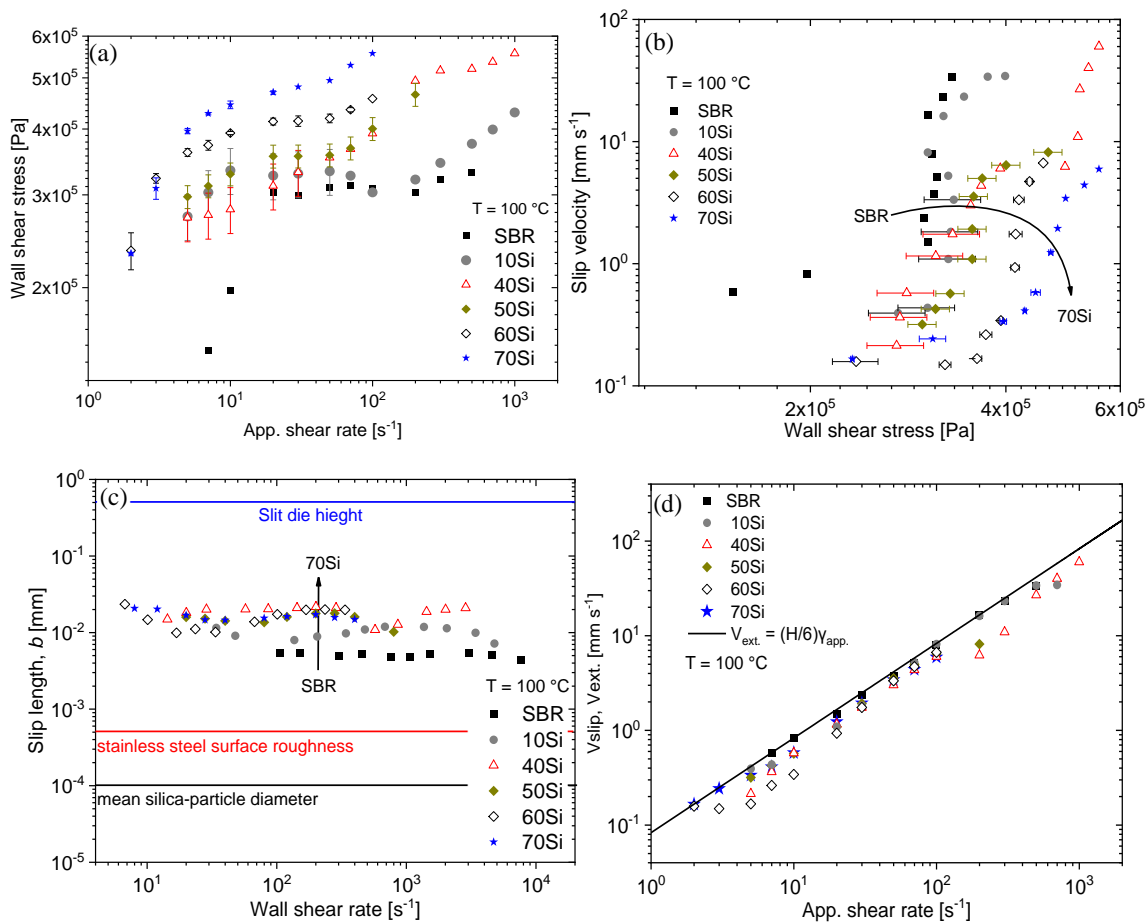
Figure 7.7. (a) Wall shear stress as a function of apparent shear rate; the magnitude values of wall shear stress are increased as the filler volume increases. (b) Slip velocity obtained by Equation (6); the slip velocity decreases as the filler volume increases at the same magnitude value of wall shear stress. (c) Slip length as a function of wall shear rate for the investigated samples; slip length is increased as the filler volume fraction increases. (c) Slip (data) and extrudate (line) velocities as a function of apparent shear rate; for all the investigated samples the magnitude of slip velocities are almost equal with the extrudate velocity, that is plug flow, or lower. The experiments carried by a slit die $H = 0.5$ mm, $W = 5$ mm and $L = 30$ mm at T = 100 °C.

One possible explanation based on the experimental results, Figure 7.7 (b), is that the slippage layer on the die wall is composed by physically grafted polymer chains and silica particle which are either captured on the roughness of the die wall and/or grafted with the polymer chains. Hence, a super-molecular architecture is captures/grafted on the die wall and basically this is the slip layer. Increasing the volume fraction of the filler, this super-molecular architecture becomes richer in solid filler. Hence, the interaction with the bulk flow become more complex and possibly the friction between the slip layer and the bulk flow is increased. Thus, increasing

the filler volume fraction, higher magnitude values of stresses need to be achieved in order to have similar numerical value for the slip velocity. Observing the slip velocity for the investigated samples which is mainly continuously monotonic as a function of wall shear stress, plug flow velocity profile is assumed, see Figure 7.7 (b). Assuming that the plug flow is developed, the slip length would have already reached its maximum value and the extrudate velocity, $V_{extr.}^{Slit} = (H/6)\dot{\gamma}_{app.}$, would have similar magnitude with the slip velocity V_s. Using the Brochard-Wyart and de Gennes interfacial rheological law,[94] $V_s = b\dot{\gamma}_{wall}$ the slip length b can be obtained. In Figure 7.7 (c) the slip length b for the investigated sample at T = 100 °C is presented. It is observed that the slip length b has reached a constant value which is not influenced by the shear rate and the magnitude of this constant value is increased from the neat SBR to the compound with 10 phr of silica and then to the compound with 40 phr of silica. After 40 phr of silica no change in the constant value of the slip length b is observed. To confirm the assumption of plug flow, $V_{extr.}^{Slit} \approx V_s$, the equation for the extrudate velocity $V_{extr.}^{Slit} = (H/6)\dot{\gamma}_{app.}$ is plotted in the Figure 7.7 (d).[95] The $V_{extr.}^{Slit}$ with the magnitude values of the V_s are compared. It is observed that the values of slip velocity overlap or are slightly below the $V_{extr.}^{Slit}$, confirming that the velocity profile is plug flow.

Table 7.5. Fitting K and n parameters obtained by the fitting to the magnitude of $\sigma_{wall} = K\dot{\gamma}_{app.}^n$ at T = 100 °C.

Name	$\sigma_{wall} = K\dot{\gamma}_{app.}^n$	
	K [Pa·s^n]	n
SBR	280159	0.022
Si10 S0.77 SA0.2	265868	0.054
Si40 S2.88 SA0.8	202342	0.150
Si50 S3.60 SA1.0	254873	0.100
Si60 S4.30 SA1.2	270456	0.125
Si70 S5.10 SA1.4	346617	0.100

7.8. Influence of filler volume fraction on extrusion instabilities

Capillary rheology experiments using capillary ($L = 30$ mm, $D = 2$ mm) and slit die ($L = 30$ mm, $W = 5$ mm, $H = 0.5$ mm) geometries are performed at T = 100 °C to investigate the extrusion flow instabilities of the studied compounds, Table 7.3. Studying the extrusion flow instabilities of the rubber compounds the following aspects will to be answered within this chapter:

(i)   Does the same compound present different surface defects while is extruded by a capillary and a slit die?

(ii)   How can the spatial characteristic wavelength λ of extrusion flow instabilities be predicted from the lab to industrial scale dies?

(iii)   What are the similarities of the surface fracture theoretical concept between the polymer melts and the investigated compounds?

(iv)   How can the modeling of the spatial characteristic wavelength contribute to develop correlations between the compound properties and the extrusion performance?

The appearance of surface fracture of the investigated samples is changing as the volume fraction of silica filler increases. Figure 7.8 (a) displays the extrudates obtained by capillary die ($L = 30$ mm, $D = 2$ mm) with increasing the volume fraction from neat SBR up to 70 phr, the pattern of the melt fracture is eliminated. Although, investigating the same samples extruded by slit die ($L = 30$ mm, $H = 0.5$ mm, $W = 10$ mm) the pattern of the melt fracture remained as the silica volume fraction increased from 10 phr to 70 phr, see Figure 7.8 (b). Observing the compound with 50 phr, it is clear that the extrudate obtained from the capillary die does not have a pattern of melt fracture as the extrudate obtained from the slit die. Similarly, for SBR compounds Viloria et al.[96,97] reported that the regular periodic pattern of the melt fracture is eliminated as the silica volume fraction increases from 20 phr to 50 phr for extrudates obtained by various capillary round dies ($D = 2$ mm, $L = 0, 8, 16,$ and 32 mm). Furthermore, Hristov et al.[98,99] investigated the extrusion behavior of numerous wood-polymer composites (WPC) with capillary die ($D = 1.5$ mm, $L = 24$ mm). The authors[98,99] observed that as the wood weight fraction increases from 5 wt.% to 60 wt.% the distortions on the extrudate surface are eliminated as well.
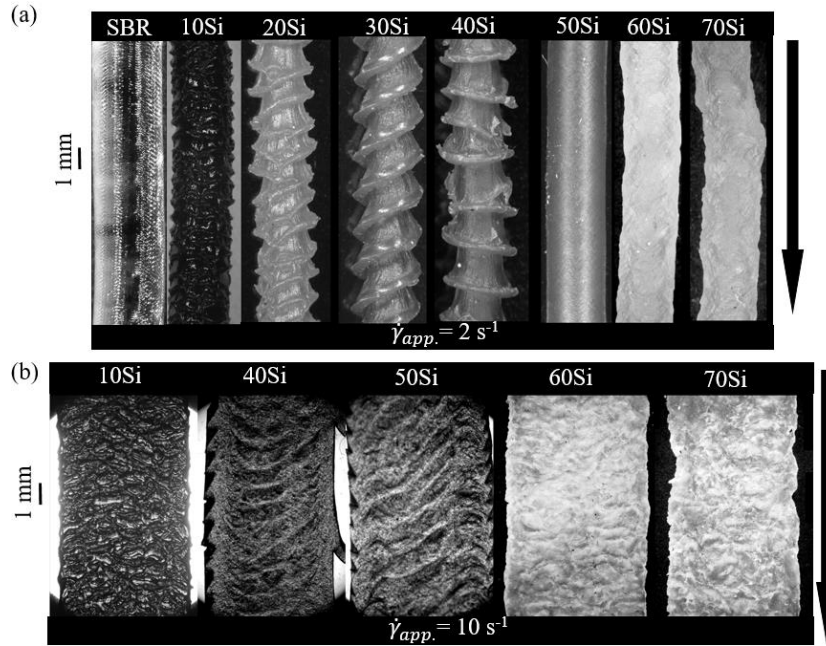
Figure 7.8. Samples investigated at T = 100 °C by (a) round capillary die (L = 30 mm, D = 2 mm) at $\dot{\gamma}_{app.}$ = 10 s^{-1} and (b) slit die (L = 30 mm, H = 0.5 mm, W =10 mm) at $\dot{\gamma}_{app.}$ = 10 s^{-1}. The arrows indicate the flow direction.

Using optical microscopy the spatial characteristic wavelength λ is quantified. A comparison between the SCW λ of the well-developed pattern between the extrudates obtained from capillary and slit die is discussed. The comparison focuses on selected samples, neat SBR, 10Si and 40Si, which they present a well-developed surface fracture on the extrudates from both dies. Figure 7.9 displays the SCW λ for the neat SBR, 10Si and 40Si investigated samples obtained from both dies. Firstly, the SCW λ obtained by the slit die have lower magnitude values from the SCW λ obtained by the capillary die, specifically they differ by a factor of three (3). Secondly, the SCW λ obtained by the slit die are shifted to higher shear rates, almost one order of magnitude. Finally, the slope of the SCW λ as a function of apparent shear rate is changing from $\lambda \sim \dot{\gamma}_{app.}^{0.5}$ for the neat SBR, to $\lambda \sim \dot{\gamma}_{app.}^{0.4}$ for the 10Si and to $\lambda \sim \dot{\gamma}_{app.}^{0.1}$ for the 40Si as the silica volume fraction increases.

The lower magnitude values of the spatial characteristic wavelength λ obtained by the slit die are explained based on the proposed model by Georgantopoulos et al.,[15] Equation (4.14). The SCW λ is increases proportional to the characteristic dimension of the die, diameter (D) for the capillary dies and height (H) for the slit dies, and the characteristic time periodicity of the instability is material dependent. The predictions of Equation (4.14) of the SCW λ for the slit dies are agree with the experimental data.[15,48]
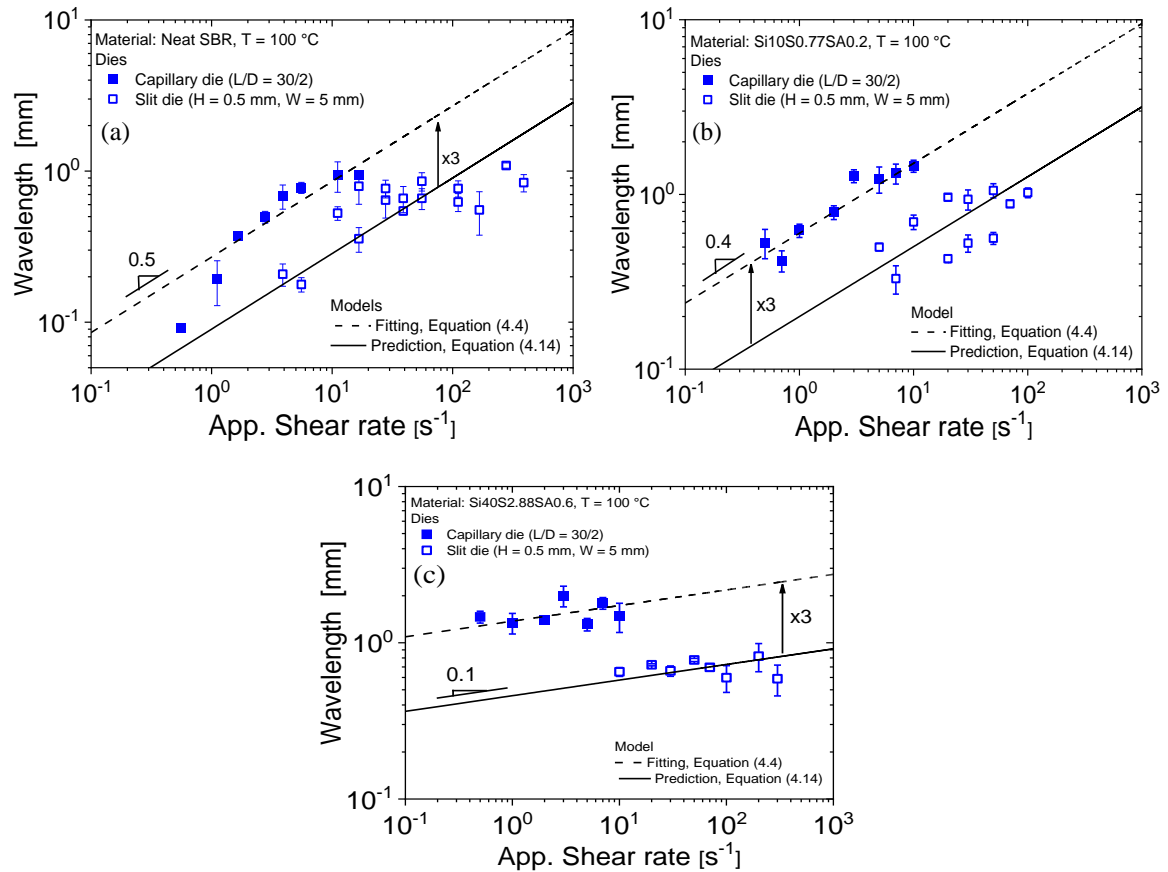
Figure 7.9. Spatial characteristic wavelength λ as a function of apparent shear rate at T = 100 °C. The experimental results are obtained by a round capillary die (L = 30 mm, D = 2 mm) and a slit die (L = 30 mm, H = 0.5 mm, W =10 mm) for (a) SBR, (b) Si10S0.77SA0.2 and (c) Si40S2.88SA0.8. The capillary die obtained data differs by a factor of three (3) from the slit die data. The scaling law of the wavelength λ as a function of shear rate is changed from 0.5 (SBR polymer) to 0.1 (Si40S2.88SA0.8). The Figure 7.9 (a) is adapted from C. K. Georgantopoulos et al., *Macromolecular Material and Engineering* 306, *2000801*, **2021**, Figure 18 (b).[15]

The shifting of the surface melt fracture onset to higher shear rates, for the neat SBR, 10Si and 40Si investigated samples, by using the slit die is explained by the surface area-to-volume aspect ratio at the die exit. To explain this, note that the origin of the surface melt fracture is associated with the intensive extensional flow deformation on the exit of the die lip.[21-39] The periodic in space pattern of the sharkskin melt fracture is resulting from two contributions of the elastic energy, the storage and dissipation.[34] During the elastic energy storage the extensional stress is increased and during the elastic energy dissipation the peeling behavior is propagating from the surface of the extrudate towards to the center of it.[16,34] Two main influence factors for the sharkskin melt fracture are used to ascribe this concept: (1) the area of the die exit region where the extensional stress is being developed and (2) the elastic behavior

of the material. Delgadillo-Velázquez et al.[100] studied a linear low density polyethylene (LLDPE) using round capillary, slit and annular dies with various dimensions. Delgadillo-Velázquez et al.[100] observed that the onset of sharkskin instability on the surface of the extrudate is postponed to higher magnitude values of the shear stress from the round capillary, to slit and then to annular die. To explain this observation, the authors[100] proposed that the delay of the onset of sharkskin is proportional to the area-to-volume aspect ratio at the die exit. For this reason, the sharkskin appeared first by using the capillary die, then the slit die and last the annular die, because the specific annular die that they used had the biggest numerical value for the area-to-volume aspect ratio.

Within this study the area-to-volume aspect ratio at the die exit for the round capillary and slit dies is used to prove that the slit die has higher magnitude of the surface area-to-volume aspect ratio than the round capillary die, for details see Appendix C. Therefore, shifting of the spatial characteristic wavelength of the sharkskin melt fracture obtained by the slit die to the higher shear rates is explained.

The last observation of the Figure 7.9 focuses on the slope change for the spatial characteristic wavelength λ as a function of apparent shear rate. The slope changes from $\lambda \sim \dot{\gamma}_{app.}^{0.5}$ for the neat SBR, to $\lambda \sim \dot{\gamma}_{app.}^{0.4}$ for the 10Si and then to $\lambda \sim \dot{\gamma}_{app.}^{0.1}$ for the 40Si. This observation is explained based on the previous reported concept[29-39] for the origin of the surface fracture and its association with the elastic behavior and the characteristic relaxation time of the samples.[16] Firstly, the numerical values of the SCW λ obtained by the 40Si are bigger than the 10Si, which 10Si has also bigger magnitude values than the neat SBR, see Figure 7.9. This can be explained based on the longest relaxation time of the material.[16] The 40Si has longest relaxation time than 10Si which has longest relaxation time than the neat SBR (see Figure 7.4 (b)), hence the time which needed to complete a spatial pattern, that is a wavelength, is longer. Secondly, as the amount of filler increases the elasticity of the samples increases, see Figure 7.5 (a). For this reason, the peeling behavior is more intense as the filler fraction is increased from neat SBR up to 40Si, see Figure 7.8 (a).[34] In Figure 7.10 a correlation between the characteristic height h of the distortions and the numerical value of G'' at $\omega = 0.63$ rad·s^{-1}, as well as the volume fraction of silica filler is presented. The spatial characteristic height h is defined as the average distance between the swelled core of the extrudate and the tip of the distortion.[16,27,28] This correlation confirms that the peeling behavior is more intense, that is higher characteristic height h, as the elasticity of the sample increases. The absence of the melt fracture pattern after 50Si from the extrudates obtained by the capillary die is discussed later.
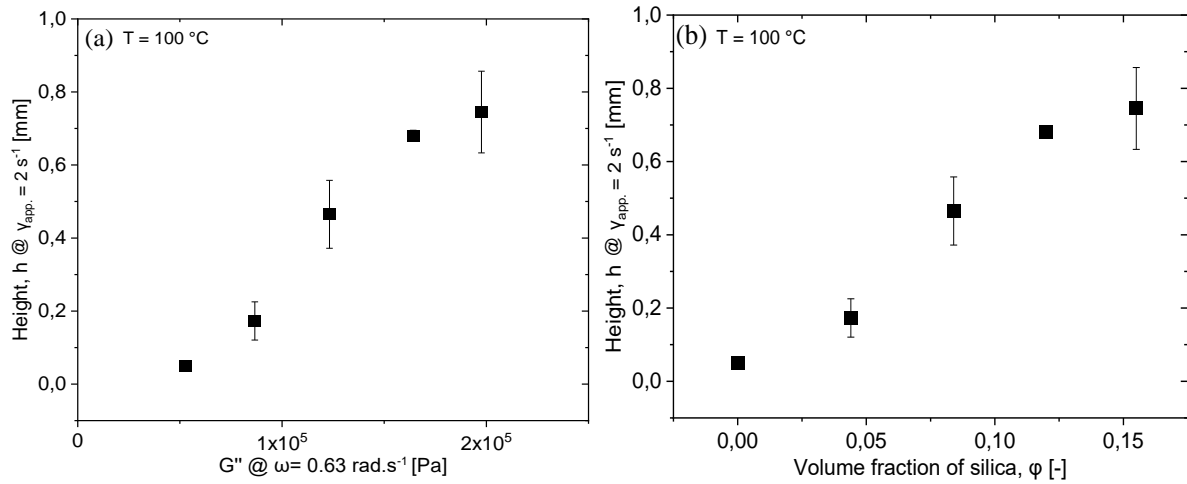
Figure 7.10. (a) Spatial characteristic height h as a function of the numerical value of G'' at $\omega = 0.63$ rad·s^{-1} and (b) spatial characteristic height h as a function of volume fraction of silica nanoparticles in the samples of interest. The numerical values of the height h are measured on the extrudates obtained by the capillary die ($L = 30$ mm, $D = 2$ mm) at $\dot{\gamma}_{app.} = 2$ s^{-1} and T = 100 °C. The extrudates are visualized at Figure 7.8 (a).

The spatial characteristic wavelength λ obtained from round capillary die ($L = 30$ mm, $D = 2$ mm) for the neat SBR, 10Si, 20Si and 40Si are presented in Figure 7.11 (a). The experimental results show an increasing trend as a function of the apparent shear rate, especially for the neat SBR and 10Si. Increasing the silica volume fraction from neat SBR to 40Si, results in bigger numerical values of the SCW λ at similar range of apparent shear rate, $0.1\ s^{-1} < \dot{\gamma}_{app.} < 10\ s^{-1}$. The experimental results are satisfactory fitted by the Inn et al.[26] model, Equation (4.39), and the ratio of extensional and shear stress Y_s/σ_x is obtained. The fitting parameters b and c for the interfacial depth parameter, $\xi = b\dot{\gamma}_{app.}^{-c}$ for the input of Equation (4.39) are listed on Table 7.6.

Table 7.6. The fitting parameters b and c for the interfacial depth parameter, $\xi = b\dot{\gamma}_{app.}^{-c}$ at T = 100 °C obtained by extrudates from capillary die ($L = 30$ mm, $D = 2$ mm).

Sample	b	c
SBR	0.99	0.045
Si10 S0.77 SA0.2	0.90	0.040
Si20 S1.44 SA0.4	0.83	0.040
Si40 S2.88 SA0.8	0.80	0.040

The spatial characteristic wavelength λ obtained from slit die (L = 30 mm, H = 0.5 mm and W = 10 mm) for the neat SBR, 10Si, 50Si, 60Si and 70Si are presented in Figure 7.11 (b). The experimental results show an increasing trend as a function of the apparent shear rate similar with the experimental data of Figure 7.11 (a). Increasing the silica volume fraction from neat SBR to 70Si, results in large numerical values of the SCW λ almost one order of magnitude difference. The experimental results are fitted by the Georgantopoulos et al.[48] model, Equation (4.40), and the ratio of extensional and shear stress Y_s/σ_x is obtained as well. The fitting parameters b and c for the interfacial depth parameter, $\xi = b\dot{\gamma}_{app.}^{-c}$ for the input of Equation (4.40) are listed on Table 7.7.
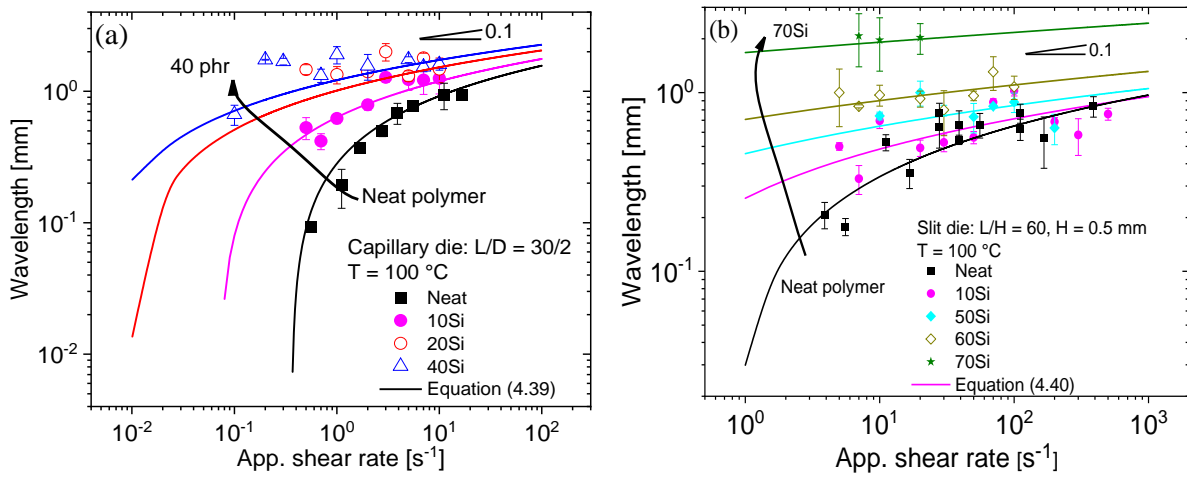
Figure 7.11. Spatial characteristic wavelength λ as a function of apparent shear rate for extrudates obtained by (a) capillary die (L = 30 mm, D = 2 mm) and (b) slit die (L = 30 mm, H = 0.5 mm and W = 10 mm) at T = 100 °C. The experimental data are fitted by (a) Equation (4.39)[26] and (b) Equation (4.40)[48] models.

Table 7.7. The fitting parameters b and c for the interfacial depth parameter, $\xi = b\dot{\gamma}_{app.}^{-c}$ at T = 100 °C obtained by extrudates from slit die (L = 30 mm, H = 0.5 mm and W = 10 mm).

Sample	b	c
SBR	0.99	0.045
Si10 S0.77 SA0.2	0.90	0.040
Si50 S3.60 SA1.0	0.80	0.040
Si60 S4.30 SA1.2	0.70	0.040
Si70 S5.10 SA1.4	0.45	0.040

The fitting parameter of extensional and shear stress Y_s/σ_x ratio on the die exit region is obtained by fitting the Equation (4.39),[26] and Equation (4.40),[48] models on the experimental data of the spatial characteristic wavelength λ in Figure 7.11. The magnitude values of the Y_s/σ_x ratio are presented as a function of volume fraction of silica, characteristic relaxation time and the numerical value of the G'' at $\omega = 0.63$ rad·s^{-1} at Figure 7.12. In Figure 7.12 (a) – (c) the magnitude values of Y_s/σ_x ratio results from the fitting of Equation (4.39) on the experimental results of Figure 7.11 (a), and in Figure 7.12 (d) – (f) the magnitude values of Y_s/σ_x ratio are obtained by the fitting of Equation (4.40) on the experimental results of Figure 7.11 (b). The behavior of the Y_s/σ_x as a function of volume fraction of silica, characteristic relaxation time and the numerical value of the G'' at $\omega = 0.63$ rad·s^{-1} is qualitatively described as an exponential decay. As the volume fraction of silica, characteristic relaxation time and the numerical value of the G'' at $\omega = 0.63$ rad·s^{-1} are increased the magnitude of the Y_s/σ_x is decreased. As the elasticity and the characteristic relaxation time of the material increases, the ratio of Y_s/σ_x on the die exit decreases. The same trend has also been mentioned in literature for different neat polymer melts.[16] The magnitude values of the Y_s/σ_x obtained by the Equation (4.39) for the capillary data are lower that then the magnitude values of the Y_s/σ_x obtained by the Equation (4.40) for the slit die. This is also observed by Georgantopoulos et al.,[48] for a polybutadiene (PBD) sample, that is the magnitude of the Y_s/σ_x ratio has bigger magnitude values for the slit rather than the capillary die. The magnitude values of the Y_s/σ_x ratio obtained from the capillary die for the neat SBR, 10Si ($\varphi = 0.044$), 20Si ($\varphi = 0.084$), and 40Si ($\varphi = 0.155$) are reaching $Y_s/\sigma_x = 1.8$ at 40Si ($\varphi = 0.155$), see Figure 7.12 (a) – (c). Hence, during the extrusion of the rubber compounds from the capillary die the stress ratio Y_s/σ_x at the die exit region is reaching numerical values which are $2 > Y_s/\sigma_x$ for the rubber compounds of 20Si ($\varphi = 0.084$), and 40Si ($\varphi = 0.155$). This observation implies that the Y_s/σ_x ratio for the 50Si ($\varphi = 0.182$) has probably even lower numerical values than the 40Si ($\varphi = 0.155$). The low numerical values of the Y_s/σ_x ratio implies a weak extensional deformation on the die exit region for those high elastic rubber compounds. This possibly explains the absence of any kind of surface melt fracture on the 50Si, 60Si, and 70Si extrudates obtained from the capillary die. Although, there is a pronounced melt fracture on the surface of the 50Si, 60Si, and 70Si extrudates obtained from the slit die, see Figure 7.8 (b). The Y_s/σ_x ratio for the 50Si, 60Si, and 70Si extrudates obtained by the slit die has numerical values which are bigger than seven, $Y_s/\sigma_x > 7$, see Figure 7.12 (d) – (f). Hence, the absence of the melt fracture on the surface of the 50Si, 60Si, and 70Si obtained from the capillary die is occurred due to the low magnitude values of the Y_s/σ_x ratio for such an elastic materials. For this reason, melt fracture on the

surface of 50Si, 60Si, and 70Si obtained by the slit die is observed due to higher magnitude values of the Y_s/σ_x ratio on the die exit region.

Capillary die
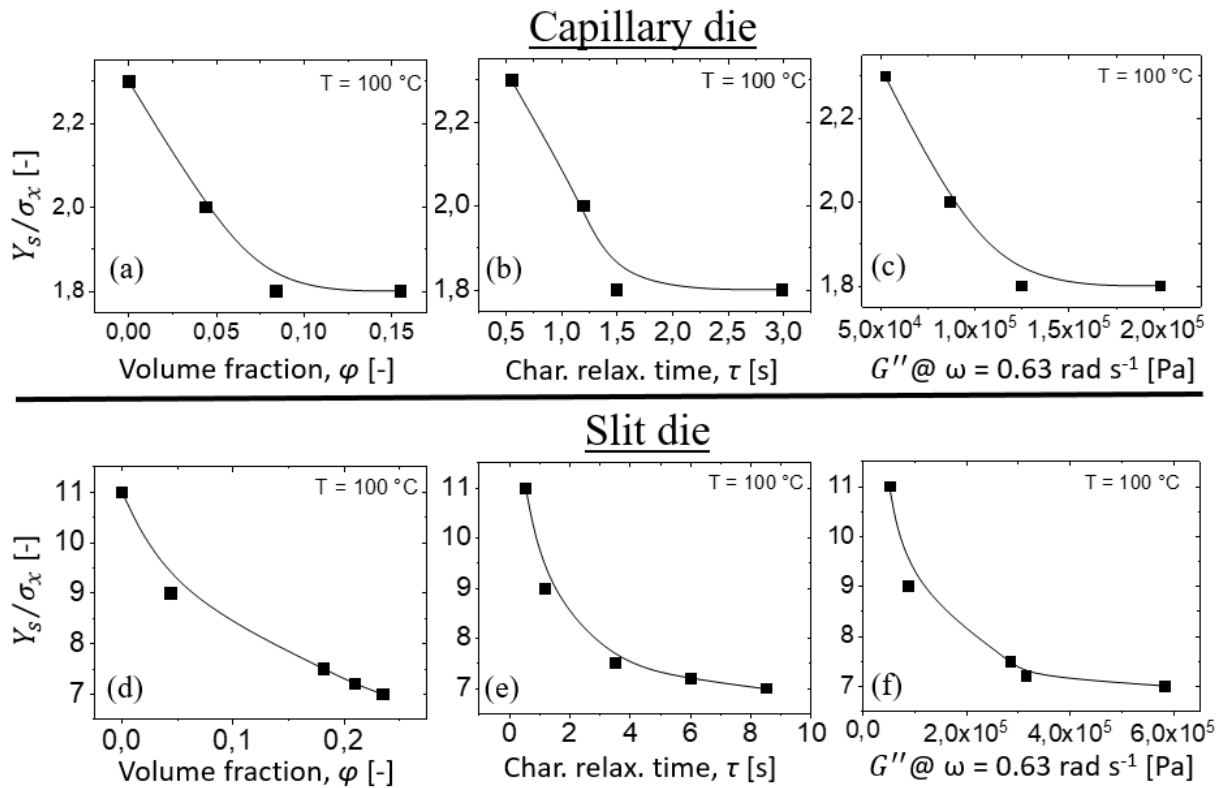
Slit die

Figure 7.12. Ratio of the extensional (Y_s) and shear (σ_x) stresses at the die exit area obtained by applying Equation (4.39) for capillary dies (a) – (c) and Equation (4.40) for slit dies (d) – (f). The magnitude values of the Y_s/σ_x is correlated with the volume fraction of silica (a), (d), the characteristic relaxation time (b), (e) and the numerical value of the loss modulus at ω = 0.63 rad·s^{-1} (c), (f). The experiments carried out at T = 100 °C using (a) – (c) capillary die (L = 30 mm, D = 2 mm) and (d) – (f) slit die (L = 30 mm, H = 0.5 mm and W = 10 mm). The indicated lines present the trend to guide the eye.

Through this chapters the following outcomes are obtained in order to address the previously mentioned questions:

(i)   The difference in surface defects of the same compound extruded by capillary and slit dies occur due to the difference in the magnitude of the stress ratio Y_s/σ_x at the die exit region.

(ii)   Slit dies present higher magnitude of the stress ratio Y_s/σ_x than the capillary dies, and for this reason surface defects for high elastic materials are present only on extrudates obtained from slit dies.

129

(iii)   The proposed correlation by Georgantopoulos et al.,[15] Equation (4.14), is in agreement and predict the spatial characteristic wavelength λ from a capillary to slit die geometry, for neat SBR and rubber compounds.

(iv)   The theoretical concept for the origin of surface fracture formation can also be adapted to explain the instability onset for the rubber compounds. The experimental results which describe how the elasticity influences the formation of the surface fracture can be found in Figure 7.10.

(v)   Based on the models for the spatial characteristic wavelength λ, Equation (4.39) and (3.30), the stress ratio Y_s/σ_x on the die exit can be obtained. Hence, the Y_s/σ_x is correlated with the compound properties (filler load, characteristic relaxation time, elasticity) and correlations, which can be used as a mapping for compounding-extrusion performance relationship, are obtained in Figure 7.12.

7.9. Influence of extrusion temperature on extrusion process

To investigate the influence of extrusion temperature on extrusion instabilities of rubber compounds, capillary rheology experiments using capillary die (L = 30 mm, D = 2 mm) are performed at T = 80 °C, 100 °C and 120 °C. Two compounds, Si10S0.77SA0.2 and Si40S2.88SA0.8 are studied as a function of extrusion temperature. The apparent steady state viscosity $\eta_{app.}(\dot\gamma)$ at three different temperatures is presented in Figure 7.13 for both compounds. The apparent steady state viscosity $\eta_{app.}(\dot\gamma)$ of the 10Si and 40Si is not affected by the applied temperature range of T = 80 °C, 100 °C and 120 °C, see Figure 7.13. The only identifiable difference on the viscosity is observed at 10Si (Figure 7.13 (a)) for $\dot\gamma_{app.}$< 2 s^{-1}.
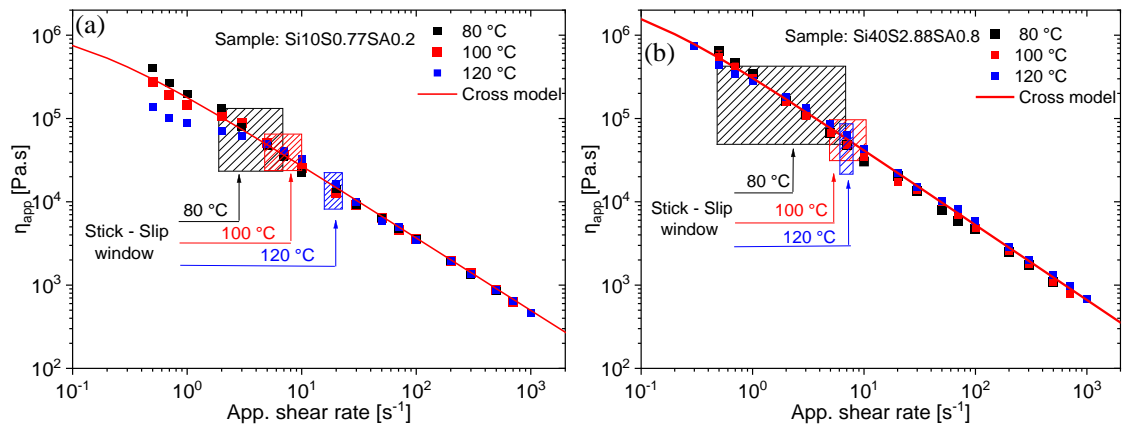
Figure 7.13. Apparent steady state viscosity $\eta_{app.}$ as a function of apparent shear rate obtained from capillary rheometer equipped with a capillary die (L = 30 mm, D = 2 mm). Extrusion temperature of T = 80 °C, 100 °C and 120 °C for (a) Si10S0.77SA0.2 and (b) Si40S2.88SA0.8

compounds. In (b) the stick-slip instability is shifted to higher shear rates as the temperature increases. The experimental data is fitted by Cross model at T = 100 °C, see Table 7.4.

The extrusion flow instabilities and especially the range of the apparent shear rates where the stick-slip instability is observed at different temperatures is discussed. For the 10Si compound the stick-slip instability is observed between $\dot{\gamma}_{app.}$ = 2 s^{-1} and 7 s^{-1} at T = 80 °C, $\dot{\gamma}_{app.}$= 5 s^{-1} and 10 s^{-1} at T = 100 °C and at $\dot{\gamma}_{app.}$= 20 s^{-1} at T =120 °C, see Figure 7.13 (a). For the 40Si, stick-slip instability is observed between $\dot{\gamma}_{app.}$= 0.5 s^{-1} and 7 s^{-1} at T = 80 °C, $\dot{\gamma}_{app.}$= 5 s^{-1} and 10 s^{-1} at T = 100 °C and at $\dot{\gamma}_{app.}$= 7 s^{-1} at T = 120 °C, see Figure 7.13 (b). Hence, the stick-slip instability limits the apparent shear rate range as the temperature increased from T = 80 °C to 120 °C. Moreover, the existence of stick-slip instability is relocated to higher apparent shear rates as the temperature increased. This observation is also mentioned in the literature for Ziegler-Natta and metallocene high density polyethylene (HDPE).[101]

Figure 7.14 shows images from Si40S2.88SA0.8 compound at T = 80 °C, 100 °C and 120 °C obtained by capillary die (L = 30 mm, D = 2 mm) at three apparent shear rates, $\dot{\gamma}_{app.}$= 2 s^{-1}, 5 s^{-1}, and 7 s^{-1}. The diagonal blue arrows within Figure 7.14 indicate that the onset of stick-slip instability is moved to higher shear rates as the extrusion temperature is elevated from T = 80 °C up to 120 °C. Moreover, the spatial characteristic wavelength λ remains almost constant on 1 mm.
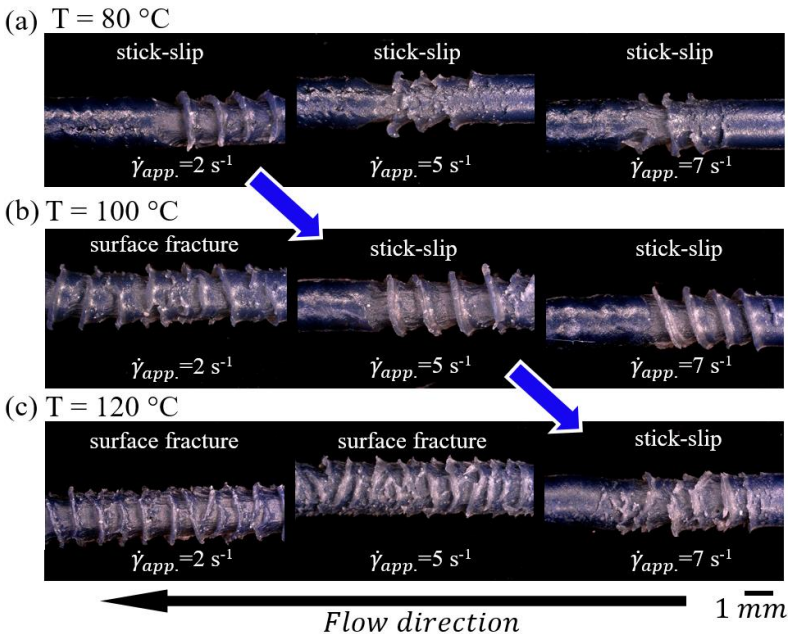
Figure 7.14. Spatial offline optical analysis of Si40S2.88SA0.8 at T = 80 °C, 100 °C and 120 °C obtained by capillary die (L = 30 mm, D = 2 mm). Within the presented range of

temperatures and apparent shear rates, the spatial characteristic wavelength remains almost constant with a value of about 1 mm. The black arrow indicates the flow direction.

The numerical values of the spatial characteristic wavelength λ of the Si10S0.77SA0.2 and Si40S2.88SA0.8 model compounds investigated at T = 80 °C, 100 °C, and 120 °C are presented in Figure 7.15. For the Si10S0.77SA0.2 compound, this temperature range influence the spatial characteristic wavelength at $\dot{\gamma}_{app.} < 2$ s^{-1}, afterwards similar values are observed, see Figure 7.15 (a). For the Si40S2.88SA0.8 model compound similar values of the spatial characteristic wavelength are observed for T = 80 °C and 100 °C. Moreover, the SCW λ obtained at T = 120 °C display lower values which do not exceed the 30% deviation from the fitting, see Figure 7.15 (b). The experimental data are fitted by Inn et al.[26] model (Equation (4.39)) at T = 100 °C.
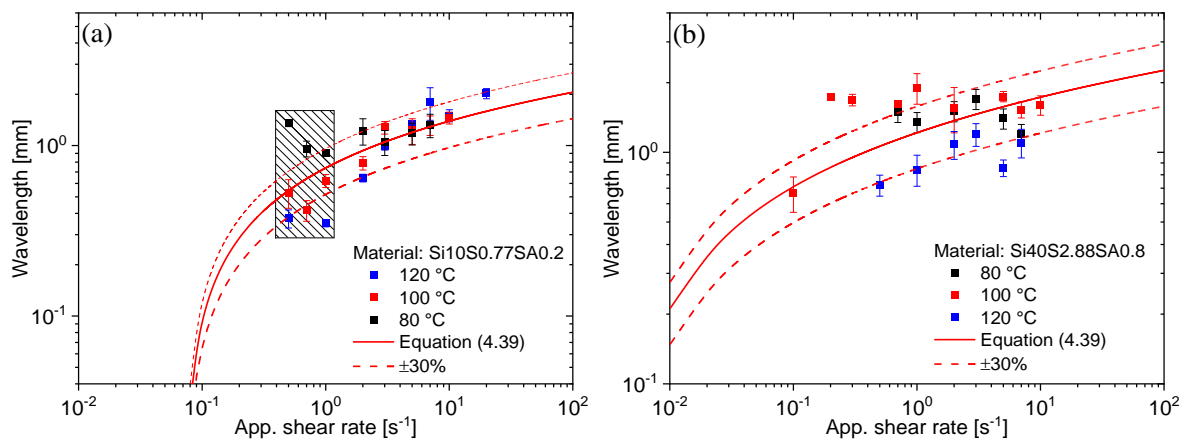
Figure 7.15. Spatial characteristic wavelength λ of extrusion flow instabilities as a function of apparent shear rate. The capillary die (*L* = 30 mm, *D* = 2 mm) at extrusion temperature of T = 80 °C, 100 °C and 120 °C for (a) Si10S0.77SA0.2 and (b) Si40S2.88SA0.8 compounds. The experimental data are fitted by Inn et al.[26] model (Equation (4.39)) at T = 100 °C.

7.10. Conclusion

The outcome of this work could serve as a guideline to quantify and model extrusion flow instabilities for both industrials and academic purposes. The correlations between the extrusion behavior of the rubber compounds and their properties (filler load, characteristic relaxation time, elasticity) could provide information which can be used from compound and extrusion engineers to determine and predict the extrusion performance of a new formulation. The following conclusions have been drawn based on the previously reported outcomes:

(i) Investigated compounds under shear flow deformation present two characteristic flow regions which are the fingerprints of the filler and the polymer matrix, respectively. At low shear deformations ($\omega < 20$ rad·s^{-1}) the flow is influenced by the filler network and a yielding behavior is observed. At high shear deformations ($\omega > 20$ rad·s^{-1}) the flow is leading by the polymer matrix.

(ii) Increasing the filler volume fraction in the rubber compounds the magnitude value of the slip velocity decreases for a constant value of the wall shear stress. This behavior is explained based on the assumption that the increases of filler volume fraction elevate the friction between the bulk flow and the wall of extrusion die.

(iii) Highly filled rubber compounds ($\varphi > 0.182$) investigated by capillary die geometry present almost a smooth surface. In contrast, when they are extruded by slit die geometry manifest extrusion flow instabilities on the surface of the extrudate. This phenomenon is explained based on the magnitude value of the stress ratio Y_s/σ_x at the die exit region. The magnitude value of the stress ratio has higher values at the die exit for the slit die and lower values for the capillary die. Hence, high elastic materials might be not able to exceed the critical stress ratio for the onset of instability extruded by capillary dies, consequently a smooth surface on the extrudate surface is observed.

(iv) For low volume fractions of filled rubber compounds ($\varphi < 0.182$) surface extrusion flow instabilities are presented in the end of capillary and slit dies. By quantifying the spatial characteristic wavelength of the instabilities obtained from the capillary die and using predictive model, Equation (4.14), the spatial characteristic wavelength for slit die geometries can be predicted.

(v) Fitting the spatial characteristic wavelength of the extrusion flow instabilities with the proposed models, Equation (4.39) and (4.40), the stress ratio Y_s/σ_x at the die exit region is obtained. The higher numerical values of the Y_s/σ_x ratio

are associated with small magnitude of the spatial characteristic wavelength. Hence, correlations between the stress ratio Y_s/σ_x and the compound properties (filler load, characteristic relaxation time, elasticity) are providing information for the surface extrusion instabilities at the end of the extruder die.

(vi) For the investigated rubber compounds the steady state viscosity is not influenced by the extrusion temperature within T = 80-120 °C. In contrast with the stick-slip instability is moved to higher shear rate as the temperature increases. In addition the spatial characteristic wavelength is not influenced more than 30% from the extrusion temperature within T = 80-120 °C.

8. Extrusion Flow Instabilities of Filled Elastomers: Influence of Filler

Within this chapter the extrusion behavior of a series of model filled compounds is investigated as a function of filler dispersion. Quantification of the spatial characteristic wavelength (λ) of the extrusion flow instabilities and the modelling of them by the previous reported models (chapter 4) enables useful correlations between molecular properties and extrusion behavior. Hence, a mapping for the extrusion behavior of the model filled systems as a function of filler dispersion is presented.

8.1. Material used in this chapter

The investigated formulations are consisted by a commercial styrene-butadiene rubber (SBR), commercial silica filler (Ultrasil 7000 GR, Evonik Industries AG), a commercial coupling agent silane (Si-69, Evonik Industries AG), and a commercial stearic acid (Evonik Industries AG) which act as a lubricant. The SBR polymer acts as the polymer matrix where the nanoparticles are dispersed. This SBR has a bimodal molecular weight distribution (see Figure 3.1) with a weight average molecular weight of $M_w = 390$ kg·mol^{-1}, dispersity index $Đ = 1.35$ and contains approximately 6 wt.% of low molecular hydrocarbons which are possibly processing agents.[15] The detailed molecular and rheological characterization of the SBR polymer matrix can be found in chapter 3, SBR B. The commercial silica (Ultrasil 7000 GR, Evonik Industries AG) has a unimodal particle size distribution (PSD) with average cluster diameter of ~0.1 μm, see Figure 7.1. The primary silica particles have an average diameter of around ~25 nm, see Figure 7.1 (a) in chapter 7. The coupling agent silane (Si-69) is used for two main reasons in the rubber compounding process. Firstly, it is chemically grafted on the surface of the silica nanoparticles, hence it is blocking the formation of clusters and agglomerations of the silica particles in order to be better dispersed in the polymer matrix. Secondly, the sulfur (S) content of the silane (Si-69) is improving the chemical crosslinking efficiency and the formation of super-molecular architectures during the curing process, which is the last processing step for a tire producer.[70-72] In Figure 8.1 the chemical groups of the silica surface, the chemical formula of the silane

(Si-69), the chemical reaction between the silane and the silica surface, and a possible configuration of the silane grafting on the silica surface are presented.[102]

8.2. Compounding process

To develop the formulation of the model systems, a typical compounding process is performed in a 1.8 liter internal mixer at chamber temperature of 50 °C and the rotor speed of 70 rpm. The dumping temperature is 150 °C and the duration of mixing is 5 to 6 min, depending on the filler amount. Silica and 90 % of the silane amount are added after an initial rubber mastication of 20 s. Then, after 90 s of mixing, the remaining 10 % of silica and stearic acid are added. The final compounds are then homogenized in a two-roll open mill at 50 °C.[84] In Table 10.1 the components of the model compounds are presented.
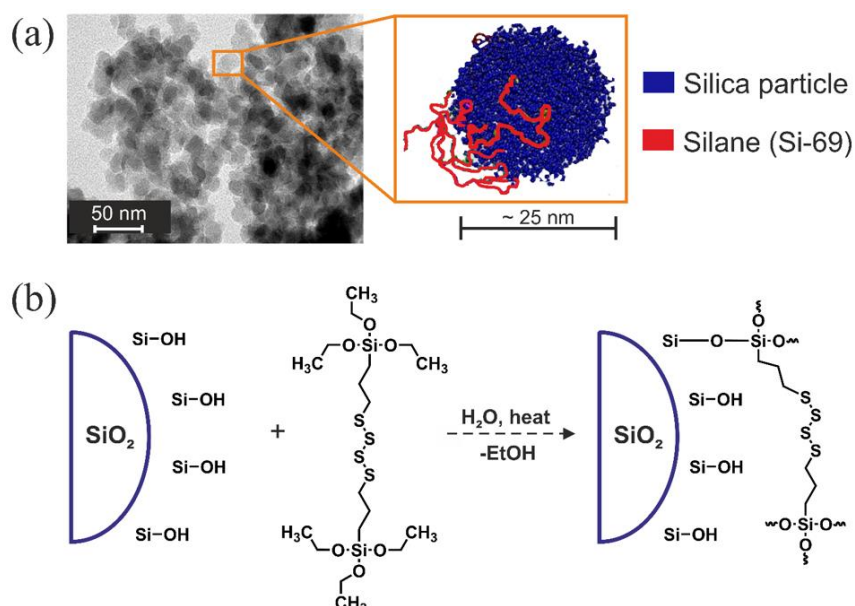
Figure 8.1. Schematic representation of (a) silica nanoparticles obtained by transmission electron microscopy (TEM). The inset show an animation of the spherical silica nanoparticle which has grafted chains of silane. (b) Presents the chemical reaction between the silica surface and the silane. The grafting of the silane on the silica surface may have numerous configurations such as tails, train, and loop. Here a possible tail configuration is presented.[102]

Table 8.1. Formulations of the model compounds based on silane amount.

Name	[a]Silica (Si) [phr]	[b]Silane (S) [phr]	[c]Stearic acid (SA) [phr]	Volume fraction of silica, φ [-]
Si40 S0.00 SA0.8		0.00		
Si40 S0.70 SA0.8	40	0.70	0.8	0.155
Si40 S1.44 SA0.8		1.44		
Si40 S2.88 SA0.8		2.88		

[a]Ultrasil 7000 GR, Evonik Industries AG. [b]Si-69, Evonik Industries AG, [c]Evonik Industries AG.

8.3. Experimental procedure

Small amplitude oscillatory shear (SAOS) experiments were performed with a rubber process analyzer (RPA), TA Instruments, close cavity rheometer. This rheometer has a 40 mm dimeter grooved geometry in order to minimize the slippage between the material and the geometry. The SAOS experiments were done at T = 100 °C within angular frequency of $\omega = 0.6$ rad·s^{-1} and 300 rad·s^{-1}. The slippage and the extrusion flow instabilities are studied via capillary rheology. A capillary rheometer Göttfert RG 50 equipped with a slit die with width $W = 5$ mm, height $H = 0.5$ mm and length $L = 30$ mm is used. Each investigated sample remained in the barrel of the capillary rheometers at T = 100 °C for 10 min to ensure uniform isothermal condition in the whole sample.

The extrudates are collected, and then optically investigated at room temperature. The optical investigation is conducted by a Keyence VHX 900F (Osaka, Japan) incident light microscope which is equipped with two zoom lenses and magnification range between 20 and 2000.

8.4 Rheological characterization linear regime

In Figure 8.2 the storage modulus, loss modulus and the magnitude of complex viscosity as a function of angular frequency for the investigated compounds at T = 100 °C are presented. In Figure 8.2 (a) and (b) the storage and the loss moduli are presented. The increase of silane content in the investigated compound decreases the magnitude of the storage moduli. In contrast, the loss moduli seems to not be influenced by this range on silane amount in the compounds.
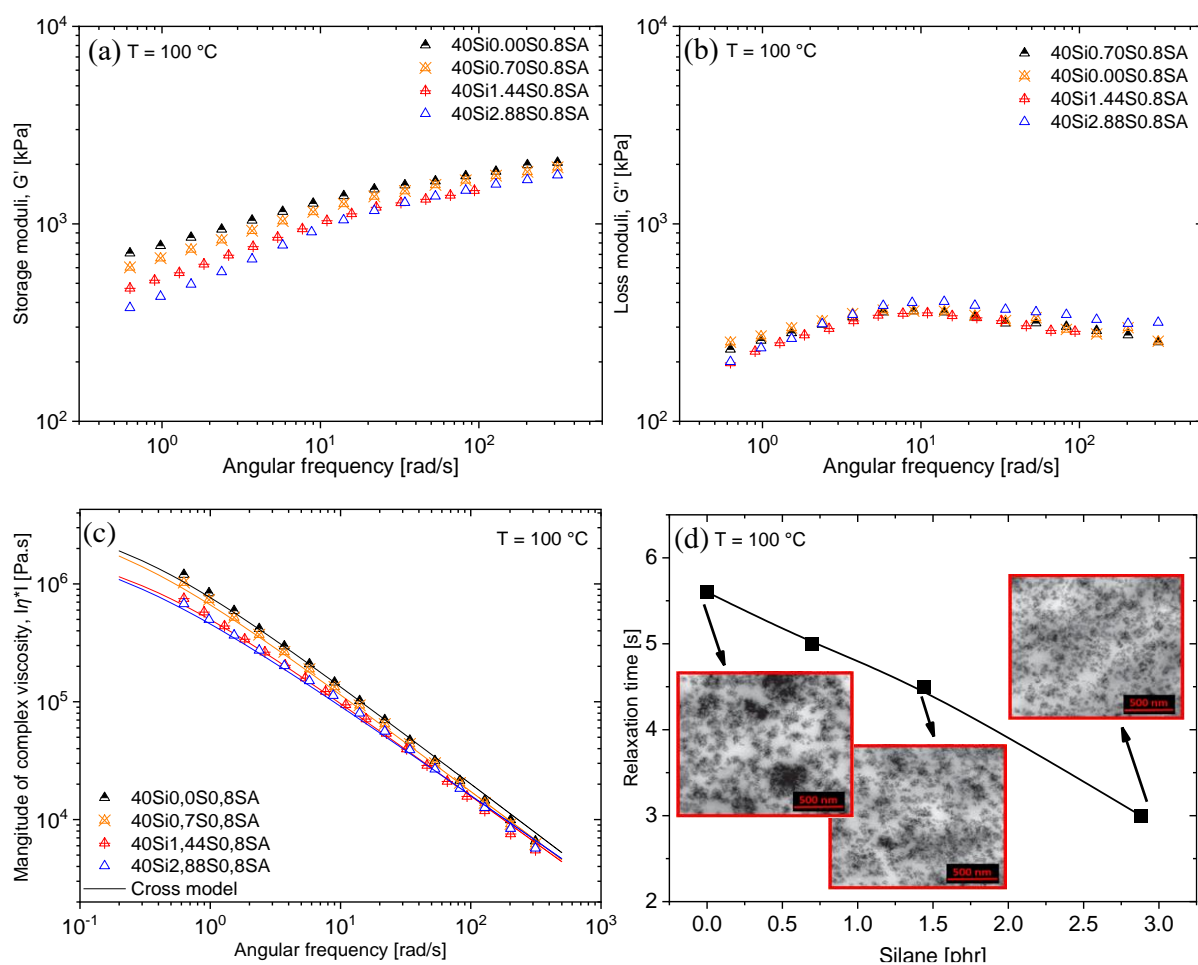
Figure 8.2. Influence of silane amount on (a) storage G' modulus, (b) loss G'' modulus, (c) magnitude of complex viscosity $|\eta^*|$ and (d) characteristic relaxation time τ of the investigated samples at T = 100 °C and $\gamma_0 = 0.3$ %. The (c) magnitude of complex viscosity $|\eta^*|$ is fitted by the Cross model and the characteristic relaxation time τ is obtained, see Table 8.2.

The magnitude of the complex viscosity is presented in Figure 8.2 (c) and it is fitted by the Cross model, $\eta(\dot\gamma) = \eta_0/(1 + (\tau\dot\gamma)^m)$ .The magnitude of complex viscosity decreases as the amount of silane is increased. This experimental observation is explained based on the better filler dispersion in the polymer matrix in absence of clusters and agglomerates.[84] Thus the increasing silane amount improve the dispersion of the silica filler in the compound.[78-84] Fitting the magnitude of complex viscosity with the Cross model the characteristic relaxation time τ is obtained. In Table 8.2 the fitting parameters of the Cross model are listed. In Figure 8.2 (d) the characteristic relaxation time τ as a function of the silane amount is plotted. As mentioned before the increases of silane amount improve the disperse-ability of the filler, hence the characteristic relaxation time τ of the compound is decreased. Inside Figure 8.2 (d) ideal schematic animations depict a theoretical arrangement of the filler for selecting silane amount.

Table 8.2. Fitting parameters of the Cross model obtained by the fitting to the magnitude of complex modulus at T = 100 °C.

Name	Cross model		
	m	τ [s]	η_0 [Pa·s]
Si40 S0.00 SA0.8	0.86	5.6	$4.5\ 10^6$
Si40 S0.70 SA0.8	0.86	5.0	$3.8\ 10^6$
Si40 S1.44 SA0.8	0.86	4.5	$2.8\ 10^6$
Si40 S2.88 SA0.8	0.86	3.0	$1.7\ 10^6$

8.5. Influence of filler dispersion on wall slippage

In order to study the influence of filler dispersion on the wall slippage and on extrusion flow instabilities in a control way, capillary rheology experiments were carried. A Göttfert RG 50 (Buchen, Germany) capillary rheometer equipped with a slit die with width $W = 5$ mm, height $H = 0.5$, mm and length $L = 30$ mm is used.[15] The choice of the slit die allows the direct extraction of the wall shear stress σ_{wall} because the aspect ratio is $L/H \geq 60$, hence the impact of exit pressure can be neglected.[41] All the rheological experiments carried out at $T = 100$ °C. The steady state viscosity as a function of apparent shear rate for all the investigated compounds is presented in Figure 8.3 (a). In small to medium magnitude of apparent shear rate, $\dot{\gamma}_{app.} < 100$ s^{-1}, the viscosity curves present differences which they are explained based on dispersion of the filler. The compound with the highest amount of silane has the lowest viscosity curve, since the filler has the best dispersion among the others. After $\dot{\gamma}_{app.} > 100$ s^{-1} the viscosity curves are overlapped to each other, since in fast shear flows the polymer matrix is dominating the flow. The wall shear stress as a function of apparent shear rate is presented in Figure 8.3 (b). The compound with poor filler dispersity (Si40S0.00SA0.8) present the highest magnitude of the wall shear stress and the compound with the better filler dispersity (Si40S2.88SA0.8) present the lowest numerical values of the wall shear stress. The wall shear stress as a function of apparent shear rate is fitted by a power law model, $\sigma_{wall} = K\dot{\gamma}_{app.}^n$, where K and n are fitting parameters, see Table 8.3.
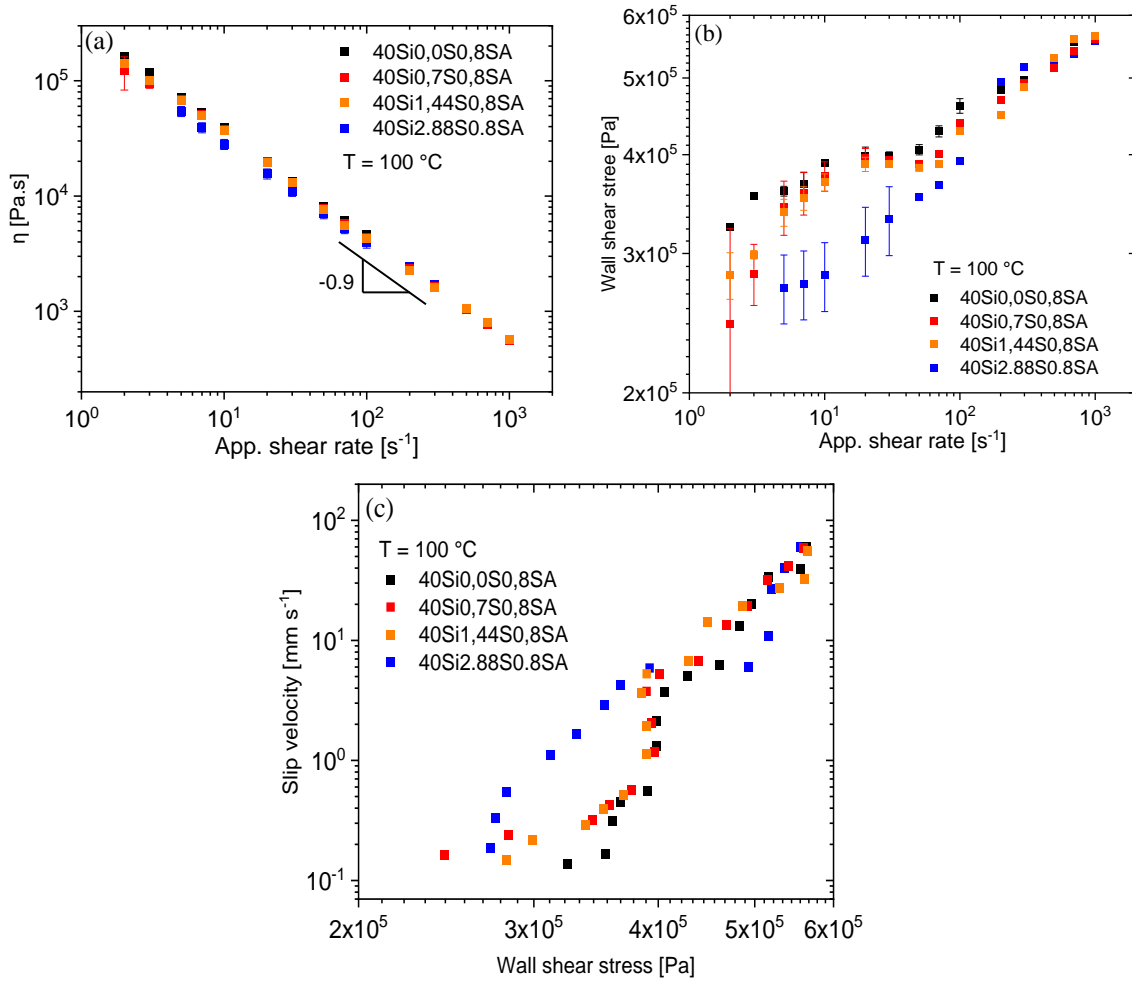
Figure 8.3. Influence of silane amount. (a) Steady state viscosity as a function of apparent shear rate, (b) wall shear stress as a function of apparent shear rate; the magnitude of wall shear stress decreases as the dispersity of the silica filler improves, below $\dot{\gamma}_{app.} < 100$ s^{-1}. (c) Slip velocity obtained by Equation (2) as a function of wall shear stress; the slip velocity increases as the silica dispersion improves at the same magnitude value of wall shear stress, below $\sigma_{Wall} < 4 \cdot 10^5$ Pa. The experiments were carried out by a slit die $L/H = 30/0.5$ at $T = 100$ °C.

Table 8.3. Fitting parameters K and n obtained by the fitting to the magnitude of $\sigma_{wall} = K\dot{\gamma}_{app.}^n$ at $T = 100$ °C.

Name	$\sigma_{wall} = K\dot{\gamma}_{app.}^n$	
	K [Pa.s^n]	n
Si40 S0.00 SA0.8	311304	0.082
Si40 S0.70 SA0.8	294945	0.088
Si40 S1.44 SA0.8	284184	0.095
Si40 S2.88 SA0.8	197128	0.156

The slip velocity as a function of wall shear stress is presented in Figure 8.3 (c). The magnitude of the slip velocity is obtained by Equation (7.5). The slip velocity is presenting two characteristic regions: (1) at $\sigma_{wall} < 4 \ 10^5$ Pa, where the compound with the better filler dispersity (Si40S2.88SA0.8) slips faster on the die wall among the others. (2) at $\sigma_{wall} > 4 \ 10^5$ Pa, the slip velocity curves for all the compounds are overlapping to each other. The concept of the slip mechanism for highly filled suspensions explains the higher magnitude of the slip velocity for the compound with the better dispersed filler (Si40S2.88SA0.8) in the first region, $\sigma_{wall} < 4 \ 10^5$ Pa.[93] That is, the filler can be better distributed in the bulk flow and not aggregate on surface of the die. In contrast, the compounds with poor dispersity of the filler are containing clusters of filler (~0.1 μm) which are difficult to be dispersed by the bulk flow.[93] These aggregates of filler are blended with the grafted polymer molecules on the surface of the die wall and it is speculated[93] that they increase the friction between the bulk flow and the slip layer on the die wall. It is known that the slip layer on the wall is composed of grafted polymer molecules and primary silica particles which generate a super-molecular architecture.[93] These super-molecular structures are either captured in the roughness of die surface or are chemically or/and physically connected with the grafted molecules on the die wall.

8.6. Influence of filler dispersion on extrusion instabilities

In Figure 8.4 the distorted surface of the extrudates from Si40S0.00SA0.8, Si40S1.44SA0.8, and Si40S2.88SA0.8 obtained by the slit die (H = 0.5 mm, L = 30 mm) at T = 100 °C is presented. The SCW λ of the extrusion instability on the surface of the extrudates is quantified by optical microscopy. Figure 8.5 (a) presents the SCW λ as a function of the apparent shear rate at T = 100 °C. The proposed qualitative model,[48] Equation (4.40), fits the experimental of the SCW λ in Figure 8.5 (a). The magnitude of the wavelength increases as the silane amount decreases. Hence, the compounds with the poorest dispersity of the filler (Si40S0.00SA0.8) manifest bigger SCW λ during extrusion, whereas the compound with better dispersity (Si40S2.88SA0.8) present the smallest wavelength. Specifically, between the Si40S0.00SA0.8 and Si40S2.88SA0.8, the difference in SCW λ is approximately ~2.5 times. No obvious difference is observed between Si40S0.70SA0.8 and Si40S1.44SA0.8. An empirical correlation between the SCW λ at $\dot{\gamma}_{app.}$=20 s^{-1} and the amount of silane coupling agent is presented in Figure 8.5 (b). It is observed the SCW λ decreases as silane amount increases with an estimated rate of -0.34.
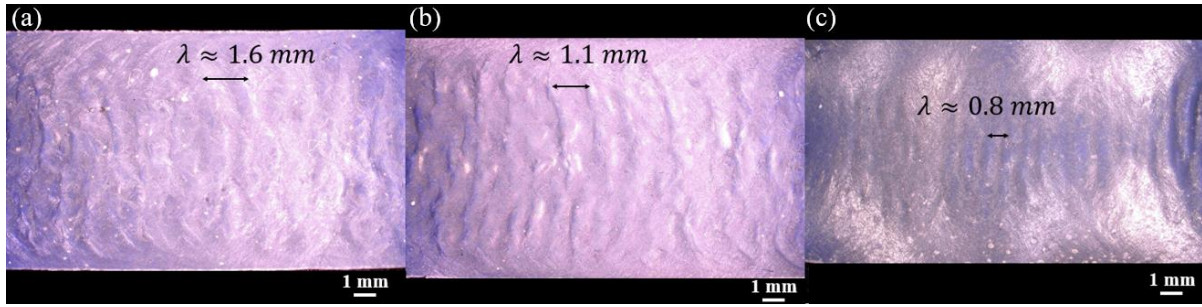
Figure 8.4. Spatial Offline optical analysis of (a) Si40S0.00SA0.8, (b) Si40S1.44SA0.8 and (c) Si40S2.88SA0.8 at $\dot{\gamma}_{app.}$= 10 s^{-1}, and T = 100 °C obtained by slit die L/H = 30/0.5.
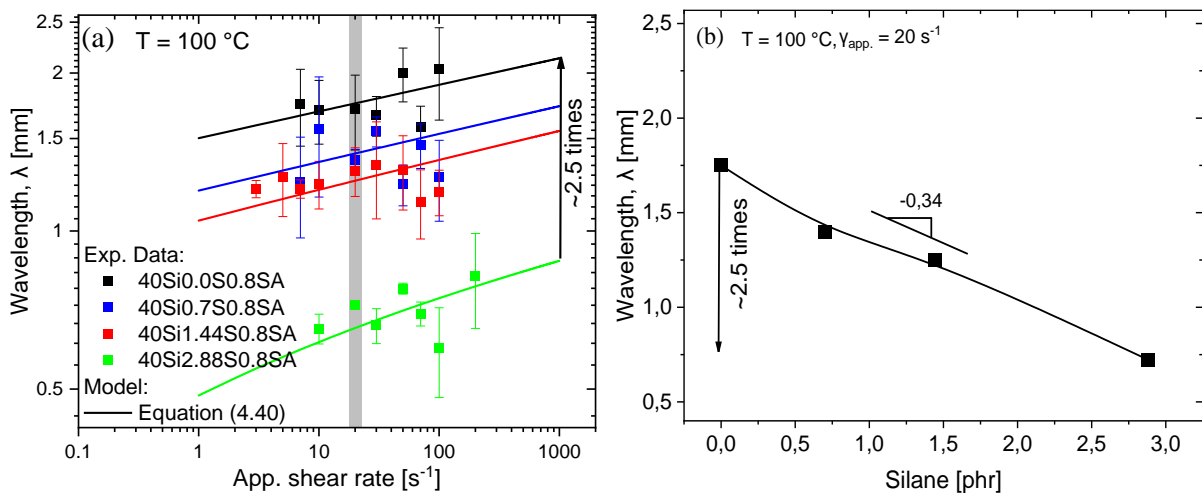
Figure 8.5. (a) Spatial characteristic wavelength as a function of apparent shear rate influenced of silane amount. The experimental data are fitted by Equation (4.40). (b) Spatial characteristic wavelength λ as a function silane amount, obtained at $\dot{\gamma}_{app.}$=20 s^{-1}. The black line guide the eye. The experiments carried by a slit die L/H = 30/0.5 at T = 100 °C.

By using Equation (4.40) in order to fit the experimental data of the SCW λ obtained by the slit die L/H = 30/0.5 at T = 100 °C, the ratio of the extensional Y_s and shear σ_x stresses at the die exit region is obtained. The ratio Y_s/σ_x is later correlated to the characteristic relaxation time τ_d, obtained by the Cross model, and the amount of silane, see Figure 8.6. Figure 8.6 (a) presents that the Y_s/σ_x decreases as the relaxation time increases, that is as the amount of silane increases. This indicates that the lower values of Y_s/σ_x , at 5.6 s of relaxation time (Figure 8.6 (a)) and 0.0 phr of silane (Figure 8.6 (b)), correspond to big a SCW λ on the surface of the extrudate, see the insert of Figure 8.6 (b).
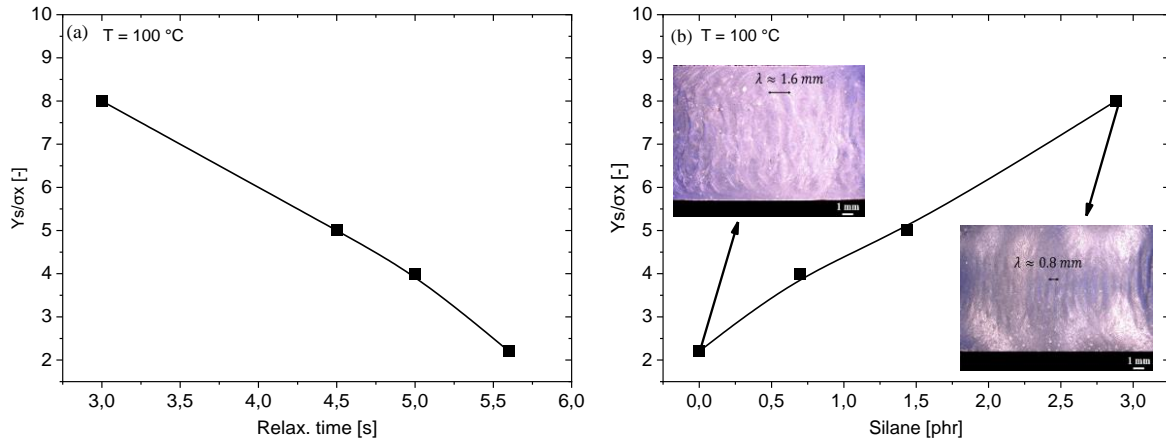
Figure 8.6. Ratio of the extensional (Y_s) and shear (σ_x) stresses at the die exit area obtained by Equation (4.40) for slit dies. The magnitude of Y_s/σ_x is correlated to the (a) relaxation time and (b) silane amount. The inset of (b) displays the extrudates from Figure 8.4. The experiments were carried out at T = 100 °C using slit die with L/H = 30/0.5.

8.7. Conclusion

This chapter studied the influence of the filler dispersion on the wall slippage and on the extrusion flow instabilities of the specific compounds. According to the outcome from the previously reported results the following conclusions can be drawn:

I)   The slip velocity of the compound with well-dispersed filler is larger than the compounds with poor-dispersed filler. Above a critical wall shear stress value, in this case σ_{Wall}>4 10^5 Pa, the slip velocity of all the compounds follow that same trend.

II) The spatial characteristic wavelength is larger for the compound with poorly-dispersed filler and smaller for the compound with well-dispersed filler. Specifically, the difference between the Si40S0.00SA0.8 and Si40S2.88SA0.8 is approximately a factor of ~2.5.

III) The correlation of the Y_s/σ_x with the characteristic relaxation time and the amount of silane indicates that a compound with large relaxation times τ_d and poorly-dispersed filler will have larger spatial wavelength.

IV) The correlation between the Y_s/σ_x and characteristic relaxation time, while the relaxation time increases as Y_s/σ_x decreases, has been mentioned in literature[20, 48] for different systems (neat SBR samples and filled rubber compounds) as well.

9. Conclusion and Outlook

This chapter summarizes and presents correlations based on the previous chapters in order to provide guidelines for the compounding and processing engineers. The correlations are based on the influence of the molecular properties (molecular weight distributions, branching), amount of filler and dispersion agent, and processing parameters (die geometry and extrusion temperatures) on the extrusion performance.

9.1. Factors influencing the extrusion process

This study focused on understanding and predicting the extrusion flow instabilities of neat rubber and filled with silica rubber compounds. In order to understand the influence of each component in the final compound a parameter analysis based on the Table 9.1 has been done. In general, rubber compounds consisted by the neat rubber which is the polymer matrix and several additives, such as filler and dispersion agent. Dispersion agent is used in order to chemically modify the surface of the filler and achieve better filler dispersion. Each of these components have a distinguish influence on the extrusion process. Except of the intrinsic properties of the rubber compound, processing parameters play a crucial role for the extrusion behavior as well. Important processing parameters for the extrusion of a rubber compound are the die geometry and the extrusion temperature.

9.2. Influence of polymer properties on extrusion process

Each of these components (neat rubber, additives and processing parameters) have investigated by the previous chapters and the following correlations were developed. Specifically, the influence of the molecular properties, such as the molecular weight distribution (MWD) and the molecular architecture (linear, branched), of the polymer matrix on extrusion behavior has been investigated, see Chapter 5, and the following correlations are obtained. In Figure 9.1 the correlations between the stress ratio Y_s/σ_x at the die exit region, spatial characteristic wavelength (SCW) λ, the characteristic relaxation time of the polymers (Figure 9.1 (a)), and

Table 9.1. Factors which are influencing the extrusion flow instabilities. Investigated by this study.

Factors		
Polymer properties	Additives	Processing parameters
Molecular weight distribution (MWD)	Filler volume fraction	Die geometry
Molecular architecture (linear, branched)	Filler dispersion agent	Extrusion temperature

the phase angle δ (Figure 9.1 (b)), that is the fingerprint of the molecular architecture, are presented. The physical interpretation of the following correlations is based on the theoretical concept for the origin of surface regular distortion on extrudate, sharkskin. The theoretical molecular mechanism for the origin of sharkskin is based on the extensional stress applied only on the outer surface of the extrudate. Hence, a perpendicular propagation of this extensional stress towards to the flow is generated and a tear behavior is initiated. Based on this, the extrusion flow can be categorized into two theoretical layers, the surface layer where the propagation of the extensional stress causes the tearing behavior and the core layer where the shear stress is dominant. Within the surface layer where the intensive extensional stress is dominant the macromolecular chains are forced to a fully stretched configuration. At the time that the macromolecular chain flows away from this extensional deformation starts to form a recoil configuration. This relaxation process from a fully stretched to a recoil conformation of the macromolecular chain possibly generates the well-developed pattern formation on the extrudate surface, so called sharkskin.

In Figure 9.1 (a) the ratio Y_s/σ_x and the SCW λ as a function of characteristic relaxation time of the polymers τ_d are presented. The SCW λ is quantified by optical microscopy, the stress ratio Y_s/σ_x is obtained by the fitting of Equation (4.39) and (4.40) on the experimental data of the SCW λ. The magnitude of the stress ratio Y_s/σ_x decreases as the τ_d increases, at the same time the SCW λ increases as the τ_d increases, as well. These trends agree with the theoretical concepts for the origin of sharkskin. The long relaxation time τ_d slow down the return to a

recoil formation from a fully stretched configuration of the macromolecular chains. That is, the oscillation last longer so the SCW λ becomes larger.
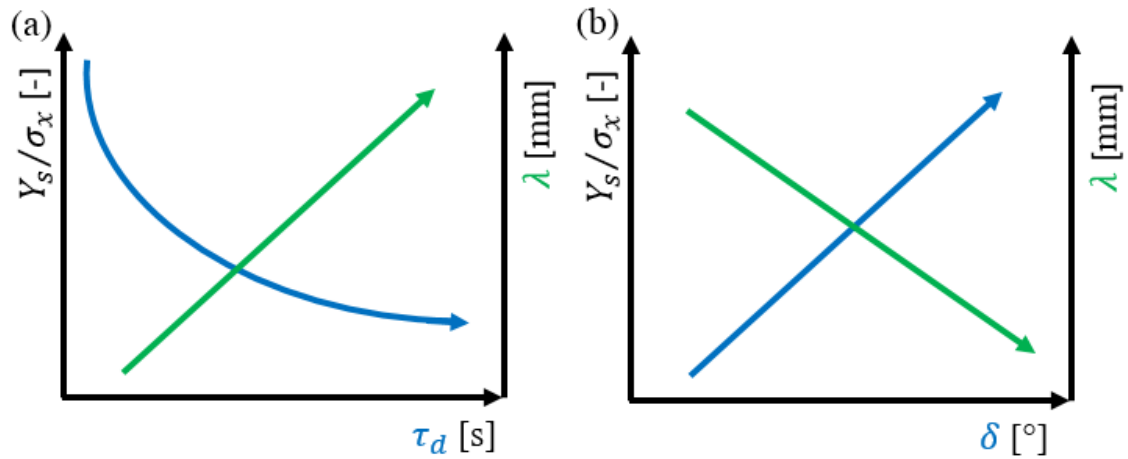
Figure 9.1. Practical correlations based on chapter 5. Influence of molecular properties on extrusion flow instabilities. (a) Y_s/σ_x versus characteristic relaxation time, τ_d and spatial characteristic wavelength versus λ versus characteristic relaxation time, τ_d. (b) Y_s/σ_x versus phase angle, δ and spatial characteristic wavelength λ versus characteristic relaxation time, δ.

In Figure 9.1 (b) the stress ratio Y_s/σ_x and the SCW λ as a function of the phase angle δ are presented. In general, the magnitude values of the phase angle δ indicate the molecular architecture (linear, branched) of the macromolecule. Low magnitude values of δ imply a more branched polymer than higher magnitude values, see Figure 5.4. The magnitude of the stress ratio Y_s/σ_x increases as the phase angle δ increases, at the same time the SCW λ decreases as the phase angle δ increases. This trend can be explained based on the theoretical concept for the origin of sharkskin as well. The branched molecules present larges SCW λ in comparison to linear, due to their complex relaxation process, which possibly explained by the complex recoil process from a fully stretched configuration.

9.3. Influence of filler and filler dispersion on extrusion process

In Figure 9.2 correlations between the additives (volume fraction of filler and dispersion agent) of the rubber compound and the extrusion performance are presented. Specifically, Figure 9.2 (a) displays the stress ratio Y_s/σ_x and the SCW λ as a function of the volume fraction of filler, φ_{filler}. The magnitude of the stress ratio Y_s/σ_x decreases as the volume fraction of filler, φ_{filler} increases, at the same time the SCW λ increases as the volume fraction of filler, φ_{filler} increases. This is explained based on the characteristic relaxation time τ_d of the compound and on the concept for the origin of sharkskin. Increasing the φ_{filler} in the compound, the characteristic relaxation time τ_d of the compound increases as well, see Figure 7.4 (b). Hence, the oscillation for the formation of the sharkskin last longer, so the SCW λ becomes larger.
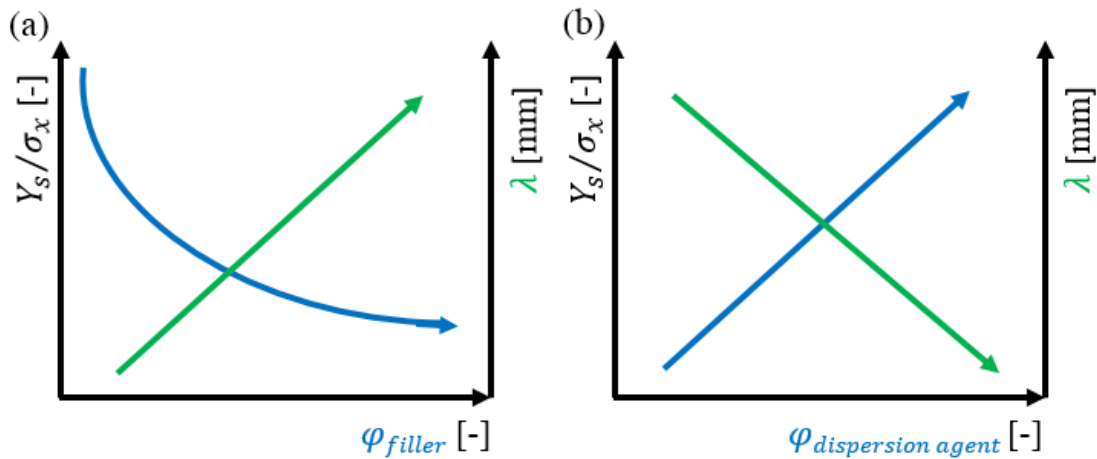
Figure 9.2. Practical correlations based on chapter 7 and 8. Influence of filler and dispersion agent volume fraction on extrusion flow instabilities. (a) Y_s/σ_x versus filler volume fraction, φ_{filler} and spatial characteristic wavelength versus λ versus filler volume fraction, φ_{filler}. (b) Y_s/σ_x versus dispersion agent volume fraction, $\varphi_{dispersion\ agent}$ and spatial characteristic wavelength λ versus dispersion agent volume fraction, $\varphi_{dispersion\ agent}$.

In Figure 9.2 (b) the stress ratio Y_s/σ_x and the SCW λ as a function of the volume fraction of dispersion agent, $\varphi_{dispersion\ agent}$ is presented. The magnitude of the stress ratio Y_s/σ_x increases as the volume fraction of dispersion agent $\varphi_{dispersion\ agent}$ increases, at the same time the SCW λ decreases as the volume fraction of filler, φ_{filler} increases. Increasing the dispersion agent in the compound, a better filler dispersion is achieved. By dispersing better the

filler inside the polymer matrix, shorter characteristic relaxation time τ_d is achieved, see Table 8.2. Hence, by increasing the dispersion agent in the compound, shorter characteristic relaxation time τ_d is achieved, that is shorter SCW λ.

9.4. Influence of processing parameter on extrusion process

Figure 9.3 presents correlations between processing parameters (extrusion die dimensions and temperature) and extrusion performance. Specifically, Figure 9.3 (a) displays the stress ratio Y_s/σ_x and the SCW λ as a function of the characteristic dimension, diameter D for round capillary and height H for slit dies, of the extrusion die. The magnitude of the stress ratio Y_s/σ_x decreases as the characteristic dimension of the die increases, at the same time the SCW λ increases as the characteristic dimension of the extrusion die increases. This can be explained based on the theoretical concept for the origin of sharkskin and specifically the "two layer" model.
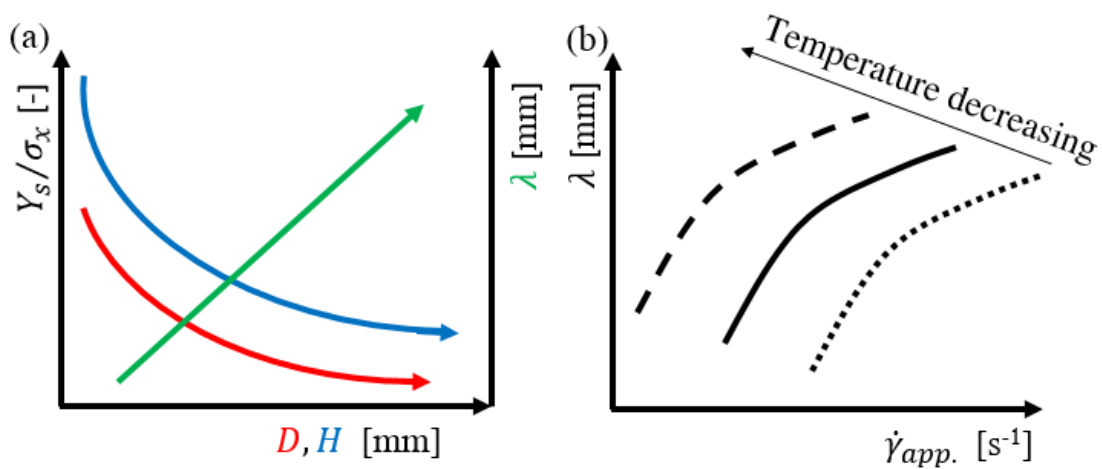
Figure 9.3. Practical correlations based on chapter 6. Influence of extrusion parameters on extrusion flow instabilities. (a) Y_s/σ_x versus characteristic dimension of extrusion die (diameter D and height H) and spatial characteristic wavelength versus λ versus characteristic dimension of extrusion die. (b) Spatial characteristic wavelength λ versus apparent shear rate $\dot{\gamma}_{app.}$ at three different temperatures.

The behavior of the stress ratio Y_s/σ_x as the characteristic dimension of the die increases is explained based on the theoretical core layer of the extrudate which is increasing as well. For

instance, during the same applied apparent shear rate, the extrudate velocity ($V_{extr.}^{Capillary}$ = $(D/8)\dot{\gamma}_{app.}$, $V_{extr.}^{Slit}$ = $(H/6)\dot{\gamma}_{app.}$) is increased as the height H or the diameter D of the die increases. Thus, the mass flux of the theoretical cross section area of the core layer is increased as the characteristic dimension of the die increases. Visual evidence can be found in Figure 6.5 and 6.7.

In Figure 9.3 (b) the stress ratio Y_s/σ_x and the SCW λ as a function of the apparent shear rate $\dot{\gamma}_{app.}$ at three different temperatures are presented. At the same apparent shear rate $\dot{\gamma}_{app.}$ the SCW λ increases as the temperature decreases. This is again explained based on the theoretical concept for the origin of sharkskin and its dependency from the characteristic relaxation time τ_d. It is known that the decrease of the temperature increases the characteristic relaxation time τ_d. Hence, based on the Figure 9.1 (a) and Figure 9.3 (b) the SCW λ increases.

9.5. Conclusions

Within this chapter practical correlations for the molecular properties and extrusion parameters with the extrusion performance, that is the extrusion flow instabilities were presented. The practical correlations which have been drawn are presented here:

I)   By increasing the characteristic relaxation time τ_d of the neat rubber, a long spatial characteristic wavelength (SCW) λ is developed at the exit of the extrusion die.

II) Branched macromolecules present long SCW λ.

III) By increasing the volume filler fraction φ_{filler} of the compound, the characteristic relaxation time τ_d of the compound increases, hence a long SCW λ is developed at the exit of the extrusion die.

IV) By increasing the dispersion agent volume fraction $\varphi_{dispersion\ agent}$ of the compound, the characteristic relaxation time τ_d of the compound decreases, hence a short SCW λ is developed at the exit of the extrusion die.

V) By increasing the characteristic dimension of the die (D or H) the SCW λ increases.

VI) By decreasing the extrusion temperature, the characteristic relaxation time τ_d increases, hence a long SCW λ is developed at the exit of the extrusion die.

References

[1] A. Leonov, A. Prokunin, Nonlinear Phenomena in Flows of Viscoelastic Polymer Fluids, Chapman & Hall, 1994.

[2] M. M. Denn, Ann. Rev. Fluid Mech. 2001, 33, 265.

[3] S. G. Hatzikiriakos, Prog. Polym. Sci. 2012, 37, 624.

[4] S. G. Hatzikiriakos, K. Migler, Polymer Processing Instabilities. Control and Understanding, Marcel Dekker 2005.

[5] R. Koopmans, C. F. J. den Doelder, J. Molenaar, Polymer Melt Fracture, CRC Press, Boca Raton 2011.

[6] S. Q. Wang, Nonlinear Polymer Rheology: Macroscopic Phenomenology and Molecular Foundation, John Wiley & Sons 2017.

[7] S. Q. Wang, in Polymers in Confined Environments, Vol. 1 (Eds: K. Binder, S. Granick, K. Binder, P. G. de Gennes, E. P. Giannelis, G. S. Grest, H. Hervet, R. Krishnamoorti, L. Léger, E. Manias, E. Raphaël, S.Q. Wang), Springer-Verlag Berlin Heidelberg 1999, Ch. 6.

[8] I. F. C. Naue, Development of Improved Rheometric Tools and Their Application on the Non-Newtonian Rheology of Polymeric Fluids, PhD Thesis, Karlsruhe Institute of Technology (KIT), Karlsruhe, Germany 2013.

[9] C. F. J. den Doelder, Design and Implementation of Polymer Melt Fracture Models, PhD Thesis, Eindhoven University of Technology, Eindhoven, Netherlands, 1999.

[10] D. Tang, F. H. Marchesini, L. Cardon, D. R. D'hooge, Macromol. Mater. Eng. 2020, 305, 2000340.

[11] A. Gansen, M. Řehoř, C. Sill, P. Polińska, S. Westermann, J. Dheur, J. S. Hale, J. Balle, J. Appl. Polym. Sci. 2020, 137, 48806.

[12] M. Jugo Viloria, Analysis and Comprehension of Flow Instabilities of Elastomer Compound, PhD Thesis, Université de recherché Paris Sciences et Lettres – PSL Research University, Paris, France 2017.

[13] M. Jugo Viloria, M. Valtier, B. Vergnes, J. Rheol. 2017, 61, 1085

[14] C. K. Georgantopoulos, I. F. C. Naue, A. Causa, L. Garro, M. Wilhelm, Annu. Trans. Nordic Rheol. Soc. 2019, 27, 151.

[15] C. K. Georgantopoulos, M. K. Esfahani, C. Botha, I. F. C. Naue, N. Dingenouts, A. Causa, R. Kádár, M. Wilhelm, Macromol. Mater. Eng. 2021, 306, 2000801.

[16] C. K. Georgantopoulos, M. K. Esfahani, C. Botha, M. A. Pollard, I. F. C. Naue, A. Causa, R. Kádár, M. Wilhelm, Phys. Fluids 2021, 33, 093108.

[17] I. F .C. Naue, R. Kádár, M. Wilhelm, Macromol. Mater. Eng. 2015, 300, 1141.

[18] H. Palza, S. Filipe, I. F. C. Naue, M. Wilhelm, Polymer 2010, 51, 522.

[19] H. Palza, B. Reznik, M. Kappes, F. Hennrich, I. F. C. Naue, M. Wilhelm, Polymer 2010, 51, 3753.

[20] C. K. Georgantopoulos, M. K. Esfahani, I. F. C. Naue, M. Wilhelm, R. Kádár, Macromol. Mater. Eng. 2022, in preparation.

[21] N. El Kissi, J. –M. Piau, J. Non-Newtonian Fluid Mech. 1990, 37, 55.

[22] F. N. Cogswell, J. Non-Newtonian Fluid Mech. 1977, 2, 17.

[23] S. Q. Wang, P. A. Drda, Y. W. Inn, J. Rheol. 1996, 40, 875.

[24] S. Q. Wang, P. A. Drda, Macromol. Chem. Phys. 1997, 198, 673.

[25] J. R. Barone, N. Plucktaveesak, S. Q. Wang, J. Rheol. 1998, 42, 813.

[26] Y. W. Inn, R. J. Fisher, M. T. Shaw, Rheol. Acta 1998, 37, 573.

[27] E. Miller, J. P. Rothstein, Rheol. Acta 2004, 44, 160.

[28] E. Miller, S. J. Lee, J. P. Rothstein, Rheol. Acta 2006, 45, 943.

[29] N. El Kissi, L. Leger, J. –M. Piau, A. Mezghani, J. Non-Newtonian Fluid Mech. 1994, 52, 249.

[30] N. El Kissi, J. –M. Piau, F. Toussaint, J. Non-Newtonian Fluid Mech. 1997, 68, 2.

[31] J. M. Piau, N. El Kissi, B. Tremblay, J. Non-Newtonian Fluid Mech. 1990, 34, 145.

[32] J. M. Piau, N. El Kissi, A. Mezghani, J. Non-Newtonian Fluid Mech. 1995, 59, 11.

[33] C. Venet, B. Vergnes, J. Non-Newtonian Fluid Mech. 2000, 93, 117.

[34] K. B. Migler, Y. Son, F. Qiao, F. Flynn, J. Rheol. 2002, 46, 383.

[35] T. I. Burghelea, H. J. Griess, H. Münstedt, J. Non-Newtonian Fluid Mech. 2010, 165, 1093.

[36] T. I. Burghelea, H. J. Griess, H. Münstedt, J. Non-Newtonian Fluid Mech. 2012, 173, 87.

[37] G. Karapetsas, J. Tsamopoulos, Phys. Fluids 2013, 25, 093105.

[38] D. Pettas, G. Karapetsas, Y. Dimakopoulos, J. Tsamopoulos, J. Non-Newtonian Fluid Mech. 2015, 224, 61.

[39] S. Varchanis, D. Pettas, Y. Dimakopoulos, J. Tsamopoulos, Phys. Rev. Let. 2021, 127, 088001.

[40] C. Botha, J. Höpfner, B. Mayerhöfer, M. Wilhelm, Polym. Chem. 2019, 10, 2230.

[41] J. M. Dealy and J. Wang, Melt rheology and its application in the plastic industry, 2nd edition, Spingel Science + Business Media Dordrecht 2013.

[42] F. A. Morrison, Understanding Rheology, Oxford University Press 2001.

[43] R. Kádár, I. F. C. Naue, M. Wilhelm, Annu. Trans. Nordic Rheol. Soc. 2014, 22, 153.

[44] A. Provenzale, L. Smith, R. Vio, G. Murante, Physica D, 1992, 58, 31.

[45] C. S. Dutcher, S. J. Muller, J. Fluid Mech. 2009, 641, 85.

[46] R. Kádár, C. Balan, Europ. J. Mech. B. Fluids 2012, 31, 158.

[47] H. Ovaici, M. R. Mackley, G. H. McKinley, S. J. Crook, J. Rheo. 1998, 42, 125.

[48] C. K. Georgantopoulos, M. K. Esfahani, M. A. Pollard, I. F. C. Naue, A. Causa, R. Kádár, M. Wilhelm, Macromol. Mater. Eng. 2022, accepted.

[49] W. Burchard, Solution Properties of Branched Macromolecules, Springer Verlag 1999.

[50] J. Brandrup, E. H. Immergut, and E. A. Grulke, Polymer Handbook, 4th edition, John 12 Wiley & Sons 1999.

[51] M. Rubinstein, R. H. Colby, J. Chem. Phys. 1988, 89, 8.

[52] M. Doi, S. F. Edwards, J. Chem. Soc. Faraday Trans. 1987, 274, 1802.

[53] L. J. Fetters, D. J. Lohse, S. T. Milner, Macromol. 1999, 32, 6847.

[54] J. E. Mark, Physical Properties of Polymer Handbook, Springer Science + Business Media, LLC 2007, Ch. 5, p. 447.

[55] S. Trinkle, P. Walter, C. Friedrich, Rheol. Acta 2001, 40, 322.

[56] S. Trinkle, P. Walter, C. Friedrich, Rheol. Acta 2002, 41, 103.

[57] F. J. Stadler, A. Nishioka, J. Stange, K. Koyama, H. Münstedt, Rheol. Acta 2007, 46, 1003.

[58] F. J. Stadler, C. Piel, W. Kaminsky, H. Münstedt, Macromol. Symp. 2006, 236, 209.

[59] J. F. T. Pittman, J. Proc. Mech. Eng. 2011, 4, 280.

[60] J. Roovers, P. M. Toporowski, Macromol. 1987, 20, 9.

[61] R. G. Larson, Macromol. 2001, 34, 13.

[62] M. T. I. Juliani, L. A. Archer, S. K. Varshney, Macromol. 2001, 34, 18.

[63] X. Chen, M. S. Rahman, H. Lee, J. Mays, T. Chang, R. Larson, Macromol. 2011, 44, 19.

[64] P. Cox, E. H. Merz, J. Polym. Sci. 1958, 28, 619.

[65] Y. W. Inn, J. Rheol. 2013, 57, 393.

[66] M. Ebrahimi, M. Ansari, S. G. Hatzikiriakos, J. Rheol. 2015, 59, 885.

[67] M. Ebrahimi, M. Ansari, Y. W. Inn, S. G. Hatzikiriakos, Phys. Fluids 2016, 28, 093101.

[68] D. Ferry, Viscoelastic Properties of Polymers, 3rd edition, Wiley 1980.

[69] J. Kiesewetter, A. Wehmeier, Evonik Advantages in the Production of Green and All-season Tires for SUVs, International Tyre Exhibition and Conference (ITEC), Akron, September 2018.

[70] M. Castellano, L. Conzatti, A. Turturro, G. Costa, G. Busca, J. Phys. Chem. B 2007, 111, 4495.

[71] K. W. Stockelhuber, A. S. Svistkov, A. G. Pelevin, G. Heinrich, Macromol. 2001, 44, 4366.

[72] Z. Tang, J. Huang, X. Wu, B. Guo, L. Zhang, F. Liu, Ind. Eng. Chem. Res. 2015, 54, 10747.

[73] V. Arrighi, I. J. McEwen, H. Qian, M. B. S. Prieto, Polymer 2003, 44, 6259.

[74] I. M. Krieger, T. J. Dougherty, Trans. Soc. Rheol. 1959, 3, 137.

[75] M. M. Rueda, M.C. Auscher, R. Fulchiron, T. Périé, G. Martin, P. Sonntag, P. Cassagnau, Prog. Polym. Sci. 2017, 66, 22.

[76] E. Guth, O. Gold, Phys. Rev. 1938, 53, 322.

[77] S. H. Maron, P. E. Pierce, J. Coll. Sci. 1956, 11, 80.

[78] J. L. Leblanc, Rub. Chem. Tech. 1981, 54, 5.

[79] J. L. Leblanc, J. Appl. Polym. Sci. 2012, 126, 408.

[80] J. L. Leblanc, M. Putman, E. Pianhanuruk, J. Appl. Polym. Sci. 2011, 121, 1096.

[81] J. L. Leblanc, G. Nijman, J. Appl. Polym. Sci. 2009, 112, 1128.

[82] J. L. Leblanc, Prog. Polym. Sci. 2002, 27, 627.

[83] L. Schwab, M. Hojdis, J. Lacayo, M. Wilhelm, Macromol. Mater. Eng. 2016, 301, 457.

[84] S. Nie, J. Lacayo-Pineda, M. Wilhelm, Soft Mater. 2019, 17, 3.

[85] Z. Zhu, T. Thompson, S. Q. Wang, E. D. von Meerwall, A. Halasa, Macromol. 2005, 38, 8816.

[86] J. L. Leblanc, Filled polymers science and industrial applications, CRC Press, Boca Raton, 2010.

[87] A. Mongruel, M. Cartault, J. Rheol. 2006, 115, 50.

[88] H. M. Hassanabadi, M. Wilhelm, D. Rodrigue, Rheol. Acta 2014, 53, 869.

[89] M. Sahimi, Applications of Percolation Theory, Taylor & Francis, 1994.

[90] A. A. Moud, J. Poisson, Z. M. Hudson, S. G. Hatzikirakos, Phys. Fluids 2021, 33, 053105.

[91] P. Wilms, J. Wieringa, T. Blijdenstein, K. van Malssen, R. Kohlus, Rheol. Acta 2021, 60, 423.

[92] J. He, S. S. Lee, D. M. Kalyon, J. Rheol. 2019, 63, 19.

[93] D. M. Kalyon, J. Rheol. 2005, 49, 621.

[94] Brochard-Wyart, P. G. de Gennes, Langmuir 1992, 8, 3033.

[95] N. Ghahramani, S. Zhang, K. A. Lyer, A. K. Doufas, S. G. Hatzikiriakos, Polym. Eng. Sci. 2021, 61, 4.

[96] M. Jugo Viloria, M. Valtier, B. Vergnes, J. Rheol. 2017, 61, 1085.

[97] M. Jugo Viloria, Analysis and Comprehension of Flow Instabilities of Elastomer Compound, PhD Thesis, Université de recherché Paris Sciences et Lettres – PSL Research University, Paris, France 2017.

[98] V. Hristov, J. Vlachopoulos, Rheol. Acta 2007, 46, 773.

[99] V. Hristov, Compos. Interf. 2009, 16, 731.

[100] O. Delgadillo-Velázquez, G. Georgiou, M. Sentmanat, S. G. Hatzikiriakos, Polym. Eng. Sci. 2008, 48, 405.

[101] M. Ansari, S. G. Hatzikiriakos, A. M. Sukhadia, D. C. Rohlfing, Polym. Eng. Sci. 2012, 52, 795.

[102] E. N. Skountzos, D. G. Tsalikis, P. S. Stephanou, V. G. Mavrantzas, Macromol. 2021, 54, 4470.

List of Figures

List of Tables

Acknowledgements

Appendix A

Figure A1. The 2D SEC-NMR data for (a) SBR A, (b) SBR B and (c) SBR C in CHCl3, with the corresponding 1D elugrams and 1D 1H-NMR solute spectra. Data acquisition per spectrum, 90° pulse, 500 ms repetition time, 4 scans/spectrum. The SEC is equipped with a semi-preparative column with length of 300 mm and inner diameter of 20 mm, enabling the MWD and chemical composition correlation. The experimental data of the (b) SBR B have been adapted from C. K. Georgantopoulos et al., *Physics of Fluids* 33, *093108*, **2021**, Figure 1.[16] Reproduced with permission from AIP Publishing, No. 5231930652686.
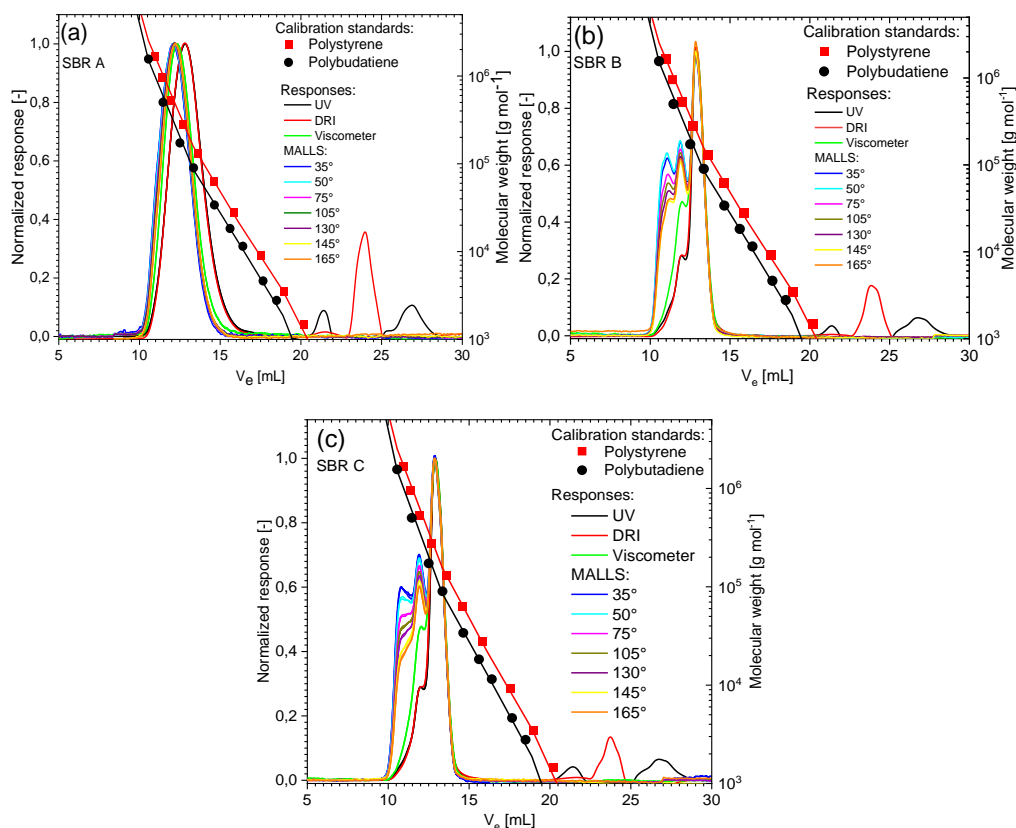
Figure A2. Quadruple detection SEC for the (a) SBR A, (b) SBR B, and (c). Ultra-violet at 254 nm (UV), differential refractive index (DRI), viscometer, and multi-angle light-scattering (MALS). The accompanying overlay illustrates elution of linear homopolymer standards of polystyrene (red squares) and polybutadiene (black circles). This SEC is equipped with an analytical column with length of 300 mm and inner diameter of 8 mm. Therefore, the elution volume changes from the Fig. 1 (b). Part of the experimental data of the (b) SBR B have been adapted from C. K. Georgantopoulos et al., *Physics of Fluids* 33, *093108*, **2021**, Figure 2.[16] Reproduced with permission from AIP Publishing, No. 5231930652686.

Appendix B
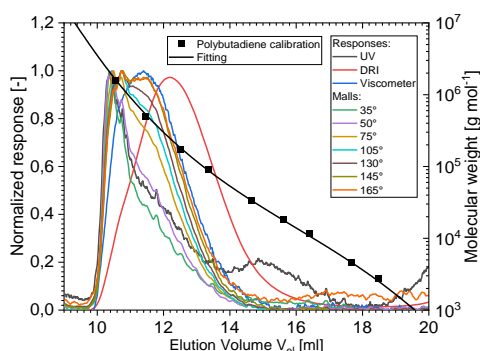
Figure B1. Quadruple-detection SEC for the investigated polybutadiene sample. Four different responses are shown: ultra-violet at 254 nm (UV), differential refractive index (DRI), viscometer, and multi-angle laser light-scattering (MALLS). The accompanying overlay illustrates elution of linear homopolymer standards of polybutadiene (black squares). Adapted from C. K. Georgantopoulos et al., *Macromolecular Material and Engineering* submitted, **2022**, Figure S1.[48]

Table B1. Maxwell modes of the investigated polybutadiene at 100 °C.

Modes	λ_i [s]	G_i [kPa]
1	23,160	13,24
2	2,670	23,37
3	0,310	84,14
4	0,035	182,20
5	0,004	275,60

Adapted from C. K. Georgantopoulos et al., *Macromolecular Material and Engineering* submitted, **2022**, Table A1 from Appendix A.[48]

Figure B2. The computer-aided designs (CAD) for both slit dies with cross-section profile (a) *slit-die-simple-profile* and (b) *slit-die-scalar-profile.* Adapted from C. K. Georgantopoulos et al., *Macromolecular Material and Engineering* submitted, **2022**, Figure S2.[48]

Appendix C

Table C1. The 6-Maxwell modes of the SBR polymer matrix at T = 100 °C.

Modes	λ_i [s]	G_i [kPa]
1	2364.25	2.8413E-23
2	147.913	2707.06
3	9.2538	14048.1
4	0.57894	120094
5	0.0362199	467200
6	0.00266	220651

In the die exit region, under similar extrusion conditions, the same numerical value for the apparent shear rate $\dot{\gamma}_{app.}$, assuming that the characteristic time periodicity τ^* of the extrusion flow instability is material dependent, the volume (V) of the material that leaves the die exit during the time τ^* at given $\dot{\gamma}_{app.}$ for the slit and capillary dies is given by Equation (C1) and (C2), respectively:

$$\mathrm{V}^{slit} = Q^{slit}\tau^*, \tag{C1}$$

$$\mathrm{V}^{capillary} = Q^{capillary}\tau^*, \tag{C2}$$

where Q is the volumetric flow rate at mm^3 s^{-1}. The extrudate velocity for the slit and capillary dies is given by Equation (C3) and (C4), respectively.

$$V_{extr.}^{slit} = (H/6)\dot{\gamma}_{app.} \tag{C3}$$

$$V_{extr.}^{capillary} = (D/8)\dot{\gamma}_{app.} \tag{C4}$$

Using Equation (C3) and (C4) the Equation (C1) and (C2) can be rewritten as,

$$\mathrm{V}^{slit} = A^{slit}(H/6)\dot{\gamma}_{app.}\tau^*, \tag{C5}$$

$$\mathrm{V}^{capillary} = A^{capillary}(D/8)\dot{\gamma}_{app.}\tau^*, \tag{C6}$$

where H is the height of the slit die, D is the diameter of the capillary die and A is the cross-section are of the respective die. Knowing that H = 0.5 mm and D = 2 mm, the Equation (C5) and (C6) yield to $\mathrm{V}^{slit} = 0.42\dot{\gamma}_{app.}\tau^*$ and $\mathrm{V}^{capillary} = 0.785\dot{\gamma}_{app.}\tau^*$. Defining the surface area-to-volume (SA/V) aspect ratio by Equation (C7) and (C8),

$$\mathrm{SA}^{slit}/\mathrm{V}^{slit} = (HW)/\left(0.42\dot{\gamma}_{app.}\tau^*\right) = (11.9)/\left(\dot{\gamma}_{app.}\tau^*\right), \tag{C7}$$

$$\mathrm{SA}^{capillary}/\mathrm{V}^{capillary} = \left(\pi r^2\right)/\left(0.785\dot{\gamma}_{app.}\tau^*\right) = (4)/\left(\dot{\gamma}_{app.}\tau^*\right), \tag{C8}$$

and then taking the ratio of (C7) and (C8), using the previous reported assumption, leads to $\mathrm{SA}^{slit}/\mathrm{V}^{slit} > \mathrm{SA}^{capillary}/\mathrm{V}^{capillary}$.

Publications

PUBLICATIONS IN INTERNATIONAL JOURNALS

1. C. K. Georgantopoulos, I. F. C. Naue, A. Causa, L. Garro, and M. Wilhelm, "Investigation of Melt Flow Instabilities in SBR: Influence of MWD and Microstructure at In Situ Pressure Fluctuations as Detected by Capillary Rheology" *ANNUAL TRANSACTIONS OF THE NORDIC RHEOLOGY SOCIETY*, 151, 27, 2019.

2. C. K. Georgantopoulos, M. K. Esfahani, C. Botha, I. F. C. Naue, N. Dingenouts, A. Causa, R. Kádár, and M. Wilhelm, "Mechano-optical characterization of extrusion flow instabilities in styrene-butadiene rubbers: investigating the influence of molecular properties and die geometry", *Macromol. Mater. Eng.*, 306, 2, 2021.

3. C. K. Georgantopoulos, M. K. Esfahani, C. Botha, M. A. Pollard, I. F. C. Naue, A. Causa, R. Kádár, M. Wilhelm, "Modeling the spatial characteristics of extrusion flow instabilities for styrene-butadiene rubbers: investigating the influence of molecular weight distribution, molecular architecture, and temperature", *Phys. Fluids*, 33, 9, 2021.

4. M. K. Esfahani, C. K. Georgantopoulos, I. F. C. Naue, J. Sunder, M. Wilhelm, "A new slit-radial die for simultaneously measuring steady state shear viscosity and first normal stress difference of viscoelastic liquids via capillary rheometry", *J. Appl. Polym. Sci.*, 139, 18, 2022.

5. Christos K. Georgantopoulos, Masood K. Esfahani, Michael A. Pollard, Ingo F. C. Naue, Andrea Causa, Roland Kádár, and Manfred Wilhelm, "Derivation of a qualitative model for the spatial characteristic wavelength of extrusion flow instabilities: Investigation of a polybutadiene rubber through capillary, slit and complex geometry extrusion dies", *Macromol. Mater. Eng.*, accepted, 2022.

6. Christos K. Georgantopoulos, Masood K. Esfahani, Ingo F. C. Naue, Manfred Wilhelm, and Roland Kádár, "Role of molecular architecture and temperature on extrusion melt flow instabilities of two industrial LLDPE and LDPE polyethylenes investigated by capillary rheology, high pressure sensitivity slit die and optical analysis", *J. Appl. Polym. Sci.*, submitted, 2022.

PUBLICATIONS IN CONFERENCEs (Presenter in bold)

Oral presentations:

1. Ch. Tsimouri, C. K. Georgantopoulos, **P. S. Stephanou**, and V. G. Mavrantzas, "Derivation of a recently proposed CCR model through the use of non-equilibrium thermodynamics", *12th Annual European Rheology Conference (AERC 2017)*, Copenhagen, Denmark, April 3-6 (2017).

2. **C. K. Georgantopoulos**, E. M. Khabazian, I. F. C. Naue, A. Causa, R. Kádár and M. Wilhelm, "Rheological investigation of extrusion flow for styrene-butadiene rubber: highly pressure sensitive slit die in comparison with capillary die", *Nordic Rheology Society Meeting*, online, 25th August (2020).

3. **C. K. Georgantopoulos**, E. M. Khabazian, I. F. C. Naue, A. Causa, R. Kádár and M. Wilhelm, "Characterization of flow instabilities for SBR materials during extrusion flow: experiments and modeling", *18th International Congress of Rheology*, online, 13 – 18 December (2020).

4. **C. K. Georgantopoulos**, E. M. Khabazian, I. F. C. Naue, A. Causa, R. Kádár and M. Wilhelm," Mechano-optical characterization of extrusion flow instabilities in styrene-butadiene rubbers: investigating the influence of molecular properties and die geometry", *Annual European Rheology Conference (AERC 2021)*, online, 13th April (2021).

5. **M. K. Esfahani**, C. K. Georgantopoulos, I. F. C. Naue, and M. Wilhelm, "Measuring elongational viscosity of LDPE with elongational viscosity fixture (EVF) up to a Hencky strain of $\varepsilon = 6.3$", *Annual European Rheology Conference (AERC 2021)*, online, 13th April (2021).

6. **C. K. Georgantopoulos**, E. M. Khabazian, I. F. C. Naue, A. Causa, R. Kádár and M. Wilhelm, "Characterization of flow instabilities of model filled systems: experiments and modeling", *International Rubber Conference*, online, 29th June (2021).

7. **C. K. Georgantopoulos**, E. M. Khabazian, I. F. C. Naue, A. Causa, R. Kádár and M. Wilhelm, "Derivation of qualitative model to predict the extrusion flow instabilities: investigating the influence of die geometry", *Nordic Rheology Society Meeting*, online, 18th August (2021).

8. **C. K. Georgantopoulos**, E. M. Khabazian, I. F. C. Naue, A. Causa, R. Kádár and M. Wilhelm, "Modeling of extrusion flow instabilities of polymer nanocomposites: Influence of filler amount", 13th Hellenic Polymer Society International Conference, Athens, Greece, 12-16 December (2021).

9. **C. K. Georgantopoulos**, E. M. Khabazian, I. F. C. Naue, A. Causa, R. Kádár and M. Wilhelm, "Wall Slip and Extrusion Behavior of Rubber Compounds: Influence of Silane Amount", 2nd International Symposium of Plastic Technology, Aachen, Germany, 12-15 March (2022).

10. **M. K. Esfahani**, C. K. Georgantopoulos, I. F. C. Naue, J. Sunder, and M. Wilhelm, "Karlsruhe die, simultaneously measuring steady state shear and first normal stress difference coefficient of LDPE via capillary rheometer at high shear rates", 2nd International Symposium of Plastic Technology, Aachen, Germany, 12-15 March (2022).

Posters presentations:

1. P. K. Vafeas, **C. K. Georgantopoulos**, C. P. Giannopoulos, "On the connection between Stokes and Papkovich-Neuber spherical eigenfunctions in Stokes Flow'', 10th Panhellenic Chemical Engineers' Conference, Patra, Greece, 4-6 June (2015) [in Greek].

2. **I. Ch. Tsimouri**, C. K. Georgantopoulos, P. S. Stephanou, and V. G. Mavrantzas, "Derivation of a recently proposed CCR model through the use of non-equilibrium thermodynamics", 11th Hellenic Polymer Society International Conference, Heraklion, Crete, Greece, 3-5 November (2016).

3. **C. K. Georgantopoulos**, I. Ch. Tsimouri, P. S. Stephanou, and V. G. Mavrantzas, "Derivation of modern rheological constitutive models through the use of non-equilibrium thermodynamics", *11th Panhellenic Chemical Engineers' Conference,* Thessaloniki, Greece, 25-27 May (2017) [in Greek].

4. **I. Ch. Tsimouri**, C. K. Georgantopoulos, P. S. Stephanou, and V. G. Mavrantzas, "Derivation of a recently proposed CCR model through the use of non-equilibrium thermodynamics", *8th International Meeting of the Hellenic Rheology Society HSR 2017*, Limassol, Cyprus, 12-14 July (2017).

5. **C. K. Georgantopoulos**, V. Dolle, and I. Vittorias, "The Identification of Arm length of Polydisperse Comb HDPE with Isolated Long Chain Branches (iLCBs)", *3th Plastic Update Conference*, Fribourg, Switzerland, 15th November (2018).

6. **C. K. Georgantopoulos**, I. F. C. Naue, A. Causa, L. Garro, and M. Wilhelm, "Investigation of Melt Flow Instabilities in SBR: Influence of MWD and Microstructure at In Situ Pressure Fluctuations as Detected by Capillary Rheology", *Nordic Rheology Society Meeting*, Gothenburg, Sweden, 21-23 August (2019).

7. **C. K. Georgantopoulos**, E. M. Khabazian, I. F. C. Naue, A. Causa, R. Kádár and M. Wilhelm, "Optical analysis as a useful tool to investigate melt flow instabilities", *18th International Congress of Rheology*, online, 13-18 December (2020).

8. **C. K. Georgantopoulos**, E. M. Khabazian, I. F. C. Naue, A. Causa, R. Kádár and M. Wilhelm, "Characterization of flow instabilities for SBR materials during extrusion flow: experiments and modeling", *Annual European Rheology Conference (AERC 2021)*, online, 13th April (2021).

9. **C. K. Georgantopoulos**, E. M. Khabazian, I. F. C. Naue, A. Causa, R. Kádár and M. Wilhelm, "Mechano-optical characterization of extrusion flow instabilities in styrene-butadiene rubbers: investigating the influence of molecular properties and die geometry", *International Rubber Conference*, online, 29th June (2021).

10. **C. K. Georgantopoulos**, E. M. Khabazian, I. F. C. Naue, A. Causa, R. Kádár and M. Wilhelm, "Derivation of simple qualitative models to predict spatial characteristics of extrusion flow instabilities", 13th Hellenic Polymer Society International Conference, Athens, Greece, 12-16 December (2021).

Curriculum Vitae

CHRISTOS K. GEORGANTOPOULOS
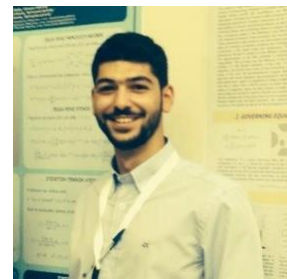
Office	**Residence**
Karlsruhe Institute of Technology (KIT)	Thujaweg 7
Institute of Technical Chemistry and Polymer Material (ITCP)	Post Code, 76149
Engesserstr. 18, Bldg. 11.23, Room 315	Karlsruhe, Germany
76131 Karlsruhe, Germany	

Tel: 00 49 721 608 48503

Tel.: 00 49 (0) 178 3099108

e-mail: christos.georgantopoulos@kit.edu (professional)

georgantopouloschris@gmail.com (private)

LANGUAGES

Native Greek, Fluent English, Intermediate German

LEISURE ACTIVITIES

Sailing races, run, theater and cooking

PERSONAL

Date of birth: September 13, 1995

Family status: Single

Citizenship: Greek

PROFESSIONAL PROFILE

An astute, PhD researcher in polymer engineering as well as specialized in rheology and processing of neat and filled polymers, with a background in chemical engineering. Specializes in polyolefin and rubber/elastomer rheological characterization, including development of qualitative models for the prediction of rheological properties and online characterization equipment. Executes the intricate details of international cooperation with excellent, proactive communication. Undertakes individual responsibilities and collaborates thoughtfully with colleagues to advocate the co-dependency between success and respect. Pursuing opportunities to optimize the work, public relations and global reach of an organization with technical and clerical insight in operations' management across public and private industry sectors.

OCCUPATION

Laboratory of Polymeric Materials (October 2018 – October 2022)
Institute of Chemical Technology and Polymer Material (ITCP), Karlsruhe Institute of Technology (KIT), Germany.
Position: PhD researcher in polymer processing and polymer engineering
Advisor: Prof. Manfred Wilhelm, Prof. Dr. Roland Kádár, Dr. Ingo Naue
Site: http://www.itcp.kit.edu/wilhelm/english/

Pirelli Tyre S.p.A. (January 2019 – April 2022)
Milano R&D department and Breuberg Factory site
Position: PhD researcher
Advisor: Dr. Andrea Causa
Site: https://www.pirelli.com/tyres/de-at/company-info

Laboratory of Polymer Rheology (April 2022 – June 2022)
Department of Chemical and Biological Engineering, University of British Columbia, Vancouver, Canada
Position: Visiting scientist
Advisor: Prof. Dr. Savvas Hatzikiriakos
Site: https://chbe.ubc.ca/profile/savvas-g-hatzikiriakos/

Laboratory of Rheology (January 2020)
Department of Industrial and Material Science, Chalmers University of Technology, Gothenburg, Sweden
Position: Visiting scientist
Advisor: Prof. Dr. Roland Kádár
Site: https://www.chalmers.se/en/staff/Pages/roland-kadar.aspx

Internship in LyondellBasell Industry (Basell Polyolefins) (June 2018 – September 2018)
Frankfurt R&D department
Position: Assistant researcher
Advisor: Dr. Iakovos Vittorias, Dr. Dolle Volker
Site: https://www.lyondellbasell.com/en/frankfurt-plant/

Laboratory of Statistical Thermodynamics and Macromolecules (May 2016 – June 2018)
Department of Chemical Engineering, University of Patras, Greece.
Position: Diploma thesis
Advisor: Prof. Dr. Vlasis G. Mavrantzas, Prof. Dr. Pavlos S. Stephanou
Site: http://lstm.chemeng.upatras.gr

Internship in LyondellBasell Industry (Basell Polyolefins) (June 2017 – August 2017)
Frankfurt R&D department
Position: Assistant researcher
Advisor: Dr. Iakovos Vittorias, Dr. Dolle Volker
Site: https://www.lyondellbasell.com/en/frankfurt-plant/

Internship in TITAN cement industry (July 2015)
Drepano TITAN plan
Position: Inter student
Advisor: Theodor Baltas
Site: http://www.titan.gr/

Laboratory of Applied Mathematics (September 2014 – May 2015)
Department of Chemical Engineering, University of Patras, Greece.
Position: Inter student
Advisor: Assistant Professor Dr. Panayiotis Vafeas
Site: http://www.chemeng.upatras.gr/laboratory-applied-mathematics

EDUCATION

PhD Candidate – Doctor rerum naturalium (Dr. rer. nat.)
Institute of Chemical Technology and Polymer Material (ITCP), Karlsruhe Institute of Technology (KIT), Germany, October 2018 – today
Thesis: "Development of Rheometric Tools to Investigate and Model Extrusion Flow Instabilities"
Advisor: Prof. Dr. Manfred Wilhelm and Prof. Dr. Roland Kádár

Master of Engineering – M. Eng. Chemical Engineering
Department of Chemical Engineering, University of Patras, Greece, September 2013 – July 2018
GPA: 7.43/10 (Very good)
Diploma thesis: "Constitutive Rheological Model for Polymeric Liquids with Variable Number of Topological Constraints"
Advisor: Prof. Dr. Vlasis G. Mavrantzas and Prof. Dr. Pavlos S. Stephanou

MILITARY SERVICE (COMPULSORY IN GREECE)
Hellenic Navy, Patra, Greece (January 2014 – January 2015). Responsible about safety and fire protection rules in Hellenic Navy base in Patra, Greece.

PROFESSIONAL GROUPS
Member of Hellenic Rheology Society (HRS) (2017 – now)
Member of Society of Rheology (SoR) (2020 – now)

AWARDS

1. Received scholarship from Erasmus PLUS (+) program for industrial internship in Frankfurt, Germany 2017 at LyondellBasell Industry, R&D department.
2. Received travel grant form Society of Rheology (SoR) for participating at *18th International Congress of Rheology (ICR)*, Rio de Janeiro, got online due Covid19 pandemic, 2020.
3. Received travel grant from Karlsruhe House of Young Scientists (KHYS) for research visit in Vancouver, Canada 2022 at University of British Columbia (UBC).